PART I

From the Lab to the Field - Recent Developments in Polymer Coated ATR Sensing for the Determination of Volatile Organic Compounds

A Thesis

Presented to

The Academic Faculty

by

Manfred Karlowatz

In Partial Fulfillment

of the Requirements for the Degree

Doctor of Philosophy in Chemistry

Georgia Institute of Technology

May 2004

PART I

From the Lab to the Field - Recent Developments in Polymer Coated ATR Sensing for the Determination of Volatile Organic Compounds

PART II

From the Field to the Lab - Investigating IR Signatures for Remote Sensing Applications

Approved by:

Dr. Boris Mizaikoff, Advisor

Dr. Jiri Janata

Dr. Frank Loeffler

Dr. Andrew Lyon

Dr. Thomas Orlando

Dr. Marcus Weck

May 5, 2004

It isn't pollution that's harming the environment. It's the impurities in our air and water that are doing it.

George W. Bush

ACKNOWLEDGEMENT

My dearest thanks and deepest respect go to my supervisor *Professor Boris Mizaikoff* who provided me with the opportunity to work in the ASL group here at Georgia Tech. Amongst many other things, his outstanding motivation abilities, profound knowledge and amazing patience make him a “boss” I dearly enjoyed working with. He and *Dr. Christine Kranz* are an incredible team and their scientific input as well as the social events around the workgroup are highly appreciated. Their guidance and inspiration helped me to grow as a scientist and person (and this it not referring to the pounds I gained throughout my stay...). And of course: Chiarra and Camillo, your beautiful paintings I received all year round and sweets donations at my birthday are highly appreciated. Thank you kids (“morningside rules!”).

Many thanks go to the whole ASL team. In the years I had the pleasure to be a part of it, we have become great friends and undoubtedly all of them contributed to making every day at work an enjoyable one!

A special thanks go to the groups of *Prof. Jiri “Art” Janata* and *Prof. Thom Orlando* for the splendid cooperation, great advice and generous access to their instruments throughout my thesis.

Furthermore, *Dr. Michael Cathcart* is highly appreciated for giving me the opportunity to start working in the exciting field of remote sensing.

I would like to thank my wonderful family, my friends and Angie for the incredible amount of love and support I receive from them. Without you this all wouldn’t have been possible!

TABLE OF CONTENTS

Chapter

ACKNOWLEDGEMENT **IV**

LIST OF TABLES **X**

LIST OF FIGURES **XII**

LIST OF ABBREVIATIONS **XVIII**

SUMMARY **XX**

1. INTRODUCTION 1

1.1. VOLATILE ORGANIC COMPOUNDS IN AQUEOUS ENVIRONMENTS 1

1.2. SCOPE OF PART 1 2

2. BACKGROUND 3

2.1. VOCS DETERMINATION STATE OF THE ART 3

2.2. OPTICAL SENSING OF VOCS IN AQUEOUS ENVIRONMENTS 4

2.2.1. Improving Selectivity and Sensitivity 7

2.2.2. Approaches to Automated Sensor Calibration 9

2.2.3. An Overview of Recent Scientific Contributions to the Field of VOCs Determination in Water by means Optical Sensor Systems 12

2.2.3.1. UV/VIS Sensors 13

2.2.3.2. Near-Infrared (NIR) Sensors 18

2.2.3.3. Mid-Infrared (MIR) Sensors 21

2.2.3.4. RAMAN Sensors 29

2.2.3.5. Laser Fluorescence Sensors 33
2.3. MID-INFRARED SPECTROSCOPY 35
2.4. ATTENUATED TOTAL REFLECTION 36
2.4.1. Principle of Attenuated Total Reflection 36
2.4.1.1. Effective Layer Thickness 39
2.4.1.2. Waveguide Materials 42
2.4.2. Recent Approaches for VOC Determination via Evanescent Wave Sensing 43
2.5. POLYMER SENSOR MEMBRANES 44
2.6. IMPROVED MODEL FOR SIMULATING DIFFUSION-BASED DATA FOR OPTICAL CHEMICAL SENSORS 47
2.6.1. Model-Based Optimized Design of Polymer-Coated Chemical Sensors 51
2.6.1.1. Physical Arrangement and Model Formulation 51
2.6.1.2. Method of Solution 54
3. RESULTS 56
3.1. LABORATORY CONDITIONS – BTX IN WATER 57
3.1.1. Introduction 57
3.1.2. Experimental Setup 58
3.1.2.1. Materials 58
3.1.2.2. Instrumentation 58
3.1.2.3. Mixmaster 59
3.1.2.4. Preparation of the Extractive Polymer Membrane 61
3.1.3. Results 63
3.1.3.1. Water Equilibration 63
3.1.3.2. BTX Enrichment Characteristics 64
3.1.3.3. Test for Field Capability: Continuous Detection of o-Xylene in a Natural Pond Water Matrix 69
3.1.4. Conclusions 72
3.2. SIMULATED FIELD CONDITIONS – VOCS DETERMINATION IN AN AQUIFER 73
3.2.1. Introduction 73

3.2.2. Experimental Setup *74*

3.2.2.1. Materials 74

3.2.2.2. Silver Halide Fibers 74

3.2.2.3. Instrumentation 75

3.2.2.4. Aquifer simulation 78

3.2.3. Sensor Calibration and Validation *80*

3.2.4. Results *84*

3.2.5. Conclusions *88*

3.3. FIELD CONDITIONS – CHLOROBENZENE IN GROUNDWATER 89

3.3.1. Experimental Setup *90*

3.3.1.1. Instrumentation 90

3.3.1.2. Preparation of the Extractive Polymer Membrane 93

3.3.1.3. Sensor System Calibration 93

3.3.2. Results *95*

3.3.2.1. SAFIRA Measurement Surrounding Conditions 95

3.3.2.2. Chlorobenzene Enrichment Behavior 97

3.3.2.3. Sensor Regeneration 102

3.3.2.4. Long Term Stability 104

3.3.2.5. Dynamic Sensor Behavior 106

3.3.3. Conclusions *107*

3.4. MODELING THE DIFFUSION BEHAVIOR OF CHEMICAL SENSORS – HOW ACCURATE ARE EXISTING MODELS? 108

3.4.1. First Case Study: A Simple Diffusion Model applied to Experimental Data *110*

3.4.2. Second Case Study: A Numerical Simulation Model based on Fickian Diffusion applied to Experimental Data *115*

3.4.3. Third Case Study: CFD Simulations (FLUENT) applied to Experimental Data ... *120*

4. CONCLUSIONS AND OUTLOOK 122

5. FROM THE FIELD TO THE LAB – INVESTIGATING IR SIGNATURES FOR REMOTE SENSING APPLICATIONS 127

6. INTRODUCTION 127

6.1. LANDMINES – A GLOBAL PROBLEM 127

6.2. COMMONLY APPLIED LANDMINE DETECTION METHODS 129

6.2.1. Ground Penetration Radar 129

6.2.2. Ultrasound 130

6.2.3. Infrared Sensor 132

6.3. CURRENT DEVELOPMENTS IN REMOTE LANDMINE DETECTION – THE DISTURBED SOIL APPROACH 133

6.3.1. Remote Sensing 135

6.3.2. Hyperspectral Imaging 136

6.4. SCOPE OF THIS THESIS 138

7. BACKGROUND 140

7.1. MID-IR SPECTROSCOPY OF MINERALS 140

7.2. MID-IR SPECTRA OF GLASSES 145

7.3. MODE SPLITTING IN MIR-SPECTRA OF CRYSTALS AND GLASSES 146

7.3.1. Impact on this Thesis 152

8. EXPERIMENTAL 153

8.1. SAMPLES 153

8.2. LABORATORY SETUP 154

9. RESULTS 156

9.1. ATR SPECTRA OF POLYDISPERSE NATURAL QUARTZ 156

9.1.1. Experimental 156

9.1.2. Wetting / Drying 157

9.1.3. Polarized Light 162

9.1.4. Conclusions 165

9.2. ATR SPECTRA OF MONO-DISPERSE SODA LIME GLASS SPHERES 166

9.2.1. Samples 167

9.2.2. Experimental 169

9.2.3. Wetting / Drying 169

9.2.4. Particle Size Dependence of Absorption Features of Soda Lime Glass Spheres in ATR Spectra 173

9.2.5. Polarized Light 179

9.2.6. Conclusions 181

10. CONCLUSION AND OUTLOOK 182

10.1. ARE ATR SPECTROSCOPIC STUDIES SUITABLE AS SUPPORTING METHOD FOR REMOTE SENSING? 182

APPENDIX 185

REFERENCES 189

LIST OF TABLES

Table 2.1 Volatile organic compounds and their maximum concentration levels for drinking water as recommended by the EPA. Reproduced from [17]. 7

Table 2.2: Waveguide materials applied at ASL for MIR evanescent field sensing. 42

Table 2.3 Comparison of $t_{95\%}$ data (time required to extract 95% of analyte amount at equilibrium conditions) for extraction of different hydrocarbons from an aqueous solution with the use of a PDMS coated NIR fiber-optic sensor system. Reproduced from [42]. 50

Table 3.1 Overview on relevant spectroscopic approaches to BTX detection in water ... 68

Table 3.2 Statistical data of the sensor calibration. Intercept *a*, slope *b*, product-moment correlation coefficient *r*, prediction error SS, standard deviation of slope s_b, intercept s_a and limit of detection LOD. n=9. 83

Table 3.3 HS-GC validation measurements of groundwater sample from shaft 5 at the SAFIRA site. 96

Table 3.4 Comparison of the ATR measurements to the HS-GC measurements 101

Table 3.5 Calculated diffusion coefficients (cm^2/s) for CB in E/P-co 114

Table 3.6 Parameters from the Bitterfeld experiments included in the Friedson and Barbari algorithm 117

Table 3.7 Calculated diffusion coefficients for the Bitterfeld field measurements via two different methods 119

Table 3.8 Comparison of the parameters of the basic flow cell used in CFD simulations (Figure 2.13 and [43]) and the flow cell used during the Bitterfeld measurements. 120

Table 6.1 Worldwide landmine distribution and clearance status 128

Table 6.2 Speed of sound in different media [213] 131

Table 8.1 Measurement Parameters for ATR studies 154

Table 9.1 Relevant properties and chemical compositions of the soda lime glass spheres. 168

Table 9.2 Band assignments for soda lime glasses with similar composition [293,294,295] 170

Table 9.3 Revised band assignments for soda lime glass as suggested by Efimov [285].. The revised bands have been shaded for clarity. 172

LIST OF FIGURES

Figure 2.1 Transmission UV spectra of 50 mg/L of the BTX compounds in aqueous solutions in a 1 cm path length quartz cuvettes [82]. 14

Figure 2.2 Comparison of absorbance measured with a 100 µg/L solution of benzene in water (bottom spectrum, scaled 16 time in the dotted spectrum on top) taken with an optical pathlength of 1 cm and absorbance spectrum measured in PDMS block (0.2 cm optical pathlength) after immersion in the solution for 60 min [55]..... 17

Figure 2.3 Illustration of evanescent wave sensing principle (circle at the right bottom) and instrumental setup of coiled fiber-optic sensor and NIR bandpass filter photometer unit (fiber sensor element installed in a flow cell) [41]. 20

Figure 2.4 Response signals vs. time obtained with the NIR evanescent wave fiber-optic photometer system (fiber length 30m) for measurements of aqueous solutions of technical grade xylene (laboratory calibration of sensor system). Absorbance over time data are given for both measuring channels of the photometer located at central wavelengths of 1715 and 1645 nm [41]. 21

Figure 2.5 The most commonly used mid-IR transparent fiber-optic materials and their relevant properties for fiber-optic sensing. It can be seen that attenuation values for the long-wave range need to be further reduced for remote sensing applications. Transmission and attenuation data are the average of reported values [46]..... 23

Figure 2.6 Trace of carbontetrachloride (CT), trichloroethylene and tetrachloroethylene (PCE) in the effluent of a dechlorination reactor measured with evanescent wave ATR-FTIR spectroscopy. The ZnSe ATR element was coated with a polyisobutadiene extraction membrane. The lines show the predicted concentration values after PLS treatment of absorption spectra. Validation with GC shows good agreement [99]..... 26

Figure 2.7 3D illustration of the FT-IR underwater instrument. Main optics and electronics originate from a Bruker Vector 22 FT-IR spectrometer. IR radiation is launched into a flexible, polymer coated AgX fiber, which penetrates the aqueous medium facilitating highly sensitive and selective IR measurements in the marine environment [101]..... 27

Figure 2.8 Sensor dynamics shown for repetitive analyte injections into the flume tank 0.62 mg/L tetrachloroethylene, 0.77 mg/L 1,2-dichlorobenzene and 3.48 mg/L of the xylene isomer mixture were injected at t = 1 min and then every 30 min. The decreases of the readings after the maxima are attributed to dilution of the analyte plume in the solution and to analyte evaporation into the

surrounding atmosphere during measurements in the open flume tank system [101]..... 28

Figure 2.9 Background-subtracted Raman spectrum of a mixture containing 70 mg/L benzene, 100 mg/L toluene and 100 mg/L p–xylene. Spectrum recorded with a liquid core waveguide setup [116]..... 31

Figure 2.10 Schematic of a fiber-optic laser induced fluorescence instrument for in-situ detection of water pollutants. PD: Photodiodes. FI: edge filter. MO: monochromator. MCP: multichannel plate image intensifier. CCD: slow-scan CCD-line camera. ADC: analog-to-digital converters [132]. 35

Figure 2.11 Illustration of the ATR principle..... 37

Figure 2.12 Exemplary enrichment curves for CB (30 ppm) into a 10 µm E/P-co layer for different flow-conditions: 10 mL/min (triangles), 100 mL/min (diamonds) and 750 mL/min (squares) [166]..... 49

Figure 2.13 Schematic of the flow cell and coordinate system for the hydrodynamic model [43]. 52

Figure 3.1 Schematic of the combination of the Mixmaster with the ATR setup for dissolved BTX measurements. 59

Figure 3.2 Front view of the Mixmaster..... 60

Figure 3.3 IR absorptions resulting from water diffusion into an E/P-co membrane with a thickness of 4.2 µm coated onto the surface of a ZnSe ATR-crystal over a period of 32 h. After 24 hours (f) equilibrium conditions are reached and no further increase in absorption is observed. 63

Figure 3.4 IR absorption spectrum of a sample mixture in aqueous solution after enrichment into an E/P-co layer. Enrichment time: 20 min, concentration: 500 ppb (v/v) each. 65

Figure 3.5 Typical enrichment curves for the BTX components in water at a concentration level of 1 ppm (v/v) each into an E/P-co coating. Equilibrium of the diffusion process is reached after approximately 18 min of enrichment time. 66

Figure 3.6 Calibration graphs for benzene, toluene and the xylene isomers in the concentration range of 0 – 1000 ppb (v/v) based on peak area integration. The error bars represent the standard deviation of five subsequent measurements 67

Figure 3.7 Trace of the peak area of the absorption band of o-xylene at 740 cm^{-1} with time during enrichment based IR-ATR sensing. Concentration trace: 50 ppm; 80 ppm; 20 ppm (in pond water; the sensor was exposed to each

concentration for approx. 30 to 35 min) followed by neat pond water for sensor regeneration. 71

Figure 3.8 Close up of the sensor head, showing the active transducer section of the fiber (1), the o-ring seal lead-troughs (2), the two stainless steel tubes containing the sensor head/fiber cable interface (3) and the fiber cables (4). For the described measurements the semicircular part covering parts of the active transducer was removed. 77

Figure 3.9 Sketch of the aquifer simulation "Munich North" (side view). 79

Figure 3.10 Linear regression (solid) and confidence intervals (P=95 %; dash dotted) of the sensor response (circles). 82

Figure 3.11 Comparison of concentrations measured by IR sensor (red), reference HS GC (green with dots) and analyte concentration added to the water stream (blue). Confidence intervals (P=95%, n=9) at $\bar{y}$ are ± 0.6 mg/L (DCB), ± 0.7 mg/L (TeCE) and ± 2.3 mg/L (TriCE), respectively. 85

Figure 3.12 During a measurement campaign of three days the single beam spectra changed in shape and overall light throughput as a result of water intrusion. The first spectrum was recorded ten hours before the first experiment (i.e. series 1), the other three at the beginning of each series, respectively. For all spectra the sensor head was immersed in water. Note the strong decrease in light throughput on the third day leading to an impaired signal-to-noise ratio. 86

Figure 3.13 Left: Scheme of the custom made flow cell. Right: Picture of the flow cell (disassembled) 91

Figure 3.14 Schematic of setup for on-site chlorobenzene measurements. 92

Figure 3.15 The C-H out of plane vibration band of CB for 5 different concentrations after partitioning into the E/P-co layer. 94

Figure 3.16 Calibration curve for 3 repetitive measurements of the calibration set of CB. Error bars are derived from the standard deviation for each data point. 95

Figure 3.17 Exemplary spectra of a groundwater sample from shaft 5 (grey line) and a calibration solution of 50 mg/L CB in water (black line). Spectra were recorded after 24 min of exposure time to the polymer coated transducer. The peak area of the band at 740 cm^{-1} is used for data evaluation. 98

Figure 3.18 Enrichment curves of CB from groundwater at SAFIRA site into the E/P-co layer at a flow rate of 4 mL/min. The 3 measurements were performed at 3 different days. 99

Figure 3.19 Enrichment curves of CB from groundwater at SAFIRA site into the E/P-co layer at a flow rate of 23 mL/min. The 2 measurements were performed at 2 different days. 100

Figure 3.20 Exemplary spectra of a groundwater sample from shaft 5 (black line) and a successively recorded spectrum after regenerating the sensor with distilled water (grey line). Enrichment time and regeneration time were both 24 min with a flow rate of 4 mL/min. The peak area of the band at 740 cm^{-1} is used for data evaluation. 102

Figure 3.21 Enrichment and regeneration cycle for CB at 4 mL/min (squares) and 23 mL/min (diamonds). 103

Figure 3.22 Long term stability test for CB measurements in groundwater. The flow rate was set to 4 mL/min. The lack of data in the time period from 400 to 900 min is due to occupancy of the spectrometer by fiberoptic measurements..... 105

Figure 3.23 Simulation of a chemical spill event, by adding a significant amount of CB to the groundwater sample (at t=14min) after the sensor system was equilibrated with the groundwater sample. 106

Figure 3.24 Enrichment curves of CB from groundwater at SAFIRA site into an E/P-co layer at a flow rate of 4 mL/min. The 3 measurements were performed at 3 different days. 111

Figure 3.25 Enrichment curves of CB from groundwater at SAFIRA site into the E/P-co layer at a flow rate of 23 mL/min. The 2 measurements were performed at 2 different days. 112

Figure 3.26 $Abs_{(t)} / Abs_{max}$ versus $t^{0.5} / d$ plot for the 5 CB enrichment experiments. The series marked with diamonds and circles refer to the high flow rate (23 mL/min) the other 3 series to the lower flow rate (4 mL/min). 114

Figure 3.27 Exemplary results from the iterations for one data series obtained with low flow rate (4mL / min, Run3) and one with high flow rate (23 mL/min, Run4). The calculated diffusion coefficients are printed in the graph. 118

Figure 3.28 Time to steady state (equilibrium) vs. flow channel height for 2 different flow velocities modeled with CFD for the basic flow cell shown in Figure 2.13... 121

Figure 6.1 Principle of Remote Sensing Techniques 135

Figure 7.1 Infrared active internal vibrations of quartz. Left: v_3-asymmetric stretch Right: v_4-asymmetric bend []. 141

Figure 7.2 Approximate frequency range of common internal vibrations of silicates, oxides and other functional groups within minerals [245]. 142

Figure 7.3 General scheme for quantitative IR band assignment for glasses. Reproduced from [285]. 151

Figure 7. 4 Scheme for quantitative IR band assignment for glasses starting from IR reflectance measurements. Reproduced from [285]. 152

Figure 8.1 Experimental setup for cyclic wetting/drying studies of quartz sand via ATR spectroscopy in the MIR regime. 155

Figure 9.1 Overview of experimental procedure. 157

Figure 9.2 Exemplary IR-ATR spectrum of pristine quartz sand (Fluka 83340). The broad absorption feature with a maximum at around 1090 cm^{-1} is attributed to asymmetric stretching vibrations, the double peak at around 800 cm^{-1} relates to a symmetric stretching of the SiO_4 unit cell and the peak at 690 cm^{-1} is related to Si-O-Si bending vibrations. The inset shows an optical microscopy image of the sample. 158

Figure 9.3 Pristine (a), dried (b) and disturbed (c) spectra of quartz sand. The sharp band around 670 cm^{-1} results from atmospheric CO_2 present after opening the sample compartment. 159

Figure 9.4 Microscopy pictures of the finest fraction (left) and the coarsest section (right) of the investigated quartz sample. 160

Figure 9.5 Dried Spectra of a mixed (a), fine (b) and coarse (c) fraction of quartz sand. The spectra of the coarse fraction were scaled, due to very weak absorption features. 161

Figure 9.6 Schematic of agglomeration process of ultrafine quartz particles on the crystal surface during the wetting / drying process. 162

Figure 9.7 ATR spectra of pristine quartz sand samples recorded at different polarization states of infrared radiation: (a) unpolarized light (grey line), (b) p-polarized light (black line), (c) s-polarized light (dotted line). 163

Figure 9.8 ATR spectra of pristine quartz sand samples recorded at different polarization states of infrared radiation: (a) unpolarized light (grey line), (b) p-polarized light (black line), (c) s-polarized light (dotted line). 164

Figure 9.9 Optical microscopy images of soda lime glass spheres. The two smallest size fractions were obtained from the MO-SCI corporation (images on top). The larger size fractions were obtained from Whitehouse Scientific (images at the bottom). 169

Figure 9.10 The ATR spectrum of 112 µm soda lime glass spheres. 170

Figure 9.11 The ATR spectrum of 112 µm soda lime glass spheres (a) compared to a transmission spectrum (KBr pellet) of a 150 to 250 µm size fraction of soda lime glass with a very similar composition (b) (spectrum reproduced from [293]). 171

Figure 9.12 Pristine (a), dried (b) spectra of the 112 µm soda lime glass spheres. 173

Figure 9.13 ATR spectra of silica-gel particles with various diameters [296]..... 174

Figure 9.14 ATR spectra of soda lime glass spheres with different diameters: 400 µm (a), 112 µm (b), 25 µm (c). 175

Figure 9.15 ATR spectra of soda lime glass spheres with different diameters: 400 µm (a), 112 µm (b), 25 µm (c), 4 µm (d) and 1 µm (e)..... 176

Figure 9.16 Normalized (at 1040 cm^{-1}) ATR spectra of soda lime glass spheres with diameters of: 400 µm (a), 112 µm (b), 25 µm (c), 4 µm (d) and 1 µm (e) 177

Figure 9.17 FTIR spectra of $Na_2O–CaO–P_2O_5–K_2O–MgO–B_2O_3–SiO_2$ glasses with different SiO_2 content: (i) 66%, (ii) 59%, (iii) 55%, (iv) 50% and (v) 42% [299]. 178

Figure 9.18 S-polarized ATR spectra of soda lime glass spheres with different diameters: 400 µm (a), 112 µm (b), 25 µm (c), 4 µm (d) and 1 µm (e). Data has been normalized in intensity. 179

Figure 9.19 P-polarized ATR spectra of soda lime glass spheres with different diameters: 400 µm (a), 112 µm (b), 25 µm (c), 4 µm (d) and 1 µm (e). 180

Figure 10.1 Schematic of the environmental chamber developed for temperature and humidity studies on ATR measurements for quartz and other minerals. 187

LIST OF ABBREVIATIONS

AgX	Silver Halide
a-SiO2	Amorphous Silica
ATR	Attenuated Total Reflection
BTX	Benzene, Toluene, Xylenes
CB	Chlorobenzene
CFD	Computational Fluid Dynamics
DCB	Dichlorobenzene
E/P-co	Ethylene/Propylene Co-polymer
EM	Electromagnetic
FEWS	Fiberoptic Evanescent Wave Spectroscopy
FIA	Flow Injection Analysis
FID	Flame Ionization Detector
FTIR	Fourier Transform Infrared
GC	Gas Chromatography
GPR	Ground Penetrating Radar
HPLC	High Pressure Liquid Chromatography
HS-GC	Head Space Gas Chromatography
IR	Infrared
IRE	Internal Reflection Element
LO	Longitudinal
LOD	Limit of Detection
MCL	Maximum Concentration Level
MCT	Mercury-Cadmium-Telluride
P&T	Purge and Trap
PCR	Principle Component Regression
PCs	Principle Components

ppb	Part Per Billion
ppm	Parts Per Million
RS	Raman Scattering
SIA	Sequential Injection Analysis
SPE	Solid Phase Extraction
SPME	Solid Phase Micro-Extraction
TCE	Trichloroethylene
TeCE	Tetrachloroethylene
TO	Transversale
US	Ultrasound
VOCs	Volatile Organic Compounds
ZnSe	Zinc Selenide

SUMMARY – PART I

The increasing interest in the research field of versatile chemical sensing systems is governed to a significant extent by the range of in-situ and on-line applications demanded in all aspects of modern instrumental analysis, such as industrial process analysis, environmental monitoring or pharmaceutical and biological/biochemical analysis. Common to these areas is the acceding effort to efficiently monitor and control various environmental, health and process related parameters with high molecular specificity. The increasing number of environmentally relevant pollutants and the demand for efficient methods to control industrial processes serve as a substantial argument for the development of rapidly responding, selective and reliable sensing devices.

Amongst the various physico-chemical transducer principles, optical sensing schemes have a promising potential as they provide the opportunity for remote sensing at a wide variety of conditions. Sensor systems operating in the mid-infrared (mid-IR) spectral region (approx. 2 – 20 µm) of the optical spectrum allow the availability of reliable and robust sensing systems with high inherent molecular specificity. Sensing applications in this spectral regime are particularly facilitated by direct evaluation of well-structured, molecule specific absorption bands resulting from the excitation of fundamental vibrational and rotational transitions of the analyte molecules.

Most mid-IR sensing approaches rely on a well established spectroscopic technique known as *attenuated total reflection* (ATR) spectroscopy probing analyte concentrations via interactions with the *evanescent field*. Along with continuous progress in the development of mid-IR-transparent optical waveguides, this method has enabled the extension of conventional IR spectroscopy towards field applicable spectroscopic sensing systems. Methods based on direct analyte interaction without chemical

modification of the waveguide surface are generally subject to interferences by IR absorbing sample components or the sample matrix itself, and generally suffer from limited sensitivity prohibiting their application in e.g. environmental trace analysis. Hence, the majority of mid-IR sensing approaches increase selectivity and sensitivity by modifying the waveguide surface with appropriate molecular recognition layers serving as solid phase extraction membrane for the analytes of interest, while simultaneously minimizing interferences of matrix components.

Contamination of drinking water, ground water and seawater with volatile organic compounds (VOCs) poses a significant health risk to humans and awareness of the public towards this matter increased considerably in recent years. Pollutants such as chlorinated hydrocarbons (CHCs), aromatic hydrocarbons (AHCs) and within the latter category especially benzene, toluene and xylenes (BTX) are among the most commonly detected organic contaminants in water. Consequently, benzene, chloroform and trichloroethylene occupy a permanent place among the 20 most relevant priority pollutants in the listings of the Comprehensive Environmental Response, Compensation, and Liability Act (CERCLA).

Standard methods for VOCs analysis include purge-and-trap (p&t) and static headspace (HS) gas chromatography (GC) combined with flame ionization detection (FID), among other GC techniques with hyphenated more sophisticated detection systems such as mass spectrometry. Complementary to these methods, solid phase extraction (SPE) techniques have been introduced for pre-concentration of environmental samples and chromatographic analysis after elution of enriched species with suitable organic solvents. Furthermore, the generally necessary sampling step for such laboratory based methods introduces a significant error source into the analysis procedure resulting from the physical properties of VOCs. Volatilization and diffusion losses make specific – and

usually expensive - sampling and storage procedures necessary. Therefore, on-site in-situ sensor systems are of particular demand in this area of environmental analytics. Preliminary works have already demonstrated the potential of evanescent wave MIR sensing for environmental monitoring. Particularly, zinc selenide (ZnSe) crystals and silver halide (AgX) fibers both coated with a thin layer of hydrophobic polymer led to promising results of such sensing schemes in recent years.

In this thesis, considerable efforts have been made to transition these devices from a laboratory environment to real world field applications detecting and quantifying VOCs in water. The presented work is divided into the following components, which ultimately led to the first successfully performed field measurement campaigns of IR evanescent field sensor system:

(i) Improvement of sensor calibration by introducing the “Mixmaster”, an automated mixing system based on sequential injection analysis (SIA) specifically adapted for accurate mixing and handling of dilute solutions of VOCs in water. Introduction of the *Mixmaster* facilitated repetitive evanescent sensor calibrations, along with more reliable and less error-prone preparation of calibration sets. Based on this system, simultaneous, quantitative detection of mixtures of BTX in water during enrichment into ethylene-propylene copolymers (E/P-co) coated onto ZnSe ATR elements has been performed. The obtained results showed accurate detection and quantification to the low ppb concentration region setting a new benchmark for laboratory based spectroscopic measurements for this group of compounds (published in *Analytical Chemistry, 2004, 76(9), 2643-2648).*

(ii) Fiber-optic evanescent field measurement campaigns based on E/P-co coated AgX fibers have been conducted at simulated field conditions at a simulated aquifer system located at the Technical University of Munich. Various VOCs

have been introduced into the water stream of the aquifer system and the concentration gradients of trichloroethylene (TCE), tetrachloroethylene (TeCE) and 1,2 dichlorobenzene (DCB) have been monitored with the sensor system. A fiber-optic sensor head in combination with a 6m long AgX fiber facilitated direct measurements in a borehole in the aquifer system, representing the first demonstration of remote groundwater monitoring by FT-IR based spectroscopic sensors. HS-GC validation measurements were in good agreement with the sensor data, although after 3 days increasing fiber degradation could be observed due to membrane delamination (published in : *Applied Spectroscopy, 2003, 57(6), 607-613* and *Water Science and Technology 2003 47(2), 121-126*).

(iii) For the first test of an ATR based polymer coated sensor system under real world field conditions measurements were performed at the SAFIRA site (German acronym for ‘‘Remediation Research in Regionally Contaminated Aquifers’’), a remediation pilot plant in the region of Bitterfeld / Wolfen (Saxonia-Anhalt, Germany). The applied sensor system consisting of an E/P-co coated ZnSe crystal mounted into a flow-cell designed and developed in the course of this work was used to accurately determine the chlorobenzene concentration in the Bitterfelder groundwater at mg/L levels. Validation was performed with HS-GC measurements. Different aspects of the sensor system including accuracy, repeatability, long term stability and dynamic behavior have been tested. An interesting aspect of these measurements was the experimental proof of the dependence of analyte extraction properties on the flow conditions of the sample matrix surrounding the extractive polymer membrane influencing the response time of the sensor system. These findings are in agreement with extensive computational fluidic dynamics (CFD) simulations, which have recently been presented by our group and collaborators. As a consequence, generally

accepted numerical models solely based on Fickian diffusion, which have been widely adopted to calculate e.g. diffusion coefficients of molecule / polymer combinations are doubted in their correctness for obtaining quantitative results (publications in preparation).

The obtained results demonstrate that MIR evanescent field sensors are suitable for in-situ analysis in environmental monitoring applications at real world field conditions.

SUMMARY – PART II

Landmine detection via remote sensing techniques is a challenging analytical and spectroscopic task. Efforts in detecting small buried objects aim at the combination of various spectroscopic techniques to assess changes in the spectral signatures of soils resulting from landmine insertion. For example, measurements of disturbed soils have shown different spectral contrast in comparison to undisturbed soils [1-5]. To date, these findings are predominantly based on experimental data obtained in real world environments using hyperspectral imaging systems. Hence, it is of great interest to fundamentally investigate the disturbed and undisturbed soil phenomena in a controlled environment. Based on these measurements reliable theoretical models can be established leading to improved interpretation of these features for landmine detection scenarios. In a first step, measurements at controlled laboratory conditions have been performed to investigate individual minerals of the soil matrix and their spectral characteristics at a variety of environmental conditions. Attenuated total reflection (ATR) spectroscopy has been identified as a suitable spectroscopic technique superior to emissivity or reflectance measurements, mainly due to its reproducibility and versatility, while contributing useful data toward fundamental understanding of spectral signatures relevant to remote sensing. Due to the high abundance in natural soils, pure quartz sand (SiO_2) has been selected as the first test matrix. For the investigation of spectral differences between pristine and disturbed quartz sand, a wetting/drying procedure with subsequent sample aerating has been developed, which in a first approximation represent, a sufficient simulation of weathering processes and their impact on related soil disturbances.

This first study could contribute substantial findings which despite of the potential usefulness have not been exploited for remote sensing data evaluation up to now.

Besides the already established differences in spectral contrast of disturbed and undisturbed soil, a strong spectral shift of the maximum of the main absorption feature at 1090 cm^{-1} could be observed. When probed with s- or p-polarized light, the quartz sample showed strong LO-TO mode splitting, which is most likely related to the Berreman effect. These findings advance the variety of spectral characteristics useful to the detection of disturbed soils (i.e. possible landmine sites) with mid-infrared imaging systems. The wetting and drying studies also reveal that the main reason for spectral differences of pristine and disturbed soils eventually relates to changes of the particle size distribution of the sample due to rearrangement of ultrafine particles facilitated by water *(in press 2004: Proceedings SPIE, 5415(Detection and Remediation Technologies for Mines and Minelike Targets IX)*

In a series of experiments mono-disperse soda lime glass spheres have been investigated at the same experimental conditions as the quartz samples in the preliminary study. By the application of these mono-disperse samples the aspect of a possible effect of various particle shapes in case of quartz samples was suppressed. It could be shown that no changes in the spectra during the wetting and drying cycles are apparent if only one size of spheres was applied. This corroborates the assumptions that a changed particle size distribution in the probed volume is the main factor for the spectral differences for disturbed / undisturbed soil systems.

Furthermore, strong spectral shifts and relative band intensity changes are observed when comparing spectra derived from different discrete particle size fractions. The most dominant relative band intensity changes could be assigned to a monotonously increasing non bridging oxygen Si-O stretch vibrational band in accordance with increasing sphere sizes. Measurements performed under linearly polarized light illuminations of the sample could corroborate this finding (publication in preparation).

The presented results advance the variety of spectral characteristics useful to the detection of disturbed soils (i.e. possible landmine sites) with mid-infrared imaging systems.

1. Introduction

1.1. Volatile Organic Compounds in Aqueous Environments

Contamination of drinking water, ground water and seawater with volatile organic compounds (VOCs) poses a significant health risk to humans [6-9] and awareness of the public towards this matter increased considerably in the recent years. Pollutants such as chlorinated hydrocarbons (CHCs), aromatic hydrocarbons (AHCs) and within the latter category especially benzene, toluene and xylenes (BTX) are among the most commonly detected organic contaminants in water [10-15]. As an example for the significance of such compounds as environmental pollutants benzene, chloroform and trichloroethylene occupy a permanent place among the 20 most relevant priority pollutants in the listings of the Comprehensive Environmental Response, Compensation, and Liability Act (CERCLA) [16].

In a 1999 report of the Environmental Protection Agency (EPA) a quite unsettling finding was that seven of the 21 listed VOCs [17] occur in all 12 States studied in the USA, in either surface or ground water systems. Those were ethylbenzene, *cis*-1,2-dichloroethane, tetrachloroethylene, trichloroethylene, vinyl chloride, 1,1,1-trichlorethane, and xylenes. Many VOCs occur in up to 30 percent of surface or ground water systems in various States [18]. This again conveys the significant need for continuous monitoring of surface and ground waters to ensure the quality of drinking water supplies.

1.2. Scope of Part 1

Important pioneering work in the field of VOCs detection via polymer coated ATR-FTIR spectroscopic sensor systems originates from continuous research in the field of vibrational spectroscopy and chemical sensor technology formerly performed at the "Chemical Sensors Laboratory" at the Institute of Analytical Chemistry, Vienna University of Technology, and now at the "Applied Sensors Laboratory" at the School of Chemistry and Biochemistry, Georgia Institute of Technology. Starting more than a decade ago [19], the first principles of IR chemical sensing systems have been established and evolved into a comprehensive body of research with a substantial diversity of research areas and disciplines involved [36,38,46,59,60,73,76,84,92,93,95,96,100,101,139, ,145,166,174,175,192].

The objective of this PhD thesis was to facilitate the transition from extensive laboratory studies to simulated and real world field measurements with IR evanescent field chemical sensor systems. This challenging task was approached by fulfilling several milestones:

- Improved calibration possibilities by introducing an automated mixing system (*Mixmaster*)
- Quantitative and simultaneous determination of multi-component mixtures of VOCs with a polymer coated ATR sensor systems
- A measurement campaign at an aquifer system under "simulated field conditions" yielding promising results with a polymer coated mid-IR fiber-optic setup
- Accomplishment of accurate determination of the chlorobenzene concentration in a natural groundwater stream by the means of the proposed sensor system

Furthermore, very recent results from CFD simulations, which lead to questioning the generally accepted assumption that the signal generation kinetics for polymer coated evanescent wave sensor systems is solely based on Fickian diffusion of the analyte molecules into the thin extractive polymer layer. Calculations and model comparisons have been conducted in order to verify if nowadays commonly used methods.

2. Background

2.1. VOCs Determination State of the Art

Standard methods for VOCs analysis include purge-and-trap (p&t) and static headspace (HS) gas chromatography (GC) combined with flame ionization detection (FID), among other GC techniques with hyphenated more sophisticated detection systems [20,21]. Complementary to these methods, solid phase extraction (SPE) techniques have been introduced for pre-concentration of environmental samples and chromatographic analysis after elution of enriched species with suitable organic solvents [22,23]. A useful review summarizing analytical techniques for the determination of organic and inorganic chemicals in natural waters, wastewater, and drinking water has been published recently by Dietrich et al [24]. Classical analytical approaches are usually confined to a laboratory environment and require costly, error-prone and time consuming sampling procedures and/or include increasingly restricted usage of organic solvents.

Hence, considerable interest in developing analytical tools for the determination of such contaminants is evident prioritizing continuous operating in-situ devices capable of VOCs detection and/or continuous monitoring as well as quantitative discrimination at trace concentration levels. Continuous water quality monitoring requires qualitative and quantitative measurement of a wide range of adverse compounds in the liquid phase or

in the gas phase. It is estimated that worldwide daily 70.000 synthetic chemicals are used, including approx. 700 different organic constituents, making quality monitoring of for instance drinking water a challenging task [25]. Hence, there is a tremendous demand for continuously operating analytical systems and it is not surprising that chemical sensor technology is among the fastest growing disciplines in modern analytical chemistry. General introductions to chemical sensors can be derived from various books [26-28] and wide variety of applications of chemical sensors has been reviewed by Janata et al. over several years [29-34]. Besides electrochemical transducers, mass-sensitive devices and thermal sensing schemes, robust and versatile optical sensors gain significant importance for environmental monitoring, process control and, the biomedical field.

2.2. Optical Sensing of VOCs in Aqueous Environments

General aspects of optical sensing will be briefly discussed in this chapter. More detailed information on optical sensors and their applications can be found in [35, 36].

Depending on the field of application, optical sensing offers several advantages over other sensing concepts. The signal is optical and, hence, not susceptible to strong magnetic fields, surface potentials, or electrical interferences, e.g. by static electricity. Low-loss optical fibers allow the transmission of optical signals over long distances, enabling remote sensing. Miniaturization allows the development of small, lightweight, and flexible sensing devices. Furthermore, optical sensors are suitable for use in harsh environments like explosion hazard areas as encountered e.g. in mining and petroleum industries.

Over the past 20 years major developments in opto-electronics and fiber-optic communications have revolutionized the telecommunications industry by providing reliable high performance telecommunications links with ever decreasing bandwidth costs. Especially, high-performance silica-based glass fibers are of crucial importance or a rapid exchange of substantial amounts of data. As a consequence of the research in this industrial field component prices have decreased and quality has improved, the ability of fiber-optic sensors to displace traditional sensors for temperature, pressure, rotation, humidity, chemical measurements and other sensor applications has been facilitated.

Two groups of fiber optic sensing systems are generally distinguished:

1. Optical sensor based on direct detection of changes of optical analyte properties or spectral characteristics (*direct sensor*).
2. Chemical optical sensors based on a variety of analyte interaction/recognition/reaction processes at the sensor surface and optical transduction of chemical signals upon interaction of the analyte with the recognition element (*indirect sensors, indicator based-sensors*).

Frequently optical sensors are also classified as follows:

1. *Intrinsic sensors*, where the analyte directly interacts with the radiation transported in the optical fiber.
2. *Extrinsic sensors*, where the analyte affects the light properties while propagating in a medium external to the fiber (in this case the fiber acts only as a waveguide to transmit light to and from the active sensing region).

The combination of these concepts has been realized as so-called *physio-chemical sensors* taking advantage of both principles, e.g. sensors based on enrichment of analytes into a polymer membrane coated onto an optical fiber surface. Such sensor membranes may generate sensor responses, due to bulk changes of optical membrane properties (e.g. refractive index) or may act as a solid phase micro-extraction (SPME) membrane for enrichment of analytes in the vicinity of the waveguide surface utilizing the evanescent field analyte detection [37-41]. Response time and sensitivity depend mainly on the partition coefficients for the respective analyte between aqueous solution and polymer membrane. Hence, thorough investigation of polymer properties is required for fine-tuning and optimization of the sensor behavior. Reversibility of the sensor system is ensured since the enrichment is entirely based on diffusion without any chemical reaction inside the membrane. Thus, concentration fluctuations resulting from a shift of the partition equilibrium conditions can be continuously measured. Recently, interest was focused on improving the response time of such sensors by evaluating diffusion derived data at times prior to reaching equilibrium conditions [42]. Another interesting contribution for improved performance of such coated fiber sensor systems was published by Phillips et al [43] showing that also surrounding flow conditions of the sensor contribute significantly to the diffusion kinetics and should be taken into account during sensor development. Excellent reviews on the various applications of fiber-optic sensors [44-46] and on polymers used for fiber-optical sensors [47] have been published recently.

2.2.1. Improving Selectivity and Sensitivity

The quest for improved selectivity and sensitivity remains the cornerstone of optical sensor technologies or, more generally, for chemical sensors. In this section the requirements for a sensor (system) specifically for the determination of VOCs in water will be discussed. In order to illustrate the challenging task of quantitative and qualitative determination of VOCs in aqueous environments all 21 VOCs listed by EPA as of contaminants regarding drinking water regulations, together with their Maximum Contaminant Levels (MCLs) are shown in Table 2.1. The MCL represents the highest level of a contamination allowed in drinking water and is an enforceable standard.

Table 2.1 Volatile organic compounds and their maximum concentration levels for drinking water as recommended by the EPA. Reproduced from [17].

contaminant	MCL (µg/L)	contaminant	MCL (µg/L)
benzene	5	trans-1,2-dicholoroethylene	100
carbon tetrachloride	5	dichloromethane	5
chlorobenzene	100	1,2-dichloroethane	5
o-dichlorobenzene	600	1,2-dichloropropane	5
p-dichlorobenzene	75	ethylbenzene	700
1,1-dichloroethylene	7	styrene	100
cis-1,2-dichloroethylene	70	tetrachloroethylene	5
1,2,4-trichlorobenzene	70	toluene	1000
1,1,1,-trichloroethane	200	vinyl chloride	2
1,1,2-trichloroethane	5	xylenes	10000
trichloroethylene	5		

A successful sensor (system) should have the ability to discriminate between 230 µg/L of p-dichlorobenzene (3-times the MCL) or the same concentration of o-dichlorobenzene (still below the MCL limit), should be immune to or calibrated against cross-interferences and changing measurement conditions (such as other contaminants, temperature, pH etc.) and deliver robust performance over a long period of application time. It is needless to say that optical sensors technologies have not yet managed to accomplish all these requirements. As recently published works show, performances and diversity of optical sensors in this field are steadily improving (see chapter 2.2.3), however, many relevant analytical tasks still are calling for the need of high-end laboratory solutions. Nevertheless, in the last years optical sensors have reached a development state, which allowed first applications in process control [48], waste water analysis and remediation [41,49] and chemical spill detection [50].

Major improvements in sensitivity and selectivity of sensor systems in the last years can be generally attributed to one of the following approaches (or combinations thereof):

(i) Application of (semi) selective membranes for analyte enrichment directly on the surface of the waveguide [37-41] and detection via evanescent wave sensing, or analyte enrichment and direct measurement in the membrane with spectroscopic techniques other than evanescent wave sensing [51-55]. Thin layers of hydrophobic polymers usually enhance the limits of detection (LODs) for various VOCs by several orders of magnitude. Enrichment into such membranes follows the principles of SPME. Further information on SPME can be derived from [22,23,56]. For a theoretical treatment of the mass transfer of volatile organic compounds into membranes from aqueous solutions refer to [57].

(ii) Methods for evaluating data have improved significantly in the last decade including partial least-squares, principle component regression, cluster analysis, and computational neural networks just to mention some of the powerful chemometric methods nowadays applied for sensor (arrays) data evaluation. Recently published work [58-60] should be highlighted, which represents interesting contributions to the problem of uncalibrated features in data sets, a problem common to many sensing devices. For further information on modern data evaluation techniques please refer to recently published books [61-63] and publications [64-69].

2.2.2. Approaches to Automated Sensor Calibration

In general, well performed calibration procedures are a basic requirement for a reliably and accurately working sensor (system). For the special case of multiple component mixtures of VOCs in water at environmental relevant concentrations this “routine” task can be problematic for following reasons:

- Reproducible preparation of accurate aqueous solutions of volatile compounds at trace level concentrations is difficult due to evaporation losses.
- Storing of standards has to be performed headspace-free and cooled.
- In general, all VOCs have a strong tendency to enrich in any polymer matrix (see sensors based on solid phase extraction principles), which limits the materials used for storing, solution delivery, sealings, gaskets, flow-cell construction etc. to glass and metals.

Unfortunately, literally all existing sensors and sensor systems require extensive calibration (“training”) prior to delivering reliable results, especially in out-of-laboratory conditions. Sensor calibration can be even more tedious in case of multi-component sensing applications usually leading to a need for advanced data evaluation methods, which can cause the calibration set to substantially increase in size. Furthermore, regularly scheduled calibration of sensors and analyzer systems is usually a necessity and tedious. This creates a high demand for reliable methods of creating accurate calibration solutions, in high numbers and if possible automated in a short time, and consequently, computer controlled automated sample preparation systems. Whereas mixing units for gas analysis are readily available, there is a lack of instrumentation for accurate preparation of liquid samples, which is surprising considering the evident need for sensor calibration in VOC analysis. Only few approaches have been presented in the field of automated sample preparation devices suitable for such calibration tasks that can handle liquids at volumes (generally >mL) suitable for optical sensors.

A system using computer-controlled micropumps for automated sample preparation was presented by Lapa et al [70]. For each analyte one pump is required with the outputs confluent at a certain point. Behind, a mixing coil is located providing homogeneous solution of different analyte portions. The setup is based on a rather high repetition rate of complete pump strokes aspirating small volumes. However, the concentrations are not constant across the entire sample volume. On account of stacked analytes, there are obvious steps apparent in the concentration profile, which are considered unsatisfactory. Furthermore, the presented setup is able to handle only up to three analytes at a time. A multi-syringe flow injection analysis (MSFIA) approach which is based on a 4-syringe burette with valve switching between the analyzer side of the system and stock solutions was published by Albertus et al.[71]. There are two main issues limiting the versatility of

this approach:

1. The number of analytes is limited to the number of syringes
2. All syringes are moved by one motor in the same way and only the valves can be switched independently making composition of different analytes difficult.

An example for sensor assessment and calibration with an automated system for handling liquids has been presented by Richards et al [72]. This approach is based on a multi (diaphragm) pump system applied for extensive data generation in conjunction with an electro-chemical sensor for testing and validating calibration models. With this system 1668 experiments were produced in approximately 60 hours in comparison to a duration of more than 2 weeks that would have been required to perform the same amount of experiments manually. However, while such systems may be suitable solutions for certain sensor assessment applications they all lack the possibility for employment for VOCs, due to the extensive use of polymer parts (pumps, tubings, storage vessels etc).
The first system especially designed for sensor calibration tasks for handling VOCs at trace concentration levels was recently presented by our research group [73]. Properties of the mixing system are assessed by mid-infrared (MIR) attenuated total reflection (ATR) spectroscopy of MeOH-acetone mixtures and via multi-component samples containing 1,2,4-trichlorobenzene and tetrachloroethylene, which are enriched into an E/P-co layer (thickness approx. 2 µm). Recorded ATR spectra are evaluated by principal component regression (PCR) algorithms. The presented sample mixing device provides reliable multicomponent mixtures with sufficient accuracy and reproducibility at trace concentration levels. In the development of this mixing system special care has been taken to minimize losses of analytes either via evaporation (head-space free mixing, storing and transport of solutions) or diffusion (full glass syringes, stainless steel

tubings). A broader overview on flow systems and their potential applications is given by Rocha et al [74]].

2.2.3. An Overview of Recent Scientific Contributions to the Field of VOCs Determination in Water by means Optical Sensor Systems

In the following chapter fundamental and recent contributions in the field of optical sensing of VOCs in aqueous environments are discussed. The overview is not intended to be comprehensive or strictly dedicated to optical sensors, but will also include other optical methods which follow the rule of generating the information on the analyte via optical light analyte interaction. The following methods will be described in the review of this analytical field:

- (Fiber)-optical sensors and sensor systems
- (Classical) spectroscopic techniques
- Laser fluorescence techniques
- Other techniques

The criteria to include contributions in this section were merely based on the applicability for (semi-)continuous monitoring, (on-site) sensing and other related application purposes and that the sensor (system) would be able to provide selectivity and sensitivity to a certain extent (no sum-parameter devices). Already established sensor systems are described more detailed, but also designs that potentially will be able to perform under field conditions in near future as well as fundamental works in that field

are briefly mentioned. The listing is structured into traditional subdivisions such as Ultraviolet / Visible (UV/VIS), Near-Infrared (NIR), Mid-Infrared (MIR), Raman, and laser fluorescence methods concluding with a short outlook on future trends. Biosensors have not been considered, as no significant contributions to VOC analysis have not been reported yet, which would fulfill the requirements mentioned above.

2.2.3.1. UV/VIS Sensors

The application of sensor systems operating in the UV/VIS spectral range is usually restricted due to the problem of interference by other components and the fact that not all chemical species have significant absorption features in this wavelength domain. Despite the fact that for the aromatic part of VOCs UV/VIS spectroscopy represents a quite sensitive tool due to strong π-π* transitions of such molecules [75]. The reason for the rather small number of contributions can be found in the very broad appearance of the absorption features in that electromagnetic region, representing a certain lack of selectivity of the spectra.

UV/VIS sensing applications for VOCs in aqueous media are quite rare. However, there are two factors that may contribute to a higher interest in sensor development in the UV/VIS domain:

- Benefiting from the highly advanced telecommunication industry, lasers and specifically waveguide materials transparent in the UV/VIS region are available and rather cheap compared to most other optical sensing techniques and
- As already mentioned above, computational capacities and powerful (multivariate) data evaluation techniques make data utilization of the strongly

overlapping spectral features of organic compounds in the UV/VIS region much easier accessible.

Figure 2.1 shows exemplary UV spectra of the BTX group to illustrate the well pronounced but overlapping spectral features of aromatics.

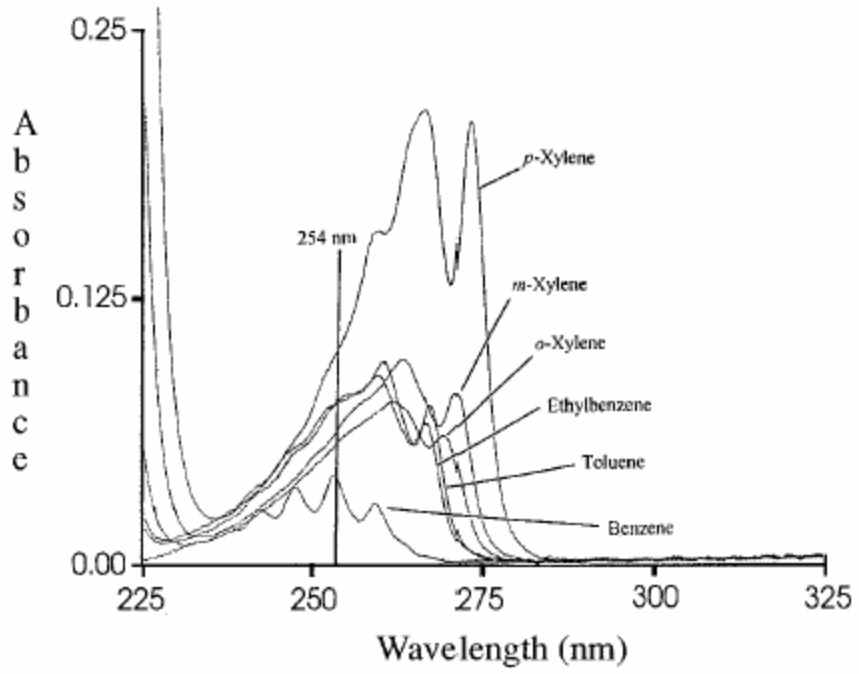

Figure 2.1 Transmission UV spectra of 50 mg/L of the BTX compounds in aqueous solutions in a 1 cm path length quartz cuvettes [82].

One example for successful implementation of innovative data utilization with traditionally obtained UV/VIS spectra of mixtures of BTX in water was published by Vogt et al [76]. An UV spectrometric method based on Ultraviolet Dynamic Derivative Spectroscopy (DDS) [77] is applied gaining selectivity and sensitivity by the use of optically generated first and second derivatives of transmission UV/VIS spectra. The

augmented spectroscopic technique is combined with chemometric algorithms like principal component regression or partial least squares, which are used for calibration of the spectrometer and quantification evaluation of spectra. Measurements were performed on mixtures containing up to 5 compounds including BTX, ethylbenzene, chlorobenzene and gasoline. The authors reported detection limits down to 50 µg/L for each analyte with a 10 cm absorption path-length and a few minutes measurement time. Apart from the inherent problems of transmission measurements including possible turbidity in real-world samples and strong interferences from uncalibrated contaminants, this approach shows the potential for on-line monitoring for all measured contaminants (with the exception of benzene) for drinking water quality [78,79].

Very recently, a miniaturized, submersible UV/VIS spectrometer for in-situ real-time measurements was presented by Langegraber et al [80] utilizing measurements in the spectral range of 200–750 nm for organic matter, suspended solids and nitrates in water. Main specifications of the spectrometric probe (dimensions: 44 mm diameter and approx. 0.6 m length) are as following:

- Measurement times of approx. 15 s, an auto-cleaning system using pressurized air - can be applied in 2″ bore holes (e.g. for groundwater monitoring)
- Utilizes a 2-beam spectrometer with a xenon lamp source - low power consumption (can be battery powered)
- Compromises a data logger on board (facilitates independent operation for one month at measurement time intervals of 30 min)
- Adjustable path length 2–100 mm for in-situ measurements

Applications have yet to be reported and already described problems with turbidity and cross interferences [78,79] may limit the field applicability of the device.

With a rather simple combination of UV/VIS transmission absorption spectroscopy with pre-selective enrichment matrices, as presented by Wittkamp and Hawthorne [52] and later shown again by Lamotte et al [55] problems with turbidity can be effectively reduced. In these contributions SPME related extractions of contaminants such as BTX and ethylbenzene etc. have been performed by applying thin (thicknesses in the mm regime) polydimethylsiloxane (PDMS) membranes as extraction matrices. UV/VIS spectra have been directly obtained with transmission spectra of the enriched contaminants in the PDMS matrix and rather low detection limits of few µg/L for most analytes could be achieved with total analysis times of less than 1 h. Figure 2.2 illustrates the enhancement in sensitivity after the extraction step for benzene as an exemplary analyte and also shows the generally broad spectroscopic features in UV/VIS spectroscopy.

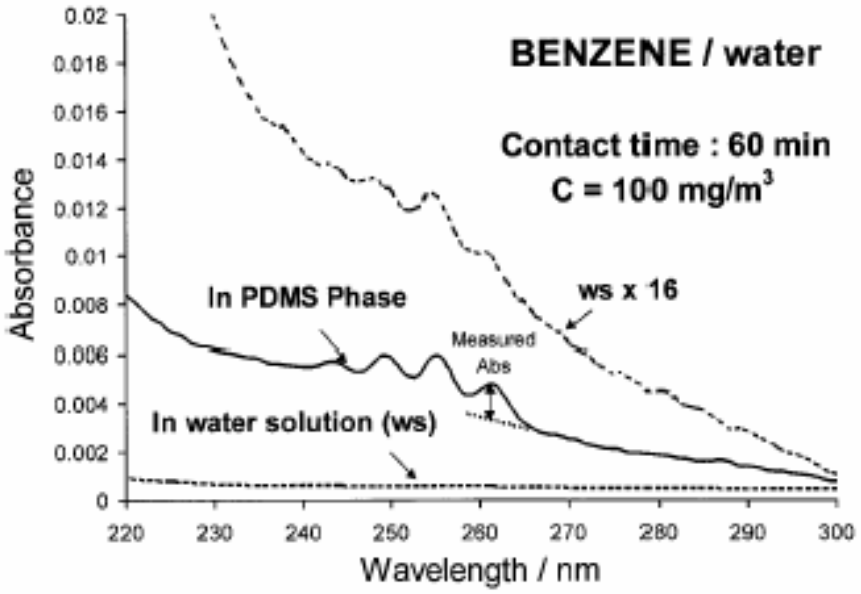

Figure 2.2 Comparison of absorbance measured with a 100 µg/L solution of benzene in water (bottom spectrum, scaled 16 time in the dotted spectrum on top) taken with an optical pathlength of 1 cm and absorbance spectrum measured in PDMS block (0.2 cm optical pathlength) after immersion in the solution for 60 min [55].

Apart from the fact that the extraction step significantly increased the sensitivity of the method, it also represents enhancement in selectivity as only rather hydrophobic and volatile contaminants are enriched in the PDMS matrix. However, a rather eminent disadvantage of this method is that at the presented stage of development only single component analysis can be performed due to the inherent strongly overlapping broad bands of practically all VOCs in the UV/VIS regime.

Few attempts have been described for VOCs determination in water via UV evanescent wave spectroscopy in conjunction with thin extractive membranes directly coated onto a sensing area of fiber-optic sensors based on the fundamental work of DeGrandpre and Burgess [81]. The only reported applications of this methodology for determination of VOCs in water were presented by Schwotzer et al. [40] and Mershman et al. [82]. Both rather similar approaches are based on a silica core plastic cladding optical fiber, where

the cladding was removed from a certain part somewhere in the middle of the fiber. This part of the fiber represents the sensing area, which is then coated with a PDMS layer (thickness in the µm regime). Analytes are enriched into this extractive membrane using a flow-cell setup and can be measured in the evanescent field if radiation is launched into the fiber. In both setups enrichment times were between 30 and 60 min, with reported limits of detection (LODs) of 10 mg/L for toluene [40] and also in the low mg/L regime for all BTX compounds and ethylbenzene as reported by [82]. Multicomponent measurements have not been performed. Due to the availability of low loss and low cost UV transmitting fibers, special applications in remote sensing for e.g. remediation processes or process control can be assumed possible.

2.2.3.2. Near-Infrared (NIR) Sensors

Plastic or silica-based glass fibers have been optimized by telecommunication industry during recent decades. Thus, robust and inexpensive optical fibers are available, which reached their theoretical attenuation limit of approximately 0.3 dB/km already in the late seventies [83]. Hence, fiber optic NIR liquid phase sensing at wavelengths < 2.5 µm utilizing overtone vibrational modes (e.g. C-H, N-H, O-H) for detecting organic compounds is a well established technology. Since overtone vibrations are in general 10-100 times weaker than corresponding ground vibrational modes in the MIR spectral range (3-20 µm), an active fiber/transducer length of 10-30 m is usually required for achieving sensitivities at trace contamination levels (µg/L). Another problem poses the limited discrimination power due to relatively unspecific absorption features in the NIR. These drawbacks are responsible for the lack of miniaturized sensor systems in this spectral region. On the other hand real remote sensing applications such as borehole

measurements can be performed due to the availability of virtually any length of fibers required. A recent general review on water quality monitoring via infrared optical sensors is given by Mizaikoff [84].

The combination of evanescent wave sensing with thin extraction membranes is widely applied in order to pre-concentrate analytes within the probed volume. The extraction membranes do also serve a second important purpose: due to their hydrophobic properties water is effectively excluded from the probed volume, reducing disturbing water background to a minimum as has initially be shown by DeGrandpre et al [81,85].

Major contributions in NIR fiber-optic sensing approaches for VOCs in water have been presented by Buerck et al [86]. PDMS coated multimode silica fibers with a low-OH quartz glass core (diameter 200 µm) have been coiled around a supporting rod for the determination of chlorinated hydrocarbons and aromatics such as trichloroethylene (TCE), toluene and p-xylene in aqueous solution during enrichment in the polymer layer with detection limits in the low mg/L region. The fiber-optic sensor could either be combined with either a NIR Fourier transform infrared (FT-IR) spectrometer or with a low cost filter photometer [87]. Using a similar setup Blair et al [88,89] showed the benefits of principal component analysis and partial least-square analysis as tools for the evaluation of such NIR spectroscopic data. Chemometrics were successfully applied to model the sensor's response to aqueous mixtures of TCE, 1,1,1-tricholorethane and toluene in concentration ranges from 20 to 300 mg/L.

Later, successful measurements of TCE in artificial aquifer systems and at field conditions have been shown with an improved portable NIR fiber-optic system with LODs just below the mg/L level [49]. In-situ measurements with the sensor system were performed in a groundwater circulation well [41], where the contamination with xylene was monitored over a time period of 4 months of continuous measurements.

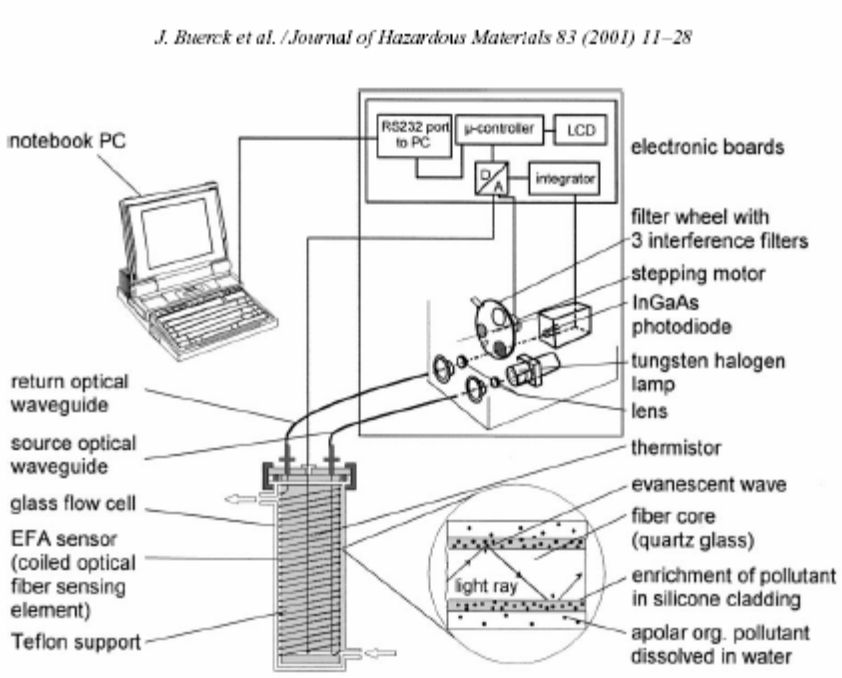

Figure 2.3 Illustration of evanescent wave sensing principle (circle at the right bottom) and instrumental setup of coiled fiber-optic sensor and NIR bandpass filter photometer unit (fiber sensor element installed in a flow cell) [41].

An illustration of the applied NIR fiber-optic sensor can be seen in Figure 2.3 and its dynamic response to technical grade xylene in a laboratory calibration experiment is shown in Figure 2.4. For the given parameters it takes about 20 min to reach equilibrium conditions for enriching xylene in the polymer layer and the analyte can be completely washed out again with water in a time frame of several minutes.

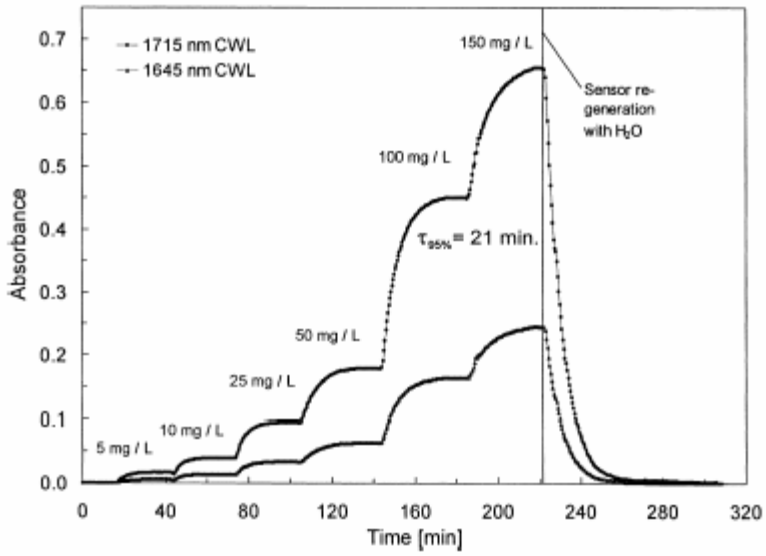

Figure 2.4 Response signals vs. time obtained with the NIR evanescent wave fiber-optic photometer system (fiber length 30m) for measurements of aqueous solutions of technical grade xylene (laboratory calibration of sensor system). Absorbance over time data are given for both measuring channels of the photometer located at central wavelengths of 1715 and 1645 nm [41].

A core-based intrinsic fiber-optic absorption sensor where the distal ends of transmitting and receiving fibers are connected by a small cylindrical section of optically clear PDMS has been developed by Klunder et at [90]. The PDMS acts as both a light pipe and a selective membrane into which VOCs are enriched during measurements. Measurement times of about 30 min and an LOD of 1.1 mg/L for TCE was achieved.

2.2.3.3. Mid-Infrared (MIR) Sensors

MIR spectroscopy operating in the spectral range from 2.3 to 25 µm is recognized as an analytical technique of persistently increasing importance. In contrast to the overtone vibrations in the NIR regime, MIR spectroscopy gives access to comparatively strong, distinct fundamental vibrational / rotational modes of organic molecules. This enables the opportunity to differentiate and quantify components according to their characteristic absorption bands. In respect to approaches for the determination of VOCs in water via

MIR spectroscopic techniques, predominately evanescent wave methodologies have been reported. This is related mainly to the fact that MIR transmission measurements in aqueous media are strongly hindered by broad and intense water absorption bands. Besides the measurement needs, the advancement and increased application of sensors based on optical waveguide technology is strongly coupled to the investigation and optimization of fiber optic materials transparent in the relevant frequency range. The rapid evolution of MIR sensors during the last decade can be mainly attributed to the development of appropriate fiber-optic materials, enabling the utilization of the wavelength range from 2 – 20 μm for sensing applications. Although the current performance of IR fiber-optic materials still requires significant improvement due to the comparatively high attenuation losses, some IR fibers and hollow waveguides are nowadays commercially available. The values presented in Figure 2.5 for the transmission range and minimum attenuation are average numbers retrieved from recently published material and shall provide a brief overview to the current state-of-the-art.

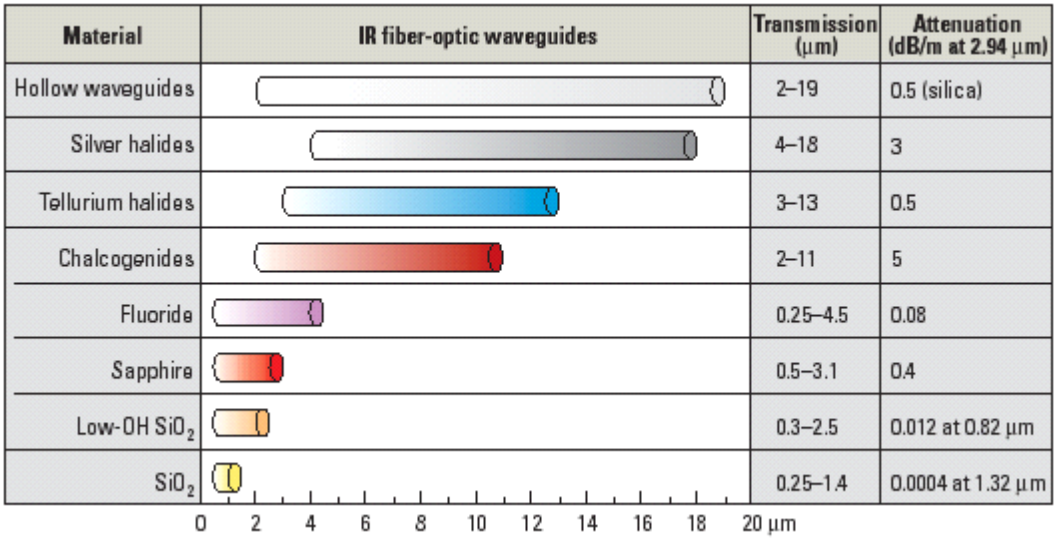

Figure 2.5 The most commonly used mid-IR transparent fiber-optic materials and their relevant properties for fiber-optic sensing. It can be seen that attenuation values for the long-wave range need to be further reduced for remote sensing applications. Transmission and attenuation data are the average of reported values [46].

Variations of these values can be mainly attributed to composition and fabrication variations of the reported materials. More details can be found in a number of reviews focused on the material properties of IR transmitting optical fibers [91,92].

Various fiber-optic based evanescent wave VOCs sensing systems applying polymer coated silver-halide (AgX) fibers (diameters: 700 to 1000 µm) coupled with FTIR spectrometers have been described during the past 15 years [37,38,39,93,94]. All contributions include coupling IR radiation of an FT-IR spectrometer into AgX fibers simultaneously acting as both, waveguide and active transducer. The active sensing area is coated with a thin hydrophobic polymer layer (thicknesses 2 to 10 µm), such as E/P-co, Teflon AF, polybutadiene, etc., enriching volatile organic pollutants. Water is effectively excluded from the measurement, since the selected polymer layer thickness is larger than the penetration depth of the evanescent field guided outside the optical

fiber. Based on this fiber-optic evanescent wave sensor (FEWS) scheme, qualitative and quantitative determination of a wide variety of organic analytes in the mg/l to the low µg/l concentration range has been demonstrated under laboratory conditions.

Very recently the first field application of a prototype MIR sensor system for the determination of VOCs in groundwater was developed and tested by our group [95]. The sensor comprises a portable FTIR spectrometer, coupled to the sensor head via AgX fiber-optical cable. A 10 cm unclad middle section of the 6 m long fiber is coated with E/P-co as extraction matrix, where evanescent wave measurements are conducted. A mixture of tetrachloroethylene, dichlorobenzene, and xylene isomers at concentrations in the low mg/L region was studied qualitatively and quantitatively in an artificial aquifer system filled with Munich gravel. This simulated real-world site at a pilot scale enables in-situ studies of the sensor response and spreading of the pollutants injected into the system with controlled groundwater flow and the analytes were clearly visible in the corresponding IR spectra. The results were validated by head-space gas chromatography using samples collected during the field measurement. The five analytes could be discriminated simultaneously, for two of the analytes the quantitative results are in agreement with the reference analysis. However, factors such as fiber long-term stability and time resolution have yet to be improved. With regard to application in real-world environments the accuracy of this method has been proven to be independent of aqueous sample turbidity, salinity or acidity at expected levels [96].

The most obvious reason for the extensive usage of AgX fibers for sensing applications is, , a transmission range down to the IR fingerprint region, as can be seen in Figure 2.5. However, certain limitations such as e.g. sensitivity to UV light and chemical susceptibility (to e.g. Cl^- ions) have to be taken into account for sensing applications [92] using these waveguide materials. However, evanescent fiber-optic sensing of VOCs in

water with other fiber materials have only been reported by Ertan-Lamontagne et al. [97] using PVC coated chalcogenide fibers and Howley et al. [98] applying PDMS coated sapphire fibers. Both contributions can be considered fundamental contributions in this field, however, suffering from rather high detection limits of tens of mg/L. Furthermore, due to the absence of evaluable data in the fingerprint spectral region, selectivity may be a permanent issue.

To date, field applications of such ATR-FT-IR sensor systems have been rarely reported. Acha et al. [48,99] developed an ATR-FT-IR sensor system for continuous online monitoring of a dechlorination process in a fixed-bed bioreactor without prior sample preparation. The sensor was based on an ATR ZnSe crystal (dimensions: 49 x 9.5 x 3mm) coated with a 5.8 µm thick polyisobutylene (PIB) extraction membrane, facilitating measurements of TCE, TeCE and carbontetrachloride (CT) at low mg/L levels in the aqueous effluent of a fixed-bed dechlorinating bioreactor. Several PLS calibration models were generated to resolve overlapping absorption bands of the chlorinated pollutants. Accuracy of this continuously monitoring ATR-FTIR sensor was validated with GC measurements. A graphical illustration of the results over time (Figure 2.6) shows that satisfying correlation is provided. Furthermore, the dechlorination process could be monitored without perturbation of any kind.

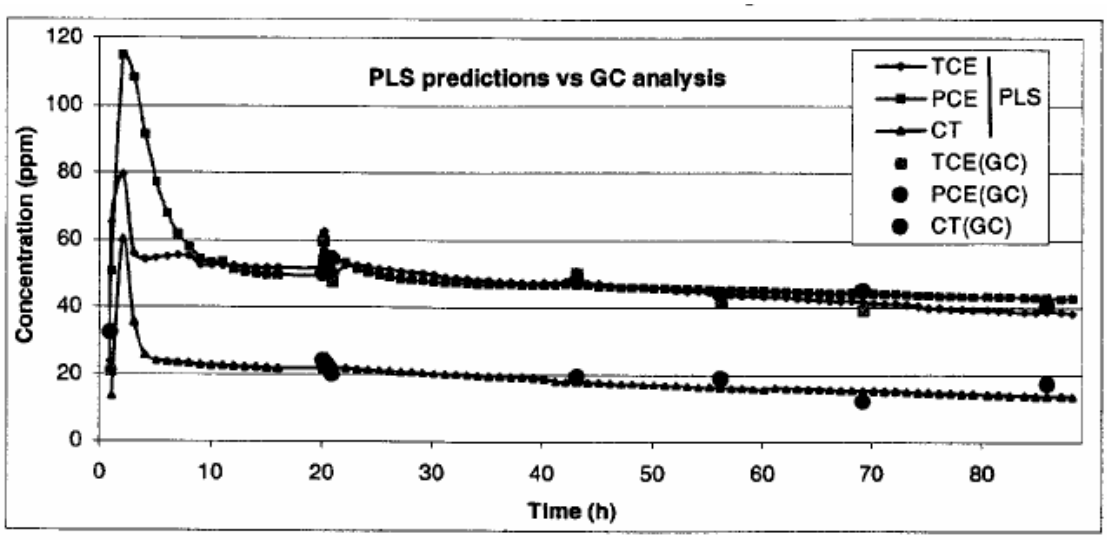

Figure 2.6 Trace of carbontetrachloride (CT), trichloroethylene and tetrachloroethylene (PCE) in the effluent of a dechlorination reactor measured with evanescent wave ATR-FTIR spectroscopy. The ZnSe ATR element was coated with a polyisobutadiene extraction membrane. The lines show the predicted concentration values after PLS treatment of absorption spectra. Validation with GC shows good agreement [99].

In order to overcome the limitations of remote sensing in the MIR regime, which are closely related to the absence of low loss waveguide materials, novel sensor systems have been developed. Kraft et al. and related papers [100,101] describe a sub-sea deployable fiber-optic sensor system for the continuous determination of a range of environmentally relevant VOCs in seawater. A suitable fiber-optic sensor head was developed using an E/P-co coated (thickness approximately 4 µm) 700 µm thick AgX fiber with approx. 38 cm active sensor length. The system was optimized in terms of sensitivity and hydrodynamics, and connected to the underwater FT-IR spectrometer. Figure 2.7 shows a 3D sketch of the underwater sensor system together with some specifications.

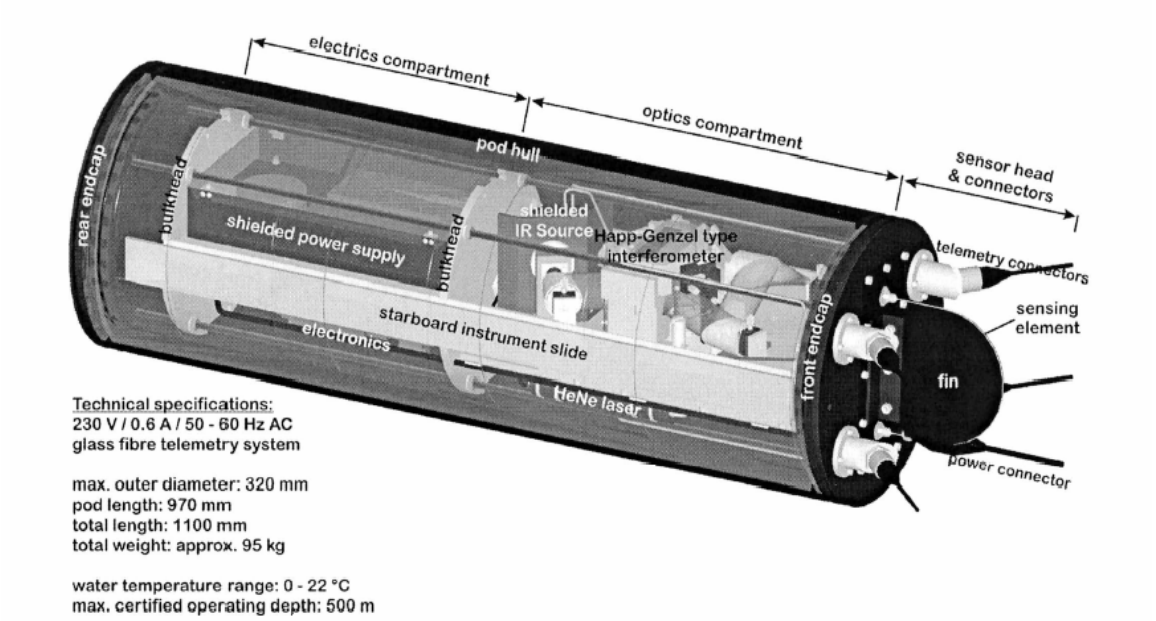

Figure 2.7 3D illustration of the FT-IR underwater instrument. Main optics and electronics originate from a Bruker Vector 22 FT-IR spectrometer. IR radiation is launched into a flexible, polymer coated AgX fiber, which penetrates the aqueous medium facilitating highly sensitive and selective IR measurements in the marine environment [101].

The sensor system was characterized in a series of laboratory and simulated field tests. Sensor characteristics from flume tank measurements with changing concentrations of xylenes, 1,2-dichlorbenzene and TeCE (Figure 2.8) show rapid dynamic response to changing concentrations. The sensor proved to be capable of quantitatively detecting a range of chlorinated hydrocarbons and monocyclic aromatic hydrocarbons in seawater down to the µg/L concentration range, including mixtures of up to 6 components.

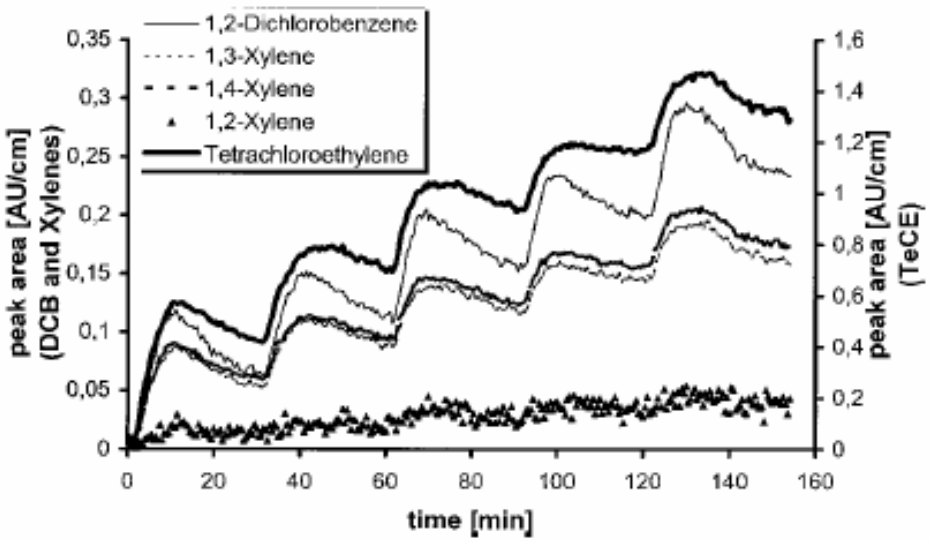

Figure 2.8 Sensor dynamics shown for repetitive analyte injections into the flume tank 0.62 mg/L tetrachloroethylene, 0.77 mg/L 1,2-dichlorobenzene and 3.48 mg/L of the xylene isomer mixture were injected at t = 1 min and then every 30 min. The decreases of the readings after the maxima are attributed to dilution of the analyte plume in the solution and to analyte evaporation into the surrounding atmosphere during measurements in the open flume tank system [101].

It has been demonstrated that varying amounts of salinity, turbidity, or humic acids, as well as interfering seawater pollutants do not significantly influence the sensor characteristics. A certain disadvantage for applications such as groundwater monitoring are the relatively large dimensions of the system. For borehole and other sensing applications, which require small systems, a prototype miniaturized MIR grating spectrometer operating in the wavelength range 8–12.5 µm has been reported [102]. The gain in applicability by miniaturization goes along with decreased performance (sensitivity), when dispersive technologies are applied for wavelength separation. Besides these drawbacks, the system is based on very similar principles as the submersible FTIR sensor system mentioned above. This measurement device may be used for organic contaminants in waste water, leakage fluids, and during remediation of

contaminated soils. However, to date the system was only tested at laboratory conditions where LODs for tetrachloroethylene around 1 mg/L could be obtained.

Besides evanescent field approaches very few alternative concepts have been reported for the MIR region. Heglund et al [103] and Merschman et al [53] applied SPME related extractions of contaminants such as BTX and ethylbenzene etc. by applying either polydimethylsiloxane (PDMS) or parafilm membranes (thicknesses around 130 µm) as extraction materials and followed by direct detection of the enriched organic analytes via FT-IR spectroscopy. LODs have been reported in the region of a few hundreds of µg/L and showed satisfying agreement with GC validation measurements [103]. However, strong absorption features of the SPME matrix renders parts of the IR spectra opaque due to total light absorption and evaporation losses during switching from extraction to detection of the analytes may be inconsistent and difficult to calibrate.

Alternative to the FT-IR approaches, the fiber-optic sensor head can be coupled to a tunable diode laser in order to enhance the sensitivity. Using lead salt lasers emitting in the MIR region a detection limit of around 22 µg/L for tetrachloroethylene has been reported [104, 105].

2.2.3.4. RAMAN Sensors

An alternative analytical method of great promise for VOCs determination in aqueous systems is provided by surface enhanced Raman scattering (SERS) [106, 107] and other variations of Raman spectroscopy with enhanced sensitivity [108]. Compared to NIR and MIR techniques, Raman spectroscopy has the inherent advantage that water only minimally interferes with the measurements. The application of Raman spectroscopy for studying environmental systems is rapidly expanding due to the

molecular specificity of this analytical technique enabling similar chemical identification as IR spectroscopy. Conventional Raman spectroscopy, however, has limited applicability for trace organic detection because of the inherently weak Raman scattering cross section. The SERS effect providing enhancement factors of up to 10^7 on Raman signals obtained from molecules adsorbed at rough metallic surfaces [106,109], has recently generated increasing interest for Raman sensing techniques. However, a limitation are potential interferences of fluorescence by various naturally occurring compounds (e.g. humic acids). Reviewing the contributions in this field would go beyond the scope of this work. More detailed information can be obtained in excellent reviews on this topic [110, 111]. Therefore, only the most relevant recent contributions to Raman based sensing will be briefly discussed.

Raman Spectroscopy

In general, conventional Raman spectroscopic techniques are not sensitive enough for most environmentally relevant concentration ranges of VOCs in water. Hence, efforts have been made developing methods to overcome this limitation. One approach published by Wittkamp et al [51] shows SPME related extractions of contaminants such as BTX and ethylbenzene etc. by applying small (diameters in the mm region) polydimethylsiloxane (PDMS) beads as extraction matrices and subsequent detection via Raman spectroscopy. Raman spectra of the enriched contaminants have been measured directly in the PDMS matrix and LODs from 1 to 4 mg/L for all analytes with a total analysis times of about 40 minutes were obtained. BTX spiked real water samples proofed the applicability of this method for field measurements.

A rather simple but effective method to increase the sensitivity of Raman spectroscopy is to design sample arrangements that increase the interrogated sample volume and thus

increase the intensity of the collected Raman signal. Walrafen et al [112] demonstrated that a hollow optical fiber enabling multiple internal reflections could be used to probe a large volume resulting in sensitivities increased by factors of 100-1000. This technology is also known as capillary waveguide or liquid-core waveguides (LCWs) spectroscopy. After the introduction of reliable, low-loss liquid-core waveguides based on Teflon-AF 2400 [113] applications of LCWs for Raman spectroscopy in general [114] and especially for VOC detection in water have been reported by several groups [115,116] with LODs in the low mg/L [115] or high µg/L region for benzene [116]. An exemplary Raman spectrum of a mixture of benzene, p-xylene and toluene recorded with a LCW setup is shown in Figure 2.9 illustrating the opportunity of multi-component detection. Apparently, the potential of this method is not fully exploited yet, and there is considerable scope that future contributions will present increased sensitivities rendering this method an interesting concept in the field of in-situ VOC analysis.

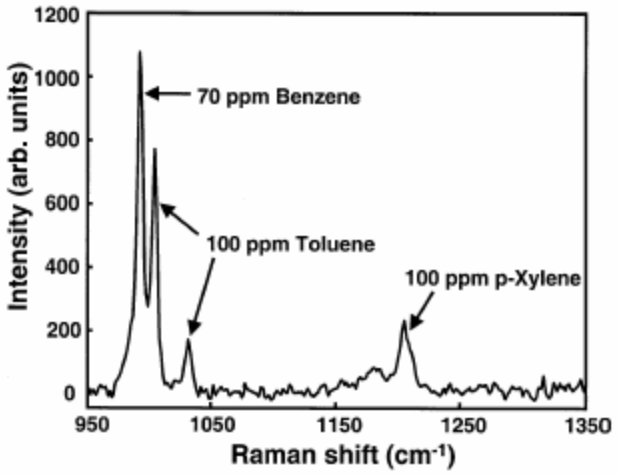

Figure 2.9 Background-subtracted Raman spectrum of a mixture containing 70 mg/L benzene, 100 mg/L toluene and 100 mg/L p–xylene. Spectrum recorded with a liquid core waveguide setup [116].

Surface-Enhanced Raman Scattering (SERS)

A series of contributions present a SERS based sensor system [117,118] applying SERS substrates that have been modified with different thioles in order to promote partitioning of VOCs into close vicinity of the SERS substrate from the aqueous phase. LODs for tetrachloroethylene and benzene of 12.6 mg/L and 7.5 mg/L have been reported. In more recent works, a SERS sensor was coupled with a flow injection analysis (FIA) system for molecular specific water analysis [119]. The flow-through cell incorporates a cascade geometry that is capable of accepting modified SERS substrates and its application to simultaneous detection of BTX applying PLS algorithms is shown. A LOD for benzene of 190 mg/L was achieved with FIA-SERS with improvements expected with future cell designs.

Recently, a laboratory-based system for measurement of organic contaminants in sea-water with sol–gel-derived SERS substrates was presented by Murphy et al [120-122]. By encapsulating silver colloids in a sol–gel-derived xerogel, SERS-active coatings were produced with high mechanical and chemical stability required for underwater field measurements. Photodegradation of the SERS layer was avoided by appropriate choice of optical components and layout. Continuous analysis was performed with two flow-through cells. The first design was a modification of a standard glass cuvette and the second an improved design an in-house-constructed aluminum cell. SERS investigations on samples with turbidities ranging from 0 to 400 NTU were performed with both cells. These tests show the suitability of the developed system for continuous monitoring of real world samples and its potential application in on-line process control. Sensitivity with a LOD of 100 µg/L for chlorobenzene are promising results for these first studies, however, the long-term stability of the substrates (half-life activity of the SERS substrate was 13 days in the best case) has to be improved for on-line monitoring systems.

2.2.3.5. Laser Fluorescence Sensors

Already 1977 Richardson et al. [123] showed that by applying lasers as excitation source for fluorescence measurements very low detection limits such as e.g. 19 µg/L for benzene as a single contaminant dissolved in water can be obtained. However, reviewing all contributions in this field would go beyond the scope of this work. An excellent overview on fluorometric determination of VOCs in water is provided in recent reviews [124-126]. In general only the aromatic compounds (BTX, ethylbenzene, chlorobenzene etc) show detectable fluorescent signatures. Chlorinated hydrocarbons (chloroform, trichloroethylene, tetrachloroethylene etc) have been successfully determined via laser induced breakdown spectroscopy (LIBS) [127] in the gas phase [128]. However, such approaches have been reported to be unsuitable to target those analytes in the liquid phase at relevant concentrations [129]. Furthermore, evident problems when analyzing multi-component mixtures such as quenching effects (e.g. “inner filter” effect [130]), low molar absorptivity and quantum yields of mono-aromatic compounds in comparison to poly-aromatic compounds leads to weak fluorescence emissions from BTX compounds and it is suggested that BTX detection is only useful via fluorometric methods if no other contamination is present [124].

The advantage of time-resolved laser fluorescent spectroscopy [131] for the analysis of environmental relevant aromatic compounds relates to the following beneficial parameters of this methodology:

- (Laser) sources and fiber materials are highly developed and cheap in the excitation wavelength range of (mostly UV).

- Aromatic compounds have a large absorption cross section in the UV and exhibit high fluorescence quantum yields.
- Using pulsed lasers fluorescence techniques, decay curves can be recorded providing additional and in some occasions selective information.

The latter is regarded as very important for environmental field analysis. In combination with effective multivariate data evaluation algorithms access to group- and molecule-specific laser fluorescence spectroscopy is provided.

One recent example for a system based on laser induced fluorescence spectroscopic measurements was selected to briefly describe the concept. A compact and mobile battery-operated laser induced fluorescence system has been presented by Karlitschek et al. [132] and related publications. The system is based on a diode-pumped solid-state laser with UV frequency conversion and a pulse duration of 7 ns. The third (355 nm) and fourth (266 nm) harmonics of the laser can be alternately used. The detection system consists of a polychromator, a gated image intensifier, and a CCD camera, which can acquire time-resolved spectra with nanosecond time resolution. A schematic of this system is shown in Figure 2.10. Fluorescence spectra, decay times, and LODs of 100 µg/L for benzene, 50 µg/L for toluene and 10 µg/L for xylenes have been measured for single contaminants in water.

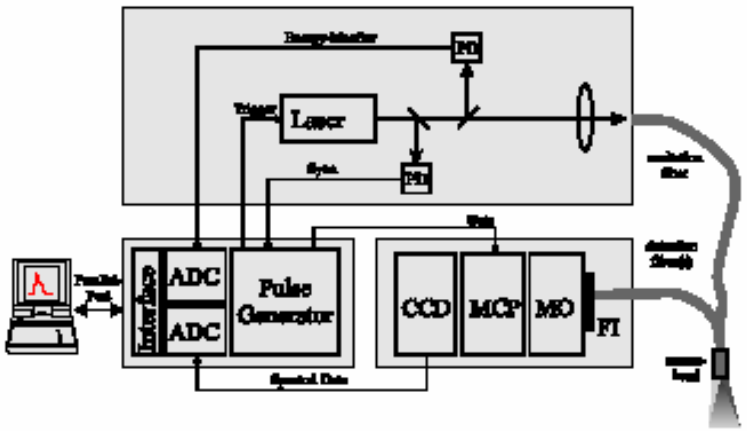

Figure 2.10 Schematic of a fiber-optic laser induced fluorescence instrument for in-situ detection of water pollutants. PD: Photodiodes. FI: edge filter. MO: monochromator. MCP: multichannel plate image intensifier. CCD: slow-scan CCD-line camera. ADC: analog-to-digital converters [132].

Results from contaminated groundwater samples show that molecular specificity can not be obtained with such sensor systems yet. However, the type of contamination can be classified in several groups (BTX, smaller PAHs, larger PAHs etc) due to the wavelength region of the fluorescence decay features and the decay times.

Alternative systems have been tested under field conditions [124,133, 134]. However, none of the approaches seems suitable for on-line sensing of BTX in water for lon-term field analysis. Even though VOCs can not be addressed via fluorescent methods reliably, such sensor systems are suitable devices for specific applications such as e.g. first assessment of contaminated sites or remediation control.

2.3. MID-Infrared Spectroscopy

The mid-IR (MIR) range covers the frequency regime from 4000 cm^{-1} (2.5 µm) to 400 cm^{-1} (25 µm). In this region of the electromagnetic spectrum, radiation stimulates

fundamental transitions between the ground state of vibrational and rotational modes of specific molecular bonds or whole molecules and their excited states. Consequently, information on the chemical functionalities and the type of molecule can be extracted. Depending on the strength of the bond, each mode is excited at a specific energy level manifesting as a characteristic band in the absorption spectrum. As vibrations of whole molecules usually require considerably lower excitation energies,, they produce highly substance specific absorption patterns at longer wavelenghts within the so-called fingerprint region (1200 cm^{-1} – 400 cm^{-1}). MIR spectroscopy is recognized as an analytical technique of persistently increasing importance and is widely used in the analytical community.

However, a major restriction of transmission based MIR measurements of VOCs in aqueous solutions are the broad and pronounced absorption bands of water in this spectral region. Furthermore, field applicability of transmission based methods is restricted due to the potential influence of turbidity in real-world samples. Hence, increasing efforts are focused on optical principles enabling molecule specific determination of organic pollutants in water, such as attenuated total reflection infrared spectroscopy (ATR-IR) [36,] in combination with extractive polymer membranes.

2.4. Attenuated Total Reflection

2.4.1. Principle of Attenuated Total Reflection

The ATR principle derives more generally from internal reflection spectroscopy and has been independently described by Harrick [135] and Fahrenfort [136] in the early 1960ies. Radiation which travels in the high refractive index ATR-element is incident at the

interface between the waveguide and a surrounding medium with lower refractive index with an angle θ. At angles $\theta > \theta_c$, where

$$\theta_c = \arcsin \frac{n_1}{n_2} \qquad (2\text{-}1)$$

is the critical angle, radiation is internally reflected. The principle of ATR spectroscopy is schematically shown in Figure 2.11.

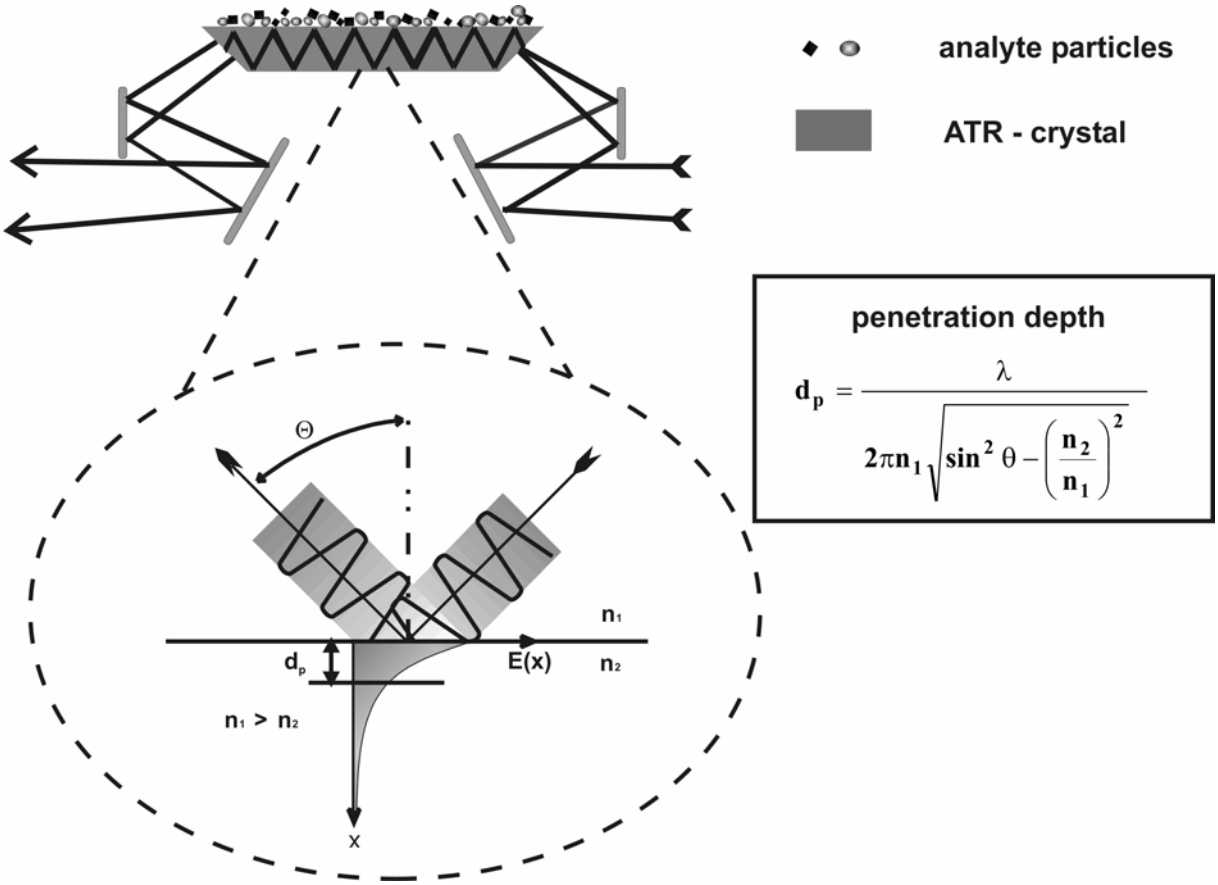

Figure 2.11 Illustration of the ATR principle.

At each internal reflection a certain amount of energy, depending on the wavelength, the refractive indices of the waveguide (n_1) and the surrounding medium (n_2, $n_1 > n_2$) and the angle of incidence, penetrates into the ambient matrix and is guided as leaky mode along the surface of the waveguide. The intensity of this evanescent field decays exponentially with distance from the internal reflection element (IRE) surface:

$$\mathbf{E} = \mathbf{E_0} \cdot \mathbf{e}^{\left(\frac{-z}{d_p}\right)} \qquad (2\text{-}2)$$

E_0 represents the wave amplitude at the interface (z = 0), d_p is the penetration depth and is defined as the distance from the IRE surface where E_0 has decreased to e^{-1} of its value at z = 0. The absorption for a specific wavelength depends on the penetration depth d_p of the associated evanescent field into the absorbing medium. The penetration depth is characterized by the following equation:

$$\mathbf{d_p} = \frac{\lambda}{2\pi \mathbf{n_1} \sqrt{\sin^2\theta - \left(\frac{\mathbf{n_2}}{\mathbf{n_1}}\right)^2}} \qquad (2\text{-}3)$$

where λ is the wavelength, n_1 and n_2 are the refractive indices of the IRE element and the ambient medium, and θ is the angle of incidence.

The penetration depth increases with increasing wavelength (λ), with decreasing angle of incidence, and with decreasing ratios of the refractive indices.

In addition, an effective layer thickness $\mathbf{d_e}$, which corresponds to the same absorption in transmission mode has been described [[137],138].

2.4.1.1. Effective Layer Thickness

In the opinion of Harrick, the interaction of the evanescent wave with the absorbing rarer medium, as calculated by the Fresnel's equations or the Maxwell's equations, does not yield any physical insight into the absorption mechanism or into the interaction of the penetrating field with the absorbing medium [135]. For this reason, he introduced the effective layer thickness as a parameter that expresses the strength of interaction of the evanescent wave with the absorbing rarer medium, and for which simple equations were found.

It is known that in the case of conventional transmission IR spectroscopy, the sample thickness is directly related to the intensity of absorption features of a sample according to Lambert-Beer's law.

From the Lambert-Beer's law, the following expression for the transmittance, $\mathbf{T}$, can be extracted:

$$\mathbf{T} = \frac{\mathbf{I}}{\mathbf{I_0}} = \mathbf{e}^{-\alpha \mathbf{d}} \qquad (2\text{-}4)$$

where $\mathbf{I_0}$ is the incident intensity, $\mathbf{I}$ is the transmitted intensity and α is the absorption coefficient (cm^{-1}), and $\mathbf{d}$ is the sample thickness (cm).

For low absorptions, i.e. $\alpha\mathbf{d} < 0.1$, we obtain:

$$\mathbf{T} = \frac{\mathbf{I}}{\mathbf{I_0}} \approx \mathbf{1} - \alpha\mathbf{d} \qquad (2\text{-}5)$$

Similarly, in the case of internal reflection, the reflectivity, $\mathbf{R}$, can be written as:

$$\mathbf{R} = \mathbf{1} - \alpha \mathbf{d_e} \qquad (2\text{-}6)$$

where $\mathbf{d_e}$ is the effective thickness.

Equation 2-6 is valid for a single reflection. For multiple reflections, the reflected power is given by:

$$\mathbf{R^N} = \mathbf{(1 - \alpha d_e)^N} \qquad (2\text{-}7)$$

where $\mathbf{N}$ is the number of reflections.

For $\alpha \mathbf{d_e}$ << 1, the reflected power becomes:

$$\mathbf{R^N} \cong \mathbf{1} - \mathbf{N}\alpha \mathbf{d_e} \qquad (2\text{-}8)$$

By comparing the low-absorption approximation expressions for transmission (Equation 2-5) and internal reflection (Equation 2-8), it can be observed that the effective thickness represents the actual thickness of a film that would be required to obtain the same absorption in a transmission measurement as that obtained in a reflection measurement. Different expressions for the effective thickness have been derived for two different cases: the semi-infinite bulk case and the thin film case.

Since in this work typical thicknesses of the polymer coatings are in the region of a few μm and therefore exceeding the penetration depth the case of a semi-infinite bulk layer will be described briefly.

Semi-infinite bulk case

For bulk materials, the electric field amplitude (see Equation 3.2) falls to a very low value within the thickness of the rarer medium, $\mathbf{d}$. The sample thickness is larger than the penetration depth ($\mathbf{d} > \mathbf{d_p}$).

In this case, the low absorption approximation for the effective thickness is calculated from the electric field for zero absorption [137,135]:

$$\mathbf{d_e} = \frac{\mathbf{n_1}}{\mathbf{n_2}} \frac{\mathbf{1}}{\mathbf{\cos\theta}} \int_0^\infty \mathbf{E(r)^2 dz} = \frac{\mathbf{n_1}}{\mathbf{n_2}} \frac{\mathbf{E_0^2}}{\mathbf{\cos\theta}} \frac{\mathbf{d_p}}{\mathbf{2}} \qquad (2\text{-}9)$$

Since $\mathbf{d_p}$ is dependent on the wavelength, the effective thickness also increases with wavelength. This is the reason why the internal reflection spectra of bulk materials show absorption bands at the longer wavelengths with relatively stronger intensity. Thus, two bands having the same intensity in transmission spectra will have unequal intensities in internal reflection spectra—the longer wavelength bands appear relatively stronger. This wavelength dependence also results in greater absorption on the longer wavelength side of single absorption band, contributing to band distortion.

2.4.1.2. Waveguide Materials

By using both, IR transparent ATR crystals and optical fibers intrinsic evanescent field sensing systems can be developed. Variations in thickness and length of the applied waveguides determine the number of internal reflections from a geometrical point of view. The refractive indices influence the penetration depth and the optical properties of the waveguide material define the attenuation losses of guided IR radiation.

Table *2.2* gives an overview on IR-ATR waveguides currently investigated at the Applied Sensors Laboratory (ASL). This table is by no means exclusive and represents only a fraction of the available IR transparent materials, as e.g. fluoride or tellurium halides can be processed into mid-IR fibers [36,46,84].

Table 2.2: Waveguide materials applied at ASL for MIR evanescent field sensing.

Material	**Waveguide type**	**Transmission range (cm^{-1})**	**Refractive index**	**General Properties**
Thallium Bromoiodide (KRS-5)	ATR crystal	20,000-250	2.37 (at 10 µm)	slightly soluble in water soluble in bases insoluble in most acids
Zinc Selenide (ZnSe)	ATR crystal	17,000-720	2.41 (at 9.5 µm)	incompatible with acids and strong alkalis insoluble in water and organic solvents
Germanium (Ge)	ATR crystal	5,500-600	4.00 (at 9.72 µm)	insoluble in water insoluble in most bases and acids
Silicon (Si)	ATR crystal	4000-1500 360-70	1.62 (at 5 µm)	insoluble in water insoluble in most acids and bases

Material	Waveguide type	Transmission range (cm^{-1})	Refractive index	General Properties
Sapphire (Al_2O_3)	Fiber	50,000-2500	1.62 (at 5 µm)	insoluble in water incompatible with strong acids and bases
Chalcogenide (AsSeTe glass)	Fiber	10,000-900	2.9 (at 10.6 µm)	insoluble in water incompatible with strong acids and bases
Silver halides - (AgX)	Fiber	2500-500	2.1 (at 10.6 µm)	insoluble in water incompatible with strong acids and bases

2.4.2. Recent Approaches for VOC Determination via Evanescent Wave Sensing

Evanescent field spectroscopy utilizes internal reflection elements based on ATR-crystals or MIR-transparent optical fibers serving as waveguide and optical transducer. Hence, absorption spectroscopy at or near the waveguide surface is enabled via the evanescent field [136,135]. Chemical MIR sensors enrich analytes into a thin polymer membrane coated onto the waveguide surface providing interaction of the evanescent field with enriched analyte molecules. Such sensor systems enable measurements within a period of several minutes instead of comparatively long analysis time for methods based on sampling and discontinuous assessment. Information derived from spectroscopic data allows identification and quantification of a wide range of VOCs at laboratory and field conditions [37,38. With regard to application in real world

environments, the accuracy of this method has been proven independent of aqueous sample turbidity, salinity or acidity at expected levels [96].

Recently, an alternative concept of polymer-coated ATR-IR sensor systems for detecting VOCs in the gas phase has been introduced by Yang et al. [141,142]. In this approach VOCs are detected in the head-space of either a heated or gas-stripped sample solution. Analytes are enriched into a thin PDMS layer, which is coated onto a suitable ATR waveguide and are spectroscopically detected. Although this setup may find its applications for instance in detection of (semi)volatile organic compounds in aggressive environments, it seems preferable to directly measure in the liquid phase for following reasons:

- Compounds with low volatility are still addressable with a direct sensor.
- Direct measurements represent the least complex sensor setup only consisting of a transducer exposed to the sample solution avoiding any prior sample preparation or extraction.
- Less analysis parameters have to be controlled compared to head-space sensing and no stripping system is required.

2.5. Polymer Sensor Membranes

Strong interferences caused by characteristic absorptions of water (O-H stretching band $\nu_{1,3}$ @ 3300 cm^{-1}, O-H-bending band ν_2 @ 1640 cm^{-1}, combination band $\nu_2+\nu_L$ @ 2100 cm^{-1} and the libration band ν_L @ 750 cm^{-1} [143]) render direct ATR spectroscopy of organic pollutants in aqueous sample matrices impossible at low concentrations. To overcome this limitation, hydrophobic polymer layers are coated onto the actively

transducing waveguide surface [37,38] following the general concept of chemical sensors [33,34]. While these membranes serve as solid phase microextraction (SPME) matrix for analyte enrichment, they also exclude water from the analytical volume probed by the evanescent field extending along the IRE surface. Sorbent extraction was developed in the 1980s and is commonly used for the extraction of organic compounds from matrices such as water, air and soil [144,56]. A solid adsorbent layer is exposed either directly to the sample matrix or to the associated headspace. Analyte molecules partition from the sample into the adsorbent layer following a gradient in chemical potential until equilibrium has been reached. In case of very large sample volumes $V_s >> V_p$, the amount of analyte *n* extracted from the sample matrix is dependent on the initial analyte concentration c_0, the partition coefficient of the analyte K_{sp} between the sample matrix and the solid phase extraction membrane and the volume of the membrane V_p following:

$$\mathbf{n = K_{sp} V_p c_0} \qquad (2\text{-}10)$$

Water / polymer partition coefficients of relatively small chlorinated VOC molecules typically range between 100 and 1000 [145]. Thus, analytes are enriched within the adsorbent layer while water is widely excluded. Under the boundary conditions of given penetration depth and fiber diameter the amount of analyte within the evanescent field and subsequently the sensitivity can only be increased by extending the length of the coated fiber, i.e. the length of the active transducer region.

The thickness of the membrane is a critical factor for solid phase extraction applications. Ideally, the polymer membrane thickness is only slightly larger than the information depth d_e, which describes the maximum distance from the waveguide surface from which relevant analytical information can be obtained [135]. Thicker coatings adversely

affect the sensor response time since analytes have to diffuse a longer distance to the waveguide surface until reaching the analytical volume probed by the evanescent field. In contrast, thinner coatings do not sufficiently exclude water from interaction with the evanescent field.

Typical requirements for a polymeric sensor coating for applications in aqueous media include:

- Low permeability for water
- Formation of non-porous layers with sufficient adhesion properties at the waveguide surface.
- Reversible enrichment of the hydrophobic analytes of interest
- Acceptable equilibration times during the enrichment process to minimize the sensor response time
- No or only weak absorption bands in the spectral region of interest (1200 cm^{-1} – 400 cm^{-1})

A number of different coating materials have been tested for their general suitability for sensing applications in aqueous environments [37,38,40,166]. Based on these results E/P-co was selected as suitable membrane material for the detection of VOCs in water. Coating procedures and characterization are described in the respective results sections.

2.6. Improved Model for Simulating Diffusion-based Data for Optical Chemical Sensors

When non-polar organic compounds in aqueous solutions are exposed to a hydrophobic membrane, they preferentially partition from the aqueous phase into the extraction layer. If this membrane is used as the coating for an IRE, the organic compounds will diffuse into the region interrogated by the evanescent field and their presence can be spectroscopically detected if the organic compound provides infrared-active absorption features.

To date, the theoretical description of enrichment processes specifically for polymer coated evanescent field based sensing systems has only been approached in a very simplified way. During the last decade a few models have been developed for different types of chemical sensors, ranging from fiber-optic chemical sensors [88,146, 147] to a dopamine biosensor [148] and thermoelectric gas sensors [149].

During characterization of the analyte transport from the aqueous phase to the probed volume of the sensor system usually following simplifications have generally been adopted:

- Since typical diffusion coefficients for molecules in dilute aqueous solutions are on the order of 10^{-5} cm^2/s [150] while diffusion coefficients for molecules in a bulk polymer are commonly two orders of magnitude lower [151], the assumption is made that transport of analyte into and through the polymer phase is the response limiting process.
- The water / polymer boundary layer has negligible effects on the mass transport rate of the analytes [152].

- Analyte transport in the polymer is exclusively governed by Fickian diffusion in an idealized (defect free) polymer layer.

Following these generally accepted simplifications the mass transport of analytes from the aqueous phase into the volume probed by the evanescent field is entirely independent of the hydrodynamic properties of the system configuration surrounding the active sensor element. Differences in enrichment times of analytes have always been related to different partition coefficients or diffusion coefficients in respect to the particular polymer matrix. Due to the absence of reference data for these values, the inaccurateness of these models has not been considered crucial. Experimental setups of published evanescent sensor systems reveal striking similarities : most devices comprise a flow-cell connected to standard laboratory peristaltic pumps. In such systems the flow-conditions can only be modified within certain limits as standard peristaltic pumps usually do not provide a wide range of flow velocities. Therefore, published flow rates usually range from 1 mL/min to 10 mL/min. Hence, published sensor performances are usually comparable in this respect [153, 154].

However, results reported from pervaporation and ultrafiltration experiments generally suggest that the flow conditions are a major parameter of influence in related applications [155-157]. Some experimental evidence on the influence of flow rates on the signal characteristics of polymer coated evanescent field sensors was given by Roy et al [158], however, without theoretical description of the observed effects. Their work presents a system based on an E/P-co coated ZnSe ATR waveguide used for the detection of various VOCs. Flow-rates are changed from static conditions up to flow rates of 750 mL/min. Exemplary enrichment curves for CB into the extractive membrane for different flow rates are shown in Figure 2.12.

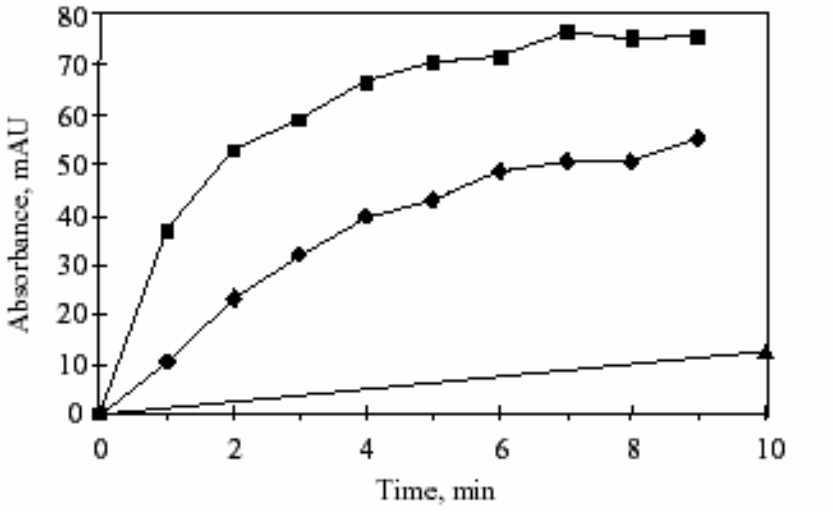

Figure 2.12 Exemplary enrichment curves for CB (30 ppm) into a 10 µm E/P-co layer for different flow-conditions: 10 mL/min (triangles), 100 mL/min (diamonds) and 750 mL/min (squares) [158].

The accelerated increase in signal for higher flow-rates indicates a diffusion limitation at the polymer-aqueous solution interface, which is explained by an immobile water boundary layer at the interface water-polymer. The thickness of this boundary layer can be estimated as a function of flow rate and the extent of agitation, or – more generally - from the flow conditions. Theoretical treatment of the influence of the stagnant surface layer in agitated solutions is given by Louch et al [159] for organic compound extraction via SPE.

Table 2.3 shows different $t_{95\%}$ data (time required to extract 95% of analyte at equilibrium conditions) for the extraction of a variety of hydrocarbons from an aqueous solution with PDMS coated NIR fiber-optic sensors demonstrating the magnitude of the effect of different agitation levels of the solution on the sensor response [42].

Table 2.3 Comparison of $t_{95\%}$ data (time required to extract 95% of analyte amount at equilibrium conditions) for extraction of different hydrocarbons from an aqueous solution with the use of a PDMS coated NIR fiber-optic sensor system. Reproduced from [42].

	$t_{95\%}$ time (min)	
compound	stirred solution	unstirred solution
trichloromethane	1.0	17.0
trichloroethene	4.0	27.2
toluene	9.3	87.0
p-xylene	11.8	236.0
trichlorobenzene	48.0	483.0
gasoline	73.0	794.3

These results lead to the following initial conclusions:

- For virtually all reported data in the field of polymer coated evanescent wave sensor systems the boundary layer (stagnant layer) is the rate limiting factor for the dynamics of the enrichment / extraction process as flow conditions have generally been in the region of strict laminar behavior (Reynolds numbers below 100 for typical flow-cells and flow-rates according to [158]).
- The higher the partition coefficient of a particular analyte the faster the solution depletes of that analyte in close vicinity of the aqueous / polymer interface. Hence, especially for analytes with a high partition coefficient the extraction rate is dependent on agitation of the solution surrounding the extractive layer.
- Only at high agitation levels (flow rates with Reynolds numbers close to turbulent flow) of the solution the boundary layer sufficiently decreases in thickness to a few µm to be neglectable [158]. Hence, only at these conditions the generally accepted results from simplified models based exclusively on Fickian diffusion into the polymer will converge with results

considering flow conditions. However, most results reported in literature to date are far from these flow rates.

2.6.1. Model-Based Optimized Design of Polymer-Coated Chemical Sensors

Based on the findings discussed in the previous section Jakusch [160] has established a fundamental model including the flow-cell geometry into a model describing the enrichment kinetics. In the following, a sound hydrodynamic theoretical model for the simulation of diffusion kinetics for polymer coated evanescent wave sensor systems has been developed in collaboration with the research group Prof. A. Fedorov (School of Mechanical Engineering, Georgia Tech) [43].

2.6.1.1. Physical Arrangement and Model Formulation

A schematic of the modeled flow-cell and coordinate system is shown in Figure 2.13.

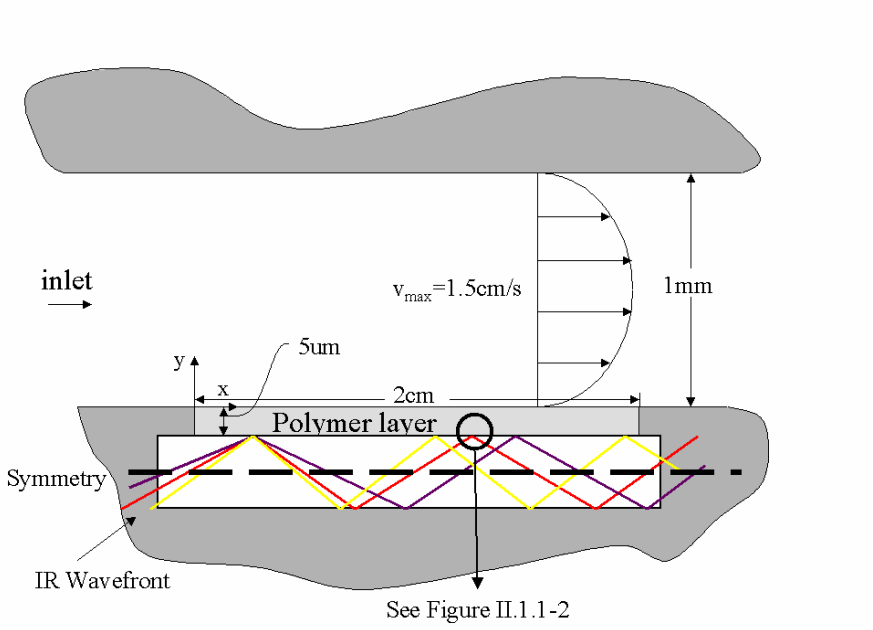

Figure 2.13 Schematic of the flow cell and coordinate system for the hydrodynamic model [43].

Transport of analyte in the flow cell containing the active chemical transducer surface is governed by the following mass and momentum conservation equations and boundary / interface conditions for analyte concentration and flow velocity:

mass conservation

aqueous phase $$\frac{\partial \mathbf{C_a}}{\partial \mathbf{t}} + \mathbf{u}\frac{\partial \mathbf{C_a}}{\partial \mathbf{x}} + \mathbf{v}\frac{\partial \mathbf{C_a}}{\partial \mathbf{y}} = \mathbf{D_a}\nabla^2\mathbf{C_a} \qquad (2\text{-}11)$$

polymer $$\frac{\partial \mathbf{C_a}}{\partial \mathbf{t}} = \mathbf{D_p}\nabla^2\mathbf{C_p} \qquad (2\text{-}12)$$

boundary conditions

$$\mathbf{C_a = C_p} \text{ and } \mathbf{C_p = 0} \text{ at the inlet} \qquad (2\text{-}13)$$

$$\frac{\partial \mathbf{C}}{\partial \mathbf{n}} = \mathbf{0} \quad \text{at all wall boundaries except for the fluid / polymer interface} \qquad (2\text{-}14)$$

$$-\mathbf{D_a}\left.\frac{\partial \mathbf{C_a}}{\partial \mathbf{y}}\right|_{\mathbf{int}} = -\mathbf{D_p}\left.\frac{\partial \mathbf{C_p}}{\partial \mathbf{y}}\right|_{\mathbf{int}} \quad \text{and} \quad \mathbf{KC_a = C_p} \qquad (2\text{-}15)$$

at the fluid / polymer interface.

Here, n is an outer normal at the boundaries, C_a and C_p are the concentrations of the analyte in the aqueous phase and polymer, respectively, D_a and D_p are the diffusivities of analyte in the aqueous phase and polymer, respectively, and K is the partition coefficient for a given analyte and polymer matrix.

momentum conservation for the fluid velocity vector $\vec{\mathbf{v}} = \{\mathbf{u}, \mathbf{v}\}$

$$\text{aqueous phase} \quad \frac{\partial \vec{\mathbf{v}}}{\partial \mathbf{t}} + \vec{\mathbf{v}} \cdot \nabla \vec{\mathbf{v}} = -\frac{\mathbf{1}}{\rho} \nabla \mathbf{P} + \nu \nabla^2 \vec{\mathbf{v}} \qquad (2\text{-}16)$$

$$\text{polymer} \quad \vec{\mathbf{v}} = \mathbf{0} \quad \text{everywhere} \qquad (2\text{-}17)$$

boundary conditions

$$\vec{\mathbf{v}} = \mathbf{0} \quad \text{at all solid walls and fluid/ polymer interface (no slip)} \qquad (2\text{-}18)$$

$$u_{inlet} = u_{max}\left(1-\left(\frac{y-h/2}{h/2}\right)^2\right)$$ fully developed Poiseuille flow profile (2-19)

at the flow cell inlet.

Here, ρ and ν are the density and viscosity of the flowing solution, respectively, P is the hydrodynamic pressure, u and v are velocity vector components in axial and transverse directions, respectively, and u_{max} is the maximum velocity at the centerline (y=h/2) of the flow cell. The assumptions made in the analysis are those of steady incompressible flow, isothermal conditions, and constant fluid viscosity and analyte diffusivity. Also, it is assumed that there are no mass sources present and any heating effects due to the evanescent field present in the polymer layer are negligible.

2.6.1.2. Method of Solution

The governing conservation equations 2-11, 2-12 and 2-16 are of parabolic type and can be effectively solved using an implicit, absolutely stable finite difference numerical integration technique [161]. However, the problem features one jump boundary condition for the analyte concentration at the fluid / polymer interface (equation 2-15), which significantly complicates the simulation procedure. Specifically, it requires a separate solution of the mass-transfer problem in the flow and polymer domains, followed by iterative coupling of these solutions, which is not only very inconvenient but also computationally a very inefficient procedure [161]. In contrast, if one could identify a new “modified” scalar variable equivalent to concentration, which is in itself, as well as the flux associated with this variable, continuous at the interface (i.e. no jump), then

computation can be performed in an efficient non-iterative manner for the combined (fluid and polymer) computational domain. To accomplish this task, the complimentary heat-transfer problem by defining an equivalent “fictitious temperature”, which is continuous at the fluid / polymer interface in the equivalent thermal domain, was solved. For the CFD simulations the commercial available software package FLUENT* was used.

For more detailed description of that transformation please refer to [43]; a short summary of the main CFD simulation results is provided in the following:

- The response time is highly dependent on the analyte diffusivity in the aqueous phase: on average, the time to reach steady state conditions drops one order of magnitude with a two-order-of-magnitude increase in diffusivity.
- For constant volumetric flow rates the optimal flow channel height is the smallest allowable height, which corresponds to the fastest sensor response.
- The least total resistance to mass transfer is achieved when the channel height is equal to or less than the concentration boundary layer thickness at the exit of the channel.
- The sensor response time linearly increases with the thickness of the polymer layer.
- The critical flow channel height for a given flow velocity is independent of the partition coefficient.

* FLUENT CFD Software, Fluent Inc: http://www.fluent.com

- The flow velocity can be used to control the optimal channel height indirectly by altering the concentration boundary layer to approache the height of the channel at the exit.
- Alternative geometries of the sensor flow-cell further improve the response time in comparison to the basic flow-cell design shown in Figure 2.13.

The relevance of these findings to data interpretation of sensing signals recorded with polymer coated evanescent field methods will be discussed in chapter 3.4.

3. Results

In this chapter results from measurements of VOCs in water by polymer coated evanescent field sensor system are presented. In principle, three main measurement series have been performed throughout this thesis at different conditions. Therefore, this chapter is divided into three sections:

i. *Laboratory Conditions:* The simultaneous and quantitative determination of BTX mixtures in water performed at the ASL laboratories at Georgia Tech. E/P-co coated ZnSe crystals were used in conjunction with the automated mixing system (Mixmaster).

ii. *Simulated Field Conditions:* Continuous monitoring of TriCE, TeCE and DCB in a the migrating aqueous phase of an aquifer system at the Technical University of Munich was conducted with an E/P-co coated AgX fiber-optic setup.

iii. *Field Conditions:* A sensor system consisting of an E/P-co coated ZnSe crystal incorporated in an improved flow-cell enabled the determination of CB in groundwater in the Bitterfelder area (Germany) at the SAFIRA remediation site.

3.1. Laboratory Conditions – BTX in Water

3.1.1. Introduction

Developing a chemical sensor usually includes the preparation of numerous solutions for calibration purposes to characterize the sensor performance. The number of solutions that have to be prepared can reach up to hundreds, depending on the analytical problem. Especially when chemometric evaluation has to be applied, a large calibration set is necessary. Due to the fact that the traditional way of preparing calibration sets by diluting stock solutions is error prone and time consuming, it is reasonable to develop automated systems for this task.

Recently, an automated and portable mixing system, based on commonly used components in sequential injection analysis (SIA) [162-164] has been introduced by our research group [73]. In this work the mixing system was applied for the precise preparation of benzene, toluene and the three xylene isomers (BTX) / water mixtures at trace level concentrations (<mg/L regime). An E/P-co coated ZnSe crystal was applied to simultaneously and quantitatively detect individual BTX components in multi-component mixtures by means of MIR-FTIR evanescent wave spectroscopy.

3.1.2. Experimental Setup

3.1.2.1. Materials

Ethylene/propylene co-polymer (60:40) was purchased from Aldrich (Milwaukee, WI). Methanol, benzene, toluene, o-xylene, m-xylene and p-xylene were purchased from Aldrich (Milwaukee, WI) and were of analytical grade. Deionized water was used for preparation of all solutions and for sensor regeneration.

3.1.2.2. Instrumentation

Data was recorded in a spectral range of 600 cm^{-1} to 1400 cm^{-1} using a Bruker Vector 22 Fourier transform infrared (FT-IR) spectrometer (Bruker Optik GmbH, Ettlingen, Germany) equipped with a liquid N_2 cooled mercury-cadmium-telluride (MCT) detector (Infrared Associates, Stuart, FL). A total of 100 scans were averaged for each spectrum with a spectral resolution of 4 cm^{-1}. For ATR measurements a vertical ATR accessory (Specac, Smyrna, GA) in combination with trapezoidal ZnSe ATR elements (50*20*2mm, 45º; Macrooptica Ltd., Moscow, Russia) and a stainless steel flow-cell (custom made, Volume: 280 µl, free contact area to ATR crystal: 5.5 cm^2) were used. A custom made mixing system (*Mixmaster*) [73] designed for handling volatile organic compounds assured accurate concentrations of sample mixtures and continuous flow of the analyte solutions through the ATR cell. A schematic of the experimental setup is shown in Figure 3.1.

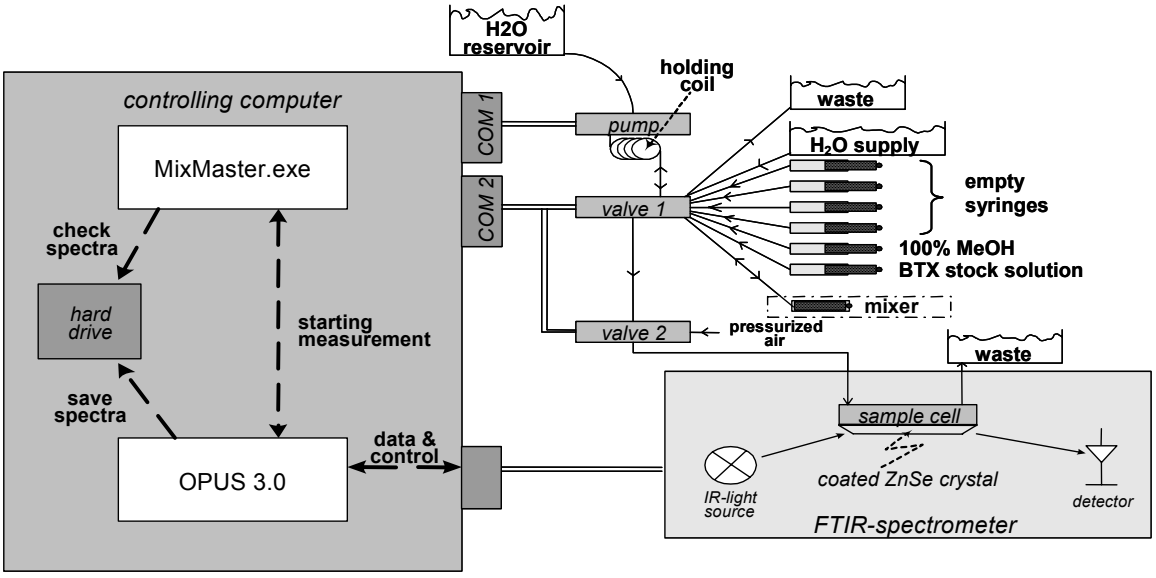

Figure 3.1 Schematic of the combination of the Mixmaster with the ATR setup for dissolved BTX measurements.

3.1.2.3. Mixmaster

In order to ensure a precise set of diluted standard solutions a software-controlled automated mixing system (*Mixmaster*) developed by our research group was applied [73]. The main components comprise a high precision piston pump (syringe volume 25000 µL), which is attached to a selection valve with 10 ports and a 2-way injection valve connected to the ATR flow-cell. A C++ software interface allows controlling all parameters of the system including piston position, pump speed, and positions of the valves. Furthermore, measurements of the FT-IR spectrometer are triggered and synchronized by the Mixmaster control software. Stainless steel tubings connected via bulk-head unions are exclusively used minimizing wall adsorption effects. By avoiding the use of polymer components within the *Mixmaster* system and by providing headspace-free storage and mixing of solutions the *Mixmaster* is especially suitable for

high-throughput investigation of volatile organic compounds, e.g. during extensive sensor optimization and calibration. A detailed description of the mixing system is given elsewhere [73] and a front view can be seen in Figure 3.2

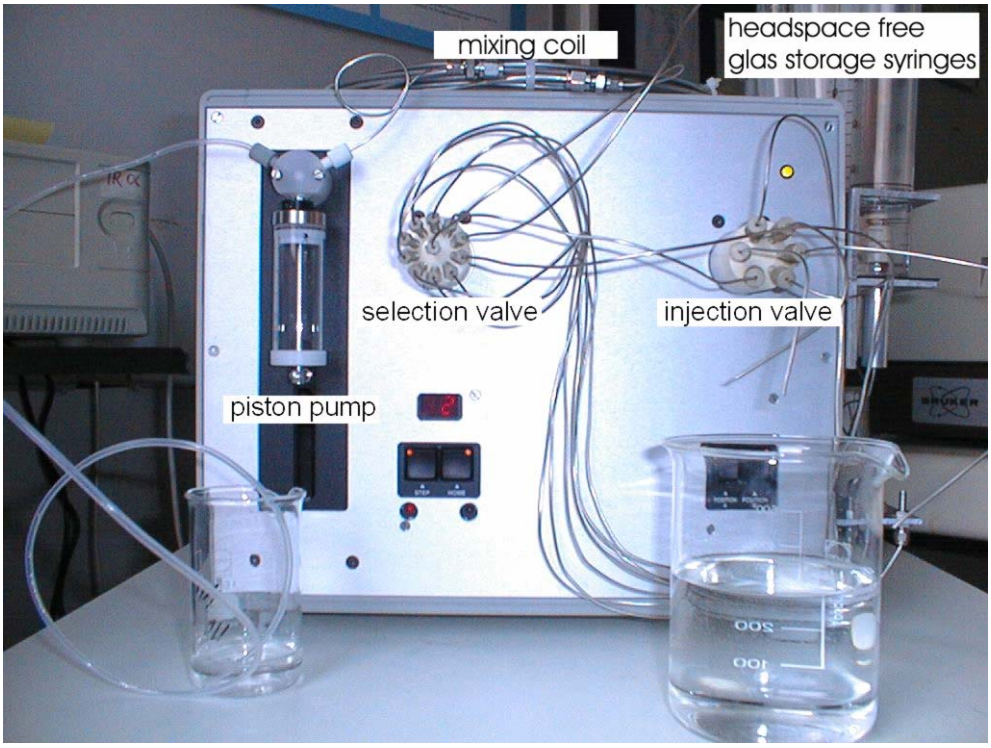

Figure 3.2 Front view of the Mixmaster

A typical measurement cycle for sensor calibration comprises following steps:

- rinsing of the cell with water.
- collecting a background spectrum.
- Preparing the analyte solution.
- Up to 20 min rinsing of the flow-cell with analyte solution while collecting absorption spectra every 2 min; (v) 25 min rinsing of the cell with deionized water to extract the analyte and regenerate the polymer layer.

The sample solution flow rate was held constant at 3 mL/min throughout all experiments. Methanol was used as a solution mediator ensuring that the BTX mixture remains dissolved in aqueous solution. Previous works have shown that this procedure has no effect on the final sensor readings [96]. Dilutions were prepared from a primary stock solution of 200 ppm (v/v) of all compounds of the BTX group in pure methanol. Thorough mixing resulted in a total methanol concentration of 0.5 % (v/v) in the investigated sample solutions. Cross interferences and thus influences on the enrichment properties due to measurement of an analyte mixture, are not to be expected in the examined concentration range presented in this study, as has been shown previously [100]

3.1.2.4. Preparation of the Extractive Polymer Membrane

A 1 % (w/v) coating solution E/P-co was prepared by dissolving 0.5 g of granular polymer under reflux in 50 ml n-hexane. Prior to coating the ATR crystal was thoroughly rinsed with methanol. Approx. 300 µL of clear, hot solution were applied to the surface of the ATR crystal using an Eppendorf pipette. The crystal was kept at room temperature for at least 2 h ensuring evaporation of most of the solvent. Subsequently, the polymer coating was exposed to hot air treatment with a hot air gun at 150 °C for 5 min to remove remaining traces of solvent. The thickness of the layer was determined by differential weighing to be 4.2 µm.

For sensing applications of trace components it is essential to coat the transducer surface with (chemo)selective membranes excluding interfering matrix components that would overlap or mask absorption features of the investigated analyte. This is of particular importance when measuring in strongly IR absorbing matrices such as water. In the present study, a thin layer of hydrophobic E/P-co is coated onto the waveguide

surface. Hydrophobic analytes partition into the hydrophobic membrane while water and other polar components are widely excluded from the analytical volume probed by the evanescent field. Additionally, the polymer coating enhances the sensitivity of the sensor by enriching hydrophobic analytes in the polymer membrane following the principles of solid phase extraction. One approach to roughly estimate the enrichment factor for a particular analyte is to relate obtained absorption peak heights from measurements with uncoated waveguides to results achieved with polymer coated transducers. However, limited solubility of BTX in water and strong absorptions of the water matrix in the fingerprint region of the MIR spectral range prohibit direct ATR measurements with uncoated crystals. Hence, analyte solutions with a concentration of 1 % in methanol have been prepared for an estimation of the achievable enrichment factors. ATR spectra of methanolic solutions have been recorded with uncoated ZnSe crystals. Peak heights for each analyte have been normalized and correlated to peak heights obtained for an enrichment measurement of a 500 ppb (v/v) aqueous analyte solution with an E/P-co coated ZnSe crystal after the partition equilibrium has been established. Following this approach, enrichment factors > 15.000 are estimated for benzene, toluene and for the xylene isomers, respectively.

Based on previous experience, E/P-co proved to be a suitable material for enrichment of a wide range of hydrophobic compounds from aqueous solutions [165,166].

3.1.3. Results

3.1.3.1. Water Equilibration

Despite the hydrophobic properties of the membrane a considerable amount of water diffuses into the polymer coating over a period of several hours causing IR absorptions as shown in Figure 3.3.

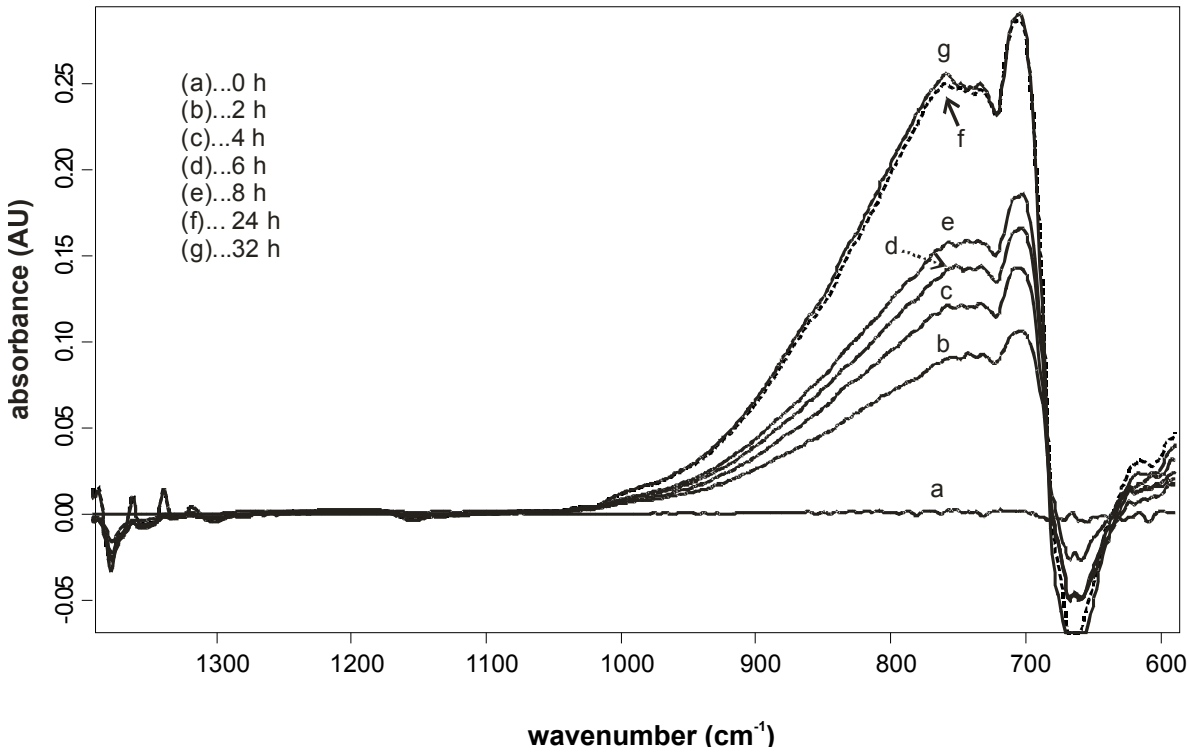

Figure 3.3 IR absorptions resulting from water diffusion into an E/P-co membrane with a thickness of 4.2 µm coated onto the surface of a ZnSe ATR-crystal over a period of 32 h. After 24 hours (f) equilibrium conditions are reached and no further increase in absorption is observed.

A broad absorption band, caused by swelling of the polymer during the water diffusion process, occurring between 1000 cm^{-1} and the cut-off frequency of the detector around 600 cm^{-1} significantly influences spectroscopic measurement due to the resulting

baseline drift. In a simple sample matrix this effect can be compensated by selecting suitable peak integration methods and integration limits. However, a stable baseline increases the reliability of the measurements and enables automated data evaluation, as shown in a recent study by our research group [59,60]. Figure 3.3 illustrates that water diffusion reaches equilibrium conditions before 24 hours of exposure to the aqueous phase. Hence, prior to analysis the coated waveguide has been equilibrated with deionized water for a period of at least 24 h.

3.1.3.2. BTX Enrichment Characteristics

Figure 3.4 shows an exemplary spectrum of a mixture of benzene, toluene and the three xylene isomers with a concentration of 500 ppb (v/v) each after an enrichment time of 20 min into an E/P-co layer. Corresponding absorption peaks have been labeled for clarity.

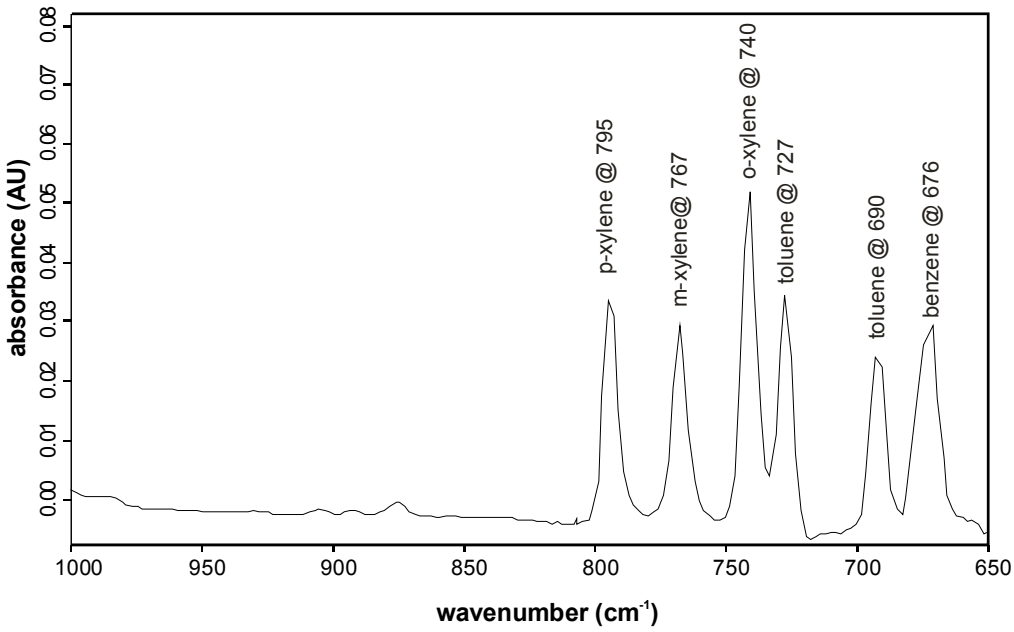

Figure 3.4 IR absorption spectrum of a sample mixture in aqueous solution after enrichment into an E/P-co layer. Enrichment time: 20 min, concentration: 500 ppb (v/v) each.

Typical absorption bands of benzene, toluene and the three xylene isomers can be identified resulting from molecule specific aromatic C–H out of plane vibrations in the fingerprint region of the mid-infrared spectral range. Band assignment has been performed via single component enrichment experiments leading to the following allocation of the absorption features: benzene at 676 cm^{-1}, toluene at 690 cm^{-1} and 727 cm^{-1}, o-xylene at 740 cm^{-1}, m-xylene at 767 cm^{-1} and p-xylene at 795 cm^{-1}. Each analyte shows distinctive absorption features, which are not or only slightly overlapping. Hence, during this first study conventional peak integration of the IR absorption bands was applied. More complex samples will be evaluated using chemometric data evaluation techniques particularly suitable for optical sensors [60].

Recently, it has been shown by Phillips et al. [43] that achieving steady state conditions for polymer coated sensor systems is not only dependent on the partitioning behavior of analytes into the polymer layer. Factors such as analyte diffusion properties within the

aqueous phase, flow channel height and flow velocity substantially affect chemical sensor response. The only tunable parameter of the ATR flow-cell used throughout the experiments was the flow velocity. Evaluating preliminary experiments the flow velocity of the analyte solution was set to 3 mL/min, which enabled measurements in the time regime of several minutes without using excessive amounts of analyte solution.

Figure 3.5 shows typical diffusion curves of the investigated analytes plotting the integrated peak area vs. the enrichment time. After 18 min of enrichment the diffusion process reaches equilibrium conditions for the given analyte mixture and data evaluated at this or at a later time delivers most reliable and sensitive results.

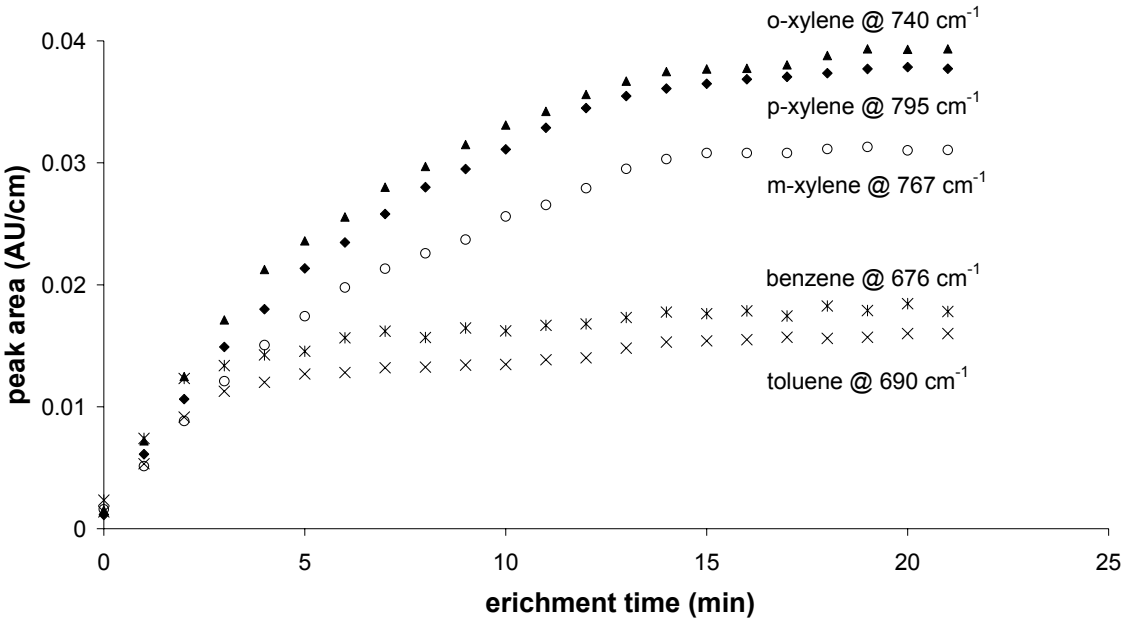

Figure 3.5 Typical enrichment curves for the BTX components in water at a concentration level of 1 ppm (v/v) each into an E/P-co coating. Equilibrium of the diffusion process is reached after approximately 18 min of enrichment time.

Figure 3.6 shows the obtained calibration curves for the investigated analytes in aqueous solution. The calibration of the sensor has been performed by five repetitive measurements of a concentration series ranging from 50 ppb (v/v) to 1 ppm (v/v) for

each analyte in the mixture. Error bars for each data point represent the calculated standard deviation derived from five repetitive measurements each. Prior to each measurement the polymer coating was regenerated by rinsing the flow-cell with water at a flow velocity of 3 mL/min for 25 min, which efficiently removed all analytes from the sensing membrane.

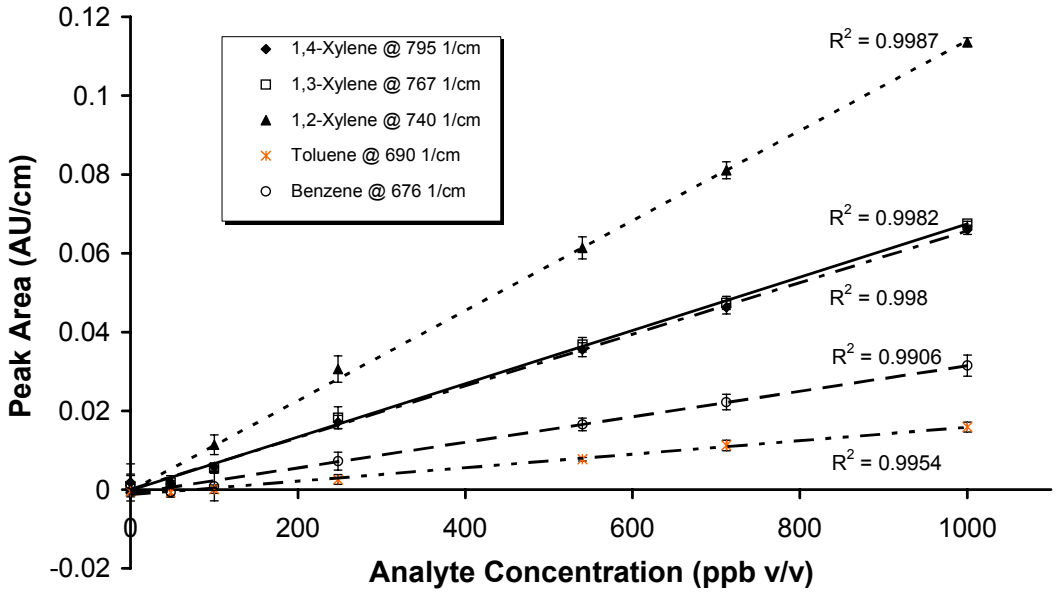

Figure 3.6 Calibration graphs for benzene, toluene and the xylene isomers in the concentration range of 0 – 1000 ppb (v/v) based on peak area integration. The error bars represent the standard deviation of five subsequent measurements

Data evaluation has been performed by peak area integration due to clear separation of the investigated absorption peaks. The integrated areas are plotted vs. the concentration resulting in linear fit functions with R^2-values generally > 0.99 included in Figure 3.6. Detection limits for each analyte in the mixture have been calculated according to IUPAC by the 3 sigma criteria (3 times standard deviation of the peak-to-peak noise related to the slope of the linear regression function) and resulted in LODs in the low ppb range in

mixture of all examined analytes. These values represent a significant improvement compared to previously reported results using head-space IR-ATR measurements for similar analytes yielding significantly higher detection limits [141,142]. The LODs from this work and other relevant spectroscopic approaches to BTX determination in water are given in Table 3.1.

Table 3.1 Overview on relevant spectroscopic approaches to BTX detection in water

reference	this thesis	142	103	55	76	167	42
method	FTIR-ATR	FTIR-ATR	FTIR transmission	UV transmission	UV derivative spectroscopy	Photo-acoustic	SPME-NIR
spme-matirx	EP/Co	PIB	parafilm	PDMS			PDMS
simultaneous detection	yes	no*	no*	no*	yes	no*	no*
time per measurement**	20 min	20 min	>30 min	90 min	1 min	40 min	20 min
benzene LOD ppb (v/v)	45		160	18	+/-50	308	
toluene LOD ppb (v/v)	80	292	652	5	+/-50	954	173
o-xylene LOD ppb (v/v)	10		72	4	+/-50		
m-xylene LOD ppb (v/v)	20		886		+/-50		
p-xylene LOD ppb (v/v)	20		57	3	+/-50		129

*… The author wants to emphasize that this statement does not imply that simultaneous detection of analytes is generally impossible with these methodologies, however, data utilized for LOD determination is derived from single analyte experiments only in the cited references.

**... This timeframe only refers to the actual measurement and doesn't account for other steps such as sensor equilibration time, calibration time, data evaluation time and so on

The sensor system presented in this work shows competitive or preferable performance in respect to LODs and measurement time to other relevant spectroscopic approaches reported for BTX analysis. Furthermore, 20 min per measurement cycle for quantitative simultaneous determination of five components is a reasonable time frame for a multitude of analytical applications including waste-water monitoring, remediation

process surveillance or drinking water monitoring contingent upon improved limits of detection. With the introduction of appropriate chemometric data evaluation techniques remote analysis will be further facilitated [59].

3.1.3.3. Test for Field Capability: Continuous Detection of o-Xylene in a Natural Pond Water Matrix

In the following experiment a preliminary test for the field applicability of sensor systems similar as described in the previous chapter is presented.

A continuous measurement series of various concentrations of o-xylene added to urban pond water is presented. The obtained data demonstrates the potential of polymer coated evanescent field sensors for real-world applications in water quality monitoring.

Materials

Ethylene/propylene co-polymer (60:40) was purchased from Aldrich (Milwaukee, WI). Methanol, o-xylene, were purchased from Aldrich (Milwaukee, WI) and were of analytical grade. Pond water was used for preparation of all solutions and for sensor regeneration. The pond water was sampled from a domestic goldfish-pond in Atlanta, GA, USA.

Preparation of Ethylene/Propylene Co-polymer Thin Film

Coating Procedure

The coating procedure adheres to the description in chapter 3.1.2.4 with following modification: 210 µL of the hot coating solution were applied resulting in a film thickness of approx. 3.3 µm determined via differential weighing. Preparation of the o-Xylene Samples A 1 % (v/v) solution of o-xylene in methanol was prepared and diluted with

pond water to 20, 50, and 80 ppm (v/v) of analyte concentration. Additional methanol was added to keep the amount of methanol constant at 1 % (v/v). The sample solutions have been freshly prepared prior to each measurement ensuring minimal losses due to evaporation.

Instrumentation

Data was recorded in the spectral range of 400 cm-1 to 1600 cm-1 using a Bruker Equinox 55 Fourier transform infrared (FT-IR) spectrometer (Bruker Optics, Billerica, MA) equipped with a liquid N2 cooled mercury-cadmium-telluride (MCT) detector (Infrared Associates, Stuart, FL). A total of 100 scans were averaged for each spectrum with a spectral resolution of 4 cm-1. For this continuous study spectra were recorded every minute for a period of approx. 8 hours. For ATR measurements a horizontal ATR accessory (Specac, Smyrna, GA) utilizing trapezoidal ZnSe ATR elements (72*10*6mm, 45º; Macrooptica Ltd., Moscow, Russia) and a stainless steel flow-cell (custom made, Volume: 2 ml, free contact area to ATR crystal: 7.2 cm²) were used. Solutions were pulled through the flow-cell via an Alitea C8-Midi peristaltic pump (Watson-Marlow Alitea, Wilmington, MA) at a constant flow rate of 4.5 mL/min.

Results

After equilibration with water as described above the sensor was exposed to neat pond water samples for several hours. No significant further changes of the absorption spectra could be observed. Following, the sensor was exposed to pond water samples spiked with o-xylene and an increasing absorption feature at 740 cm^{-1} (aromatic C–H out of plane vibration of o-xylene) could be observed after a measurement time of one minute already.

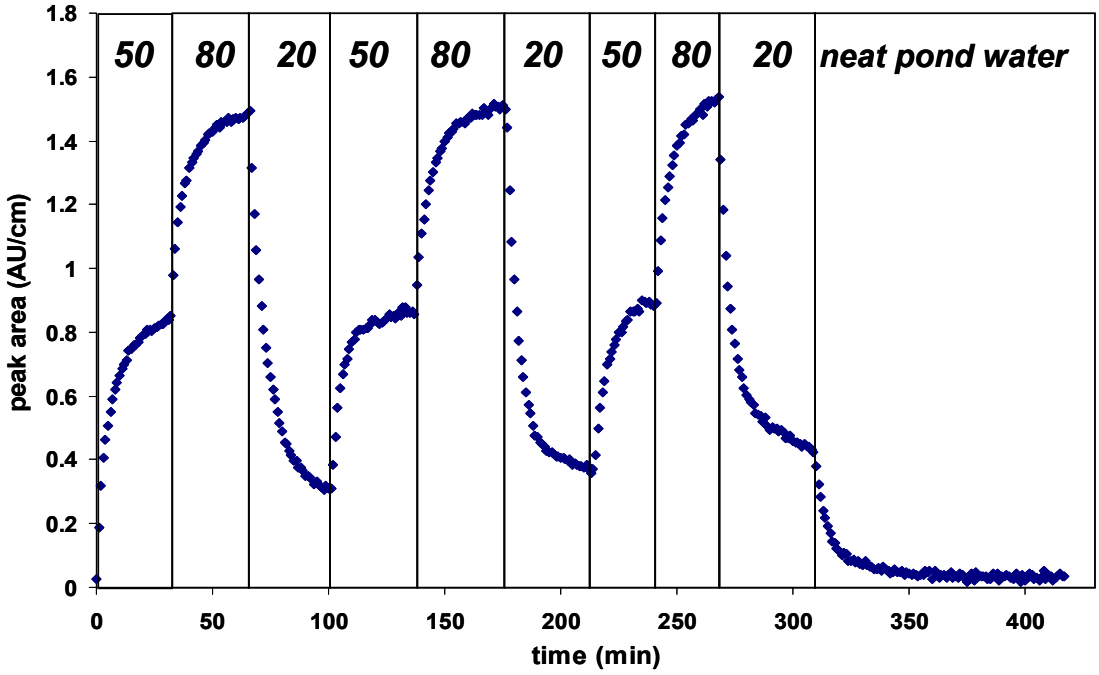

Figure 3.7 Trace of the peak area of the absorption band of o-xylene at 740 cm^{-1} with time during enrichment based IR-ATR sensing. Concentration trace: 50 ppm; 80 ppm; 20 ppm (in pond water; the sensor was exposed to each concentration for approx. 30 to 35 min) followed by neat pond water for sensor regeneration.

Figure 3.7 shows the continuous measurement of o-xylene in pond water over a period of 8 hours for a repetitive concentration trace of 3 different levels (50, 80, and 20 ppm v/v). Concentrations have been changed every 30 to 35 minutes. The trace at 740 cm^{-1} clearly shows that o-xylene partitioning never reaches equilibrium conditions for the selected observation window. However, it is evident that the response time of the sensor to changing concentrations of the sample solution is < 1 min, which is an essential aspect for rapid on-line data evaluation and e.g. threshold monitoring. Appropriate multivariate data evaluation techniques, which should enable prediction of the equilibration concentration of analytes for a calibrated system after very short enrichment times are currently developed in our research group. Slightly increasing peak area values from one repetition to the next along with a minute positive off-set after

regenerating the sensor with neat pond water (see minute 300 to 420) indicate that the broad water absorption band in the spectral region between 1000 cm-1 and the cut-off frequency of the detector (around 600 cm-1) was still slightly increasing throughout the measurement. Recently, our research group has developed a multivariate method for automated recognition and correction of baseline drifts [59,60]. As most chemical sensing systems are affected by baseline drifts due to ageing, degradation, and swelling of the molecular recognition interface, this generic solution enables the application of membrane based sensing devices in real-world environments.

3.1.4. Conclusions

A new approach for simultaneous and direct detection of benzene, toluene and the three xylene isomers (BTX) in aqueous solution based on polymer coated mid-infrared evanescent wave sensors has been presented. Investigated sensor characteristics include the enrichment time, sensor sensitivity and reproducibility. Linear relationships between characteristic absorption peak areas vs. input concentrations with R^2-values > 0.99 could be obtained for each analyte along with high reproducibility for 5 consecutive measurements. With the presented measurement setup equilibrium conditions for this diffusion based sensor were achieved within approx. 18 min, which is comparable to other membrane based chemical sensor systems. Sensitivity in the low ppb (v/v) region for all BTX compounds and during simultaneous detection experiments represent a significant improvement compared to any ATR-IR sensor reported to date for this class of analytes. At the present stage of development the sensor system is already suitable as analytical device for online, in-situ process monitoring of multiple organic components at low ppb concentrations. Further optimization of the presented method includes

aspects such as flow cell design for minimized response time and chemometric data evaluation enabling remote operation. Hence, multi component measurements with FTIR-ATR techniques in the low ppb to sub ppb region are foreseeable in the near future.

3.2. Simulated Field Conditions – VOCs Determination in an Aquifer

3.2.1. Introduction

These measurements were conducted as part of the IMSIS (In-situ Monitoring of Landfill Related Contaminants in Soil and Water by Infrared Sensing, EVK1-CT-1999-00042) project in order to show the applicability of polymer coated ATR sensor systems at in the field sensing tasks. Measurement conditions at such aquifer systems are highly similar to real world conditions with the advantage that analytes can be introduced at known concentrations. In order to directly detect pollutants in the boreholes of the aquifer system a fiber-optic sensing approach was applied. A specially designed sensor head assembly with 6 m long AgX fibers was developed in collaboration with the research group of Prof. Abraham Katzir (Tel-Aviv University). Analytes of environmental significance (TriCE, TeCE and DCB) have been detected and quantified in high agreement with HS-GC validation measurements throughout this test.

3.2.2. Experimental Setup

3.2.2.1. Materials

E/P-co, with 60% ethylene content was obtained from Sigma-Aldrich (Sigma-Aldrich Handels GmbH, Austria); all other chemicals were of analytical grade. Aqueous stock solutions for sensor calibration were prepared with deionized water. The aquifer system was operated with conventional tap water.

3.2.2.2. Silver Halide Fibers

The silver halide (AgX) fibers used during this study have a composition of $AgCl_{0.4}Br_{0.6}$ [168,169]. Core only fibers have been used with a diameter of 900 µm, a refractive index of 2.13 @ 10 µm and an average damping factor of 0.2 dB/m @ 10.6 µm. AgX fibers are ideally suitable for the proposed sensing application due to high mechanical flexibility, an optical window between 3000 cm^{-1} and 500 cm^{-1}, robustness in the required temperature range from -10° C to +40° C and, finally, long shelf- and application lifetime. However, silver halides are chemically instable when exposed to UV radiation (photolysis), base metals (e.g. aluminum; cementation), hydrogen sulfide (formation of insoluble Ag_2S) and halide ions (complex formation). Thus, sensor head, coating and fiber cables have to ensure appropriate protection of the fiber from environmental impact.

3.2.2.3. Instrumentation

FT-IR

All measurements were performed with a Bruker Vector 22 FT IR spectrometer (Bruker Optik GmbH, Ettlingen, Germany) equipped with a LN_2 cooled mercury-cadmium-telluride (MCT) detector (detectivity D^*=3×10^{10} cm $Hz^{1/2}$ W^{-1}, 0.01 cm^2 detector element, Infrared Associates, Inc., Stuart, FL, U.S.A.). Light coupling from the spectrometer into the fiber optic waveguide and to the detector at the distal end of the fiber was achieved by a custom-built mirror arrangement utilizing one off-axis parabolic mirror (focal length *f*=50.8 mm) at the spectrometer/fiber interface and two similar mirrors (*f*=43 mm) at the fiber/detector interface. SMA compliant connectors for silver halide fiber based optical cables in combination with xyz-positioners ensure rapid and reproducible alignment and connection of the fiber optic probe. For all measurements 100 spectra were averaged with a spectral resolution of 4 cm^{-1} in the spectral range of 4000 cm^{-1} to 400 cm^{-1}. The setting of the aperture after the light source (SiC globar) was open; apodization was a medium Norton-Beer algorithm.

Head Space Gas Chromatography (HS GC)

The HS GC reference analysis was done on a HP 5890 series II GC equipped with flame ionization detection (FID) and electron capture detection (ECD) capability. A Dani HSS 86.50 headspace autosampler (Dani, Milao, Italy) was coupled to the HS GC system. A J&W Scientific Inc. DB-624 capillary column (30 m x 0.250 mm, 1.4 µm stationary phase) was used with nitrogen as carrier and make up gas. Samples were softly shaken for 6 min in the autosampler and injected afterwards using a split/splitless injector kept at 120 °C. The temperature program started at 80 °C for 10 min followed by a ramp to 150

°C at 20 °C/min and finished holding a temperature of 150 °C for 5 min. The detectors were kept at a temperature of 200 °C.

Sensor Head and Fiber Cables

Measurements under field conditions demand careful design of the sensing system and particularly of the sensor head and the fiber optic cables. The mechanical construction of the sensor head has to protect the active sensing region of the fiber at any given time from mechanical damage, while being small enough to be lowered into groundwater monitoring wells with inner diameters of usually 5 cm. Furthermore, unrestricted intimate contact between the active transducer and the probed aqueous phase has to be ensured. Finally, the fiber has to be protected from mechanical damage by strain, squeezing or overbending. Following these requirements a sensor probe was developed and optimized during several field measurement campaigns.

Figure 3.8 Close up of the sensor head, showing the active transducer section of the fiber (1), the o-ring seal lead-troughs (2), the two stainless steel tubes containing the sensor head/fiber cable interface (3) and the fiber cables (4). For the described measurements the semicircular part covering parts of the active transducer was removed.

The prototype sensor head is shown in Figure 3.8 and features a fiber mount made from black Teflon with two O-ring sealed watertight stainless steel lead-throughs accommodating the active sensing zone of the fiber as a loop with a bending radius of 40 mm. Attached to the Teflon mount are two stainless steel tubes forming the interface to the fiber cable and providing water tight sealing and pull relief by O-ring sealed fittings. Each leg of the fiber cable is approx. 3 m long and the silver halide fiber is contrived into dual-layer tubing (inner tubing diameter: 1 mm; outer tube diameter: 8 mm). Connectors attached at the end of the fiber cables follow the SMA standard and hold onto the fiber and the tubing by a watertight O-ring system.

Coating of the sensing zone is performed from a solution of 2.1 % (w/v) E/P-co in hexane/octane (1:1), which was refluxed until fully dissolved. The exposed central section of the fiber was manually dipped twice into the hot E/P-co solution and after

approx. 45 min. once into the same solution at ambient temperature. Afterwards the coating was homogenized with a heat gun set to approx. 100° C for approx. 5 min.

3.2.2.4. Aquifer simulation

The pilot scale aquifer simulation allows studying water flow and analyte dispersion in soil under defined conditions. A stainless steel tank with dimensions of 10 m×1 m×2 m (L×W×H) was filled with soil from the Munich Gravel Plain, a quaternary calcareous and very heterogeneous gravel (permeability coefficient k_f = 7×10^{-3} m/s). A bridge-slot screen on both ends of the tank separates two approx. 10 cm wide compartments from the soil-bed. Water guided into the front compartment (volume V=104 L), i.e. the mixing chamber, will continuously flow through the bridge-slot screen into the soil bed following a 1 % slope. At the rear end of the aquifer system the water is drained through a constant head setup. By varying the height of the run off the hydraulic gradient can be varied between 1 % and 10 %. The water flow $\dot{\mathbf{V}}$ was set to 20 L/min 2.5 weeks before the actual measurements to ensure equilibrium conditions within the soil bed. The water inlet of the front mixing chamber has several nozzles below the water table to homogeneously spread water flowing into the chamber. Additionally, the tubing is filled with a diffuser material (steel wool) further improving the water/analyte mixing process. Analytes are added as highly concentrated methanolic solutions upstream from the nozzle arrangement to the influent water by a peristaltic metering pump. Since the selected model analytes do not dissolve easily in water, they are regarded as dense, nonaqueous phase liquids (DNAPL) and a supplementary solvent has to promote their solubility, as opposed to natural environments where such analytes dissolve at a longer time scale [170].

Furthermore, the content of the mixing chamber is cycled by a submersible pump at a rate of 6 L/min. The distributed injection of the analytes and the circulation via the submersible pump in the mixing chamber closely resemble the concept of a perfectly stirred tank reactor (PSR). The PSR assumes a homogeneous analyte concentration c within the volume of the reactor and its efflux. If the influent concentration c_0 is a function of time t, the generic solution for the concentration $c(t)$ in the reactor is given by

$$c(t) = e^{-t/\tau}\left[C_0 + \frac{1}{\tau}\int_0^t e^{s/\tau} c_0(s)\,ds\right] \qquad (3\text{-}1)$$

where C_0 is the initial concentration within the PSR and τ is the dwell time, respectively [171].

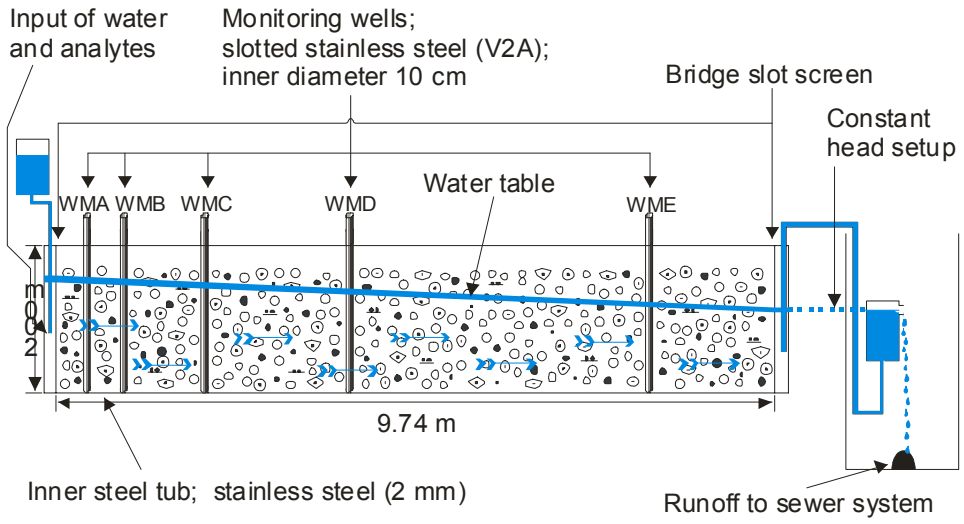

Figure 3.9 Sketch of the aquifer simulation “Munich North” (side view).

Five monitoring wells made from slotted stainless steel tubes are accessible along the aquifer system. With an inner diameter of 150 mm, sensors and sampling lines can be directly introduced into the groundwater flow. All wells cover the entire height of the soil bed allowing measurements in all possible depths (Figure 3.9).

3.2.3. Sensor Calibration and Validation

The aim of the following experiments was to study (a) the sensor response to different analyte concentration profiles, (b) the differences in the response behavior of the sensor readout vs. reference analysis based on off-line HS GC and (c) long-term stability and field readiness of the sensing system. Representative results from several field measurement campaigns are conclusively discussed below demonstrating the feasibility of the proposed mid-infrared chemical sensing concept for the determination of VOCs under field conditions.

Ten hours prior to the first experiment the sensor was installed in monitoring well "WMB", approx. 45 cm below the water surface (water temperature was constant at $\approx$10.2° C) and kept at this location during the whole measurement campaign. Well "WMB" is located 93 cm downstream of the mixing chamber. At an average water flow rate of 20 L/min analytes arrive in well WMB approx. 30 min after their injection to the influent water stream (Figure 3.9). The high water flow rate resulting in a short dwell time τ of 5.2 min only, the multi nozzle array and the pump assisted water recirculation within the mixing chamber lead to a better sample homogenization as observed during previous field experiments, where formation of two phase regions and strong analyte evaporation effects at a flow rate of 6 L/min (τ = 17 min) were evident [95].

Three different analytes, 1.2-dichlorobenzene (DCB), TeCE and TriCE, were selected as relevant model analytes, and their respective characteristic absorption bands in the mid-infrared spectral range were evaluated. At 1036 cm^{-1} and 748 cm^{-1} the aromatic C-Cl stretching vibration and aromatic C-H out of plane vibration of DCB can be observed. TeCE exhibits a strong absorption feature of the C-Cl stretching vibration at 911 cm-1 and TriCE shows two features at 842 cm^{-1} and 932 cm^{-1} respectively. Quantitative information was obtained by conventional evaluation of the respective peak areas as the spectral features appear well separated in the ATR spectrum. Spectra were recorded in 5 min intervals while samples for reference HS GC analysis were collected semi-automatically with a computer-controlled multichannel peristaltic metering pump approx. every 30 min. Sensor and sampling line were placed at the same depth. Hence, the reference samples were collected from the water volume also probed by the IR sensor. Before each sample collection cycle the sampling lines were drained to a waste container for one minute by flushing with water from the monitoring well avoiding adsorption losses to the wall of the tubing and carry-over artifacts.

To study the sensor response to different concentration gradients, three different analyte input functions where defined. In the first run, two rectangular peaks of equal width (120 min) and height (DCB, TeCE and TriCE: 4 mg/L) were injected. Selected concentrations correspond to the order of magnitude of contamination levels found in leachates collected from landfills and contaminated sites. In the second run, two rectangular sample peaks of almost equal width (peak one: 135 min, peak two: 119 min) were injected. The second injected peak had twice the height of the first peak (peak one: DCB and TeCE: 4 mg/L, TriCE: 8 mg/L). In the last experiment analyte concentrations were stepwise increased and decreased subsequently (DCB and TeCE: 4 mg/L, 8 mg/L, 6 mg/L, 4 mg/L; TriCE: double concentration of DCB). Each concentration level was kept for 90 min.

Sensor calibration was performed after the field measurements at laboratory conditions. For the calibration the sensor was immersed into a beaker filled with 1 L of distilled water magnetically stirred for rapid homogenization. Defined amounts of methanolic stock solution containing 10.000 ppm (v/v) of each DCB, TeCE and TriCE were added to the beaker with an adjustable pipette (Transferpette 100-1000, Eppendorf, Hamburg, Germany). Spectra were recorded in 5 min intervals for 40 minutes to monitor sensor response.

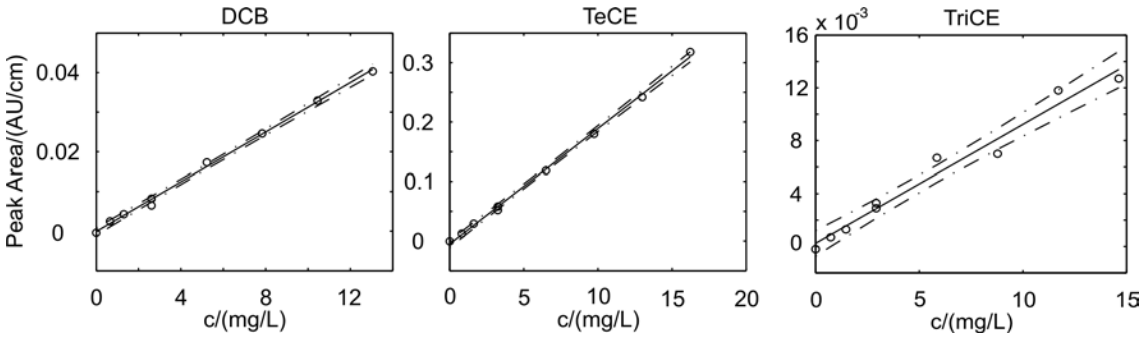

Figure 3.10 Linear regression (solid) and confidence intervals (P=95 %; dash dotted) of the sensor response (circles).

For each concentration step the respective maximum in peak area was used for calculation of the calibration curve. The sensor was calibrated for concentrations in the range between 0 ppm (v/v) and 10 ppm (v/v) (Figure 3.10). The resulting calibration data is given in.

Table 3.2.

Table 3.2 Statistical data of the sensor calibration. Intercept *a*, slope *b*, product-moment correlation coefficient *r*, prediction error SS, standard deviation of slope s_b, intercept s_a and limit of detection LOD. n=9.

Substance	Peak	*a*	s_a	*b*	s_b	*r*	LOD[1)]	SS
	cm^{-1}	AU cm^{-1}	AU cm^{-1}	AU L $mg^{-1}cm^{-1}$	AU L $mg^{-1}cm^{-1}$		mg L^{-1}	mg^2 L^2
DCB	1036	-0.0001	0.0004	0.0031	0.0001	0.9987	0.8	0.4532
TeCE	911	-0.0049	0.0025	0.0194	0.0003	0.9991	0.8	0.4788
TriCE	932	0.0002	0.0004	0.0009	0.0001	0.9866	2.8	5.8846

3.2.4. Results

The experiments demonstrate for the first time that continuous online monitoring of VOCs in groundwater over a period of three days is feasible with the mid-infrared fiber optic sensor probe developed in this study. The aquifer simulation facility grants conditions in an outdoor environment similar to those found at contaminated sites or landfills. In Figure 3.11 the concentration data obtained from the IR sensor during the three experimental series is compared to reference data acquired from simultaneously collected samples analyzed by HS GC.

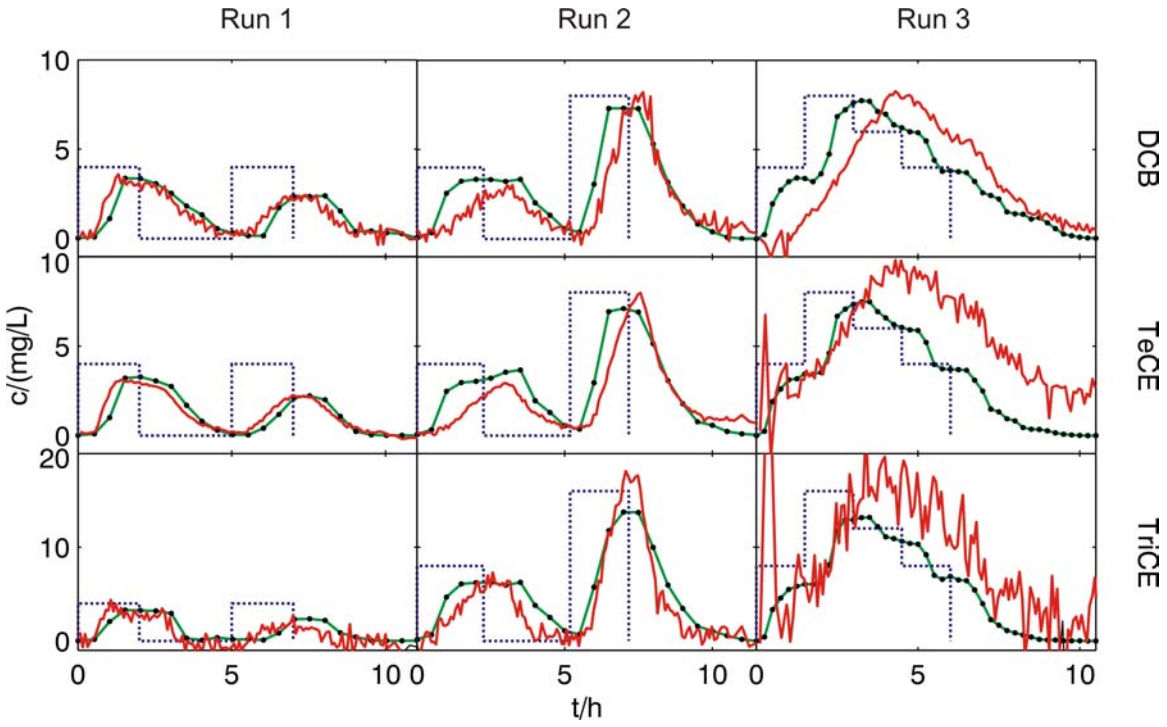

Figure 3.11 Comparison of concentrations measured by IR sensor (red), reference HS GC (green with dots) and analyte concentration added to the water stream (blue). Confidence intervals (P=95%, n=9) at $\bar{y}$ are ± 0.6 mg/L (DCB), ± 0.7 mg/L (TeCE) and ± 2.3 mg/L (TriCE), respectively.

The two rectangular sample peaks injected to the influent during series one were monitored simultaneously by the IR sensor and samples analyzed by HS GC as reference. Although the two peaks were equal in width and height, the recorded HS GC reference concentration profiles differ from each other. The first peak appears broader (peak one 2.5 h, peak two 2.2 h) and higher (peak one 3.4 mg/L, peak two 2.4 mg/L) than the second peak. During the first day the IR sensor response was faster compared to the HS GC reference. The maximum sensor readout was observed 0.2 h (average for the three analytes) before the maximum reference values. This trend was continued in the second peak. In general, reference data shows a high degree of agreement with the sensor data, i.e. 97 % of the DCB, 96 % of the TeCE and 100 % of the TriCE reference values are within the confidence interval of the sensors data.

During the progress of series two agreement between sensor and reference data is not as good as during day one. Again, two peaks have been introduced to the mixing chamber, and the sensor shows much slower response to the rise in concentration for the first peak. Peak concentrations are recorded 0.4 h (DCB), 0.7 h (TeCE) and 0 h (TriCE) after the respective reference values reached their concentration maxima. Also, no distinct concentration plateau as observed in the reference measurements could be determined.

The third day of measurements is characterized by a strong drop in overall light throughput within the fiber optic sensor system (Figure 3.12).

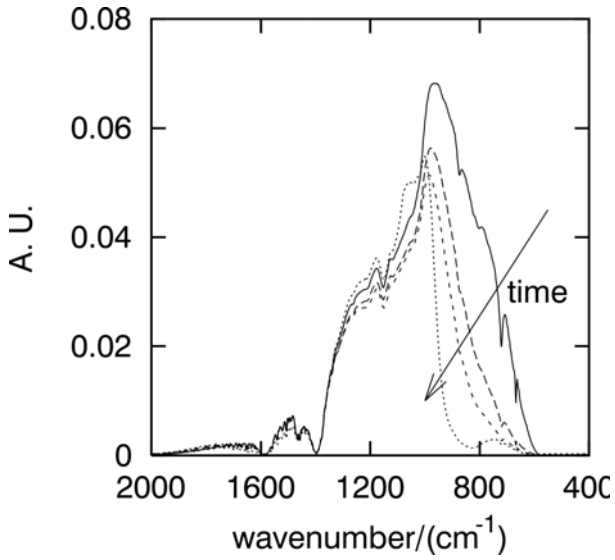

Figure 3.12 During a measurement campaign of three days the single beam spectra changed in shape and overall light throughput as a result of water intrusion. The first spectrum was recorded ten hours before the first experiment (i.e. series 1), the other three at the beginning of each series, respectively. For all spectra the sensor head was immersed in water. Note the strong decrease in light throughput on the third day leading to an impaired signal-to-noise ratio.

Evidently, due to a leak in the sensor head water made contact with the silver halide fiber and thus caused strong absorption losses. This hypothesis is supported by the

observed reversibility of the effect as light throughput and characteristics of the single beam IR spectrum recovered after storage of the sensor in a dry place for several days.

The absorption band of DCB was least effected by this change in light throughput, thus the DCB data shows the best agreement with the reference values during the third day of the field measurements. Sensor and reference show the same maximum concentration values (~7.9 mg/L), however, sensor data appears delayed by 1 h. During stepwise decrease of analyte concentration the time shift between reference values and sensor readout in fact decreases and after 10 h the reference values are again located within the confidence interval of the sensor data.

Despite successful field tests the experiments revealed that during a period of three days changes of the coating absorption behavior are observed affecting the sensor response time. Effectively, this results in a drift of the baseline in the IR absorption spectra and is introducing errors during evaluation of the obtained concentration values. Recently, two novel chemometric methods based on principal component regression (PCR) have been developed in our research group automatically compensating for baseline drifts as integrated algorithm of chemometric data evaluation schemes. Since baseline drifts are broad features compared to analyte absorption peaks the drift contributions can be modeled by polynoms orthogonal to the principal components modeling the concentration result (‘polyPCA’). In a second, more sophisticated approach, drift components are modeled by synthetic pseudo-principal components along with conventional principal components characterizing the analyte peaks (‘pPCA’) [59,60]. Both algorithms have successfully been tested with synthetic spectra and real-world data acquired with mid-infrared chemical sensors and will substantially improve field applicability of chemical sensors in general [60].

Recently, organically modified sol-gels have successfully been tested as novel enrichment matrix in combination with planar infrared waveguides [172-174] and coated onto the surface of silver halide fibers [175].

3.2.5. Conclusions

In this chapter the concept of a fiber optic mid-infrared sensor system for on-line and in-situ monitoring of VOCs in groundwater has been investigated and successful applied during aquifer field studies. During the course of a three day field experiment in an artificial aquifer system the sensor data showed high agreement with the reference data acquired by conventional HS GC analysis of collected water samples with respect to the found concentration maxima and the progression of the analyte concentration levels with time. Due to baseline separated analyte absorption bands in the mid-infrared conventional peak integration methods were used to gain quantitative information. Over time, presumably a delamination process of the E/P-co coating changed the behavior of the sensor system. Response times increased, so that the determined concentration maxima were shifted backwards in time when compared to the reference analysis. Furthermore, decreased light throughput in the relevant portion of the spectral window resulted in a lower signal to noise ratio. The experiments have shown that a better understanding of the long time behavior and ageing of the coating materials is of great importance for successful application of the sensor system. In measurement scenarios where the sensor is deployed and used for autonomous online monitoring, stability of the sensor characteristics are of vital importance.

3.3. Field Conditions – Chlorobenzene in Groundwater

The first tests of ATR based polymer coated sensor systems under real world field conditions were performed at the SAFIRA site (German acronym for ‘‘Remediation Research in Regionally Contaminated Aquifers’’), a remediation pilot plant, in the region of Bitterfeld / Wolfen (Saxonia-Anhalt, Germany) [176,177].

The ground water aquifer in this region has been contaminated over an area of 25 km^2, with a total volume of approximately 200 million m^3, due to activities in open cast lignite mining and related chemical industries for more than 100 years [178]. Since a few years, a local aquifer in the southeast of the city Bitterfeld, contaminated mainly with chlorobenzene (CB), was selected to develop and test new in situ reactive barrier technologies within the German ground water remediation project SAFIRA [179]. The reactive barrier technologies are based on various chemical, physical, and biological processes. The entire on-site pilot plant in Bitterfeld consists of 5 shafts, each with a depth of 23 m and a diameter of 3 m, and a shaft-to-shaft distance of 19 m, housing a total of 20 reactors [177,179].

The following systems are being tested as part of in situ technologies:

- Biodegradation of chlorinated contaminants in an anaerobic/microaerobic system
- Adsorption and simultaneous microbial degradation on activated carbon
- Zeolite-supported palladium catalysts
- Membrane-supported palladium catalysts
- Oxidative solid metal catalysts
- Activated carbon filtration

- Anaerobic microbial degradation of pollutants
- Combination of redox reactors

The subsurface consists predominantly of gravel, which is embedded in lignite and Bitterfeld mica sand. Three aquifers are separated by watertight layers; the reactors of the in situ pilot plant are supplied exclusively with ground water from deeper zones of the quaternary aquifer. In the quaternary aquifer, the contaminants are strongly stratified: groundwater from 5 to 9.5 m in depth is almost non-polluted; in a depth of 9 to 16 m, CB is the dominating contaminant at a concentration of approximately 2 mg/L; in 16 to 22 m of depth, CB concentrations increase to levels up to 51 mg/L. Since the beginning of the measurements in 1997, the hydrochemical parameters and the concentrations of the pollutants in the quaternary aquifer have not changed [176]. The comparatively high contamination levels coinciding with presumably constant concentration levels, along with modern, flexible sampling systems rendered the SAFIRA site highly suitable for first field measurements with the developed IR chemical sensor systems.

3.3.1. Experimental Setup

3.3.1.1. Instrumentation

Sensor Calibration

Data was recorded in a spectral range of 600 cm^{-1} to 1400 cm^{-1} using a Bruker Equinox 55 FT-IR spectrometer (Bruker Optics Inc., Billerica, MA) equipped with a liquid N_2 cooled mercury-cadmium-telluride (MCT) detector (Infrared Associates, Stuart, FL). Flow speed: 4.5 mL/min.

Field Measurements

Data was recorded in a spectral range of 600 cm^{-1} to 1400 cm^{-1} using a Bruker Vector 22 FT-IR spectrometer (Bruker Optik GmbH, Ettlingen, Germany) equipped with a liquid N_2 cooled mercury-cadmium-telluride (MCT) detector (Infrared Associates, Stuart, FL).

Parameters Applicable to Both Scenarios

A total of 100 scans were averaged for each spectrum with a spectral resolution of 4 cm^{-1}. For ATR measurements, a horizontal ATR accessory (Specac, Smyrna, GA) in combination with trapezoidal ZnSe ATR elements (72*10*6mm, 45º; Macrooptica Ltd., Moscow, Russia) and an aluminum flow-cell (custom made, Volume: 2 mL, free contact area to ATR crystal: ~7.2 cm^2) were used. A schematic and a picture of the flow-cell is shown in Figure 3.13. An Alitea C8-Midi peristaltic pump (Watson-Marlow Alitea, Wilmington, MA) was used to ensure continuous flow of the analyte solutions through the ATR cell. In order to minimize adsorption and diffusion losses stainless steel tubing was exclusively used to deliver analyte solutions to the flow cell. A schematic illustration of the setup is shown in Figure 3.14.

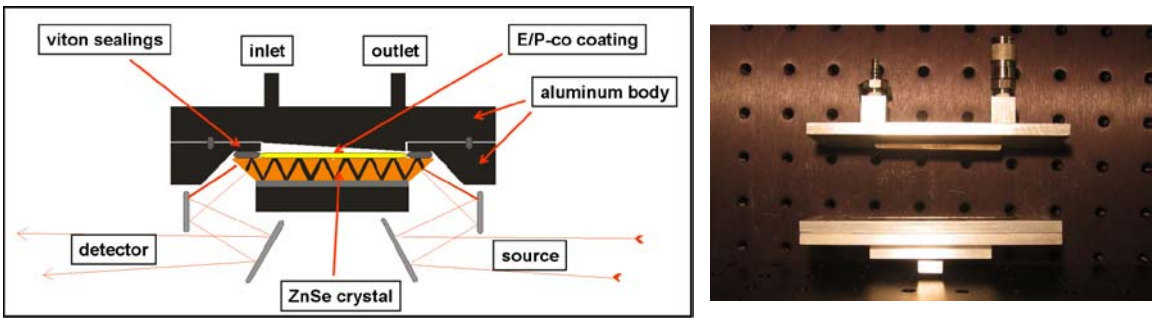

Figure 3.13 Left: Scheme of the custom made flow cell. Right: Picture of the flow cell (disassembled)

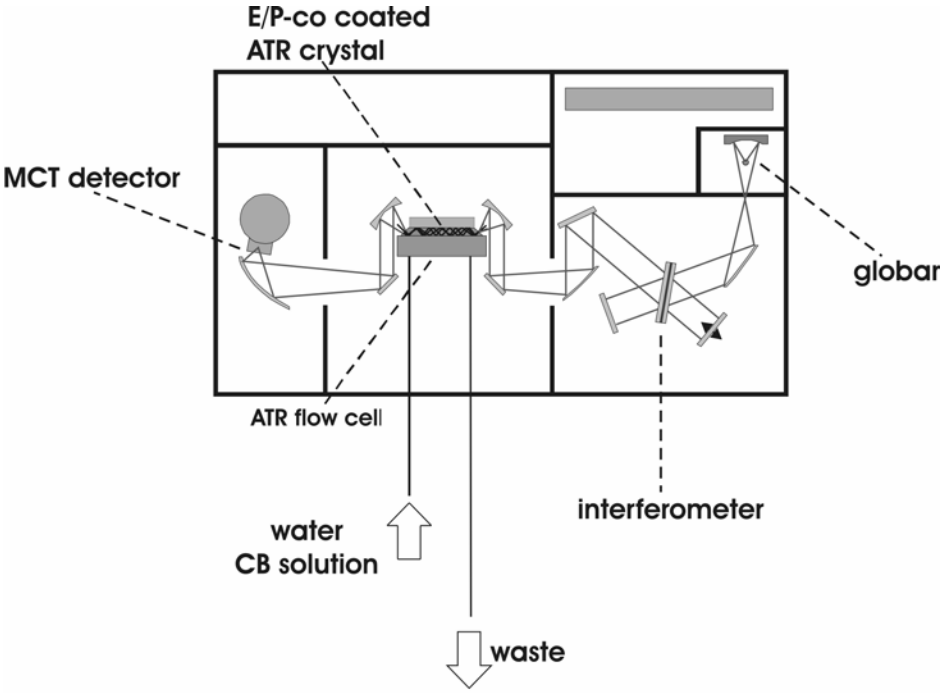

Figure 3.14 Schematic of setup for on-site chlorobenzene measurements.

HS-GC Validation Measurements

The HS GC reference analysis was done on a HP6890 series II GC equipped with flame ionization detection (FID). An Agilent 7694 headspace autosampler was coupled to the HS-GC system. A Chrompack CP-Sil 6B capillary column (30 m x 0.250 mm, 50 µm stationary phase) was used with nitrogen as carrier and make up gas. Samples were softly shaken and extracted at 60°C for 60 min in the autosampler and subsequently injected using a split/splitless injector kept at 250 °C. The temperature program started at 45°C for 5 min followed by a ramp to 200 °C at 20°C/min and finished holding a temperature of 200 °C for 3 min. The detector was kept at a temperature of 280 °C.

3.3.1.2. Preparation of the Extractive Polymer Membrane

A 1 % (w/v) coating solution of E/P-co was prepared by dissolving 0.5 g of granular polymer under reflux in 50 ml n-hexane. Prior to coating, a new ATR crystal was thoroughly rinsed with methanol. About 210 µL of clear, hot solution were applied to the surface of the ATR crystal using an Eppendorf pipette. The crystal was kept at room temperature for at least 2 h ensuring evaporation of most of the solvent. Subsequently, the polymer coating was exposed to hot air treatment with a hot air gun at 150 °C for 5 min to remove remaining traces of solvent and then kept tempered at 80°C in an oven overnight. The thickness of the layer was determined by differential weighing to be 3.2 µm.

3.3.1.3. Sensor System Calibration

Among all VOCs chlorobenzene (CB) is the main pollutant in the groundwater aquifer around the SAFIRA site by several orders of magnitude. According to previously published data on the composition and concentrations of the pollutant cocktail in the groundwater of the Bitterfeld region [176] calibration for CB of the sensor system was conducted in the concentration range from 10 mg/L to 80 mg/L at the ASL laboratory at Georgia Tech. Field measurements were conducted applying a (smaller) Bruker Vektor 22 FT-IR spectrometer. The high agreement of the results obtained under field conditions and the laboratory measurements demonstrate the transferability of the calibration data.

Prior to the calibration measurements the coated sensor element was submersed in water and equilibrated over night. Following, the calibration set consisting of 10 mg/L, 20

mg/L, 30 mg/L, 50 mg/L and 80 mg/L of CB in water was measured regenerating the E/P-co layer after each calibrant. From the MIR absorption spectra of CB, the band with the highest intensity (aromatic C-H out of plane vibration around 740 cm^{-1}) was selected for data evaluation via peak integration.

Figure 3.15 shows the significant part of the CB absorption spectrum for 5 different concentrations of CB in water after partitioning into the E/P-co layer for 24 minutes.

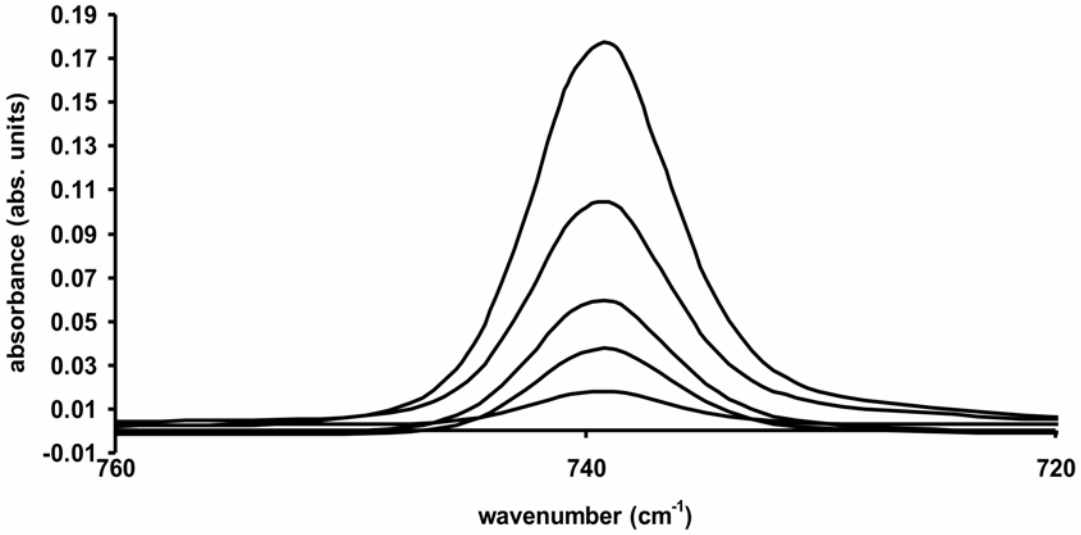

Figure 3.15 The C-H out of plane vibration band of CB for 5 different concentrations after partitioning into the E/P-co layer.

Data evaluation in this case could be performed by simple band integration, as there is only one compound present in the solution. Calibrations have been performed before and after the measurement campaign with approx. 4 weeks of time lapse in between the first and the last calibration set. Figure 3.16 shows a linear calibration derived from band integration for 3 repetitive (1 measured before and 2 after the measurement campaign) runs of the calibration set.

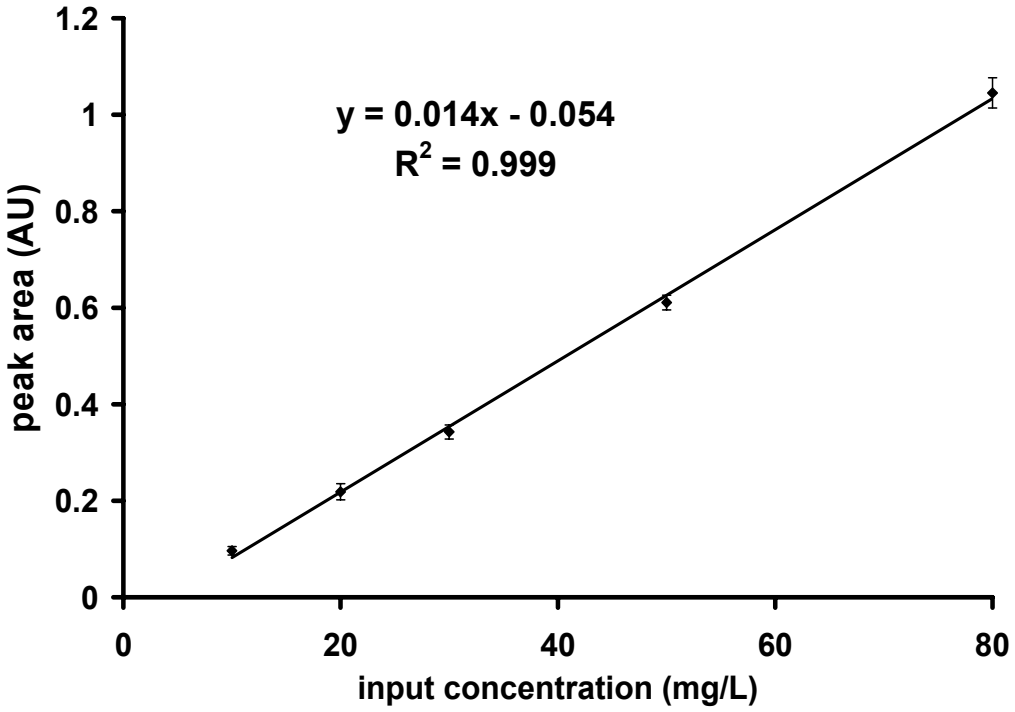

Figure 3.16 Calibration curve for 3 repetitive measurements of the calibration set of CB. Error bars are derived from the standard deviation for each data point.

The acceptable linearity and the small standard deviation proof that the sensor provides superior stability despite being submersed in a highly polluted sample during the measurement campaign, the mechanical stress of being transported and several drying/wetting cycles.

3.3.2. Results

3.3.2.1. SAFIRA Measurement Surrounding Conditions

The SAFIRA site offers an automated sampling system. A partial flow of groundwater is permanently pumped from various depths in the shafts through an array of glass bottles,

which are placed in a cooled storage chamber in the adjacent analytical laboratory and from there back to the reactors for remediation procedures. The same flow configuration is available for water exiting the reactors after the remediation processes. Thus, samples can be conveniently collected from the glass bottles in the laboratory environment rather than descending instrumentation into the shafts. For this first test of an ATR based sensor system for groundwater monitoring it was decided to perform repetitive measurements of water from one shaft for several days in order to verify accuracy and stability of the developed sensor system at field conditions. Concentration levels in the groundwater flow in the Bitterfeld region can be considered constant for the measurement period of several days [176]. Table 3.3 shows the concentration and composition of the groundwater revealing chlorobenzene as the main pollutant by almost 2 orders of magnitude.

Table 3.3 HS-GC validation measurements of groundwater sample from shaft 5 at the SAFIRA site.

sample	*B5-HB*
date	*9/22/2003*
chlorobenzene	***27.92 mg/l***
ethylene	*12.19 µg/l*
vinylchloride	*0.05 mg/l*
1,2-trans-dichloroethylene	*0.04 mg/l*
1,2-cis-dichloroethylene	*0.06 mg/l*
benzene	*0.13 mg/l*
2-chlortoluolene	*0.05 mg/l*
1,4-dichlorobenzene	*0.52 mg/l*
1,2-dichlorobenzene	*0.29 mg/l*

Besides the listed pollutants, the groundwater is characterized by rather high hydrogensulfide contents (up to 5 mg/L) and low concentrations of inorganic pollutants (e.g. heavy metals, arsenic, etc.). Other noteworthy characteristics are high levels of sulfate (up to 1000 mg/l) and chloride (approx. 1300 mg/l).

3.3.2.2. Chlorobenzene Enrichment Behavior

After sensor equilibration with distilled water over night, a stable baseline without noticeable spectral changes due to water diffusion was obtained. Subsequently, groundwater was pumped through the flow cell and spectra were recorded every 2 min until equilibrium was reached. Figure 3.17 shows exemplary spectra of a groundwater sample from shaft 5 and a calibration solution of 50 mg/L CB in water. Besides a concentration related difference in band intensities and the bands related to E/P-co swelling (approx. 780 cm^{-1} – 800 cm^{-1}), both spectra appear to be identical. Hence, we can deduct that all contaminants except chlorobenzene are below the threshold level of detection for this sensor system. The aromatic C-H out of plane vibration of CB around 740 cm^{-1} was selected for data evaluation via peak integration.

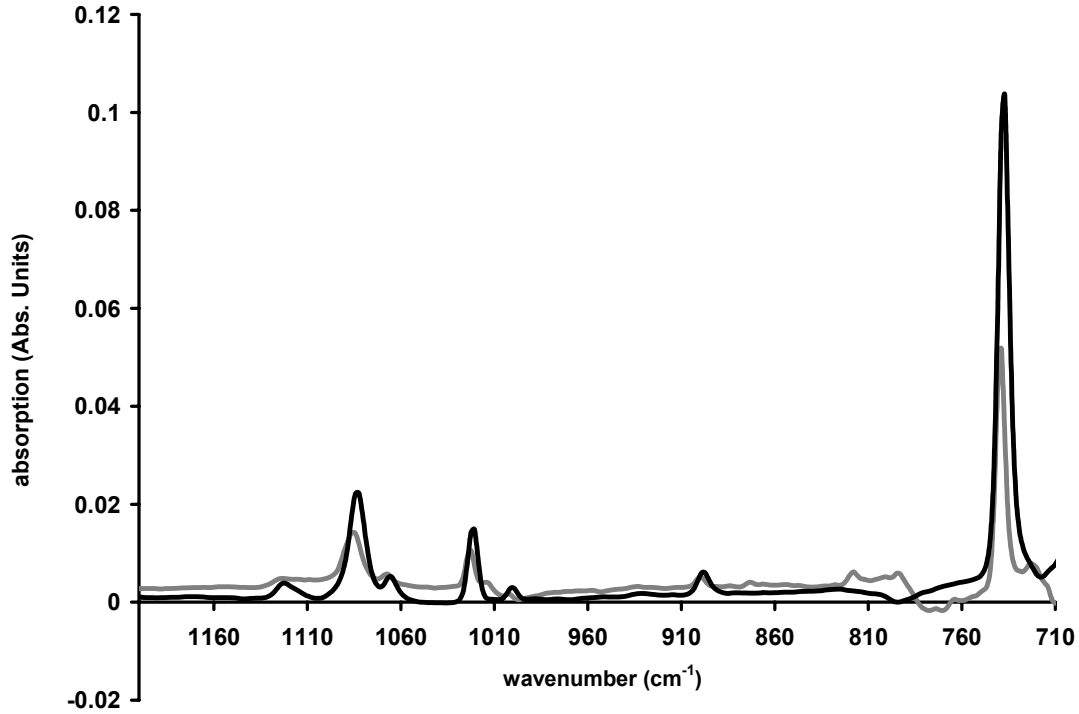

Figure 3.17 Exemplary spectra of a groundwater sample from shaft 5 (grey line) and a calibration solution of 50 mg/L CB in water (black line). Spectra were recorded after 24 min of exposure time to the polymer coated transducer. The peak area of the band at 740 cm^{-1} is used for data evaluation.

A small but noticeable detail can be extracted from the comparison of the spectra in Figure 3.17:

The groundwater spectrum (and all other spectra recorded at the SAFIRA site), is blue shifted by about 3 cm^{-1}. This is explained by the fact that the Vector 22 instrument used on-site had not been calibrated for a number of years and obviously drifted in the wavelength accuracy over that long period of time. This could be compensated for by adapting the spectral region of the band integration during data evaluation in respect to the calibration measurements (performed on the Equinox 55).

Figure 3.18 and Figure 3.19 show the enrichment behavior of CB into the E/P-co layer by plotting the peak area (740 cm^{-1} band) over time for 2 different flow rates of the sample solution (Figure 3.18: 4 mL/min; Figure 3.19: 23 mL/min).

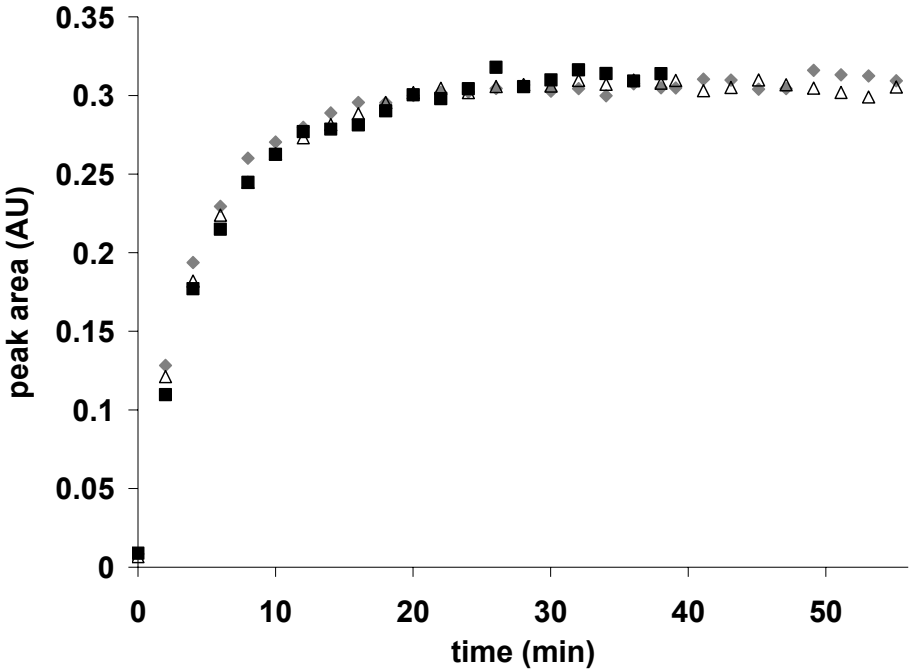

Figure 3.18 Enrichment curves of CB from groundwater at SAFIRA site into the E/P-co layer at a flow rate of 4 mL/min. The 3 measurements were performed at 3 different days.

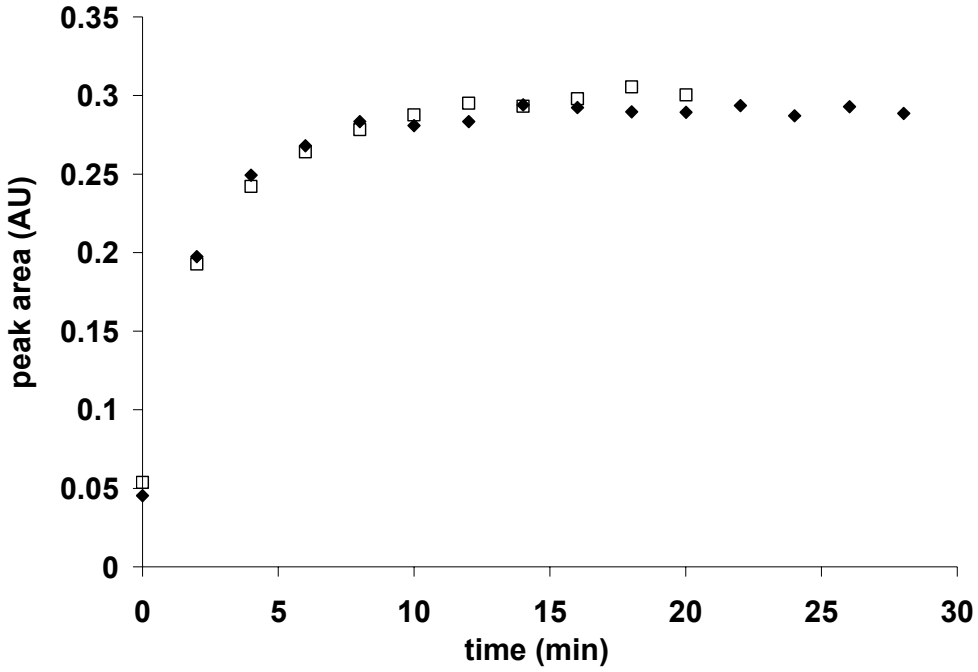

Figure 3.19 Enrichment curves of CB from groundwater at SAFIRA site into the E/P-co layer at a flow rate of 23 mL/min. The 2 measurements were performed at 2 different days.

It can be seen that after reaching equilibrium conditions the peak area remains almost identical for both flow rates, while for the higher flow rate the equilibrium is reached faster. These results indicate that changes in the flow conditions above the polymer layer affect the response time of the sensor. The dependence of the response time on the flow rate or, more specifically, the flow conditions above the extractive membrane has only recently been studied for infrared sensors accounting for results reported from pervaporation and ultrafiltration experiments, which suggested such dependencies [155-157]. Some experimental considerations of these effects were discussed by Roy et al [158]. Extensive CFD simulations have been presented by Phillips et al [43] and Louch [159] on related issues. For a detailed description of the influence of the flow velocity on the equilibration process please refer to chapter 2.6.

A promising result for future IR chemical sensor applications is the obtained reliable and stable performance over a time period of at least 5 days at field conditions. We feel confident to extrapolate this time span significantly considering that the calibration data has been recorded over a period of several weeks prior to and after the field measurement campaign without deviation in performance.

To verify the accuracy of the ATR measurements, the peak areas of the absorption feature at 740 cm^{-1} of all 5 measurement periods have been evaluated with a linear regression function (Figure 3.16) and the values have been compared to the HS-GC validation measurement (Table 3.4).

Table 3.4 Comparison of the ATR measurements to the HS-GC measurements.

	Run 1	*Run 2*	*Run 3*	*Run 4*	*Run 5*
measured conc. CB (mg/L)	**28.71**	**27.54**	**31.05**	**28.01**	**29.05**
HS-GC (mg/L)	27.92	27.92	27.92	27.92	27.92
differnce mg/L	0.79	0.38	3.13	0.09	1.13
error %	2.82	1.36	11.21	0.31	4.03

With an average deviation of only 1.10 mg/L (3.94%) to the validation measurement the ATR sensor system provided surprisingly accurate results. Additionally, these results verify that it is valid to calibrate such a sensor systems at laboratory conditions, still yielding reliable accurate results at field conditions. In this first study the cocktail of pollutants present in the groundwater (although at lower concentrations than CB), the difference in pH level and the measurements at cooled conditions (groundwater samples was at least several degrees Celsius colder than the laboratory calibration samples) did not significantly affect the sensor system performance.

3.3.2.3. Sensor Regeneration

In this series of experiments it has been observed that the enrichment of CB into the E/P-co layer was completely reversible. In Figure 3.20 exemplary spectra of a groundwater sample from shaft 5 and a successively recorded spectrum after regenerating the sensor with distilled water are shown. The enrichment step was performed until equilibrium was reached (approx. 24 min at a flow rate of 4mL/min) and sensor regeneration was performed by rinsing the flow cell with distilled water for the same period of time and at the same flow rate.

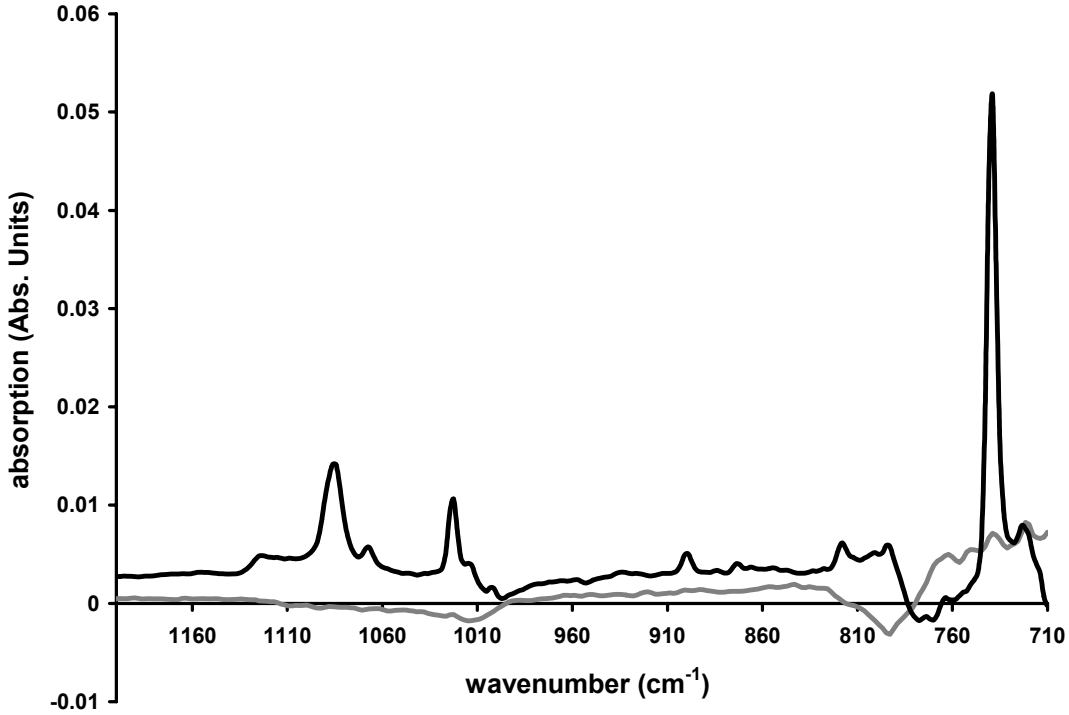

Figure 3.20 Exemplary spectra of a groundwater sample from shaft 5 (black line) and a successively recorded spectrum after regenerating the sensor with distilled water (grey line). Enrichment time and regeneration time were both 24 min with a flow rate of 4 mL/min. The peak area of the band at 740 cm^{-1} is used for data evaluation.

It is evident that an equally long regeneration time is not sufficient for complete CB removal from the E/P-co layer, as a weak absorption feature at 740 cm^{-1} can still be observed.

In Figure 3.21 enrichment of CB into the polymer and sensor regeneration are plotted for 2 flow rates, 4 mL/min and 23 mL/min, respectively. As expected, the curve for the higher flow rate reaches equilibrium conditions faster and shows a more rapid depletion of the analyte within the polymer layer during the regeneration step.

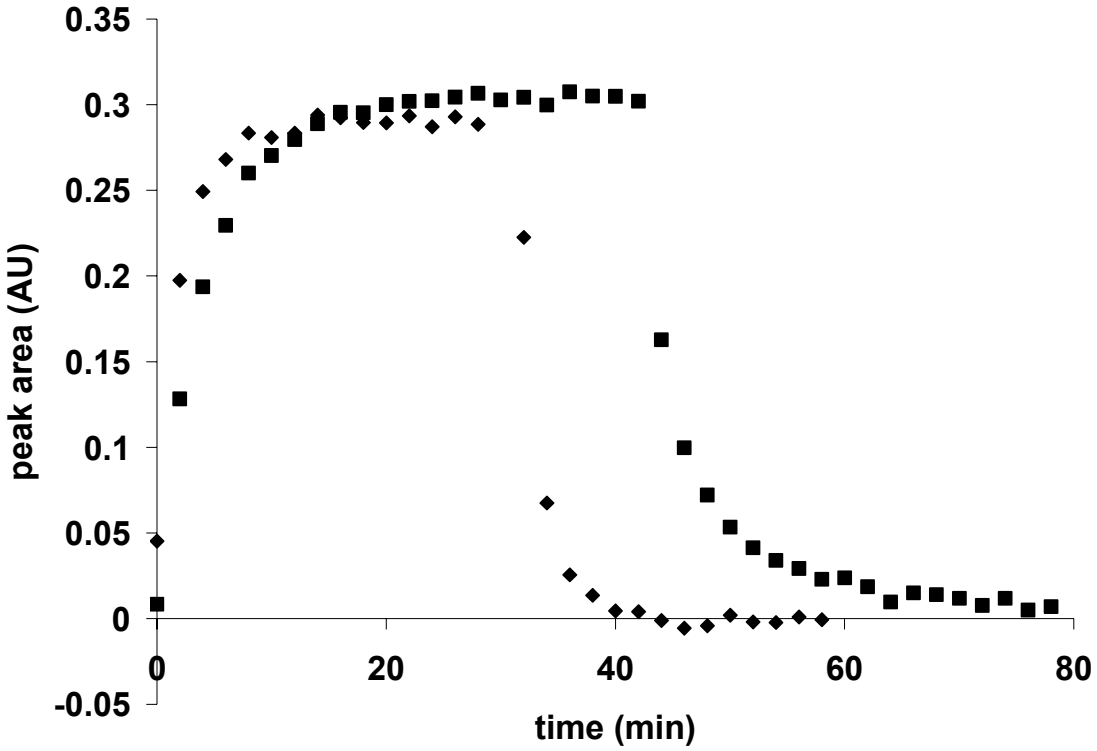

Figure 3.21 Enrichment and regeneration cycle for CB at 4 mL/min (squares) and 23 mL/min (diamonds).

According to these results, the time needed for performing one full enrichment / regeneration cycle for CB with concentrations in the mg/L range at a flow rate of

23 mL/min can be estimated at around 30 min. For lower flow-rate this time easily exceeds 60 min.

However, it can also be concluded that CB completely diffuses out of the polymer layer when regenerated with distilled water (no “memory effect”), potentially enabling numerous measurement cycles with a single sensor system.

3.3.2.4. Long Term Stability

An important figure of merit for the performance of a chemical sensor (system) is its ability to provide accurate readings over a long period of time and without the need for sensor re-calibration or other measures interrupting a continuous monitoring process. In the case of polymer coated ATR sensor systems based on infrared spectroscopy such events may include for example:

- a drifting baseline
- changes in the extraction performances of the polymer layer (biofouling, extensive swelling, etc.)
- degradation of the IRE (e.g. oxidation processes)

As already mentioned, a promising result was the fact that the performance of the sensor system for single measurement procedures was not significantly affected during a time period of several weeks, including the calibration measurements. Nevertheless, for detecting e.g. baseline drifts it is necessary to perform a single continuous measurement over a longer period of time (Figure 3.22).

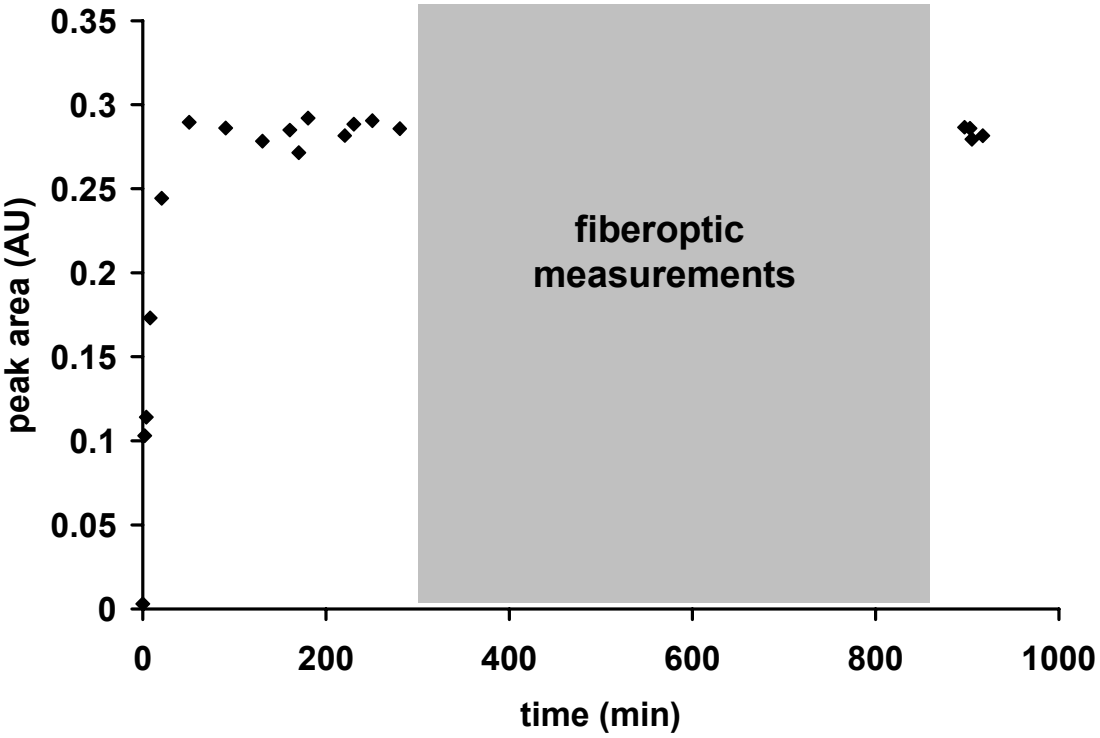

Figure 3.22 Long term stability test for CB measurements in groundwater. The flow rate was set to 4 mL/min. The lack of data in the time period from 400 to 900 min is due to occupancy of the spectrometer by fiberoptic measurements.

This measurement period covered 15 h revealing no significant deviation of the peak area of CB in groundwater once equilibrium was reached. The lack of data in the time period from 400 to 900 min is due to occupancy of the spectrometer by fiberoptic measurements. These data provide a first indication that the developed sensor systems have the potential for delivering reliable results also in case of a continuous monitoring scenario over extended periods of time.

3.3.2.5. Dynamic Sensor Behavior

In the following experiments a change of contamination level was introduced to the sample by adding CB to the groundwater. The resulting sensor behavior provides insight on the dynamic performance of the sensor system and the response to a concentration gradient in the groundwater aquifer, for instance in case of a chemical spill event. For these experiments the sensor system was continuously measuring groundwater and after equilibrium was reached a significant amount of CB was added to the sample (at t=14 min, total CB concentration increased to approx. 100 mg/L).

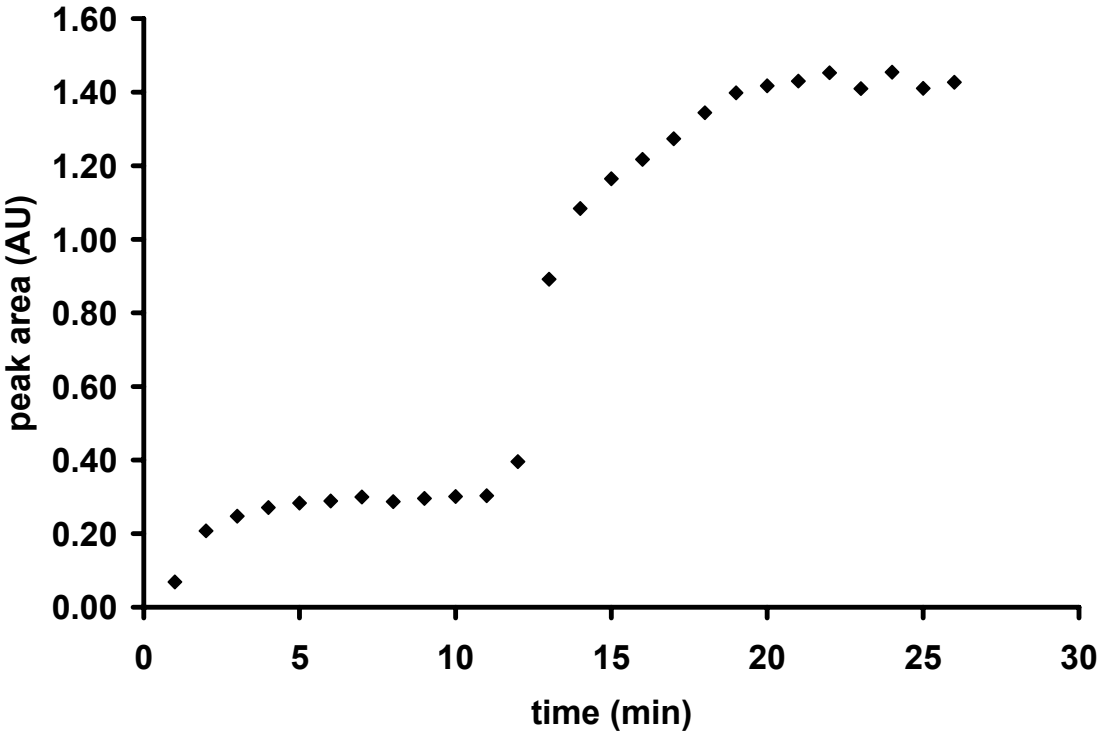

Figure 3.23 Simulation of a chemical spill event, by adding a significant amount of CB to the groundwater sample (at t=14min) after the sensor system was equilibrated with the groundwater sample.

In Figure 3.23 the response of the sensor to a substantial increase of pollutant can be observed as an immediate increase in peak area of the respective band of CB. Approx. 10 min after the spiking event the increase in peak area levels off again approaching equilibrium conditions. Analogous to all other experiments, the response time to a change of analyte concentration occurs in < 2 min, which is sufficient to serve as a chemical spill detector in groundwater streams.

3.3.3. Conclusions

The first measurement campaign deploying a polymer coated IR-ATR sensor system at field conditions has successfully been performed for the determination of chlorobenzene in the groundwater aquifer of a remediation site:

- Performance of the sensor was accurate and stable over a period of time of several weeks.
- Quantitative results were in excellent agreement with HS-GC validation measurements.
- The cocktail of pollutants present in the groundwater did not significantly affect the sensor performance, no cross-interference could be detected.
- Calibration of such sensor systems at laboratory conditions has proven to be valid; the performance was not affected by the pH level and turbidity of the real world sample.
- The effect of changing flow conditions on the equilibrium times has experimentally been confirmed, as suggested by CFD simulations.

- The enrichment of CB into the polymer membrane was completely reversible and there was no indication of an observable memory effect.
- The sensor performed for individual measurements and in continuous monitoring operation, and proved suitable during the simulation of a chemical spill event.
- The minimum measurement repetition time for a complete enrichment and sensor regeneration cycle for the available setup was determined to be approx. 30 min, however, could be improved with higher sample flow rates and the introduction of an optimized flow cell geometry.
- Dynamic sensor behavior has been shown to be < 2 min for increasing and decreasing pollutant concentration in the analyzed sample. A timescale sufficient for remediation processes.

3.4. Modeling the Diffusion Behavior of Chemical Sensors – How Accurate are Existing Models?

It has been confirmed during the studies of this thesis that sensor response times to changes in analyte concentrations usually occur at very short time scales (Figure 3.23). According to these measurements the response time of a detectable change in signal can be estimated to be less than 2 min, resulting in a significant increase of the absorption peaks after analyte introduction. This behavior has been observed for all analytes that have been studied throughout this thesis. For many monitoring applications this will be a satisfactory time resolution for detecting significant changes in the probed

sample. In addition, commonly applied FT-IR instrumentation allows to increase the measurement rate. If needed, time resolutions at the order of a few seconds can thereby be achieved.

In case of accurate quantification, the most common solution is to perform data evaluation as soon as diffusion equilibrium conditions are reached. Depending on the experimental circumstances, this time frame can range from a few minutes up to several hours. For many applications this time frames are not acceptable and considerable efforts are directed toward lowering sensor response evaluation times, usually by evaluating data prior to equilibrium conditions. A good overview on different approaches based strictly on gradient methods of diffusion curves for off-equilibrium data evaluation has been given by Buerck et al. [42]. In this work, it is shown that the gain in evaluation time usually comes along with a loss in sensitivity as a consequence of the evaluation of fewer data points.

Hence, an evaluation algorithm, which could “predict” diffusion curves based on first physical principles, should deliver more accurate results even working with a very limited number of data points. Some approaches have been presented with numerical algorithms exclusively based on Fickian diffusion of analytes in the polymer membrane. The most widely used algorithm nowadays has been introduced by Fieldson and Barbari [185], however, this algorithm – as will be discussed in chapter 3.4.2 - entirely neglects the critical influence of the flow conditions.

Recently performed CFD simulations (chapter 2.6.1) predict a significant influence of the flow conditions in the surrounding solution of the polymer membrane on the sensor response. These predictions could be verified with experimental data in the studies encompassed in this thesis (chapter 3.3.2.2).

In the following chapters the diffusion coefficient of CB in E/P-co will be calculated with two of the commonly applied models. It will be shown that the introduction of a varying

flow rate leads to contradicting results rendering these models insufficient for describing the real world measurement situation in dynamic (flow based) chemical sensor systems. Hence, published diffusion coefficients, which have been determined with such models via data derived from polymer coated IR-ATR sensor systems, are presumably incorrect and should be evaluated with caution. Furthermore, it will be shown that the predicted trends from CFD simulations can be observed in the experimental data, which leads to the conclusion that the consideration of flow conditions with models for diffusion based IR-ATR chemical sensors is inevitable.

3.4.1. First Case Study: A Simple Diffusion Model applied to Experimental Data

Based on a very simplified, but generally accepted method for the determination of the diffusion coefficient of a compound penetrating a polymer membrane, it will be demonstrated that incorrect results will be obtained if the flow conditions are neglected. For this test, a data set from the field measurements with the developed IR-ATR sensor system described in chapter 3.3 is utilized, as it has been obtained with constant experimental parameters, except for a variation of the flow rate.

The data set consists of 5 measurements of the same groundwater sample (refer to chapter 3.3 for a detailed description of the experiment), with a CB concentration of 27 mg/L. The enrichment process of CB into the E/P-co layer (thickness: 3.2 µm) was evaluated via peak integration of the aromatic C-H out of plane vibration (around 740 cm^{-1}). Three runs have been performed at a flow rate of 4 mL/min (Figure 3.24) and two runs at a flow rate of 23 mL/min (Figure 3.25).

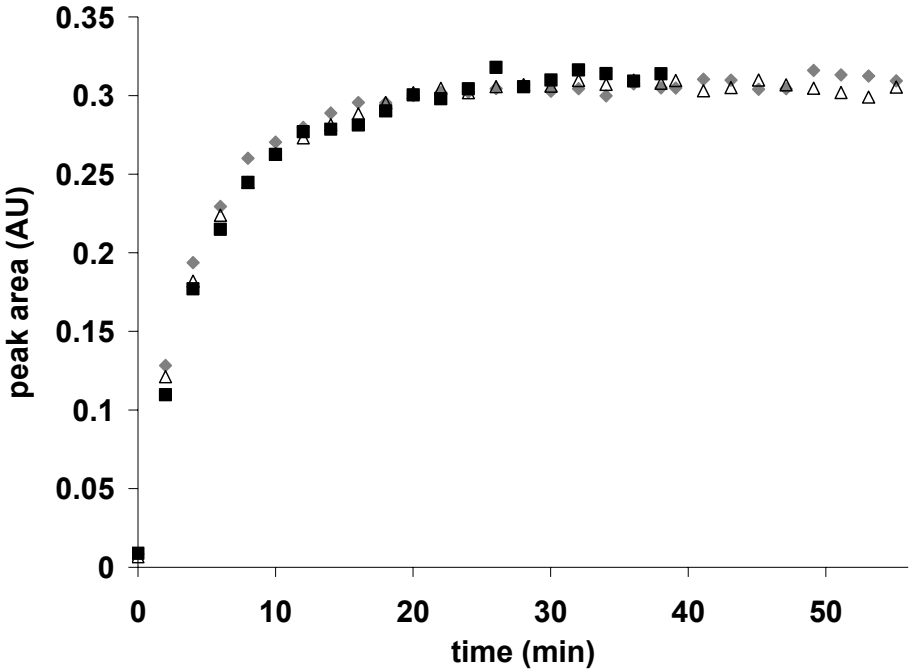

Figure 3.24 Enrichment curves of CB from groundwater at SAFIRA site into an E/P-co layer at a flow rate of 4 mL/min. The 3 measurements were performed at 3 different days.

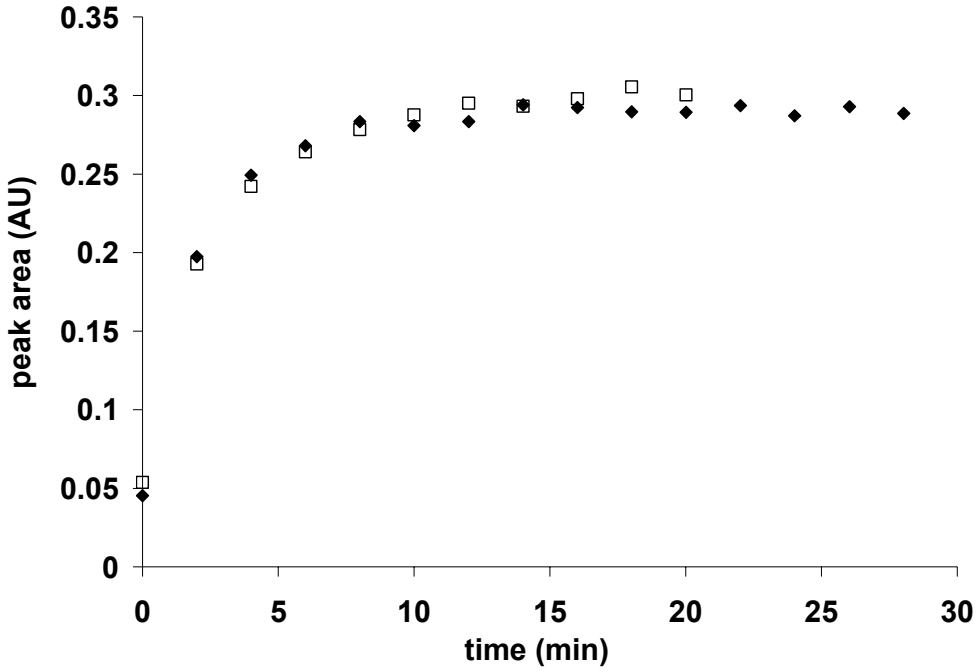

Figure 3.25 Enrichment curves of CB from groundwater at SAFIRA site into the E/P-co layer at a flow rate of 23 mL/min. The 2 measurements were performed at 2 different days.

The difference in flow rate clearly has an impact on the enrichment process. The measurements performed with 23 mL/min more rapidly reach equilibrium conditions. A calculation example will show that neglecting the impact of the flow conditions leads to misleading results, for instance if the diffusion coefficient is derived from such enrichment data. The only published value for a diffusion coefficient of CB in E/P-co was given by Goebel et al [180] as $5 \cdot 10^{-9}$ cm^2/s, derived with stopped-flow experiments using a box model algorithm, which will not be described in more detail in this thesis [180,181]. Generally, the one-dimensional molecular diffusion in a polymer film with a constant diffusion coefficient can be described by the second Fickian law [182].

$$\frac{\partial c}{\partial t} = D \frac{\partial^2 c}{\partial x^2} \qquad (3\text{-}2)$$

where *c* is the concentration of the penetrant, *D* is the diffusion coefficient and *x* the direction normal to the facet of the IRE element.

If a polymer film is placed into contact with a solution containing a diffusant, it has been shown that under certain boundary condition (no diffusion at the edges of the film) the mass transported at the time *t* can be expressed by [182,183]

$$\frac{M_t}{M_{max}} = 4\left(\sqrt{\frac{D}{\pi}}\right)\frac{\sqrt{t}}{d} \qquad (3\text{-}3)$$

where M_{max} is the mass uptake at saturation, M_t is the mass uptake at time *t*, *d* is the film thickness, and *D* the diffusion coefficient. It has been demonstrated that for $M_t/M_{max}<0.5$ the diffusion coefficient of the diffusing species can be derived according to [184]

$$D = \frac{\pi}{16} I_s^2 \qquad (3\text{-}4)$$

where I_s is the initial slope in a plot of M_t/M_{max} versus $t^{0.5}/d$. In a simplifying assumption, M_t and M_{max} can be regarded as absorption intensities Abs_t and Abs_{max} of characteristic peaks of the respective analyte. The resulting graph is shown in Figure 3.26.

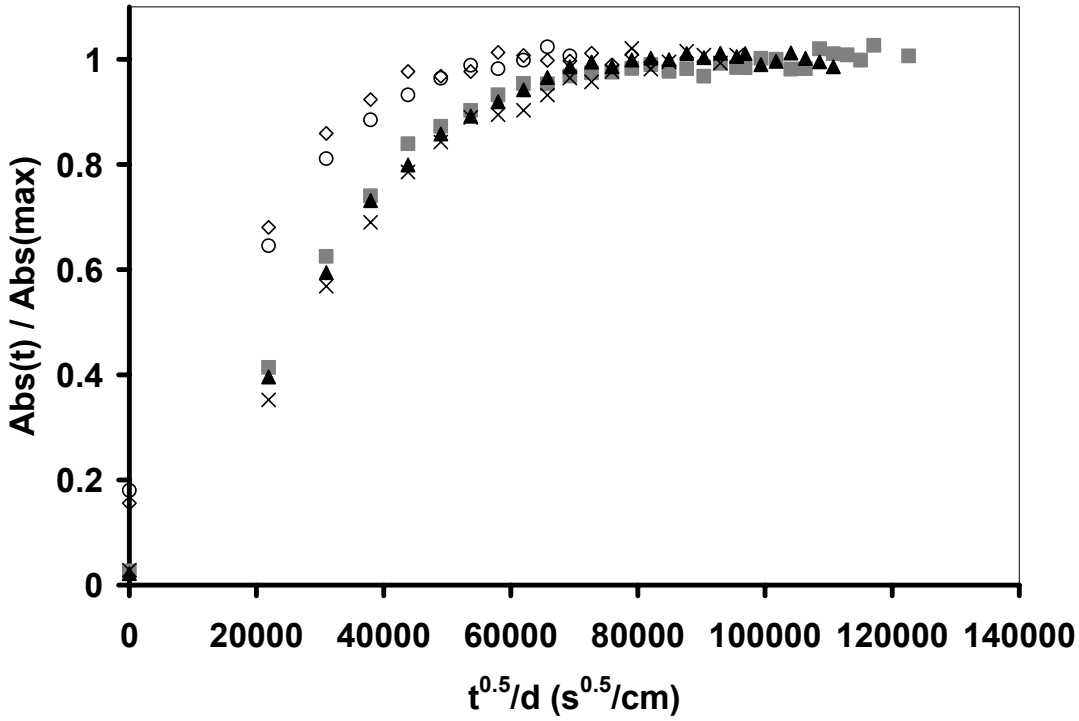

Figure 3.26 $Abs_{(t)} / Abs_{max}$ versus $t^{0.5} / d$ plot for the 5 CB enrichment experiments. The series marked with diamonds and circles refer to the high flow rate (23 mL/min) the other 3 series to the lower flow rate (4 mL/min).

Finally, the diffusion coefficients are derived by extracting the initial slopes of the 5 data series and applying equation 3-4. The results are listed in Table 3.5.

Table 3.5 Calculated diffusion coefficients (cm^2/s) for CB in E/P-co

	flow rate 4 mL/min			*flow rate 23 mL/min*	
initial slope	1.77E-05	1.73E-05	1.71E-05	2.04E-05	2.12E-05
diffusion coefficient (cm^2/s)	6.12E-11	5.86E-11	5.72E-11	8.21E-11	8.86E-11
average diffusion coefficient (cm^2/s)	**$5.90 \cdot 10^{-11} \pm 2.0 \cdot 10^{-12}$**			**$8.53 \cdot 10^{-11} \pm 4.6 \cdot 10^{-12}$**	

The discrepancy of the averaged diffusion coefficients for the two flow rates proves the necessity of considering the flow conditions within the model for the enrichment studies

and render quantitative calculations or modeling based on such deficient algorithms insufficient.

3.4.2. Second Case Study: A Numerical Simulation Model based on Fickian Diffusion applied to Experimental Data

A widely accepted numerical simulation algorithm based on Fickian diffusion has been introduced by Fieldson and Barbari [185] and will be described briefly in the following.

For one-dimensional molecular diffusion in direction x into a polymer film with a constant diffusion coefficient, the basic expression for transient Fickian diffusion is given by Fick's second law (equation 3-2 page 112):

$$\frac{\partial \mathbf{c}}{\partial \mathbf{t}} = \mathbf{D}\frac{\partial^2 \mathbf{c}}{\partial \mathbf{x}^2} \qquad (3\text{-}5)$$

where c is the concentration of the penetrant and D is the diffusion coefficient. The diffusion coefficient defines the flux for a given concentration gradient enabling quantization of the diffusion process for the investigated system conditions. Using initial conditions and boundary conditions for the case of constant surface concentration with no transport of penetrant through the lower polymer interface (i.e. x=0), Fieldson and Barbari [185] combined and integrated the concentration profile with the infrared evanescent field intensity to obtain an analytical solution for the case of a single diffusant, i.e. one-dimensional Fickian diffusion. The derived expression is as follows:

$$\frac{A(t)}{A_\infty} = 1 - \frac{8}{\pi d_p \left(1 - e^{-\frac{2L}{d_p}}\right)} \sum_{n=0}^{n=\infty} \frac{e^g \left[f e^{-\frac{2L}{d_p}} + (-1)^n \left(\frac{2}{d_p}\right) \right]}{(2n+1)\left(\frac{4}{d_p^2} + f^2\right)} \qquad (3\text{-}6)$$

where:

$$f = \frac{(2n-1)\pi}{2L} \qquad (3\text{-}7)$$

$$g = \frac{-D(2n+1)^2 \pi^2 t}{4L^2} \qquad (3\text{-}8)$$

L is the thickness of the polymer membrane, $A(t)$ the absorbance of the measured band at any time (t), A_∞ the absorbance at equilibrium, and d_p the depth of penetration of the evanescent field given by equation 2-3 (page 38). As all other parameters are known, the diffusion coefficient (D) of the penetrant in the polymer may be calculated by regressing experimental absorbance data with equation 3-6. Several groups have and are still applying this algorithm to directly calculate diffusion coefficients from enrichment data obtained with polymer coated evanescent wave sensing systems [186-190] extracting small organic molecules from aqueous solution. Based on the findings described in the previous chapter it is questionable that this algorithm is comprehensive enough to deliver “absolute values” for the diffusion coefficients, as again the effect of the flow conditions is neglected. To support this statement the algorithm was again applied to the experimental data obtained during the measurement campaign in

Bitterfeld, where data at two different flow velocities have been recorded, while other parameters remained constant (Figure 3.24 & Figure 3.25).

The numerical iteration was performed with a visual basic script (see appendix), which was incorporated into an already existing graphical interface for data evaluation developed by our research group. All experimental parameters such as penetration depth, polymer membrane thickness, and measurement time have been included following the actually performed experiments in Bitterfeld (Table 3.6).

Table 3.6 Parameters from the Bitterfeld experiments included in the Friedson and Barbari algorithm.

parameter	**symbol**	**value**
refractive index of crystal	n_1	2.41
refractive index of E/P-co	n_2	1.48
evaluated wavelength	λ (cm)	1.35E-03
angle of incidence	θ	45
polymer layer thickness	L (cm)	3.2E-04
time for iteration algorithm	t (s)	3000
number of iterations	n	100

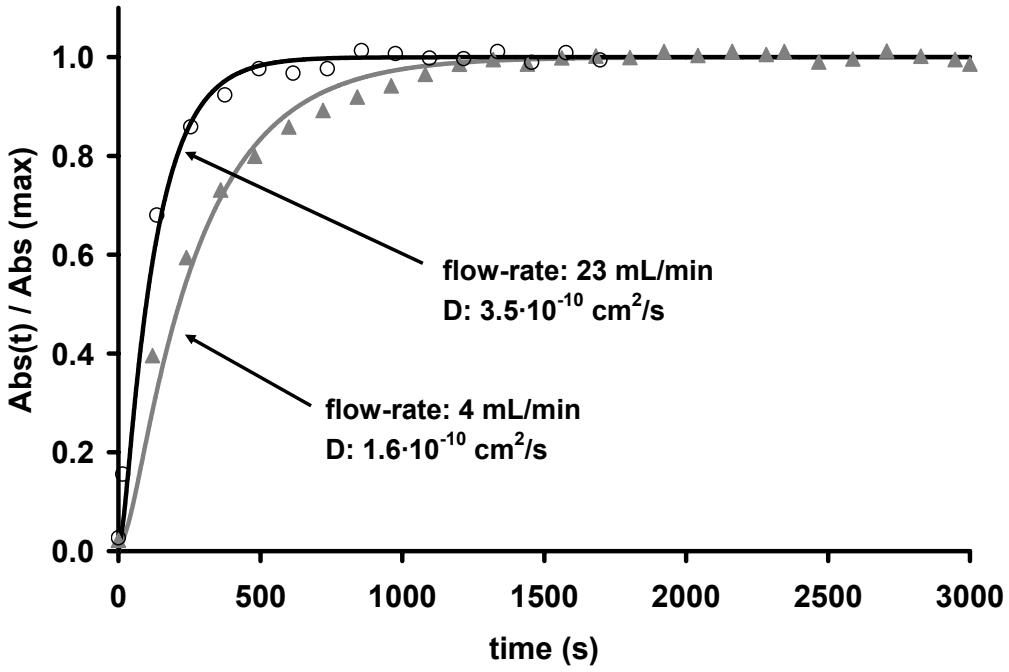

Figure 3.27 Exemplary results from the iterations for one data series obtained with low flow rate (4mL / min, Run3) and one with high flow rate (23 mL/min, Run4). The calculated diffusion coefficients are printed in the graph.

A diffusion curve is simulated utilizing the parameters listed in Table 3.6 and adapted by varying the diffusion coefficient until best fit with the experimental data is achieved.

Exemplary results from the iterations are shown in Figure 3.27 for one data series obtained with low flow rate (4mL / min, Run3) and one with high flow rate (23 mL/min, Run4). The diffusion coefficients derived from that algorithm for all 5 measurement series together with the values obtained with the “initial slope” method (chapter 3.4.1) are listed in Table 2.1.

Table 3.7 Calculated diffusion coefficients for the Bitterfeld field measurements via two different methods

	flow rate 4 mL/min			*flow rate 23 mL/min*	
Fieldson and Barbari	Run1	Run2	Run3	Run4	Run5
diffusion coefficient (cm^2/s)	1.55E-10	1.40E-10	1.60E-10	3.50E-10	3.00E-10
average diffusion coefficient (cm^2/s)	**$1.52 \cdot 10^{-10} \pm 1.0 \cdot 10^{-11}$**			**$3.25 \cdot 10^{-10} \pm 3.5 \cdot 10^{-11}$**	
Initial Slope					
slope	1.77E-05	1.73E-05	1.71E-05	2.04E-05	2.12E-05
diffusion coefficient (cm^2/s)	6.12E-11	5.86E-11	5.72E-11	8.21E-11	8.86E-11
average diffusion coefficient (cm^2/s)	**$5.90 \cdot 10^{-11} \pm 2.0 \cdot 10^{-12}$**			**$8.53 \cdot 10^{-11} \pm 4.6 \cdot 10^{-12}$**	

The results show very clearly the susceptibility of these two methods to variations of the flow conditions, as both algorithms show a significant difference in the value of the calculated diffusion coefficient of up to a factor of 2 when the flow rate is changed from 4 to 23 mL/min. Furthermore, results derived from the Fieldson and Barbari algorithm do not correlate with the "initial slope" method by at least a factor of 3. Goebel et al [180] determined *D* for the diffusion of CB in E/P-co in similar experiments but with a chromatographic box model to be $5 \cdot 10^{-9}$ cm^2/s. This is the only reference value found in literature determined with a similar method, however, its correctness is also questionable as the applied model is again not taking varying flow conditions into account.

However, algorithms such as the Fieldson and Barbari model could still be used for predictive determination of parameters such as the t_{95} value, if experimental parameters are kept constant. However, it is evident that accurate determination of the diffusion coefficient by polymer coated IR-ATR spectroscopic experiments is only possible by extensive CFD simulations.

3.4.3. Third Case Study: CFD Simulations (FLUENT) applied to Experimental Data

In this chapter findings based on the newly developed CFD model are applied to data obtained during the field measurements with the IR-ATR sensor system described in chapter 3.3.

Unfortunately, the software package was not available for simulations during this thesis. However, some interesting consequences can be derived from the initial simulations based on the model flow cell (Figure 2.13) performed by Phillips et al [43 191] in collaboration with our research group.

In this section it will be shown that the results obtained with the measurement setup during the Bitterfeld campaign are in agreement with the results modeled via CFD simulations.

Due to the different parameters used for the CFD simulations and the actual experimental parameters (see Table 3.8) all conclusions at this stage are only qualitative. Nevertheless, they clearly indicate that the predicted trends from the model are experimentally observable.

Table 3.8 Comparison of the parameters of the basic flow cell used in CFD simulations (Figure 2.13 and [43]) and the flow cell used during the Bitterfeld measurements.

	baseline flow-cell parameters	**experimental flow-cell parameters**
flow-channel length	2 cm	7 cm
flow-channel height	1mm	3 mm
polymer layer thickness	5 µm	3.2 µm
flow-speed - slow	0.15 cm/s	0.25 cm/s
flow-speed - fast	1.5 cm/s	1.4 cm/s

CFD simulations using FLUENT have been performed investigating the effect of the flow velocity on the time the sensor system needs to reach diffusion equilibrium conditions (time to steady state). All parameters except the channel height of the experimental flow cell were comparable to the basic flow cell geometry and the results for velocities of 0.15 cm/s and 1.5 cm/s are shown in Figure 3.28.

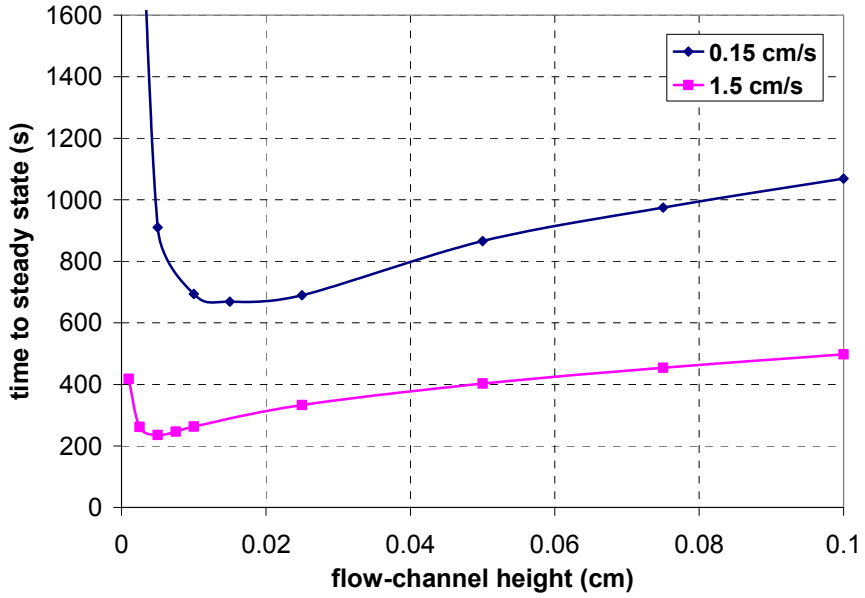

Figure 3.28 Time to steady state (equilibrium) vs. flow channel height for 2 different flow velocities modeled with CFD for the basic flow cell shown in Figure 2.13.

Figure 3.28 shows that the enrichment time is increasing with decreasing velocity. Hence, it takes much longer to saturate the polymer with analyte. The reverse is true for an increase in velocity. The change in optimal height is also due to the thickness of the concentration boundary layer that changes with the flow velocity. The relationship between the channel height and the concentration boundary layer thickness controls the maximum resistance in the flow cell. As the flow velocity increases, the thickness of the concentration boundary layer at the exit of the channel decreases. Thus, the optimal (critical) height at which the advection resistance becomes equivalent to the diffusion

resistance also decreases. Furthermore, if the channel height decreases to very small values, it can be expected that practically every analyte molecule will be partitioning into the polymer layer promoting the trend to longer equilibrium times.

However, the experimental flow cell used in the Bitterfeld campaign had a flow channel height of approx. 3 mm (in contrast to < 0.1 mm of the simulated flow cell), therefore, exceeding the range of the simulation. It can be extrapolated though that the trend of increasing equilibrium times will be continued when further increasing the channel height. This should hold true for both flow velocities, clearly indicating that in general there is a difference in equilibrium times for different flow rates. Evidently, the CFD simulations has have been performed with comparable flow velocities to the experimental data. In the simulation, a change of flow velocity by a factor of 10 changes the equilibration time approx. by a factor of 2, which is of the same order of magnitude as observed in the experimental data at two different flow velocities (see chapter 3.2.4).

In summary, CFD simulations seem to reflect real world measurement situations much more accurately than the currently applied and generally accepted models, which have been discussed and compared in this thesis. Consequently, it should be of substantial interest to implement CFD simulations as a routine tool for simulating the behavior of polymer coated IR-ATR sensors along with advanced flow cell design.

4. Conclusions and Outlook

With steadily increasing use of synthetic and natural organic compounds in industry and agriculture their impact as pollutants in air, water and soil ecosystems is generating an increasing threat to the environment. Amongst other pollutants volatile organic compounds (VOCs) represent a major threat to ground water and surface water, due to

their high abundance in industrial processes. It is a known fact that the significance of such compounds as environmental pollutants benzene, chloroform and trichloroethylene occupy a permanent place among the 20 most relevant priority pollutants in the listings all over the globe.

Contemporary analysis of VOCs in groundwater mostly relies on headspace gas chromatography (HS-GC). HS-GC is a classical off-line technique requiring substantial preparation steps prior to analysis: (i) sampling, (ii) sample transportation and storage, and (iii) depending on analyte concentration and matrix composition sample clean-up and preconcentration procedures. An increased number of processing steps before the actual analysis promotes introduction of errors and is above all time consuming. Consequently, novel analytical technologies should readily assist pollution screening and site-assessment procedures demanding for low cost, rapid and reliable sensor systems capable of quantitative online in situ measurements with high molecular selectivity under field conditions. Mid-IR based spectroscopic techniques represent a feasible and valuable approach for establishing in situ sensing systems with high inherent molecular specificity. In this thesis, the capability of polymer coated ATR-FTIR sensor systems for on site, sensing / monitoring applications in the field could be proved. Based on preliminary experiments the extractive polymer membrane consisted out of a several µm thick layer of E/P-co coated onto either a ZnSe ATR crystal or onto a silver halide fiber. First simultaneous, quantitative determination of environmentally relevant mixtures of BTX in water at trace level concentrations under laboratory conditions showed the suitability of the proposed sensor system for demanding analytical tasks. For the first time LODs for a multi-component measurements, measured with diffusion based evanescent wave sensor systems were determined to be in the low µg/L region for all members of the BTX group. An important part of this improvement in sensitivity can be related to the introduction of the *Mixmaster* an automated mixing system, specially

designed for handling diluted solutions of VOCs. This system can be applied for extensive sensor calibration, hence improving reliability and reproducibility of tedious calibration tasks, by eliminating manual sample preparation as an error source.

Two major measurement campaigns could be fulfilled in the scope of this thesis. The first one at artificial aquifer system, enabling the continuous simultaneous monitoring of three relevant pollutants TriCE, TeCE and DCB could be accomplished. A 6 m long AgX fiber, partially coated with E/P-co acting as both transducer and fiber-optic sensor head enabled the direct determination of the three compounds in a borehole of the aquifer system. Very good agreement with simultaneously performed HS-GC validation measurements showed the enormous potential of this method. However, a steadily increasing degradation process of the physically and chemically vulnerable AgX fiber could be observed throughout the measurement duration of three days. An eminent lack of highly transmitting and chemically inert fiber materials in the MIR is still a common problem, which hopefully will be resolved in the future. It might also be considered to improve AgX stability via ultra protective coatings, similar to the approach as has been shown for ATR crystals recently [192].

The second measurement campaign in the Bitterfelder groundwater at the SAFIRA remediation site showed that evanescent wave spectroscopic setups based on ZnSe ATR crystals show a much better stability, showing no signs of degradation for a period of several weeks. The sensor system, consisting of an E/P-co coated ZnSe crystal mounted into a flow-cell, was able to measure CB in highly contaminated groundwater samples in high agreement with HS-GC validation measurements. Apart from the accuracy of the system other parameters such as long term stability, dynamic sensor behavior and reversibility of the enrichment process have been successfully tested throughout these measurements, the being first ones conducted under field conditions for a polymer coated ATR-FTIR sensor system. Furthermore, it could be experimentally

shown that flow-conditions in the solution in contact with the extractive membrane have a high impact on the signal generation kinetics for the described sensor system, or diffusion based evanescent wave sensor system in general. This has been overseen by the scientific community for years and was predicted by extensive CFD simulations recently. With the calculation of the diffusion coefficient of CB in E/P-co with using different models, it could be demonstrated, that methods like the numerical algorithm introduced by Fieldson and Barbari, which are solely based on Fickian diffusion of the analyte in the polymer layer lead to incorrect results. The CFD simulations seem to reflect real world situations much better than the other models, which have been discussed. Therefore it should be of a high interest to implement such simulations as a regular tool for polymer coated ATR sensor development and evaluation, especially as the preliminary results have shown such tools maybe very helpful in flow-cell design in the future.

PART II

From the Field to the Lab - Investigating IR Signatures for Remote Sensing Applications

A Thesis

Presented to

The Academic Faculty

by

Manfred Karlowatz

In Partial Fulfillment

of the Requirements for the Degree

Doctor of Philosophy in Chemistry

Georgia Institute of Technology

May 2004

5. From the Field to the Lab – Investigating IR Signatures for Remote Sensing Applications

6. Introduction

6.1. Landmines – A Global Problem

More than 26,000 people are killed or maimed by mines every year, which is equivalent to one victim every 20 min. For example, in Cambodia one out of every 236 people is a landmine amputee. The casualty ratio rises to one out of every 140 people in Angola, which has more mines than people. In addition to fatal casualties and enormous financial losses, mines ruin large areas of fertile farmland and waterways. In Cambodia, approximately 40% of the rice fields have been mined and abandoned [193]. Most tragically, many victims are children and most mine-afflicted countries are among the poorest countries. Worldwide landmine distribution and its clearance status are summarized in Table 6.1.

Table 6.1 Worldwide landmine distribution and clearance status

Countries	Mines (10^6) UN[a]	USSD[b]	Cleared mines	Mined area (km^2)	Cleare area (km^2)	Casualties[c]
Afghanistan	10	7	158000	550~780	202	300~360/month
Angola	15	15	10000	Unknown	2.4	120~200/month
Bosnia	3	1	49010	300	84	50□month
Cambodia	6	6	83000	3000	73.3	38786 or 100/month
Croatia	3	0.4	8000	11910	30	677
Egypt	23	22.5	11000000	3910	924	8301
Eritrea	1	1	Unknown	Unknown	2.48	2000
Iran	16	16	200000	40000	0	6000
Iraq	20	10	37000	Unknown	1.25	6715
Laos	NA	NA	251	43098	Unknown	10649
Mozambique	3	1	58000	Unknown	28	1759
Somalia	1	1	32511	Unknown	127	4500
Sudan	1	1	Unknown	800000	0	700000
Vietnam	3.5	3.5	58747	Unknown	65	180□month

[a]UN Landmine Database 1997 [193]

[b]US State Department Report ‘‘Hidden Killer 1998. The Global Landmine Crisis’’ [194].

[c]Casualty reporting varies drastically among countries; estimates provided by UN or the host government [195]

Because of the potentially catastrophic results of unintentional mine encounters, the process of detecting and removing mines (“demining”) is particularly important. Manual demining is extremely dangerous; one deminer has been killed for every 2,000 mines removed, with even more civilian victims. The cost to purchase and position a typical antipersonnel mine ranges from $3 to $30, while the cost to remove a single mine ranges from $300 to $1000. The European Commission and the United States have invested 138 million dollars for demining activities during last two years [193]. However, these cleared mines are just the tip of the iceberg. In 1994, approximately 200,000 mines were removed, while two million new mines were planted. Many experts believe that it would take more than ten centuries to remove every mine in the world with the

current clearance rate, even if no additional mines were planted. Because mines can be made of both metallic and nonmetallic materials, detection using only conventional metal detectors is not sufficient. Reports also indicate that metal detectors are subject to many false alarms in former battlefields due to the presence of small fragments of munitions. Although manual detection ("probing"), works well for a wide variety of mines, high labor cost and the slow pace involved are encouraging development of alternative techniques. Although some military demining equipment has been developed and used during the Gulf War by the US Army, civilian related demining ("humanitarian demining") is quite different from the military work. The object of humanitarian demining is to find and remove abandoned landmines without any hazard to the environment. The UN requires a probability of 99.96% mine detection accuracy to find a 4 cm radius object at a 10 cm depth, and a localization ability of up to a 0.5m radius [193]. To meet the strict requirements for humanitarian demining, various techniques in the area of sensor physics, signal processing, and robotics have been studied during the last decade. Most mine detection techniques consist of sensor, signal processing, and decision processes. For the sensor part, ground penetration radar (GPR), infrared (IR), and ultrasound (US) sensors are among the most commonly applied techniques nowadays [195] and will be briefly described in the next section.

6.2. Commonly Applied Landmine Detection Methods

6.2.1. Ground Penetration Radar

GPR consists of an active sensor, which emits electromagnetic (EM) waves through a wideband antenna and collects signals reflected from its surroundings. The principle of

GPR is almost the same as in a seismic wave measurement system except for the carrier signal. The commonly used frequency band of the GPR, EM wave is between 100 MHz and 100 GHz [196]. This band is wide enough to carry the necessary information. Reflection occurs when the emitted signal encounters a surface between two electrically different materials. The direction and intensity of the reflection depend on the roughness of the surface and electrical properties of the medium material [196]. A rough surface reflects the incident wave in a diffused manner, while a smooth surface tends to reflect the wave in one direction, where the angle between the surface normal and the reflected wave is the same to the angle between the surface normal and the incident wave. The electrical properties of the medium determine the amount of refraction and absorption of the EM waves and subsequently affect the direction and intensity of the reflection. The penetration depth of the wave into soil usually depends on two factors, the humidity in the soil and the wavelength of the EM wave [7]. The content of water in the soil significantly reduces the depth of penetration of a wave with relatively shorter wavelength. Based on the reflection and penetration properties, GPR works best with low-frequency EM waves in dry sand. Low-frequency signals, however, tend to make low-resolution maps of data, which decreases the accuracy of mine detection. Since the EM waves cannot penetrate water, GPR cannot detect underwater mines, which are common in many countries [194].

6.2.2. Ultrasound

The audio frequency range is between 20 and 20,000 Hz. Ultrasonic waves have the frequency band above this audible range. The principle of ultrasonic sensing systems is

very similar to GPR except that ultrasound uses much lower frequency waves than the GPR system.

The ultrasonic system emits ultrasound signals and collects reflected signals from the surroundings. Note that a sound wave propagates as a mechanical disturbance of molecules in the form of waves [197], while a radar signal makes no physical disturbance in the medium. When a sound wave propagates through a medium, the wave consists of the molecules of the medium oscillating around their equilibrium position.

The speed of sound is dependent on the physical properties, density, and elasticity of the medium. The speed of sound propagation, denoted by c, is given as

$$\mathbf{c} = \mathbf{f} \cdot \lambda \qquad (6\text{-}1)$$

where f represents the wavelength of the wave, and f the frequency. Sometimes c is a material constant. In a uniform homogeneous medium, the ultrasound wave propagates along a straight line and is reflected and refracted when the wave encounters a boundary between two different media. At the boundary, the speed of the wave and the density of the medium affect the behavior of propagation. In mine detection, the frequency of the ultrasound wave decides the penetration depth as is also true for GPR. The lower frequency wave tends to penetrate further than the high frequency wave [195].

Table 6.2 Speed of sound in different media [195]

material	steel	lead	water	soft tissue	bones
speed of sound (m/s)	5000	1300	1460	1500	2500–4900

The ultrasound wave propagates well in humid or underwater conditions, but it is significantly attenuated in air, while the EM wave of GPR behaves oppositely at the same conditions. Table 6.2 summarizes the speed of sound propagation in different materials.

6.2.3. Infrared Sensor

Since visualization is easier than with other sensors, the IR spectral range has widely been applied for mine detection. However, the performance of IR is highly dependent on the environment at the moment of measurement. There are two different methods for sensing IR waves. Passive IR systems sense only natural radiation from the object, while active IR systems need an extra heat source and receive radiation created by that heat source after interaction with the sample surface [198].

Dynamic Thermography

The general concept of using IR thermography for mine detection is based on the fact that mines may have different thermal properties from the surrounding material. If the response is due to an energy flux that varies with time, the objects will follow a temperature curve that will not coincide with the soil. When this contrast occurs by alteration of the heat flow due to the presence of the buried mine, it is called the v*olume effect* [195]. On the other hand, when the contrast results from the disturbed soil layer created by the burying operation, this is called the *surface effect* [195]. The surface effect is detectable only for a limited time after mine burial. During this detectable period the thermal contrast is quite distinctive. Once a sequence of images has been acquired,

various processing techniques can be applied to enhance the contrast between the potential targets and background, which is called *dynamic thermography* [199].

However, at present, the application of thermography in landmine detection mainly focuses on soil surfaces [200] and thin subsurface soil layer detection, e.g. detection of objects with depths less than 5 mm [201] or equal to 8 mm [202], which is still far from satisfying considering UN imposed requirements for buried landmine removal of at least 130 mm of depth penetration [203]. There are two main groups of factors limiting depth sensitivity of thermography: (i) variations and non-homogeneities of mine-neighboring soil [200], and (ii) the diffusive character of the thermal response of buried objects, which is intrinsically linked to heat conduction in the examined region of soil [201].

The influence of these effects is generally seen in randomly distributed changes of projections of buried object boundaries and in the suppression of thermal contrast caused by local difference in thermal characteristics, respectively. These limitations have been known for some time and have caused the focus on research and development for detection of surface laid mines and shallowly buried (flush buried) mines. Hence, detecting deeply buried landmines is a subject rarely investigated [204], which results in the absence of rather important data on buried conditions in realistic mine affected regions.

6.3. Current Developments in Remote Landmine Detection – The Disturbed Soil Approach

In order to overcome some of the eminent problems of remotely detecting buried landmines, considerable efforts were focused on detecting the changed adjacent soil conditions (“disturbed soil”) rather than detecting the buried object itself. The advantage

of that approach is obvious: in order to put a landmine into place, the soil around has to be moved (disturbed), including the soil at the surface. If the disturbed soil exhibits different spectroscopic characteristics than undisturbed (pristine) soil, the location where the mine was buried is spectroscopically "labeled". Hence, these spectroscopic changes would also be observable at the soil surface with the conditions at the surface being responsible for the majority of the emitted and/or reflected spectrum of the soil.

In 1998 Johnson et al. showed that there are significant spectral contrast differences of spectra of pristine and disturbed soils predominantly in the LWIR[†] region of the electromagnetic spectrum [5]. Hence it was proposed that hyperstrectral imaging in the atmospheric window of approx. 8-12 µm is a potentially useful method for determining possible mine spots in future. Hyperspectral imagers operating in this wavelength region have already been presented, with the most prominent example being the Airborne Hyperspectral Imager (AHI) system [2].

The problem of "disturbed soil" and its applicability for reliable detection of buried objects has drawn substantial interest in the remote sensing community. Derived from the few published works on the investigations of the disturbed soil phenomena the following findings can be summarized:

- The difference in spectral contrast is strongest immediately after the disturbing event [1].
- The strength of these effect decays over time, most likely due to weathering processes (wind, rain, erosion, etc.) [1].
- The difference in spectral contrast may be related to a difference in particle size distribution at the surface between disturbed and pristine soil [1,5].

[†] In the remote sensing community the expression LWIR (long wave infrared radiation) is the commonly used equivalent expression for the MIR (mid-IR) region used by spectroscopists.

However, for exploitation of this phenomenon in field applications there are still too many uncertainties that have not yet been investigated. Prior to elucidating the necessary experiments in order to understand the spectroscopic features of disturbed and pristine soils, brief insight into remote sensing techniques is given.

6.3.1. Remote Sensing

Remote sensing is the science of acquiring information about the Earth's surface without actually being in physical contact by sensing and recording reflected or emitted energy and processing, analyzing, and applying that information.

In remote sensing applications, this process involves interaction between incident radiation and the targets of interest. This is exemplified by the use of remote sensor systems involving the following main elements (Figure 6.1):

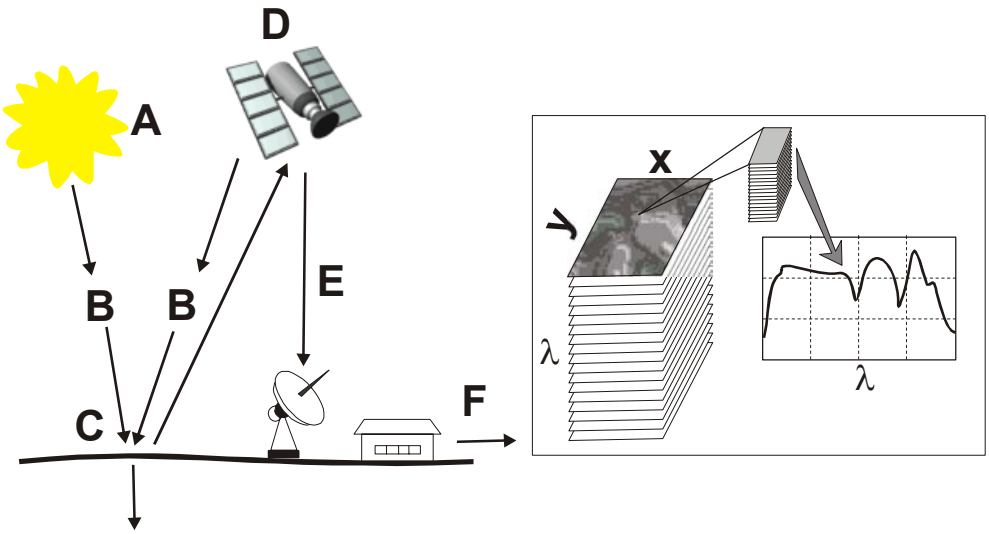

Figure 6.1 Principle of Remote Sensing Techniques

1. **Energy Source or Illumination (A)** - the first requirement for remote sensing is an energy source, which illuminates or provides electromagnetic energy to the target of interest.
2. **Radiation and the Atmosphere (B)** - as energy travels from its source to the target, it will interact with the atmosphere it passes through. This interaction may occur twice as the energy travels from the target to the sensor.
3. **Interaction with the Target (C)** - once energy makes its way to the target through the atmosphere, it interacts with the target depending on the properties of both the target and the radiation.
4. **Recording of Energy by the Sensor (D)** - after energy has been scattered by, or emitted from the target, a sensor is required (remote - not in contact with the target) to efficiently collect and record the electromagnetic radiation.
5. **Transmission, Reception, and Processing (E)** – the signal generated by energy recorded at the sensor has to be transmitted to a receiving and processing station, where the data are processed into an image (hardcopy and/or digital).
6. **Interpretation and Analysis (F)** - the processed image is visually and/or digitally/electronically interpreted to extract information about the target, which was illuminated.

6.3.2. Hyperspectral Imaging

During the last 15 years a new sensor type called imaging spectrometers has been developed [2,205,206,207]. Recently, the term hyperspectral imaging has been established for these systems, which can be considered synonymous with imaging spectrometry. Imaging spectrometry is defined as the acquisition of images in many

(hundreds or more) of contiguous, registered, spectral bands, such that each pixel has a complete attached radiance spectrum. From the radiance spectrum, an apparent reflectance spectrum can be derived by modeling and removing the absorption and scattering effects of the atmosphere. The term “apparent reflectance” is used because the surface irradiance is a function of topographic slope and aspect and cannot be directly derived from the radiance data itself. While the absolute reflectance is unknown, the relative reflectance among spectral channels is correctly derived. The shape of the spectral reflectance curves ultimately contains information on the chemical composition. Image-derived reflectances can be analyzed in the same fashion as laboratory-produced reflectance spectra. Hence, the entire range of chemometric analysis techniques is applicable to data derived from hyperspectral images. However, the process of calibration is much more cumbersome since no pixel is compositionally pure and sampling a typical pixel (nominal size: 20 x 20 m) of a surface for analysis by a primary method is easily subject to error. New techniques such as pixel unmixing using the statistics of the image data themselves are proving valuable to quantitatively derive the composition and relative abundance of individual components making up a pixel [208]. The reflectance data contain information on surface material composition, provided that sufficient spectral resolution is available. Weathered surfaces containing OH-bearing minerals such as clays, have diagnostic overtone combination absorptions that fall within the atmospheric windows in the 1–20 μm region. Hence, minerals have diagnostic spectral features that can be mapped using imaging spectrometry. Because of their molecular structure, solids and liquids do not allow rotational degrees of freedom, and no hyperfine features are observed in the reflectance spectrum. Therefore, sampling the spectrum at 10 nm intervals is sufficient to resolve the most prevalent diagnostic absorption bands found in materials covering the Earth’s surface.

Sensor Technology

In general, there are two engineering implementations of imaging spectrometers: the *whiskbroom* is an opto-mechanical system, the *pushbroom* a solid-state system. The opto-mechanical systems utilizes an oscillating or spinning mirror prior to the foreoptics to scan across the flight direction building up an image as the platform moves downtrack. The entrance slit to the spectrometer is placed in the focal plane of the telescope using line-array detectors. The Airborne Visible/Infrared Imaging Spectrometer (AVIRIS), flown aboard the NASA ER-2 at 20 km altitude, is the best-known opto-mechanical hyperspectral imaging system [209].

In the case of the *pushbroom* technique a linear array of detectors located at the focal plane of the image formed by lens systems which are "pushed" along in the flight track direction are applied. Each individual detector measures the energy for a single ground resolution cell and thus the size of the detectors determines the spatial resolution of the system. A separate linear array is required to measure each spectral band or channel. For each scan line, the energy detected by each detector of each linear array is sampled electronically and digitally recorded.

A complete introduction to the complex field of remote sensing and hyperspectral imaging can be either found in published books [210-212] or via permanently available and frequently updated web tutorials [213, 214].

6.4. Scope of this Thesis

Landmine detection via remote sensing techniques is a challenging analytical and spectroscopic task. For example, measurements of disturbed soils have shown different spectral contrast in comparison to undisturbed soils [1-5]. However, these findings are predominantly based on experimental data obtained in real world environments using

hyperspectral imaging systems, where many environmental parameters of influence can easily obscure the results. Evidently, measurements at such uncontrollable conditions do not represent the desired general conditions for principal studies.

Hence, it is of great interest to fundamentally investigate the disturbed and undisturbed soil phenomena in a controlled environment. Based on these measurements, reliable theoretical models could be established leading to improved interpretation of these features during landmine detection scenarios.

In a first step, measurements at controlled laboratory conditions have been performed to investigate individual minerals of the soil matrix and their spectral characteristics at a variety of environmental conditions. Attenuated total reflection (ATR) spectroscopy has been identified as a suitable spectroscopic technique superior to emissivity or reflectance measurements, mainly due to its reproducibility and versatility, while contributing useful data toward fundamental understanding of spectral signatures relevant to remote sensing. Due to the high abundance in natural soils, pure quartz sand (SiO_2) has been selected as the first test matrix.

For the investigation of spectral differences between pristine and disturbed quartz sand, a wetting/drying procedure with subsequent sample aerating has been developed, which in a first approximation represents a sufficient simulation of weathering processes and their impact on related soil disturbances.

In order to support the hypothesis that spectral differences of pristine and disturbed soils mainly result differences in particle size distributions of the probed surface, soda lime glass spheres of different diameters have been investigated in a next step.

It is assumed that the findings and the deductions drawn from these first measurements significantly improve the understanding of the spectroscopy of pristine and disturbed soil samples and are a starting point for extensive series of studies investigating different soil components in scalable laboratory experiments.

7. Background

7.1. Mid-IR Spectroscopy of Minerals

In the following chapter the fundamentals of the MIR spectroscopy of minerals will be discussed with main focus on the interpretation of the vibrational spectrum of quartz, which is the relevant mineral predominantly investigated in this thesis.

The spectral features of minerals in the MIR range considered here are the result of vibrational transition processes. Their number, intensity and shape are dependent on atomic masses, interatomic force fields and, particularly, molecular geometry. One goal of spectroscopic investigations is to quantitatively describe the vibrational process enabling the origin of each absorption band to be traced. Sophisticated calculations have been made consistent with observations at least for some minerals [215], although not necessarily claiming correctness. Even if a vibrational mode is precisely understood, it is virtually impossible to describe such a motion simply and concisely for such complex structures as silicates. Consequently, one must rely on some very general descriptions, such as "Si-O symmetric stretch," to denominate the vibrations predominantly involving the symmetric expansion and contraction of the silicon-oxygen bonds.

Using such simplified visualizations, we can successfully generalize the fundamental aspects of the spectral behavior of minerals.

For example, atoms with low mass vibrate at higher frequencies (shorter wavelengths) than heavier atoms when substituted into the same crystalline structure. However, higher bond strengths also result in higher frequencies of vibrational transitions. This change in bonding within silicates is related to the degree of polymerization of the SiO_4

ion [216]. This results in a systematic change in wavelengths of the fundamental vibration bands of silicates as the framework structure ultimately is based on isolated tetrahedra. Finally, bond-stretching vibrations in covalent structures are located at higher frequencies than bending modes. Such internal molecular vibrations are typically found at higher frequencies than lattice modes [217].

In summary, the most prominent features in infrared spectra of minerals can be understood in the context of the generalized descriptions of the main vibrational features as outlined above and are described below for different types of minerals. The attribution of more complex vibrational features resulting from overtones and combination bands of the internal vibrations and lattice modes is more speculative in nature, even for the simplest minerals.

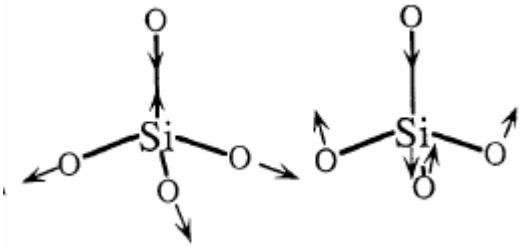

Figure 7.1 Infrared active internal vibrations of quartz. Left: ν_3-asymmetric stretch Right: ν_4-asymmetric bend [218].

For many minerals, the types of vibrational modes may be divided into two main categories: *internal modes* and *lattice modes*. Internal modes are vibrations which can be associated with those of a molecular unit, shifted (and possibly split) by interaction with the crystalline environment into which the molecular unit is bonded: the vibrations of the silica tetrahedron shown in Figure 7.1 are typical examples of these types of motions, which give rise to internal modes. Such internal modes are typically associated

with the most strongly bonded units in a crystal, and thus with the highest frequency vibrations of a given material. Here, it should be mentioned again that even the simple picture of molecular vibrations is often complicated by the presence of interacting molecular units within a crystal. For example, it is difficult to associate different bands in feldspars with stretching vibrations of distinct AlO_4 or SiO_4 tetrahedron due to interlinking tetrahedra. A silica symmetric stretching vibration such as is shown in Figure 7.1 will involve a stretching motion of the adjoining AlO_4 tetrahedron, and vibrations of these two species must be viewed as coupled within such structures.

Lattice modes comprise both a range of (often comparatively low frequency) vibrations not readily describable in terms of molecular units, and so-called external modes. External modes are those involving motions of a molecular unit against its surrounding lattice: for example, displacement of a SiO_4 tetrahedron against the surrounding lattice.

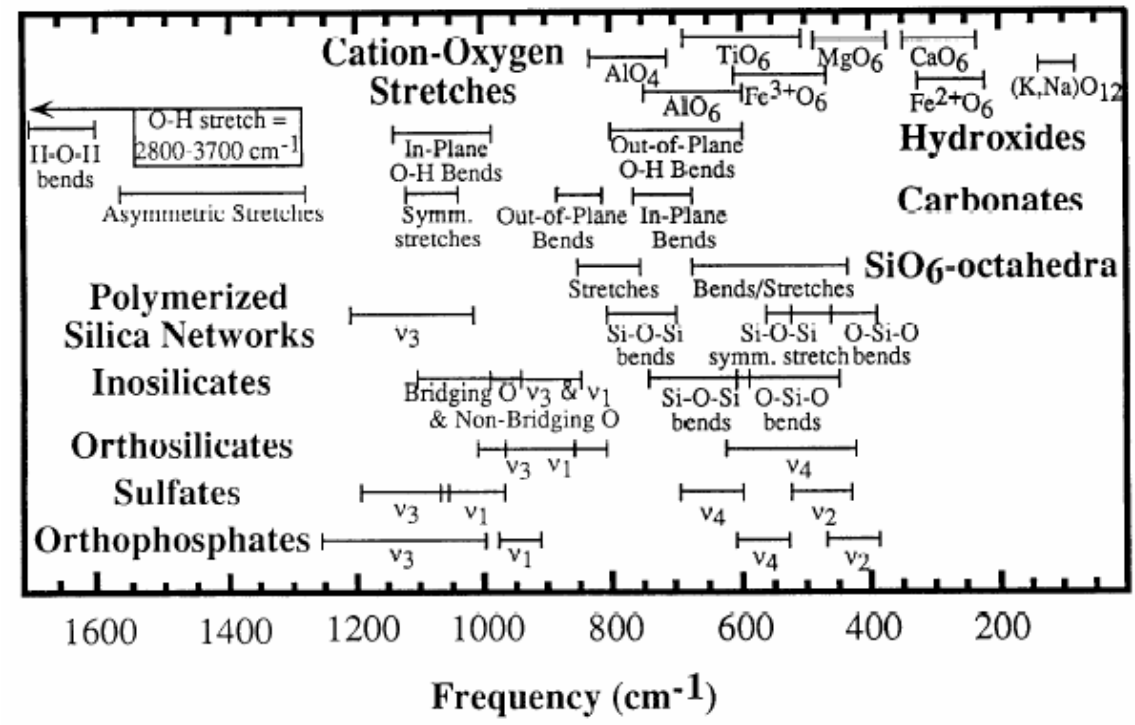

Figure 7.2 Approximate frequency range of common internal vibrations of silicates, oxides and other functional groups within minerals [218].

The most intense spectral features of quartz, occurring between 830 and 1250 cm^{-1} (8 to 12 μm), are generally simplified as fundamental asymmetric Si-O-Si stretching vibrations. The appearance of these features typically changes in reflectance measurements. For example, the weak side band near 1180 cm^{-1} (8.5 μm) in the transmittance spectrum of quartz appears as well-defined lobe of a prominent reflectance doublet between 1000 and 1250 cm^{-1} (8 and 10 μm). The reflectance spectrum of quartz glass displays a much weaker short-wavelength lobe.

Approximate frequency ranges of common internal vibrations of silicates, oxides and other functional groups within minerals are summarized in Figure 7.2 [218]. These most intense features are located within the atmospheric window (700 to 1250 cm^{-1}; 8-14 μm), rendering them most useful for remote sensing of silicates [216].

The second most intense silicate bands are broadly characterized as O-Si-O deformation or bending modes, which occur in the region of 400 to 560 cm^{-1} (18-25 μm). Weaker bands in quartz spectra between 670 and 830 cm^{-1} (12 - 15 μm) have been attributed to symmetric Si-O-Si stretching vibrations [217]. When some of the silicon atoms are replaced by aluminum, as in feldspar minerals, additional Si-O-Al stretching vibrations are added. For example, albite displays eight characteristic bands in its spectrum between 500 to 830 cm^{-1} (12-20 μm). Again, such bands are greatly simplified or eliminated in the spectra of glasses [219]. Additional weak bands are displayed as troughs between 400 to 1450 cm^{-1} (3-7 μm). Such bands in silicate spectra have largely been ignored because they are usually too weak to be observed in transmittance spectra. However, they can be very useful in spectral identification of fine particulate minerals and rocks, where these features appear quite prominent [220]. Since these features have not been assigned with any certainty, such bands are usually referred to as overtone/combination tone bands of internal and lattice modes.

It is well known that glass spectra of mineral compounds show differences in the spectral appearances, which have been attributed generally to broadening of the bands [217]. However, broadening does not sufficiently explain the reduced intensity of the 1180 cm^{-1} (8.5 μm) band in the spectrum of glass compared to that of crystalline quartz. An alternative explanation is that the short-wavelength lobe of the quartz reflectance doublet is not entirely resulting from internal molecular vibrations, but depends to some extent on the long-range order in the crystal [221]. A brief description of the progress in the understanding of the vibrational spectra of glasses is given in the next section.

7.2. Mid-IR Spectra of Glasses

The spectroscopy of glasses has been somewhat neglected in solid state physics over the last century, as compared to the amount and quality of work performed on crystalline structures. The early frontiers of solid state spectroscopy have targeted understanding of periodic materials, for which progressively more refined experiments were performed and supported by elegant theories. Resulting, the structural, mechanical, thermal, electronic, optical, and magnetic properties of perfect crystals are nowadays known in considerable detail. To the extent that defects could be treated as perturbations of otherwise periodic structures, experiments and related theories met with considerable success. This also applies to the vibrational properties of defective and mixed crystals, elaborated by Lifshitz and Maradudin, among others [222].

This situation radically changes considering glasses, owing to the lack of periodicity, which initially led to substantial difficulties in experiments, analytical theories and simulations [223]. This explains why the field of structural glasses remained relatively unexplained for many decades. However, due to significant efforts in this field of research this situation is improving steadily and for a big part the progress in glass analytics is due to optical investigations.

The systematic observation of optical spectra resulting from glasses started in the 1950s using both Raman scattering (RS) and IR spectroscopic techniques [83].

Unfortunately, long-range electric forces, the so-called Coulomb forces have been neglected for the description of the optical behavior of glasses until the late 1970s. The importance of electric forces was first recognized by Galeener and Lucovsky, who reported transverse optical (TO) and longitudinal (LO) TO-LO mode splittings in silica

(and ν-GeO_2) and thereby contributed considerably to the clarification of their optical spectra [224,225].

It was then realized from IR and RS spectra of glasses that these were “distressingly similar to a smeared-out version of the corresponding crystal”, as described by e.g. Gaskell et al. [226,227]. In comparison to the “parent crystal”, quite generally one anticipates three types of contributions in the optical spectra of the corresponding glasses:

a. There must be bands directly related to the bands of the crystals (e.g. to the bands of quartz in the case of silica), which are active in the corresponding glass. These will occur blurred due to the disordered structure.
b. Forbidden bands of the crystals may appear active in the corresponding glass, as the selection rules are likely to be relaxed by disorder.
c. Defects that are absent from the parent crystals may occur in glasses, such as e.g. small rings of repeating Si-O units in the case of silica. If such defects are optically active and sufficiently prevalent, they may contribute to the optical spectrum.

7.3. Mode Splitting in MIR-Spectra of Crystals and Glasses

In recent years, especially the interest in semiconductors and accordingly the demand for improved analysis of thin amorphous SiO_2 (a-SiO_2) layers, promoted a higher output of scientific literature in the field of optical glass analysis.

Thorough investigations on both the structure and the defects present within thin films formed on silicon is of crucial importance in microelectronics. IR spectroscopy is a

powerful tool for such investigations providing information on the structure, thickness, density, carrier concentration and several other important properties of thin films. Unfortunately, some aspects of these methods and the resulting spectroscopic data are still not entirely understood. In particular and despite an enormous amount of work dedicated to analyzing the structure of a-SiO_2 using IR spectroscopy, the interpretation of some spectral features observed at normal and oblique incidence of light, especially in the spectral region of 1000 – 1300 cm^{-1}, is still a matter of substantial debate [228- 254]. Although these spectral features are generally accepted to originate mostly from asymmetric stretching vibrations of Si-O-Si bridging sequences [255], different interpretations are still prevalent in the relevant literature. Galeener [225] attributed the partially resolved pair of peaks in the reflectivity spectrum of bulk a-SiO_2 to an asymmetric stretching vibration of the bridging oxygens parallel to the Si-Si direction plus some Si-cation motion, which could be resolved via Kramers-Kronig analysis of transverse optical (TO) and longitudinal (LO) components arising from long-range Coulomb coupling. The TO component involves nonzero derivatives at the equilibrium inter-nuclear configuration for dipole moment components perpendicular to the propagation vector of the phonon waves, whereas the higher-frequency LO component involves dipole moment changes parallel to the propagation vector.

In the case of thermal SiO_2 films, Boyd [231] suggested the occurrence of some shorter bonds within each SiO_4 tetrahedron in order to explain a slightly asymmetric peak near 1080 cm^{-1}. This feature is typical for IR transmission spectra of thin films, which did not exhibit the high-frequency shoulder of thicker films at approx. 1200 cm^{-1}. In contrast, Huebner et al. [245] used IR transmission spectroscopy at oblique incidence (55° off-normal) to simultaneously detect the TO and LO components, at 1091 and 1260 cm^{-1}, respectively, for 500 nm thick thermal SiO_2 films. Olsen and Shimura [233] used multiple internal reflectance at 60° incidence with linearly polarized light and they were able to

detectthe TO and LO components at 1080 and 1240 cm^{-1} in 3 nm thick SiO_2 films using parallel polarized (p) light. In perpendicular polarized (s) light essentially only the TO mode was detected.

In crystals, these mode splittings arise as a result of long-range Coulomb forces, which are a consequence of the internal electric field created by the motions of the ions during the vibrations. In glasses, there is also some theoretical support for the occurrence of mode splitting effects [239], in particular discussed in the work of de Leeuw and Thorpe [229]. In their work they calculated the optical response of a computer-generated random network with 1536 ions. By introducing long–range Coulomb forces in an exact way LO-TO split vibrational mode frequencies were obtained. In contrast, Phillips [228] has suggested that LO-TO splittings imply a macroscopic polarization effect accompanying the vibrational modes, which is not possible in the continuous random network model of glass structures [243]. Consequently, the vibrational spectra of a-SiO_2 were associated with a para-crystalline model, including a large density of Si=O bonds on internal surfaces, where LO-TO pairs would physically be possible.

Because of the transverse character of electromagnetic radiation, in conventional transmission spectroscopy at normal incidence only TO modes can be detected. It was shown by Berreman [232] that transmission spectra of crystal films at 30° off normal incidence enable the detection of LO modes, which has also been observed for thermal a-SiO_2 thin films, in both transmission [245] and ATR measurements [233]. Berreman's argument substantiates in showing that for crystalline thin films zone-center (long wavelength) phonons have a wave vector perpendicular to the film surface, such that normal incidence radiation can only interact with TO vibrations (parallel to the surface). In contrast, the p-polarized component of oblique incident radiation has sub-components parallel and perpendicular to the film surface, which can excite both TO and LO phonons, respectively. Almeida et al. [246] suggested that this argument can be

extended to the case of bulk samples and the high-frequency LO mode of bulk a-SiO_2, which was detected by diffuse-reflectance FT-IR spectroscopy during variation of the incidence angle between 20° and 70°.

Kirk [235] quantitatively analyzed the IR-absorption spectrum of a-SiO_2 in terms of its TO-LO vibrational modes. Disorder induced mechanical coupling between the asymmetric O-Si-O stretch (AS_1) mode (in-phase motion of adjacent O atoms) and the relatively optically inactive O-Si-O asymmetric stretch (AS_2) mode (out-of-phase motion of adjacent O atoms) was introduced into the oscillator model. Coupled AS_1- and AS_2-mode LO-TO frequency pairs were experimentally observed as peaks at 1076-1256 and 1160-1200 cm^{-1}, respectively, in oblique incidence p-polarized absorption spectra of thin thermally grown a-SiO_2 films. Two other LO-TO mode pairs were observed in these spectra as absorption peaks at approx. 810-820 and 457-507 cm^{-1}. The simplest form of the coupled-mode model consistent with experimental data is one in which the AS_1-mode LO-TO frequency splitting is resulting from the AS_1 transverse effective charge and the AS_2-mode LO-TO splitting relates to the mechanical coupling between these two modes and not to the AS_2 transverse effective charge, which is negligibly small.

However, this assignment has been questioned by Almeida [243] based on his own reflectance measurements and theoretical calculations of transmittance and reflectance spectra performed by Phillips [238] for a-SiO_2 films at different angles of incidence. Later, Gole et al. [242] and Shaganov et al [252] suggested a reassignment of a section of the 1176 cm^{-1} band to the Si=O stretching mode of silanone-based oxyhydrides, based on their quantum chemical calculations. This type of vibration is observed on oxidized porous silicon structures, which have crystalline Si in their core and SiO_x (x=1,2) at their surface.

Discussions about the exact assignments of the spectral features of amorphous and crystalline SiO_2 structures extended into the present literature [247,253,254] and will not

be further discussed within the scope of this thesis, as the most important aspects have been summarized in the section above.

Quantitative band assignments and calculations for glasses naturally become even more complicated when the material is composed of more than one basic unit. One of the wide varieties of mixed glass compositions, soda lime glass spheres have been investigated in this thesis (chapter 9.2), since (a) their main component (~70%) is SiO_2, thus findings presumably can be related to the quartz results and (b) such glass spheres are available in mono-disperse samples in a wide size regime (nm to mm).

Current approaches to the problem of connecting the vibrational spectra with the structures of glasses are still restricted to the qualitative evaluation of experimentally recorded IR or Raman spectra. and subsequently applying semi-quantitative calculations to fit the empirical data [256, 257].

Quantitative analyses usually involve, as the necessary first stage, data treatment intending to converting the recorded spectra into “reduced” spectra, considering only main spectral features [258]. Moreover, the vibrational spectra of inorganic glasses are multiband spectra with overlapping bands virtually always present. Therefore, spectral data evaluation for quantitative data treatment should always include the deconvolution of the multiband spectrum into individual bands. Interpretation of the obtained individual bands remains a challenging task due to a multitude of effects of vast variety of vibrational active structures such as (i) particular types of polyhedra, (ii) R-X-R bridges (R being Si, P, etc. and X being O, F, S, etc.) and $(RX_m)^{n-}$ terminal groups, and (iii) superstructural units (various SiO_4 rings for example), amongst others [237,250,257,258,259]. The problem of reasonable selection of fragments to be separated is related to the problem of changes in a spectrum resulting from an isolated molecule-like monomer vs. a polymeric structure. Atomic displacements in a structural group entering into a polymeric crystal lattice or glass network necessarily cause atomic

displacements in neighboring groups. As a result, the vibrational selection of a polymeric lattice or network significantly differs from those of the normal modes of an isolated group. Due to the lack of translational symmetry in a glass network, it is even more difficult to specify the degree of interaction of vibrations within a network and the actual "dimensions" of a region, which gives rise to a certain band. As a result, current approaches to the formation of vibrational spectra resulting from glasses provide a variety of different answers to these questions.

In summary, a general scheme for quantitative band assignment and a scheme related in more detail to IR reflection spectra are shown in Figure 7.3 and Figure 7.4, respectively [257,259].

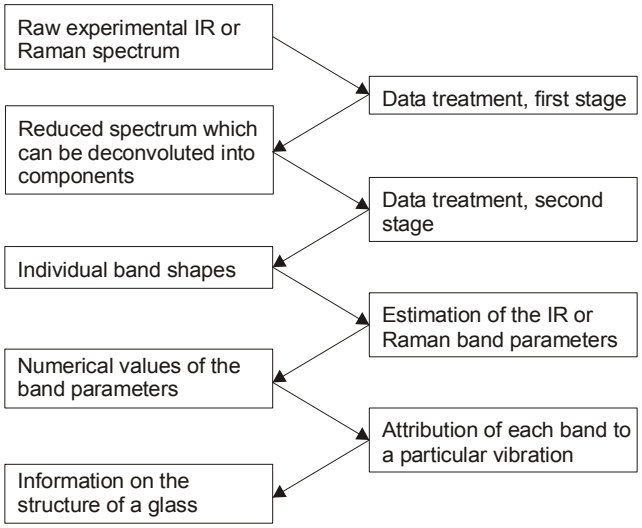

Figure 7.3 General scheme for quantitative IR band assignment for glasses. Reproduced from [257].

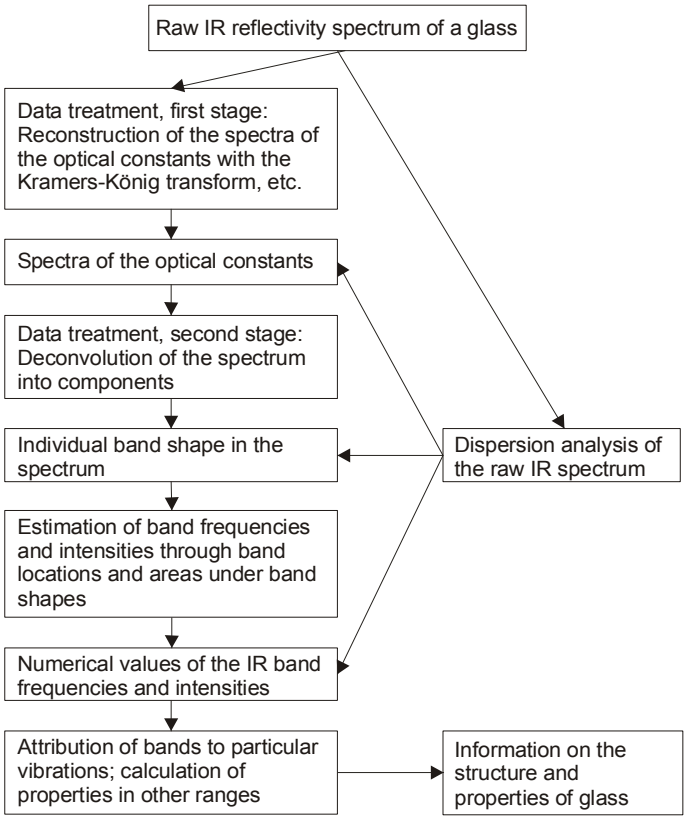

Figure 7.4 Scheme for quantitative IR band assignment for glasses starting from IR reflectance measurements. Reproduced from [257].

7.3.1. Impact on this Thesis

The absence of a comprehensive model providing sufficient explanation of the IR spectra of quartz and amorphous silica solids does not represent a significant drawback the this first study on the exploitation of IR-ATR data for improvements in understanding remote signatures of such materials. Effects such as the disturbed/undisturbed soil problem can still be investigated and obtained results will be traced back to theories such as the Berreman effect and LO-TO splitting. As the main consensus of the works referenced in this thesis [232-272] it can be concluded that in both cases, for quartz and a-SiO_2, the band positions and intensities depend at a basic level on a set of main

parameters, which are defined for the experimental conditions in the presented studies as follows:

- Polarization state of the incident light: measurements will be performed at unpolarized, p-polarized, and s-polarized illumination conditions.
- Angle of incidence: in the presented ATR setup the sample will be interrogated with a broad angular distribution of incident light (~45° +/- 15°). Thus, “bulk” responses of the sample will be obtained.
- Film thickness and/or particle size: natural quartz samples with non-uniform size distribution will be investigated in order to simulate field conditions. Furthermore, mono-disperse soda lime glass spheres will be used as samples to prove the influence of the particle size on the resulting ATR spectra. By using spherical particles signal dependencies on particle shape are effectively eliminated.

The experimental section is divided into experiments with natural quartz samples (chapter 9.1) assessing the general applicability of this measurement approach, and experiments with mono-disperse soda lime glass spheres (chapter 9.2) for a deeper insight into the signal generation with particles of controlled geometry and dimensions.

8. Experimental

8.1. Samples

Natural quartz samples were obtained from Ward’s Natural Science (Rochester, NY). 1 – 3 µm and 4 – 10 µm soda lime glass spheres were purchased from the MO-SCI Corporation (Rolla, MO), all larger spheres were obtained from Whitehouse Scientific Ltd. (Waverton, Chester, UK).

Methanol for cleaning ATR crystals has been purchased from Aldrich (Milwaukee, WI) and was of analytical grade.

8.2. Laboratory Setup

Instrumentation

Data was recorded in a spectral range of 4000 cm^{-1} to 400 cm^{-1} with a Bruker Equinox 55 Fourier transform infrared (FT-IR) spectrometer (Bruker Optics Inc., Billerica, MA) equipped with a liquid N_2 cooled mercury-cadmium-telluride (MCT) detector (FTIR-22-1.0, Infrared Associates, Stuart, FL). A total of 100 scans were averaged for each spectrum with a spectral resolution of 1 cm^{-1}. A complete list of the measurement parameters is given in Table 8.1

Table 8.1 Measurement Parameters for ATR studies

Zero Filling Factor	2	*Instrument Type*	EQUINOX55
Stored Phase Mode	No	*Number of Background Scans*	100
Start Frequency Limit for File	6000 cm^{-1}	*Acquisition Mode*	Double Sided
End Frequency Limit for File	400 cm^{-1}	*Correlation Test Mode*	No
Phase Resolution	8	*Delay Before Measurement*	0
Phase Correction Mode	Mertz	*Stabilization Delay*	0
	Blackman-Harris		
Apodization Function	3-Term	*Wanted High Frequency Limit*	7800 cm^{-1}
High Folding Limit	7900.32 cm^{-1}	*Wanted Low Frequency Limit*	400 cm^{-1}
Low Folding Limit	0 cm^{-1}	*Sample Scans*	100
Sample Spacing Divisor	2	*Resolution*	1 cm^{-1}
Actual Signal Gain	1	*Beamsplitter Setting*	KBr
Switch Gain Position	14070	*Iris Aperture*	2300 µm
Gain Switch Window	300	*Low Pass Filter*	Open
		Scanner Velocity	11 ; 100.0 KHz

A horizontal ATR accessory (Specac, Smyrna, GA) equipped with trapezoidal ZnSe ATR elements (72*10*6 mm, 45º; Macrooptica Ltd., Moscow, Russia) was used. A holographic thallium bromoiodide (KRS-5) polarizer (period: 0.25 µm, Specac, Smyrna, GA), which was mounted in a motorized polarizer rotation unit (#A121, Bruker Optics Inc, Billerica, MA), was applied for measurements at linear polarized light conditions. A schematic of the experimental setup is shown in Figure 8.1

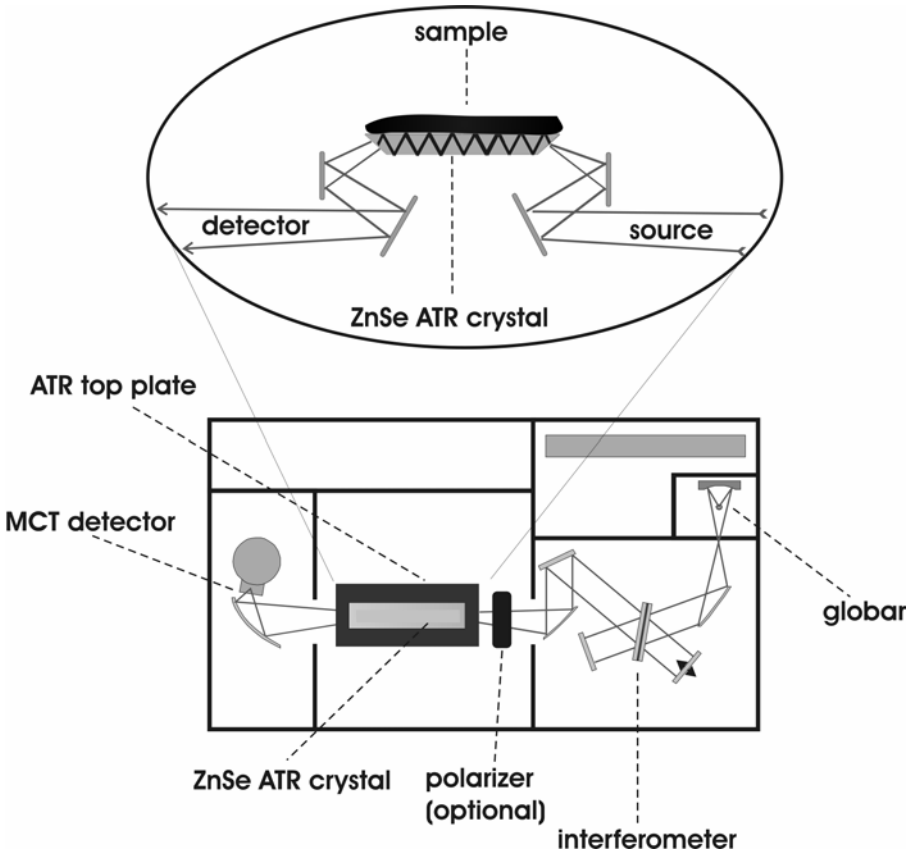

Figure 8.1 Experimental setup for cyclic wetting/drying studies of quartz sand via ATR spectroscopy in the MIR regime.

9. Results

9.1. ATR Spectra of Polydisperse Natural Quartz

9.1.1. Experimental

The ZnSe crystals have been thoroughly cleaned with methanol prior to measurements and reference spectra of bare crystals at unpolarized, p- and s-polarized illumination conditions have been recorded. Approx. 2 – 3 g of quartz sand were applied onto the crystal ensuring complete coverage of the crystal surface with a layer thickness of several millimetres, definitely exceeding the penetration depth of the evanescent field within the investigated spectral range. Following spectral measurements of the “pristine” quartz spectrum, the weathering process was simulated by addition of few droplets of deionized water to form a slurry. Within a timeframe of few hours the majority of the aqueous phase is evaporated, evident by decreasing water absorption bands (e.g. at 1650 cm^{-1}), which were continuously monitored. In this study, spectra of the quartz sample after the wetting/drying cycle will be referred to as “dried” spectra. Finally, a disturbance event was introduced by stirring up the dried quartz sand sample using a plastic spatula. Consequently, spectra recorded after the disturbance event are referred to as “disturbed” spectra. This cyclic procedure has been investigated at unpolarized, p-polarized and s-polarized illumination conditions and related to the corresponding reference spectra. The resulting evanescently recorded absorption spectra have been compared and analyzed at the conditions schematically summarized in Figure 9.1.

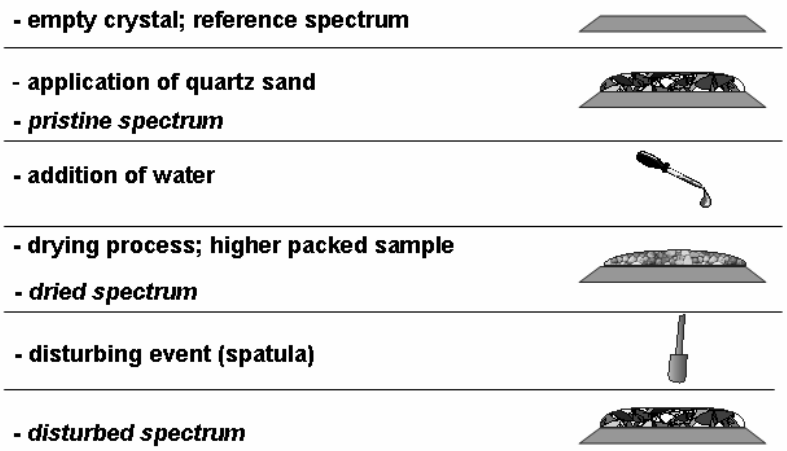

Figure 9.1 Overview of experimental procedure.

9.1.2. Wetting / Drying

As can be seen in Figure 9.2, IR-ATR spectroscopy is a highly suitable, yet comparatively simple method providing infrared spectra of quartz sand. This method allows investigation of a wide variety of samples including other minerals, clays or soil samples at constant and highly reproducible measurement conditions (data not shown). In the IR spectrum of pristine quartz, the broad absorption feature with a maximum around 1090 cm^{-1} is attributed to asymmetric SiO_4 stretching vibrations. The less intense double peak located at around 800 cm^{-1} is due to symmetric stretching and the peak at 690 cm^{-1} is related to Si-O-Si bending transitions.

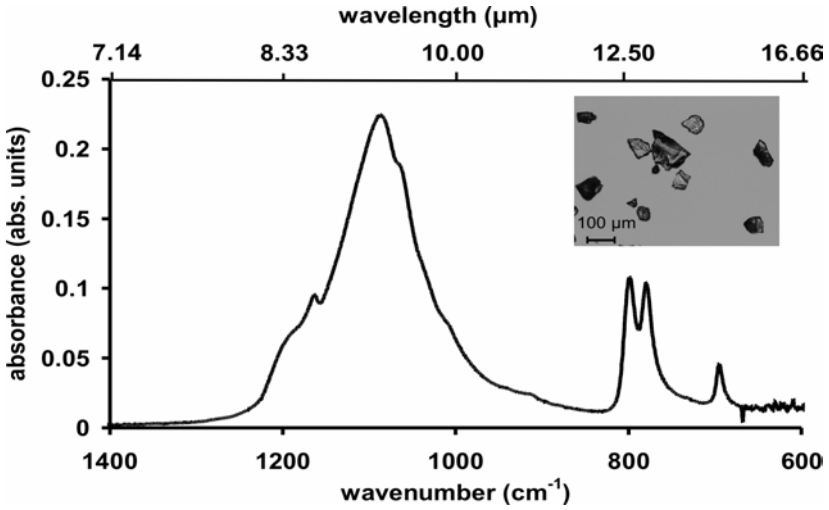

Figure 9.2 Exemplary IR-ATR spectrum of pristine quartz sand (Fluka 83340). The broad absorption feature with a maximum at around 1090 cm^{-1} is attributed to asymmetric stretching vibrations, the double peak at around 800 cm^{-1} relates to a symmetric stretching of the SiO_4 unit cell and the peak at 690 cm^{-1} is related to Si-O-Si bending vibrations. The inset shows an optical microscopy image of the sample.

In Figure 9.3, the comparison between a pristine, dried and disturbed spectrum of quartz sand following the wetting/drying cycle described in the experimental section shows some initially surprising differences. The dried spectrum shows significantly higher absorption features throughout the entire investigated spectral range. This circumstance can be explained by a much higher compactness of the quartz particles resulting from the submersion in water. While the initial (pristine) state of the quartz sand typically shows a high void volume in between the particles mostly due to friction and static forces, the addition of water promotes filling of the interstitial spaces by compacting of the sample leading to an increased density of the sample packed onto the ATR crystal surface. Therefore, more sample material is present within the evanescent field leading to higher intensity of the absorption features. After disturbing the sample by stirring the compacted quartz sand with a spatula, the absorption intensities return to near their initial values.

Most importantly, these findings are in agreement with field and laboratory remote sensing studies, where changes in spectral contrast have been reported as the predominant difference between spectra of pristine and disturbed soils [1,2,5].

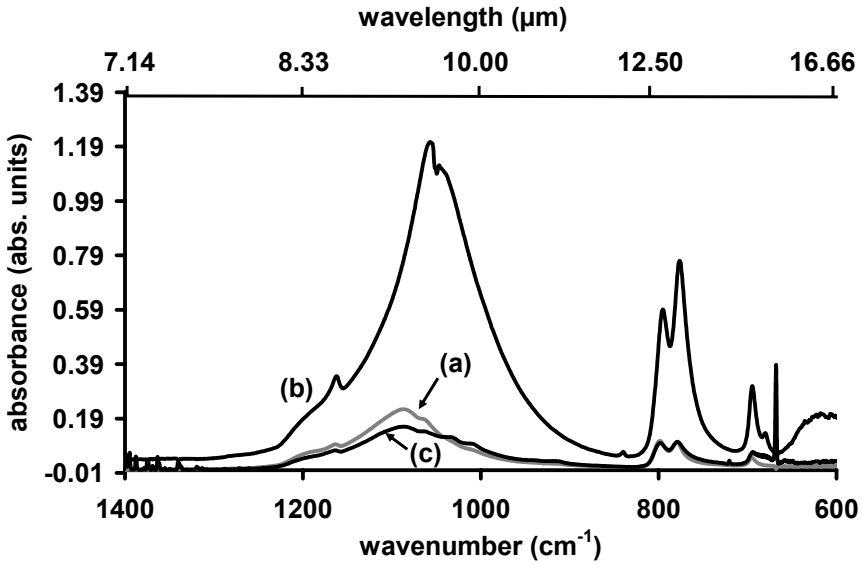

Figure 9.3 Pristine (a), dried (b) and disturbed (c) spectra of quartz sand. The sharp band around 670 cm^{-1} results from atmospheric CO_2 present after opening the sample compartment.

Another noticeable difference is the change of shape and shift of spectral position of the maximum associated with the main absorption feature. We observe a reversible shift of the peak maximum from 1090 cm^{-1} (pristine sample) to 1060 cm^{-1} (dried sample), and back to 1090 cm^{-1} (disturbed sample). This phenomenon was reproducibly observed when the same sample was cycled several times in the order wetting/drying/disturbing (data not shown). This apparently significant and pronounced spectral shift may potentially be a characteristic spectral feature useful to remote detection of disturbed soil sites. In depth investigations of this effect led to the following hypothesis.

The addition of water promotes ultra-fine particles (<10µm), which initially adhere to larger particles, into a suspension state facilitating mobility within interstitial spaces.

Potentially driven by capillary forces, these particles accumulate at or close to the surface of the ZnSe crystal during the drying process. Evidence is derived from removing the majority of the quartz sample layer from the ATR crystal after complete water evaporation and still detecting a layer of ultrafine particles adhering to the surface of the crystal. To further prove this assumption some grams of quartz sample have been suspended in acetone in a vial which was closed severely shaken and a sample has been drawn from the immediately formed sediment, representing the most coarse fraction of the investigated multi-disperse quartz sample (for a comparison of the finest and coarsest fractions of this sample see Figure 9.4).

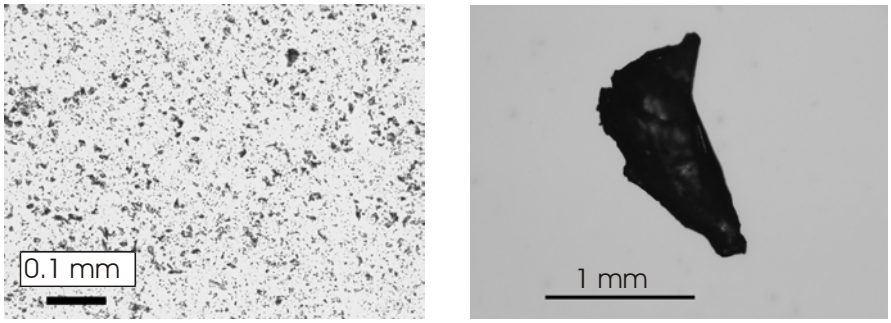

Figure 9.4 Microscopy pictures of the finest fraction (left) and the coarsest section (right) of the investigated quartz sample.

This coarse fraction when measured alone, produced only very weak absorption features, even after a wetting and drying step. In Figure 9.5 the dried spectra of the initial quartz sample, the coarse fraction and the fine fraction, which was obtained as described above are shown.

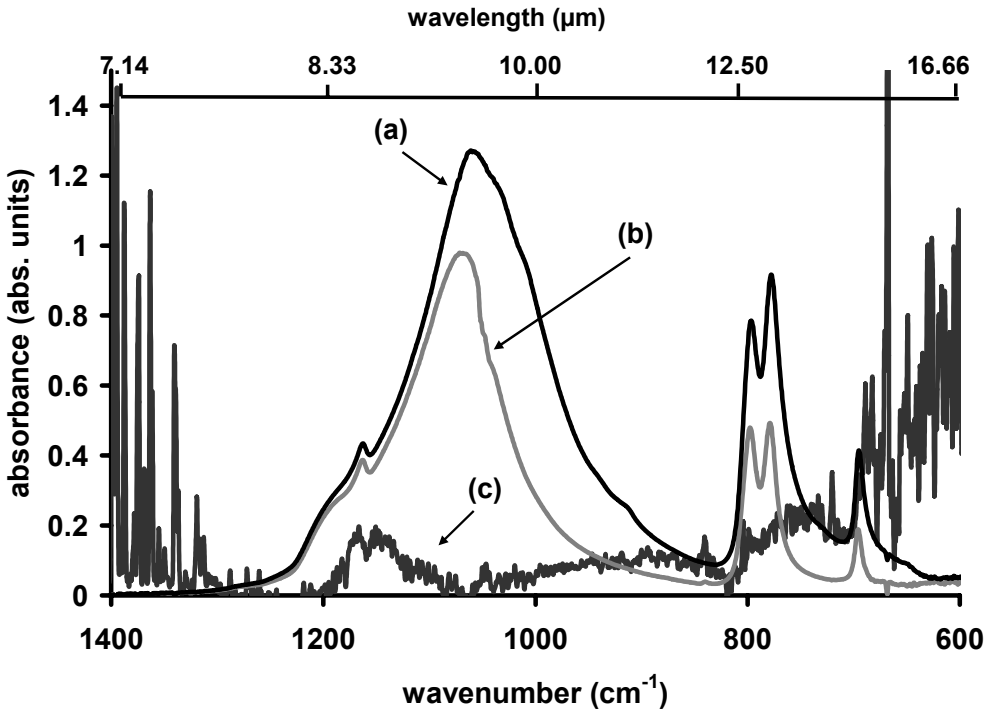

Figure 9.5 Dried Spectra of a mixed (a), fine (b) and coarse (c) fraction of quartz sand. The spectra of the coarse fraction were scaled, due to very weak absorption features.

It can be clearly seen that the spectrum of the mixed (unaltered) quartz resembles the spectrum from the fine fraction to a high extent. The difference in intensities can be related to the fact that during the removing of the major part of the quartz, the ATR element was not completely covered with sample. Consequently, the particle size distribution of the sample is changing throughout the simulated weathering process facilitating migration of ultrafine particles into interstitial spaces of larger grains detected by an increased abundance of material within the analytical volume probed by the evanescent field resulting in dramatically increasing absorption intensities recorded in the spectrum of the dried sample. A schematic of these findings is shown in Figure 9.6.

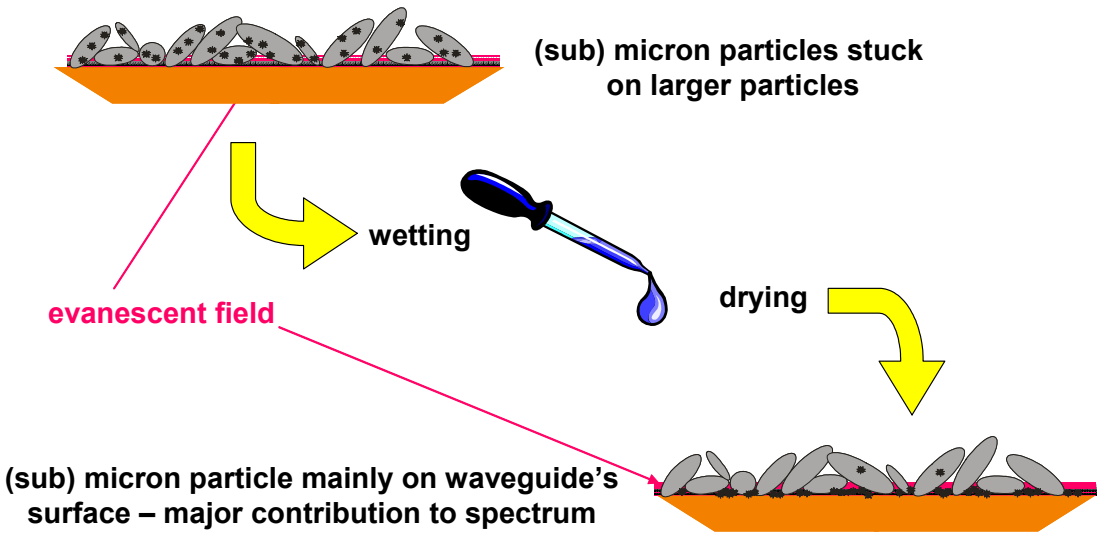

Figure 9.6 Schematic of agglomeration process of ultrafine quartz particles on the crystal surface during the wetting / drying process.

Additionally it is obvious that the peak maximum of the major absorption feature around 1100 cm^{-1} (asymmetric stretch vibrations) is clearly shifted from the coarse to the fine fraction, showing an obvious particle size dependency.

These findings appear plausible and in analogy to previous reports hypothesizing that changes in particle size distribution when investigating undisturbed vs. disturbed soils are a major contribution to the detected differences in the respective spectra [1,5,260].

Judging from these preliminary results the logical next step is to perform studies with polarized light, followed by investigations of mono-disperse samples. Soda lime glass spheres are commercially available in a wide range of particle sizes and therefore have been selected for further investigations (chapter 9.2).

9.1.3. Polarized Light

The influence of using s- and p-polarized radiation to probe quartz sand reveals further interesting spectral aspects of the sample. ATR spectra of a pristine (Figure 9.7) and

dried (Figure 9.8) quartz sand samples have been recorded with unpolarized (a), p-polarized (b) and s-polarized (c) infrared radiation.

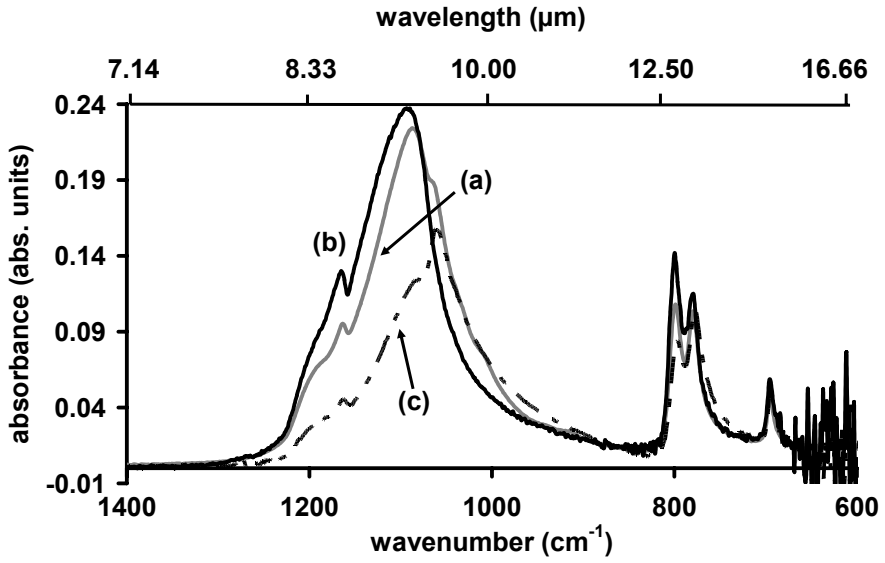

Figure 9.7 ATR spectra of pristine quartz sand samples recorded at different polarization states of infrared radiation: (a) unpolarized light (grey line), (b) p-polarized light (black line), (c) s-polarized light (dotted line).

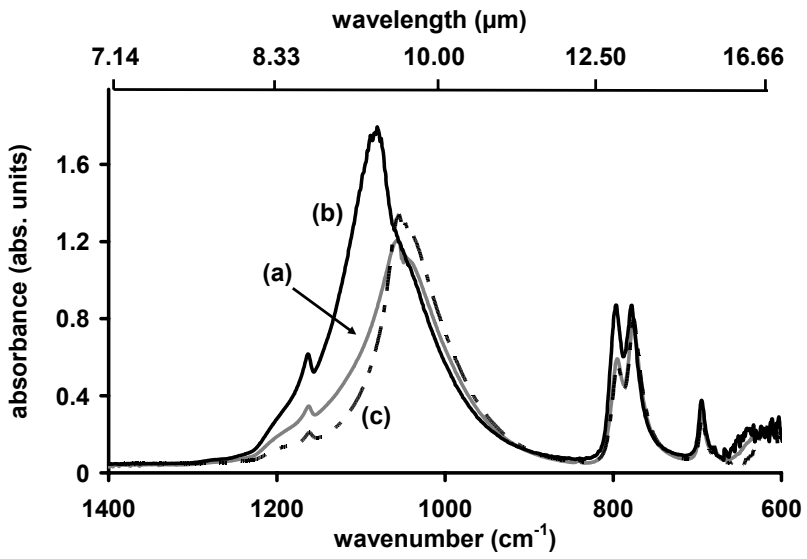

Figure 9.8 ATR spectra of pristine quartz sand samples recorded at different polarization states of infrared radiation: (a) unpolarized light (grey line), (b) p-polarized light (black line), (c) s-polarized light (dotted line).

The pronounced splitting of the dominant absorption feature at 1090 cm^{-1} in both cases is presumably related to a transversal optical (TO) and longitudinal (LO) mode splitting of the asymmetric stretch vibrational mode for SiO_2 as described by Berreman in 1963 [232]. Berreman disapproved of the commonly accepted assumption that IR-spectra of cubic crystals only show vibrational features of TO modes when probed with p-polarized light. He showed that this assumption only holds true for the case of perpendicular light incidence, but was shown to be incorrect for thin films of SiO_2 crystals and oblique incidence angles of light. He related his results in a rather general approach to “special boundary conditions” applicable to thin (semi infinite) films. Harbecke et al. [244] proved that illumination with p-polarized light results in spectral features at the frequencies of TO and LO resonances in reflection and transmission spectra. The LO structure is generated by the surface charges due to the normal component of the electric field. However, it is a prerequisite that the thickness of the film is small compared to the wavelength in vacuum. Furthermore, LO frequencies not only depend on the resonance

frequency of the microscopic oscillator, but also on the dielectric background. Therefore, this effect is related to macroscopic properties of the film. For example, the frequency position of the LO resonance can shift depending on the compactness of the deposited material. From this, the so called Berreman thickness can be derived, which is the film thickness responsible for the maximum effect.

In 1988 Kirk [235] published a contribution for the quantification of mode splitting in case of SiO_2 films. According to his theory, TO-LO splitting occurs for two main reasons: (i) As_1 (asymmetric vibration, O-atoms in phase) mode: LO-TO splitting occurs due to transverse effective (surface) charges, and (ii) As_2 (asymmetric vibration, O-atoms 180 degree out of phase to each other): splitting occurs due to mechanical coupling between the LO and TO mode.

In the same year Piro et al.[236] conducted the first ATR measurements with 2 mm thick α-quartz plates observing LO-TO splitting of the vibrational modes in a thick quartz film and showed that this effect is not limited to ultrathin layers.

From the results shown in Figure 9.7 and Figure 9.8 it can be concluded that the Berreman effect is also observable for particulate materials and is not a unique property of films. This effect has been observed for particulate films for the first time in the course of this study.

9.1.4. Conclusions

It has been shown that IR-ATR spectroscopy in the mid-infrared band provides a reliable methodology for fundamental spectroscopic studies of quartz sand, which potentially benefit interpretation of data provided by the remote sensing community. Besides the already established differences in spectral contrast of disturbed and undisturbed soil, a strong spectral shift of the maximum of the main absorption feature at 1090 cm^{-1} could

be observed. When probed with s- or p-polarized light, the quartz sample showed strong LO-TO mode splitting, which is most likely related to the Berreman effect. These findings advance the variety of spectral characteristics useful to the detection of disturbed soils (i.e. possible landmine sites) with mid-infrared imaging systems. The wetting and drying studies also reveal that the main reason for spectral differences of pristine and disturbed soils eventually relates to changes of the particle size distribution of the sample due to rearrangement of ultrafine particles facilitated by water.

These preliminary results strongly propose the potential of ATR spectroscopic methods for the investigation of signatures derived from remote sensing. Not only the difference in spectral contrast of disturbed and pristine soil could be reproduced, also the assumption of particle size related origin of this phenomenon could be shown. Furthermore, derived from the presented results so far unnoticed spectral shifts in spectra of disturbed and pristine samples was observed clearly, being possibly an exploitable feature for remote disturbed soil detection. In order to render these results useful for remote sensing purposes several experimental studies seem necessary, especially the investigation of mono-disperse samples seems unavoidable, before any quantification and model building for observed effects such as LO-TO mode splitting and absorption intensities can be performed.

Additionally, it is suggested to perform diffuse reflectance measurements applying the same wetting and drying cycles with similar samples in order to ensure that these findings are in coherence with the presented ATR measurements.

9.2. ATR Spectra of Mono-disperse Soda Lime Glass Spheres

In the following section mono-disperse samples (soda lime glass spheres) will be investigated at the same experimental conditions as the quartz samples in the previous

chapter. Resulting, particle size related changes in the spectra during the wetting and drying cycles should be eliminated. Furthermore, the aspect of a possible effect of various particle shapes in case of quartz samples will be suppressed. It is also expected that for at least larger spherical particles the coverage of at the surface of the ATR element will be closely to the most dense packing state and occurring changes in spectral shapes can be associated solely with the different discrete particle size of the sample.

9.2.1. Samples

1–3 µm and 4–10 µm soda lime glass spheres were purchased from the MO-SCI corporation (Rolla, MO), all larger spheres were obtained from Whitehouse Scientific Ltd. (Waverton, Chester, UK).

It should be mentioned that the investigated samples had to be obtained from two different sources in order to cover particle sizes from 1 to >100 µm size regime as the entire dimensional range is not available from one provider. Relevant properties of the materials are listed in Table 9.1. However, the data sheets for both samples mentioned that chemical compositions (and thus the expected absorption spectra) may vary from batch to batch.

Table 9.1 Relevant properties and chemical compositions of the soda lime glass spheres.

Chemical Composition	**MO-SCI Corp.**	**Whitehouse Scientific**
Silica (SiO_2)	65-75%	72.50%
Aluminum oxide (Al_2O_3)	1-5%	0.40%
Calcium oxide (CaO)	9-12%	9.80%
Magnesium oxide (MgO)	1-5%	3.30%
Sodium oxide (Na_2O)	10-20%	13.70%
Iron Oxide (Fe_2O_3)	< 0.3%	0.20%
Physical Properties		
Specific Gravity	2.5 (g/cm^3)	2.49 (g/cm^3)
Index of Refraction	1.51	1.51
Softening Temperature	650°C	740°C
Coefficient of Thermal Expansion	$9x10^{-6}$/°C (30-300°C)	$7.75\ x10^{-6}$/°C (30-300°C)
Diameter	1 - 3 µm 4 - 10 µm	25 - 32 µm 112 - 125 µm 400- 425 µm

In the following sections spheres with diameters of “1-3 µm“ will be named “1 µm“, and “4–10 µm“ will be named “4 µm”, etc..

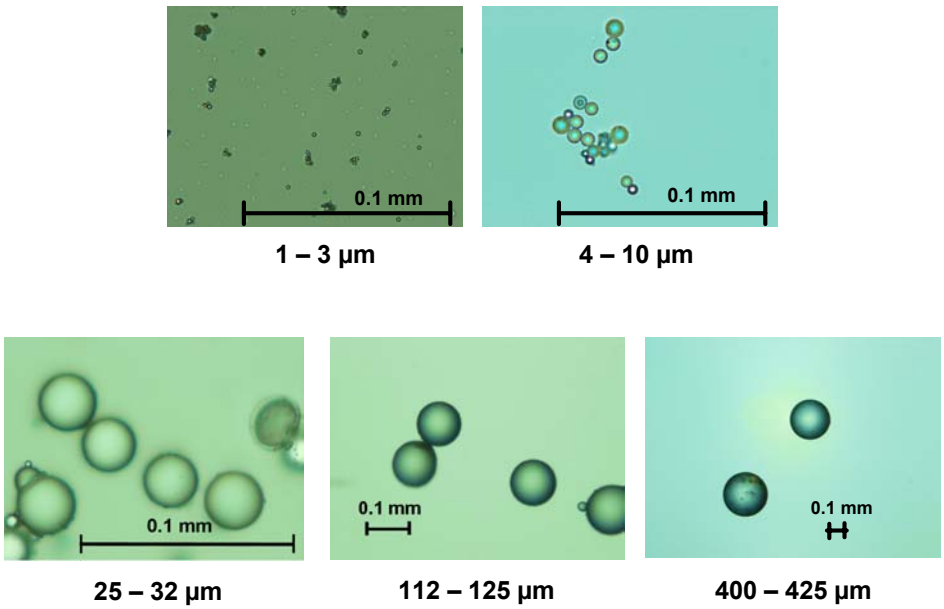

Figure 9.9 Optical microscopy images of soda lime glass spheres. The two smallest size fractions were obtained from the MO-SCI corporation (images on top). The larger size fractions were obtained from Whitehouse Scientific (images at the bottom).

Optical microscopy images of the different glass sphere batches show high quality of the samples except for rare defects, as can be seen in the lower left image of Figure 9.9. Judging from various images of each batch, the number of shape defects and size outliers are insignificantly small and should not significantly influence the obtained IR-ATR spectra.

9.2.2. Experimental

Setup and experimental procedures are similar to the study on quartz samples. Refer to chapter 8.2 and chapter 9.1.1 for details.

9.2.3. Wetting / Drying

In Figure 9.10 the ATR spectrum of the 112 µm spheres are shown illuminated with unpolarized light. Band assignments are given in Table 9.2 [261-263].

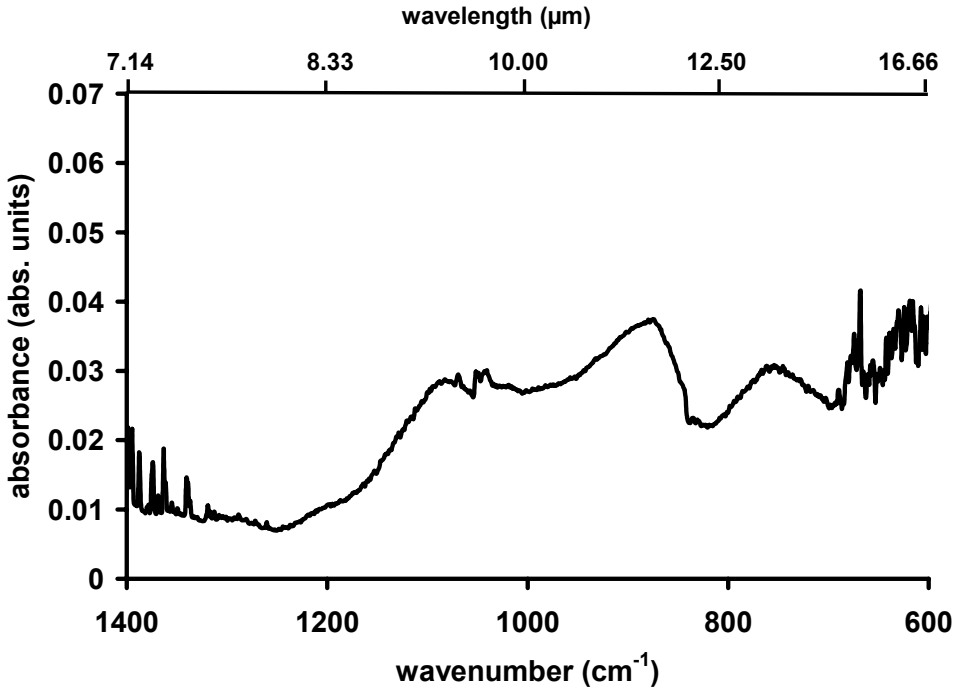

Figure 9.10 The ATR spectrum of 112 µm soda lime glass spheres.

It is clearly observable that the glass sphere spectra show band broadening in comparison to the crystalline quartz spectra, as predicted by theory [218,221].

Table 9.2 Band assignments for soda lime glasses with similar composition [261,262,263]

Peak position (cm^{-1})	Appearance	Assignment
460–480	very sharp	bending vibrations of Si–O–Si linkages
640–680	shoulder	Si–O–Si and O–Si–O bending modes
775–800	sharp	symmetric stretching vibration of [O–Si–O] bonds
960	shoulder	vibration of nonbridging oxygens
1050–1060	broad and very sharp	antisymmetric stretching + vibrations of bridging oxygens
1120	shoulder	Si–O–Si antisymmetric vibrations of bridging oxygens

However, these band assignments have to be considered with caution, as the only obtainable reference of glass with exactly the same composition (Abo-Naf et al. [[261]) shows relating absorption spectra, which resemble the spectra of this thesis only

remotely. A comparison of a transmission spectrum of soda lime glass particles of relatable size (150 to 250 µm) recorded with the KBr pellet technique from the work Abo-Naf with ATR results for soda lime glass spheres is shown in Figure 9.11.

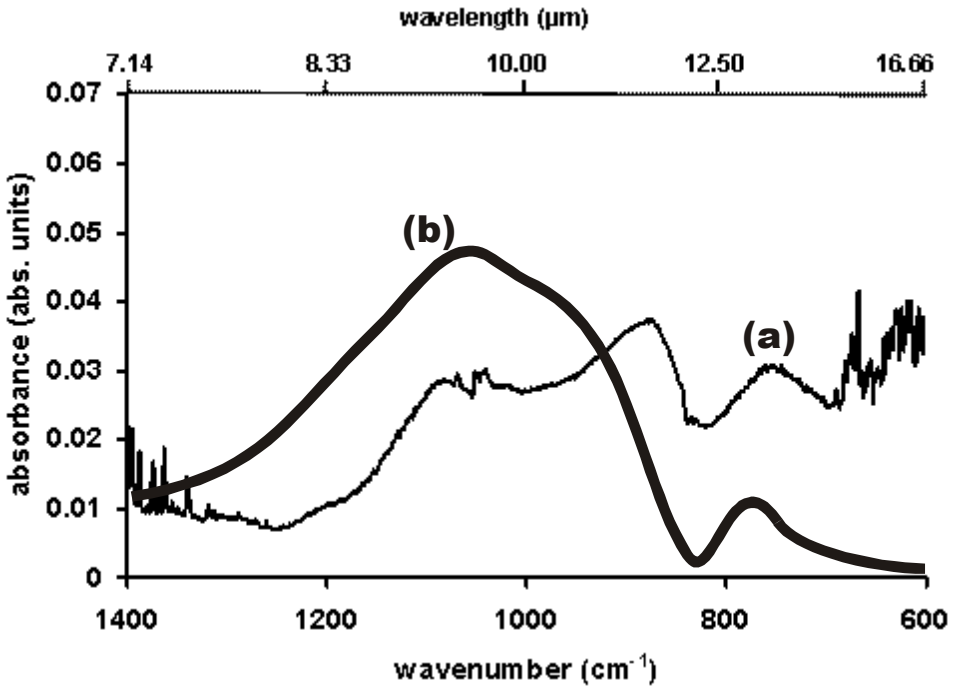

Figure 9.11 The ATR spectrum of 112 µm soda lime glass spheres (a) compared to a transmission spectrum (KBr pellet) of a 150 to 250 µm size fraction of soda lime glass with a very similar composition (b) (spectrum reproduced from [261]).

Especially the band at 960 cm^{-1} (assigned to vibrations of non-bridging oxygens) is of much higher relative intensity than in the cited reference (small shoulder). Another interesting fact is that this reference indicates no contribution of NaO_2 related vibrations in the band assignments, despite it's the rather high content in the sample.

Efimov [257,258] contradicts these band assignments and describes a semi-empirical model, which complements the soda lime glass spectra recoded in this study in a much more satisfactory way. Within the spectra of alkali disilicate crystals, the range of the Si-

O-Si asymmetric stretches can extend down to 900 cm^{-1}, whereas the range of non-bridging oxygen vibrations never extends to frequencies lower than 1000 cm^{-1}. Therefore, band assignments as given in Table 9.2 should be reversed for these two vibrational modes. Furthermore, it is illustrated that the TO mode of the asymmetric stretch vibrations of Si-O-Si is increasingly red-shifted with an increase of Na_2O content. In [257] Efimov presents experimental data and calculations to determine the band position of this asymmetric Si-O-Si vibration to be located around 960 cm^{-1} for a Na_2O-$2SiO_2$ glass providing the strongest oscillator of all vibrational modes at this frequency position. This change of band assignment together with the band positions from Table 9.2 seem to be in better agreement with the measured spectra in this section. Furthermore, as this band corresponds to a strong TO mode, it should be strongly pronounced in measurements with s-polarized light (see chapter 9.2.5). An overview of the revised band assignments is given in Table 9.3.

Table 9.3 Revised band assignments for soda lime glass as suggested by Efimov [257].. The revised bands have been shaded for clarity.

Peak position (cm^{-1})	**Assignment**
460–480	bending vibrations of Si–O–Si linkages
640–680	Si–O–Si and O–Si–O bending modes
775–800	symmetric stretching vibration of [O–Si–O] bonds
900-1000	antisymmetric stretching + vibrations of bridging oxygens
1000-1050	vibration of nonbridging oxygens
1120	Si–O–Si antisymmetric vibrations of bridging oxygens

Similar to the quartz experiments, wetting/drying cycles were investigated with the pristine and dried spectra of the soda lime glass spheres shown in Figure 9.12.

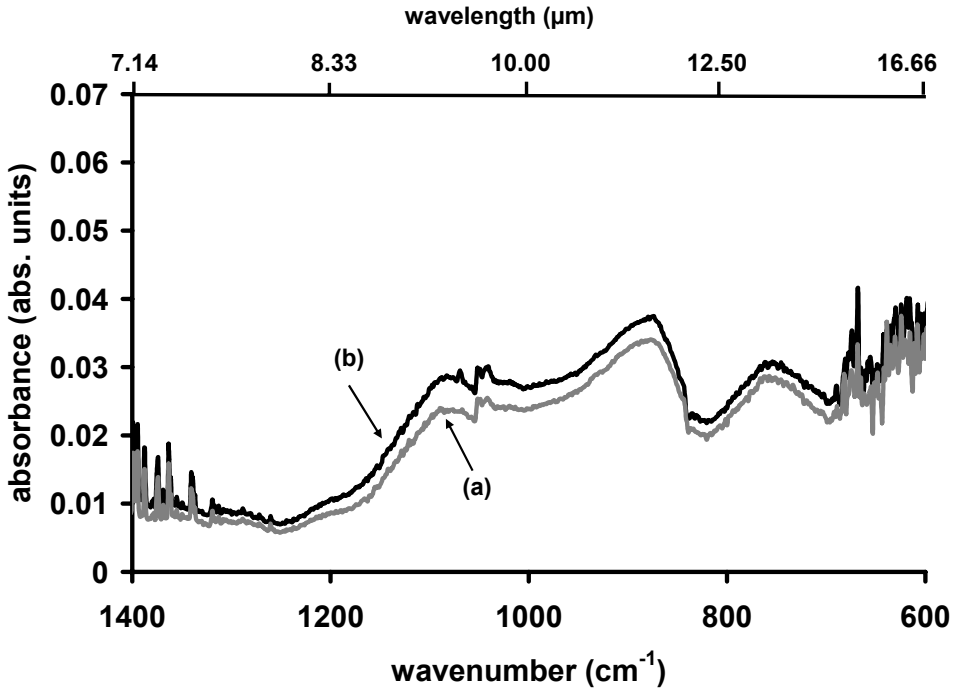

Figure 9.12 Pristine (a), dried (b) spectra of the 112 µm soda lime glass spheres.

The only observable difference in the pristine and dried spectra of the sample is expressed by a small change in spectral intensity, which is related to minor re-arrangements of the spheres during the wetting step. This result is expected given the monodispersity of the spheres already densely packed at the ATR crystal surface and strongly corroborates the assumption that spectral shifts upon wetting and drying are solely related to particle sizes if a fraction of significantly smaller particles is present.

9.2.4. Particle Size Dependence of Absorption Features of Soda Lime Glass Spheres in ATR Spectra

The particle size dependent of ATR spectra of soda lime glass spheres for 3 different diameters (25 µm, 112 µm and 400 µm) are shown in Figure 9.14. The most prominent trend observable is that smaller spheres produce spectra with higher absorption

intensities. This is expected due to the much lower void volume in between the particles on the surface. Upon deposition onto the ATR element surface, these samples seemed to form a film with highly dense uniform surface coverage, which could be visually observed for the larger spheres. In such cases, band intensities derived via ATR techniques might be used as a tool for particle size determination as has been shown for instance by Yoshidome et al. [264], providing (close to) complete coverage of the ATR element.

Apart from the expected change in spectral intensities, there is also a significant blue-shift of the absorption feature around 960 cm^{-1} (asymmetric Si-O-Si stretch vibration) with increasing particle size. In the work of Yoshidome et al. [264], where different sized silica spheres (sizes: 0.81 to 5.2 µm) were investigated, shifting of peaks was not reported. Although, when visually evaluating the published data it appears that shifts are also present in their study, however, apparently have been overlooked (Figure 9.13).

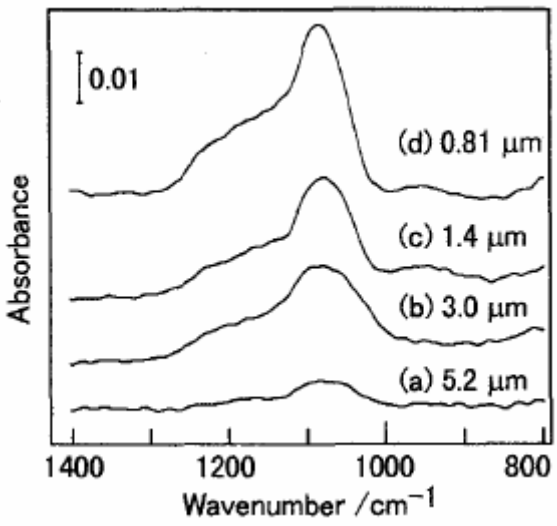

Figure 9.13 ATR spectra of silica-gel particles with various diameters [264].

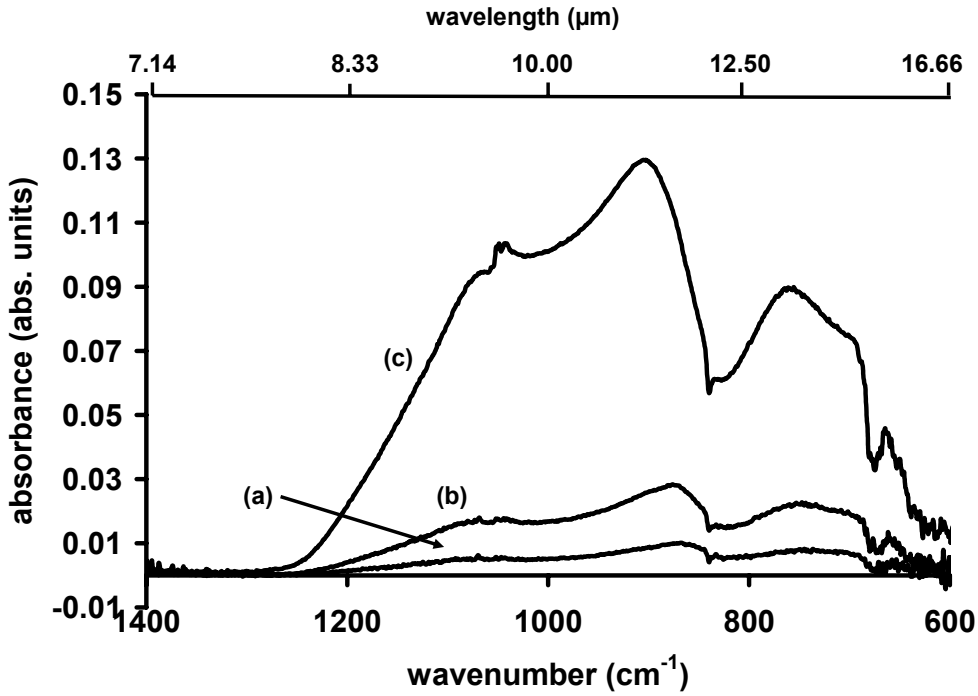

Figure 9.14 ATR spectra of soda lime glass spheres with different diameters: 400 µm (a), 112 µm (b), 25 µm (c).

It is a known problem for ATR spectroscopy of powders that if particles are sufficiently small, electrostatic forces will produce particle conglomerates and distribution by simply applying the powder onto the ATR surface will not ensure complete coverage.

In case of the glass spheres used in this study this was almost certainly the case for the two smallest fractions (1 and 4 µm). A possible solution to this problem is to suspend these samples in a volatile liquid (e.g. chloroform), apply the suspension onto the crystal and wait for solvent evaporation leaving a generally rather homogeneous film on the substrate. However, in case of strongly absorbing materials the amount of solids has to be optimized so that the resulting layer thickness does not produce spectra where total absorption takes place. This happened in several unsuccessful tries with different amounts of deposited suspension. Hence, an alternative approach for the two smallest sphere sizes was developed. In order to obtain useful spectra the powders were gently

pressed onto the ATR element via an aluminum block throughout the entire measurements, which finally yielded satisfactory results.

ATR spectra of all soda lime spheres in the range from 1 to 400 µm are shown in Figure 9.15.

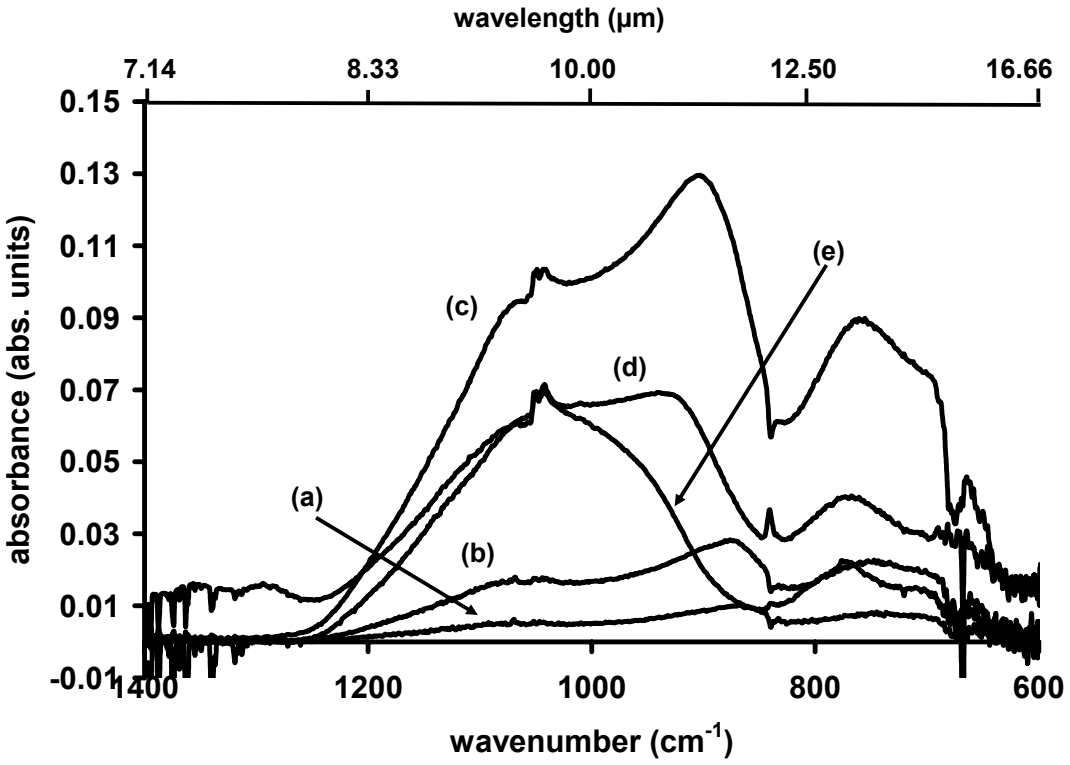

Figure 9.15 ATR spectra of soda lime glass spheres with different diameters: 400 µm (a), 112 µm (b), 25 µm (c), 4 µm (d) and 1 µm (e).

The uncertainty of complete coverage of the two smallest fractions is confirmed by the fact that they apparently do not follow the logical trend showing the most intense absorption features. However, a very interesting size-related effect can be observed: the initially most intense band at 960 cm^{-1} is continuously decreasing in intensity and is practically vanished in the spectrum of the 1 µm spheres. In order to be able to follow this trend more precisely, the spectra have been normalized at 1040 cm^{-1}, as this band

appears to be a spectral region where only minor changes occur throughout the variation of sphere diameters (Figure 9.16) .

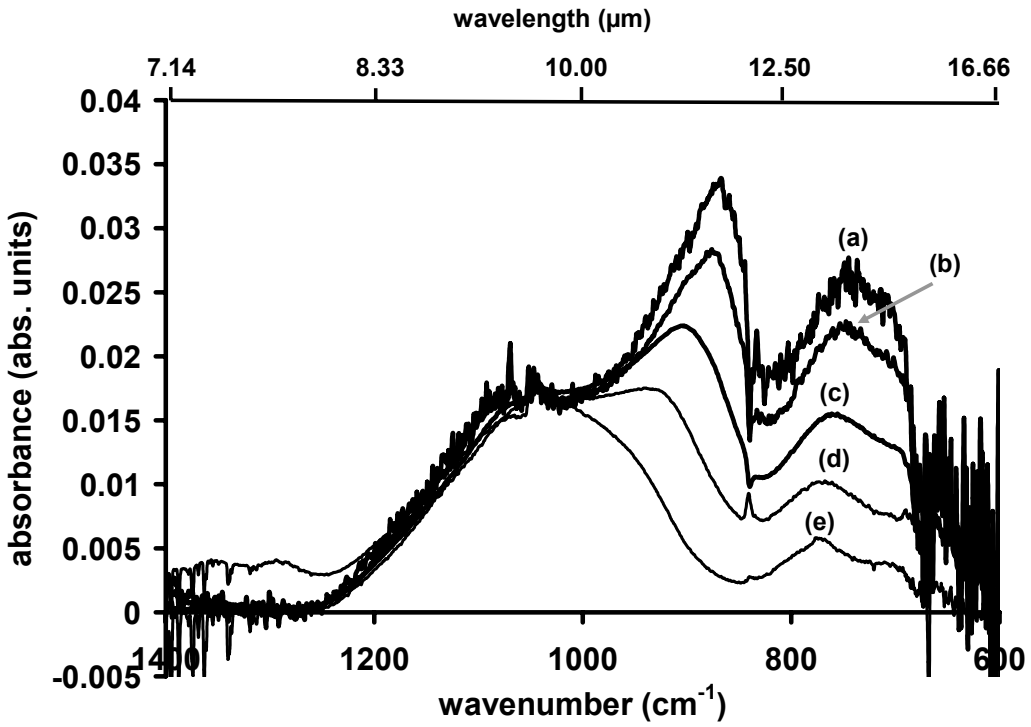

Figure 9.16 Normalized (at 1040 cm^{-1}) ATR spectra of soda lime glass spheres with diameters of: 400 µm (a), 112 µm (b), 25 µm (c), 4 µm (d) and 1 µm (e).

It appears that normalization at a frequency of 1040 cm^{-1} is a valid operation, as the higher frequency component of the recorded spectra appears very similar for all particle diameters.

Assuming band assignments (Table 9.3) are correct, a monotonously decreasing intensity of the TO mode of the non bridging oxygen (NBO) vibrational band (~870 cm^{-1} for the 400 µm spheres) with decreasing particle size is observable. It should be mentioned that due to the normalization of the spectra this decrease is to be recognized as a relative change in absorption in relation to the other absorption features. The initial strong intensity of NBO vibrational band can be explained by the high content of cations

the glass composition (Na^{+}>10%, Ca^{2+}~10%, Fe^{3+}~0.5%), which strongly promote the abundance of NBO sites [265-267]. The cations provoke the disruption of the amorphous network due to the breaking of some of the Si–O–Si bonds leading to the formation of nonbridging oxygen groups (Si–O–NBO). According to the spectra shown in Figure 9.16, the number of NBO sites is increasing together with particle size, which is expressed by the increasing intensity of the respective absorption band in respect to the other spectral features. In their work, Serra et al. [267] show that similar effects can be observed due the influence of cation / SiO_2 ratio in glasses as shown in Figure 9.17.

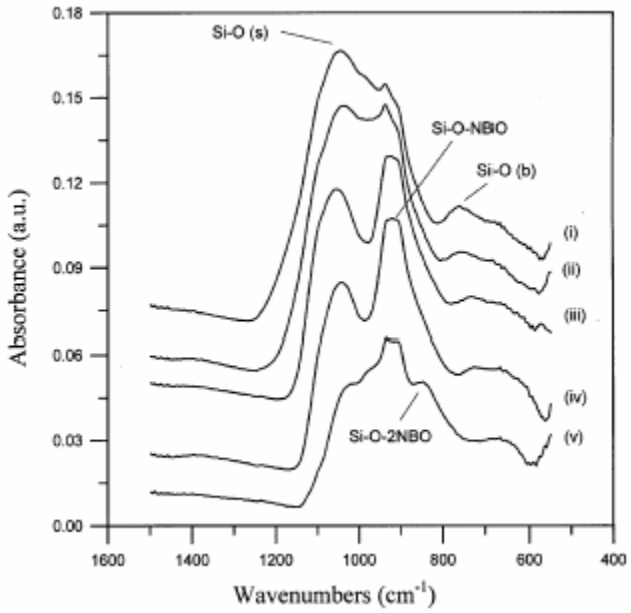

Figure 9.17 FTIR spectra of Na_2O–CaO–P_2O_5–K_2O–MgO–B_2O_3–SiO_2 glasses with different SiO_2 content: (i) 66%, (ii) 59%, (iii) 55%, (iv) 50% and (v) 42% [267].

It can be seen that a decreasing SiO_2 content goes along with a strong rise of the Si-O-NBO feature around 900 cm^{-1}.This indicates that the results shown in Figure 9.16 do not necessarily prove a particle size related effect, but could also arise from a systematic - particle size related - change in composition of the glass spheres during the

manufacturing process. In order to clarify such assumptions a chemical analysis of the soda lime glass spheres is suggested for future studies.

9.2.5. Polarized Light

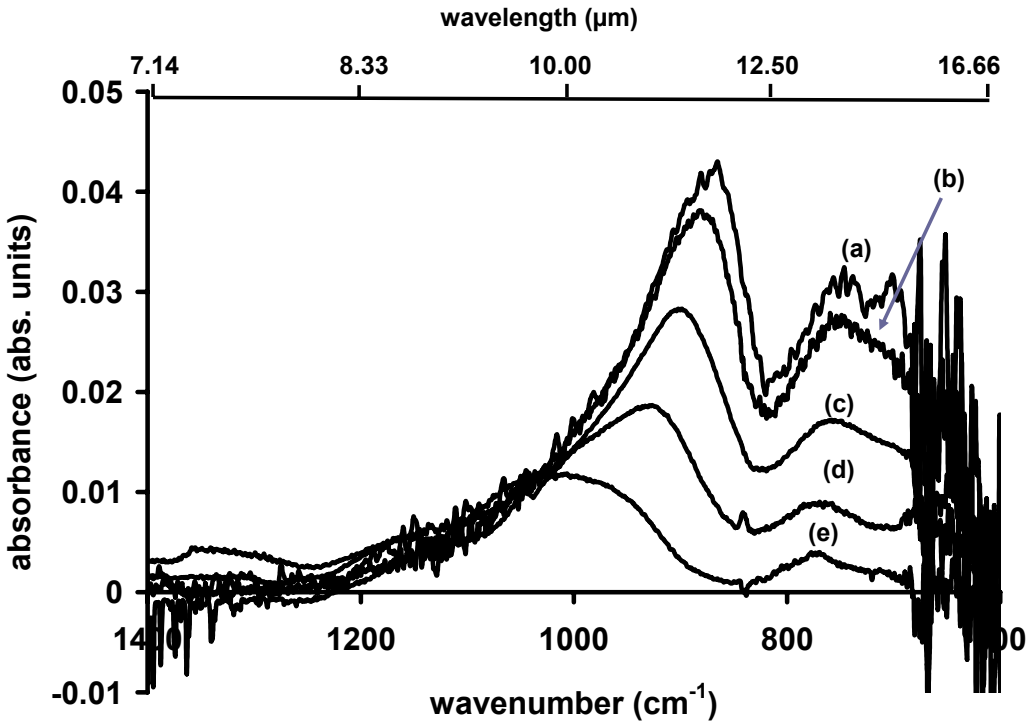

Figure 9.18 S-polarized ATR spectra of soda lime glass spheres with different diameters: 400 μm (a), 112 μm (b), 25 μm (c), 4 μm (d) and 1 μm (e). Data has been normalized in intensity.

Figure 9.18 shows the ATR spectra of all sizes of the glass spheres under s-polarized illumination. Theoretically, only TO modes should be observable. At least three modes are immediately noticeable:

- ~750 cm^{-1} (symmetric Si-O-Si stretch vibration)
- ~ 880 – 940 cm^{-1} (shifting, decaying NBO stretch vibration)

- ~1050 cm^{-1} (asymmetric Si-O-Si stretch vibration)

These band assignments are based on the considerations discussed earlier in chapter 9.2.3 (page 169).

The most obvious trend in these spectra can be attributed to the strong decrease of the intensity of the NBO stretch vibrational band with decreasing particle size. This mode expresses a strong apparent blue shift as well, exclusively based on the evaluation of the shift of the maximum peak position shifting from ~ 880 to 940 cm^{-1} for the examined particle sizes. However, the substantial shift of the peak maximum over almost 80 wavenumbers is at least partly promoted due to the strong overlaps of the absorption features in the spectra.

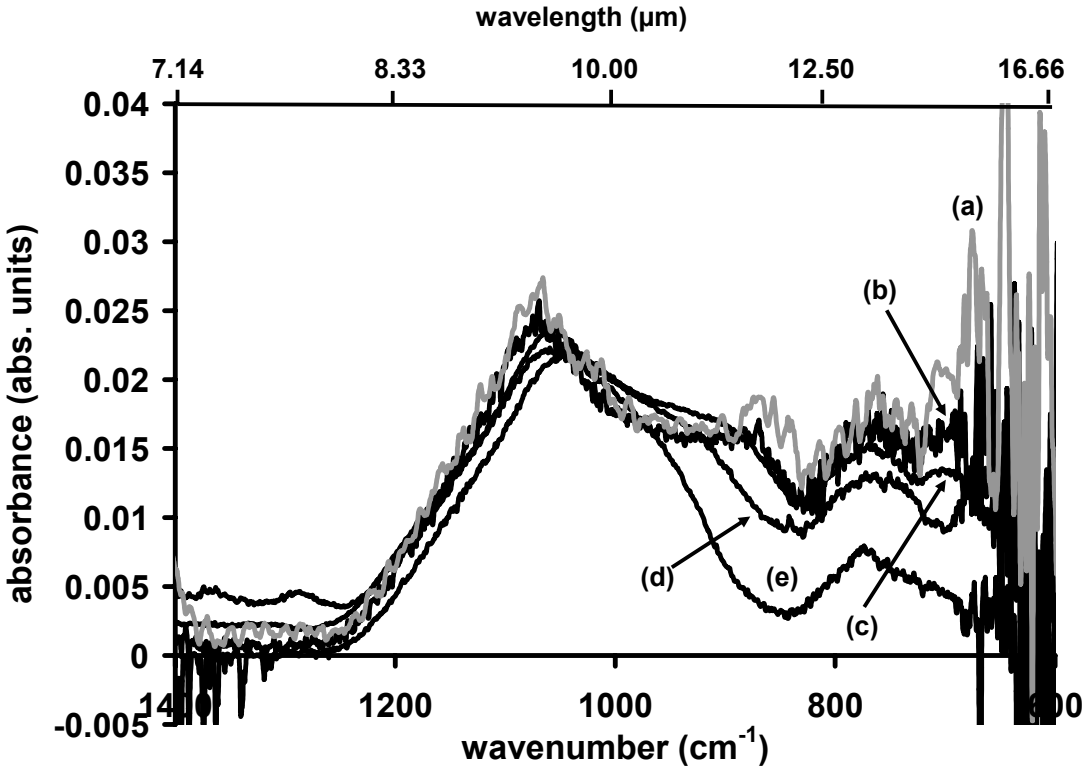

Figure 9.19 P-polarized ATR spectra of soda lime glass spheres with different diameters: 400 µm (a), 112 µm (b), 25 µm (c), 4 µm (d) and 1 µm (e).

Figure 9.19 shows the ATR spectra of all sizes of the glass spheres under p-polarized illumination. Theoretically, LO modes should be strongly expressed and TO modes should be visible to a lower extent. It is known that LO modes only express minor dependency on peak position and peak width upon varying layer thickness [see e.g. 254,257]. The experimental data corroborate these assumptions: the major absorption feature shifts by approx. 15 cm^{-1} from ~1050 to 1065 cm^{-1} with increasing particle diameter. The changes in the spectra in the longer wavelength region are attributed to also expressed TO modes of the glass spheres. Usually, band intensity and peak widths of LO modes show strong dependency on the angle of incidence e.g. [252**Error! Bookmark not defined.**]. However, with the present ATR setup this parameter is in principle fixed and cannot be reproduced in the course of these experiments.

9.2.6. Conclusions

ATR measurements of mono-disperse soda lime glass spheres lead to the following conclusions

- Wetting and drying studies of a sample consisting of glass spheres of only one particle size showed no differences in the pristine and dried spectrum. This circumstance is another indication that the different spectral properties of disturbed and pristine soils are a particle size related effect.
- Particle size dependent ATR spectra of the soda lime glass spheres showed significant changes in the relative band intensities of the absorption features. After band assignment it could be concluded that the intensity of the non bridgin oxygen stretch vibration band (~860 cm^{-1}) decreased with decreasing sphere diameters in respect to the other major absorption features.

- Experiments under s- and p-polarized illuminations corroborated the proposed band assignments and effects.
- The present setup with a broad angle distribution of the incident light in respect to the ATR element surface is suitable for showing general trends, but represents a problem for detailed evaluation of the spectra as LO-TO mode splitting effects are strongly dependent on the angle of incidence.
- For quantitative results it is recommended to modify the sample illumination technique in order to be able to address different, defined angles of incidence.

10. Conclusion and Outlook

10.1. Are ATR spectroscopic Studies suitable as supporting Method for Remote Sensing?

It has been shown that Mid-IR-ATR spectroscopy provides a reliable methodology for fundamental spectroscopic studies of quartz sand, which potentially benefit interpretation of data provided by the remote sensing community. Besides the already established differences in spectral contrast of disturbed and undisturbed soil, a strong spectral shift for quartz samples of the maximum of the main absorption feature at 1090 cm^{-1} could be observed. When probed with s- or p-polarized light, the sample showed strong LO-TO mode splitting, which is most likely related to the Berreman effect. These findings advance the variety of spectral characteristics useful to the detection of disturbed soils (i.e. possible landmine sites) with mid-infrared imaging systems. The wetting and drying

studies also reveal that the main reason for spectral differences of pristine and disturbed soils eventually relates to changes of the particle size distribution of the sample due to rearrangement of ultrafine particles facilitated by water.

These preliminary results strongly propose the potential of ATR spectroscopic methods for the investigation of signatures derived from remote sensing. Not only the difference in spectral contrast of disturbed and pristine soil could be reproduced, also the assumption of particle size related origin of this phenomenon could be shown. Furthermore, derived from the presented results so far unnoticed spectral shifts in spectra of disturbed and pristine samples was observed clearly, being possibly an exploitable feature for remote disturbed soil detection.

A Mid-IR-ATR study of mono-disperse soda lime glass spheres with diameters in the range from 1 to 400 µm subsidized the findings of the quartz measurements and due to the more defined sample led to deeper insight of the reasons for spectral changes in relation for the disturbed and undisturbed soil problem.

Wetting and drying studies of a sample consisting of glass spheres of only one particle size showed no differences in the pristine and dried spectrum., which is in high agreement with the assumption that different spectral properties of disturbed and pristine soils can is related to particle size. Furthermore, in the comparison of ATR spectra of different mono-disperse glass spheres, relative band intensity shifts were observed, another potentially interesting finding for remote sensing of disturbed soils. The results showed a relative intensity change of the TO non bridging oxygen stretch vibrational band in respect to other major bands in the spectra. This vibrational mode becomes less pronounced with decreasing sphere diameters. Measurements performed under s- and p-polarized illumination of the sample corroborated these findings. However, in order to perform quantitative data evaluation, a modified setup is recommended where the angle of incidence of the IR radiation can be chosen.

In order to render these results useful for remote sensing purposes fundamental experimental studies seem necessary, especially the investigation of mono-disperse quartz samples are needed, before profound quantification and model building for observed effects such as LO-TO mode splitting and absorption intensities can be performed.

For further studies an environmental chamber has been developed, which is compatible with the laboratory based ATR setup. It allows to control relevant parameters such as temperature and humidity, which potentially influence the spectral behavior of samples in the field (see Appendix, Figure 10.1).

Additionally, it is suggested to perform diffuse reflectance or emissivity measurements applying the same wetting and drying cycles with similar samples in order to ensure that the presented ATR measurements are in coherence with data derived from remote sensing.

APPENDIX

Instruments and Major Components

Instruments, components	Brand, specification etc.	Company
FT-IR spectrometer	Bruker Vektor 22 Bruker EQUINOX 55	Bruker Optics Inc (Billerica, MA, USA)
Vertical ATR Module	Standard Mirror Bench	Specac Inc. (Smyrna, GA, USA)
Horizontal ATR Module	Standard Mirror Bench	Specac Inc. (Smyrna, GA, USA)
MCT detector	D316-type	Infrared Associates (Stuart, FL, USA)
ZnSe ATR elements	50*20*2 mm, 45°, trapezoid	Macrooptica Ltd. (Moscow, Russia)
ZnSe ATR elements	72*10*6 mm, 45°, trapezoid	Macrooptica Ltd. (Moscow, Russia)
Breadboard	Aluminium, 30*60*1.27 cm	Thorlabs (North Newton, NJ, USA)
High precision piston pump 10-port selection valve 6-port injection valve	Cavro XL3000, vol. 25,000 µL Valco C25Z-3180EMH Valco C22Z-3186EH	Global FIA Inc (Fox Island, WA, USA)
Profilometer	Dektak^3	Veeco/Sloan Technology (Santa Barbara, CA, USA)
Spin-coater	WS-400A-6NPP-LITE	Laurell Technologies Corporation (North Wales, PA, USA)

Visual Basic Script for Modeling Diffusion via Fieldson and Barbari (Chapter 3.4.2)

```
Private Function CalcF(n As Long, _
l As Double) As Double
CalcF = ((2 * n + 1) * PI) / (2 * l)
End Function

Private Function CalcG(D As Double, _
n As Long, _
l As Double, _
t As Long) As Double

CalcG = (-D * (2 * n + 1) ^ 2 * PI ^ 2 * t) / (4 * (l ^ 2))

End Function

Private Function CalculateA(n As Long, t As Long) As Double

Dim dSum As Double
Dim l As Long

For l = 0 To n
dSum = dSum + (Exp(CalcG(mdD, l, mdL, t)) * (CalcF(l, mdL) * Exp((-2 * mdL) / mdDp) + (-1) ^ l *
(2 / mdDp))) / ((2 * l + 1) * (4 / (mdDp ^ 2) + (CalcF(l, mdL)) ^ 2))

Next

CalculateA = 1 - (8 / (PI * mdDp * (1 - Exp((-2 * mdL) / mdDp)))) * dSum

End Function
```

The Environmental Chamber

For investigating the effects of varying temperature and humidity on ATR spectra of quartz (and other minerals) a small environmental chamber (volume approximately 500mL) has been developed for future use (Figure 10.1).

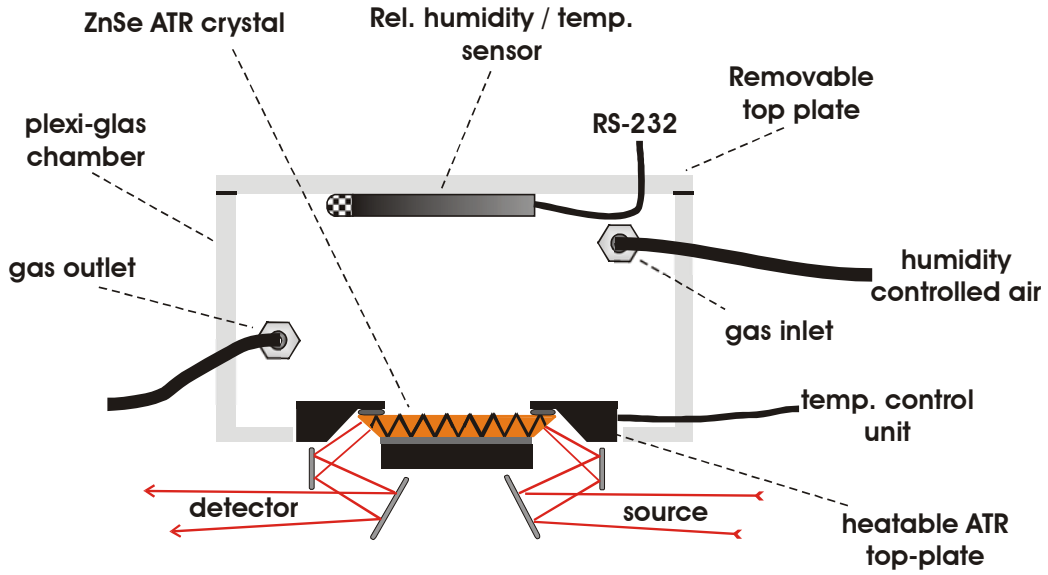

Figure 10.1 Schematic of the environmental chamber developed for temperature and humidity studies on ATR measurements for quartz and other minerals.

Major parts are labeled in the schematic picture, a brief description of the components is as follows"

- Humidity and temperature validation: Omega, OM-CP-RHTEMP101 is a miniaturized RH/T sensor that can be used as a datalogger
- Heatable ATR-setup: Specac Inc. 11155, allows controlled heating (constant temperatures and temperature ramps) of the ZnSe crystal from room temperature up to 150 °C via an external temperature controller.

- Humidity controlled air: with the help of a relative humidity controlling system from (Sable Syste,s, DG-1) allows to introduce an airflow of controlled humidity (working range: approx. 10 to 90% RH, accuracy +/- 1%) or drive humidity ramps / cycles.
- housing: this first generation environmental chamber consists of an easy accessible (sample introduction, disturbing...) plexi-glass material, which is glued together and provides sufficient sealing to the outside.

The environmental chamber is fully assembled, is being tested for stability and general performance.

REFERENCES

1 J. E. McFee, H. T. Ripley *Detection of buried landmines using a casi hyperspectral image*" Detection and Remediation Technologies for Mines and Minelike Targets II, ed A. C. Dubey, SPIE, 1997, Vol **2079**, 738-749.

2 P. G. Lucey, T. J. Williams, M. Winter, *Two years of operations of AHI: a LWIR hyperspectral imager*, Infrared Imaging Systems: Design, Modeling, and Testing XI, ed. G. Holst, SPIE, 2000, Vol. **4030**, 31-40

3 C. A. DiMarzio, T. Vo-Dinh, H. E. Scott, *Some Approaches to Infrared Spectroscopy for Detection of Buried Objects*, Detection and Remediation Technologies for Mines and Minelike Targets III, eds A. C. Dubey, J. T. Broach, SPIE, 1998, Vol **3392**, 158-166.

4 H. T. Haskett, R. Rupp, T. Moore *Quantitative performance of buried mine hyperspectral reflectance signatures (.35-2.5µm) in various soils* Detection and Remediation Technologies for Mines and Minelike Targets V, eds A. C. Dubey, J. F. Harvey, J. T. Broach, R. E. Dugan, SPIE, 2000, Vol **4038**, 886-899.

5 J. R. Johnson, P. G. Lucey, K. A. Horton, E. M. Winter, "Infrared Measurements of Pristine and Disturbed Soils 1. Spectral Contras Differences between Field and Laboratory Data", Remote Sensing of the Environment, 1998, **64**, 34–46.

6 L. Ritter, K. Solomon, P. Sibley, K. Hal, P. Keen, G. Mattu, B. Linton, *Sources, Pathways, and relative risks of contaminants in surface water and groundwater: a perpective prepared for the walkerton inquiry*, Journal of Toxicology and Environmental Health Part A, 2002, **65(1)**, 1-142

7 P. Williams, L. Benton, J. Warmerdam, P. Sheehan, *Comparative risk analysis of six volatile orga*nic *compounds in california drinking water*, Environmental Science and Technology*,* 2002, **36(22)**, 4721–4728.

8 P. T. C. Harrison, *Health effects of environmental chemicals,* R. M. Harrison (Editor) Pollution: Causes, Effects and Control, (4th edition), 2001, 500-523.

9 J. H. Sevigny, M. J. Tindal, G. L. Robins, W. Staudt, L. Serbin, *Importance of different volatile petroleum hydrocarbon fractions in human risk assessment*, Human and Ecological Risk Assesment 2003, **9 (4),** 987-1001.

10 B. C. J. Zoeteman, K. Harmsen, J. B. H. J. Linders, C. F. H. Morra, W. Slooff, *Persistent organic pollutants in river water and groundwater of the Netherlands,* Chemosphere 1980, **9(4)**, 231-249.

11 W. Giger, C. Schaffner, *Ground water pollution by volatile organic chemicals Studies in Environmnental*, Science, 1981, **17**, 517-522.

12 S. Ramamoorthy, S. Ramamoorthy, *Chlorinated Organic Compounds in the Environment,* Lewis, 1997, Boca Raton, Fla.

13 T. Trouwbourst, *Groundwater pollution by volatile halogenated hydrocarbons; sources of pollution and methods to estimate their relevance*, Science Total Environment 1981, **21**, 41-46.

14 P. J. Squillace, M. J. Moran, W. W. Lapham, *Volatile organic compounds in untreated ambient groundwater of the united states, 1985-1995*, Environmental Science and Technology, 1999, **33(23)**, 4176-4187.

15 P. J. Squillace, J. C. Scott, M. J. Moran, B. T. Nolan, D. W. Kolpin, *VOCs, pesticides, nitrate, and their mixtures in groundwater used for drinking water in the united states*, Environmental Science and Technology 2002, **36(9)**, 1923-1930.

16 Permanent Website: http://www.atsdr.cdc.gov/clist.html.

17 EPA 811-F-95-004-T, *Contaminant Specific Fact Sheets - Volatile Organic Chemicals*, Oct 1995.

18 EPA 816-R-99-006, *A Review of Contaminant Occurrence in Public Water Systems*, Nov 1999.

19 R. Krska, E. Rosenberg, K. Taga, R. Kellner, A. Messica, A. Katzir, *Polymer coated silver halide infrared fibers as sensing devices for chlorinated hydrocarbons in water,* Appl. Phys. Lett., 1992, **61(15)**, 1778-1780.

20 E. Martinez, S. Lacorte, I. Lobet, P. Viana, D. Barcelo, *Multicomponent analysis of volatile organic compounds in water by automated purge and trap coupled to gas chromatography-mass spectrometry*, Journal of Chromatography A, 2002, **959(1-2)**, 181–190.

21 M. Rosell, S. Lacorte, A. Ginebreda, D. Barcelo, *Simultaneous determination of methyl tert.-butyl ether and its degradation products, other gasoline oxygenates and benzene, toluene, ethylbenzene and xylenes in Catalonian groundwater by purge-and-trap-gas chromatography-mass spectrometry*, Journal of Chromatography A, 2003 ,**1007(1-2)**, 209-210 .

22 M. C. Hennion, *Solid-phase extraction: method development, sorbents, and coupling with liquid chromatography*, Journal of Chromatography A, 1999, **856(1-2)**, 3–54

23 I. Liska, *Fifty years of solid-phase extraction in water analysis - historical development and overview*, Journal of Chromatography A, 2000, **885(1-2)**, 3–16.

24 A. M. Dietrich, W. F. daCosta, *Measurement and monitoring of pollutants. Chemical species,* Water Environment Research, 1997, **69(4)**, 391-403.

25 H. C. Hennion, V. Pichon, D. Barcelo, *Surface water analysis (trace-organic contaminants) and EC regulations*, Trends in Analytical Chemistry, 1994,**13(9)**, 361-372.

26 W. Goepel, J. Hesse, J. N. Zemel (Editors), *Sensors*, VCH, Weinheim, Germany 1995.

27 R. F. Taylor, J. S. Schultz (Editors) *Handbook of Chemical and Biological Sensors,* Institute of Physics, Bristol, UK, 1996.

28 B. R.Eggins, Chemical Sensors and Biosensors, John Wiley & Sons, West Sussex, UK 2002.

29 J. Janata; A. Bezegh *Chemical sensors*. Analytical Chemistry, 1988, **60(12)**, 62R-74R

30 J. Janata, *Chemical sensors*, Analytical Chemistry, 1990, **62(12)**, 33R-44R

31 J. Janata, *Chemical sensors*, Analytical Chemistry, 1992, **64(12)**, 196R-219R

32 J. Janata, M. Josowicz, D. M. DeVaney, *Chemical sensors*, Analytical Chemistry, 1994, **66(12)**, 207R-228R

33 J. Janata, M. Josowicz, P. Vanysek, D. M. DeVaney, *Chemical Sensors*, Analytical Chemistry, 1998, **70(12)**, 179R – 208R.

34 J. Janata, *Centennial retrospective on chemical sensors*, Analytical Chemistry, 2001, **73(5)**, 150A-153A

35 O. S. Wolfbeis (Editor), *Fiber Optic Chemical Sensors and Biosensors*, Vol. 1, CRC Press, Boca Raton, Fl, 1991.

36 G. Holst, B. Mizaikoff, *Optical fiber sensors for environmental applications. Handbook of fiber optic sensing technology: principles and application*, J. M. Lopez-Higuerra (Editor), John Wiley & Sons Ltd, 2002, 729-755.

37 R. Krska, K. Taga, R. Kellner, *New IR fiber-optic chemical sensor for in-situ measurements of chlorinated hydrocarbons in water*, Applied Spectroscopy, 1993, **47(9)**, 1484-1487.

38 B. Mizaikoff, R. Goebel, R. Krska, K. Taga, R. Kellner, M. Tacke, A. Katzir, *Infrared fiber-optical chemical sensors with reactive surface coatings*, Sensors and Actuators B, 1995, **29(1-3)**, 58-63.

39 J. E. Walsh, B. D. MacCraith, M. Meaney, J. G. Vos, F. Regan, A. Lancia, S. Artjushenko, *Sensing of chlorinated hydrocarbons and pesticides in water using polymer coated mid-infrared optical* fibers, Analyst, 1996, **121(6)**, 789-792.

40 G. Schwotzer, I. Latka, H. Lehmann, R. Willsch, *Optical sensing of hydrocarbons in air or in water using UV absorption in the evanescent field of fibers*, Sensors and Actuators B, 1997, **38(1-3)**, 150-153.

41 J. Buerck, S. Roth, K. Kraemer, M. Scholz, S. Klaas, *Application of a fiber-optic NIR-EFA sensor system for in-situ monitoring of aromatic hydrocarbons in contaminated groundwater*, Journal of Hazardous Materials, 2001, **83(1-2)**, 11-28.

42 J. Buerck, M. Schlagenhof, S. Roth, H. Mahieu, *Kinetic evaluation method of SPME-NIR measurements of analytes with long equilibration time Field*, Analytical Chemistry and Technology, 2001, **5(3)**, 131-142.

43 C. Phillips, M. Jakusch, H. Steiner, B. Mizaikoff, A. G. Fedorov, *Model-based optimal design of polymer-coated chemical sensors*, Analytical Chemistry, 2003, **75(5)**, 1106-1115.

44 O. S. Wolfbeis, *Fiber-optic chemical sensors and biose*nsors, Analytical Chemistry 2000, **72(12)**, 81R-89R.

45 O. S. Wolfbeis, *Fiber-optic chemical sensors and biosensors*, Analytical Chemistry, 2002, **74(12)**, 2663-2678.

46 B. Mizaikoff, *Mid-IR fiber-optic sensors*, Analytical Chemistry, 2003, **75(11)**, 258A-267A.

47 F. Baldini, S. Bracci, *Polymers for optical fiber sensors Polymer*, Sensors and Actuators, 2000, 91-107.

48 V. Acha, M. Meurens, H. Naveau, S. N. Agathos, *ATR-FTIR sensor development for continous on-line monitoring of chlorinated aliphatic hydrocarbons in a fixed-bed bioreactor*, Biotechnology and Bioengineering, 2000, **68(5)**, 473-487.

49 J. Buerck, M. Mensch, K. Kraemer, *Field Experiments with a portable fiber-optic sensor system for monitoring hydrocarbons in water Field*, Analytical Chemistry and Technology, 1998, **2(4)**, 205-219.

50 J. Buerck, S. Roth, K. Kraemer, H. Mathieu, *OTDR fiber-optical chemical sensor system for detection and location of hydrocarbon leakage*, Journal of Hazardous Materials, 2003, **102(1)**, 13-28.

51 B. L. Wittkamp, D. C. Tilotta, *Determination of BTEX compounds in water by solid-phase microextraction and Raman spectroscopy*, Analytical Chemistry, 1995, **67(3)** 600-605.

52 B. L. Wittkamp, S. B. Hawthorne, *Determination of aromatic compounds in water by solid phase microextraction and ultraviolet absorption spectroscopy. 1. Methodology*, Analytical Chemistry 1997, **69(6)**, 1197-1203.

53 S. A. Merschman, S. H. Lubbad, D. C. Tillota, *Poly(dimethylsiloxane) films as sorbents for solid-phase microextraction coupled with infrared spectroscopy*, Journal of Chromatography A, 1998, **829(1+2)**, 377-384.

54 D. C. Stahl, D. C. Tilotta, *Partition infrared method for total gasoline range organics in water based on solid phase microex*traction, Environmental Science and Technology, 1999, **33(5)**, 814-819.

55 M. Lamotte, P. Fornier de Violet, P. Garrigues, M. Hardy, *Evaluation of the possibility of detecting benzenic pollutants by direct spectrophotometry on PDMS solid absorbent*, Analytical and Bioanalytical Chemistry, 2002, **372(1)**, 169-173.

56 J. Pawliszyn, *Solid phase microextraction – Theory and practice*, (1st ed.) Wiley, New york, NY, 1997.

57 J. Olsson, G. Traegardh, F. Lipnizki, *The influence of permeant and membrane properties on mass transfer in pervoration of volatile organic compounds from dilute aqueous solutions Separation*, Sciences and Technology, 2002, **37(6)**, 1199-1223.

58 D. M. Haaland, D. K. Melgaard, *New prediction-augmented classical least-squares (PACLS) methods: application to unmodeled interferents*, Applied Specroscopy, 2000, **54(9)**, 1303-1312.

59 F. Vogt, B. Mizaikoff, *Secured PCR (sPCR) for detection and correction of PCR calibration model failures induced by uncalibrated spectral features, Journal of Chemometrics*, 2003, **17(4)**, 225-236.

60 F. Vogt, B. Mizaikoff, *Introduction and application of secured principal component regression for analysis of uncalibrated spectral features in optical spectroscopy and chemical sensing*, Analytical Chemistry, 2003, **75(13)**, 3050-3058.

61 J. Einax, H. W. Zwanziger, S. Geiss, *Chemometrics in Environmental Analysis*, VCH, Weinheim Germany, 1997.

62 K. R. Beebe, R. J. Pell, M. B. Seasholtz, *Chemometrics: A practical guide*, Wiley, New York, N.Y., 1998.

63 R. G. Brereton, *Chemometrics: Data Analysis for the Laboratory and Chemical Plant*, John Wiley & Sons, New York, N.Y. 2003.

64 D. M. Haaland, E. V. Thomas, *Partial least-squares methods for spectral analysis. 1. Relation to other quantitative calibration methods and the extraction of qualitative information*, Analytical Chemistry 1988, **60 (11)**, 1193-1202.

65 E. V. Thomas, D. M. Haaland, *Comparison of multivariate calibration methods for quantitative spectral analysis*, Analytical Chemistry, 1990, **62 (10)**, 1091-1099.

66 D. M. Haaland, L. Han, T. M. Niemczyk, *Use of CLS to understand PLS IR calibration for trace detection of organic molecules in water*, Applied Spectroscopy 1999, **53(4)**, 390-395.

67 M. Blanco, J. Coello, H. Iturriaga, S. Maspoch, J. Pages, *NIR calibration in nonlinear systems: different PLS approaches and artificial neural networks*, Chemometrics and Intelligent Laboratory Systems, 2000, **50(1)**, 75-82.

68 P. C. Jurs, G. A. Bakken, H. E. McClelland, *Computational methods for the analysis of chemical sensor array data from volatile analytes*, Chemical Reviews, 2000, **100(7)**, 2649-2678.

69 D. M. Haaland, *Synthetic multivariate models to accommodate unmodeled interfering spectral components during qualitative spectral analysis*, Applied Spectroscopy, 2000, **54(2)**, 246-254.

70 R. A. S. Lapa, J. L. F. C. Lima, B. F. Reis, J. L. M. Santos, E. A. G. Zagatto, *Multi-pumping in flow analysis: concepts, instrumentation, potentialities*, Analytica Chimica Acta, 2002, **466(1**), 125-132.

71 F. Albertus, B. Horstkotte, A. Cladera, V. Cerda, *A robust multisyringe system for process flow analysis. Part I. On-line dilution and single point titration of protolytes*, Analyst, 1999, **124(9)**, 1373-1381.

72 E. Richards, C. Bessant, S. Saini, *A liquid handling system for the automated acquisition of data for training, validating and testing calibration models*, Sensors and Actuators B 2003, **88(2)**, 149-154.

73 F. Vogt, M. Karlowatz, M. Jakusch, B. Mizaikoff, *The automated sample preparation system MixMaster for investigation of volatile organic compounds with mid-infrared evanescent wave spectroscopy*, Analyst, 2003, **128(4)**, 397-403.

74 F. R. P. Rocha, B. F. Reis, E. A. G. Zagatto, J. L. F. C. Lima, R. A. S. Lapa, J. L. M. Santos, *Multicommunication in flow analysis: concepts, applications and trends*, Analytica Chimica Acta, 2002, **468(1)**, 119-131.

75 R. M. Silverstein, G. C. Bassler, T. C. Morill, *Spectrometric Identification of Organic Compounds*, John Wiley and Sons, New York, NY, 1981.

76 F. Vogt, M. Tacke, M. Jakusch, B. Mizaikoff, *A UV spectroscopic method for monitoring aromatic hydrocarbons dissolved in water*, Analytica Chimica Acta, 2000, **422(2)**, 187-198.

77 F. Vogt, M. Tacke, W. Bohmer, *Selective measurement of aromatic hydrocarbons in water by use of UV derivative spectroscopy*, Spectroscopy Europe, 1999, **11(5)**, 12,14,16,18.

78 E. Huber, M. Frost, *Light scattering by small particles Aqua*, 1988, **47(2)**, 87-94.

79 K. Sturmwohrer, N. Matsche, S. Winkler, *Influence of changes of the wastewater composition on the applicability of UV-absorption measurements at combined sewer overflows Water*, Science and Technology, 2003, **47(2)**, 73-78.

80 G. Langergraber, N. Fleischmann, F. Hofstadter, *A multivariate calibration procedure for UV/VIS spectrometric quantification of organic matter and nitrate in wastewater*, Water Science and Technology, 2003, **47(2)**, 63-71.

81 M. D. DeGrandpre, L. W. Burgess, *Long path fiber-optic sensor for evanescent field absorbance measurements*, Analytical Chemistry, 1988, **60(23)**, 2582-2586.

82 S. A. Mershman, D. C. Tilotta, *Fiber-optic sensor for aromatic compounds in water based on solid-phase microextraction and ultraviolet evanescent wave absorption spectroscopy*, Applied Spectroscopy, 1998, **52(1)**, 106-111.

83 T. Miya, Y. Terunuma, T. Hosaka, T. Miyashita, *Ultimate low-loss single-mode fiber at 1.55 μm*, Electronics Letters 1979, **15(4)**, 106-108.

84 B. Mizaikoff, *Infrared optical sensors for water quality monitoring Water*, Science and Technology, 2003, **47(2)**, 35-42.

85 M. D. DeGrandpre, L. W. Burgess, *A fiber-optic FT-NIR evanescent field absorbance sensor*, Applied Spectroscopy, 1990, **44(2)**, 273-279.

86 J. Buerck, J.-P. Conzen, B. Beckhaus, H.-J. Ache, *Fiber-optic evanescent wave sensor for in-situ determination of non-polar organic compounds in water*, Sensors and Actuators B, 1994, **18(1-3)**, 291-295.

87 E. Sensfelder, J. Buerck, H.-J. Ache, *Determination of hydrocarbons in water by evanescent wave absorption spectroscopy in the near-infrared region*, Fresenius' Journal of Analytical Chemistry, 1996, **354(7-8)**, 848-851.

88 D. S. Blair, L. W. Burgess, A. M. Brodsky, *Evanescent fiber-optic chemical sensor for monitoring volatile organic compounds in water*, Analytical Chemistry, 1997, **69(13)**, 2238-2246.

89 D. S. Blair, J. Bando, *Quantitative monitoring of volatile organic compounds in water using an evanescent fiber optic chemical sensor*, Environmental Science and Technology, 1998, **32(2)**, 294-298.

90 G. L. Klunder, R. E. Russo, *Core-based intrinsic fiber-optic absorption sensor for the detection of volatile organic compounds*, Applied Spectroscopy 1995, **49(3)**, 379-385.

91 J. S. Sanghera, I. D. Aggarwal, *Infrared fiber optics*. Boca Raton: CRC Press, 1998.

92 B. Mizaikoff, B., Lendl, *Handbook of Vibrational Spectroscopy*, J.M. Chalmers, P.R. Griffiths (Editors), John Wiley & Sons, Ltd, 2002,1560-1573.

93 M. Jakusch, B. Mizaikoff, R. Kellner, A. Katzir, *Towards a remote IR fiber-optic sensor system for the determination of chlorinated hydrocarbons in water*, Sensors and Actuators B, 1997, **38(1-3)**, 83-87.

94 F. Regan, B. D. MacCraith, J. E. Walsh, K. O'Dwyer, J. G. Vos, M. Meaney, *Novel Teflon-coated optical fibers for TCE determination using FTIR spectroscopy*, Vibrational Spectroscopy, 1997, **14(2)**, 239-246.

95 H. Steiner, M. Jakusch, M. Kraft, M. Karlowatz, T. Baumann, R. Niessner, W. Konz, A. Brandenburg, K. Michel, C. Boussard-Pledel, B. Bureau, J.Lucas, Y. Reichlin, A. Katzir, N. Fleischmann, K. Staubmann, R. Allabashi, J. M. Bayona, B. Mizaikoff, *In-situ sensing of volatile organic compounds in groundwater: First field tests of a mid-infrared fiber-optic sensing system*, Applied Spectroscopy, 2003, **57(6)**, 607-613.

96 M. Kraft, B. Mizaikoff, *A MID-infrared sensor for monitoring of chlorinated hydrocarbons in the marine environment*, International Journal Environmental Analytical Chemistry, 2000, **78(3-4),** 367–383.

97 M. C. Ertan-Lamontagne, S. R. Lowry, W. R. Seitz, S. A. Tomellini, *Polymer-coated tapered cylindrical ATR elements for sensitive detection of organic solutes in water*, Applied Spectroscopy, 1995, **49(8)**, 1170-1173.

98 R. Howley, B. D. MacCraith, K. Dwyer, H. Masterson, P. Kirwan, P. McLoughlin, *Determination of hydrocarbons using sapphire fibers coated with poly(dimethylsiloxane)*, Applied Spectroscopy, 2003, **57(4)**, 400-406.

99 V. Acha, M. Meurens, H. Naveau, S. N. Agathos, *Detoxification of a mixture of aliphatic chlorinated hydrocarbons in a fixed-bed bioreactor: continuous on-line monitoring via an attenuated total reflection-Fourier transform infrared sensor,* Water Science and Technology, 1999, **40(8)**, 41-47.

100 B. Mizaikoff, *Mid-infrared evanescent wave sensors – a novel approach for subsea monitoring*, Measurement Science and Technology, 1999, **10(12)**, 1185-1194.

101 M. Kraft, M.Jakusch, M. Karlowatz, A. Katzir, B. Mizaikoff, *New frontiers for mid-infrared sensors: Towards deep sea monitoring with a submarine FT-IR sensor system*, Applied Spectroscopy, 2003, **57(6)**, 591-599.

102 T. Beyer, P. Hahn, S. Hartwig, W. Konz, S. Scharring, A. Katzir, H. Steiner, M. Jakusch, M. Kraft, B. Mizaikoff, *Mini spectrometer with silver halide sensor fiber for in-situ detection of chlorinated hydrocarbons*, Sensors and Actuators B, 2003, **90(1-3)**, 319-323.

103 D. L. Heglund, D. C. Tilotta, *Determination of volatile organic compounds in water by solid phase microextraction and infrared spectroscopy*, Environmental Science and Technology, 1996, **30(4)**, 1212-1219.

104 R. Krska, R. Kellner, U. Schiessl, M. Tacke, A. Katzir, *Fiber optic sensor for chlorinated hydrocarbons in water based on infrared fibers and tunable diode lasers*, Applied Physics Letters, 1993, **63(14)**, 1868-1870.

105 J. F. Kastner, M. Tacke, A. Katzir, B. Edl-Mizaikoff, R. Goebel, R. Kellner, *Optimizing the modulation for evanescent-wave analysis with laser diodes (EWALD) for monitoring chlorinated hydrocarbons in water*, Sensors and Actuators, B: Chemical, 1997, **38(1-3)**, 163-170.

106 R. K. Chang, T. E. Furtak (Editors), *Surface-enhanced Raman scattering*, Plenum New York, 1982.

107 J. Corset, J. Aubard, *Special Issue--Surface Enhanced Raman Scattering: New Trends and Applications,* Journal of Raman Spectroscopy, 1998, 29(8), 1-113.

108 S. P. Mulvaney, C. D. Keating, *Raman Spectroscopy*, Analytical Chemistry, 2000, **72(12)**, 145-157. (title missing)

109 D. L. Jeanmaire, R. P. Van Duyne, *Surface Raman spectroelectrochemistry. Part I. Heterocyclic, aromatic, and aliphatic amines adsorbed on the anodized silver electrode*, Journal of Electroanalytical Chemistry and Interfacial Electrochemistry, 1977, **84(1)**, 1-20.

110 T. L. Williams, T. W. Collette, *Environmental applications of Raman spectroscopy to aqueous systems*, Practical Spectroscopy, 2001, **28**, 683-731.

111 T. W. Collette, T. L. Williams, *The role of Raman spectroscopy in the analytical chemistry of potable water*, Journal of Environmental Monitoring, 2002, **4(1)**, 27-34.

112 G. E. Walrafen, J. Stone, *Intensification of spontaneous Raman spectra by use of liquid core optical fibers*, Applied Spectroscopy, 1972, **26(6)**, 585-589.

113 R. Altkorn, E. Koev, A. Gottlieb, *Waveguide capillary cell for low-refractive-index liquids*, Applied Spectroscopy, 1997, **51(10)**, 1554-1558.

114 M. Holtz, P. K. Dasgupta, G. Zhang, *Small-volume Raman spectroscopy with a liquid core waveguide*, Analytical Chemistry, 1999, **71(14)**, 2934-2938.

115 C. M. Stellman, K. J. Ewing, F. Bucholtz, I. D. Aggarwal, *Determination of BTEX contaminants in water via a long-pathlength fiber-optic Raman 'dip-stick'*, Sensors and Actuators B, 1998, **53(3)**, 173-178.

116 S. Tanikkul, J. Jakmunee, M. Rayanakorn, K. Grudpan, B. J. Marquardt, G. M. Gross, B. J. Prazen, L. W. Burgess, G. D. Christian, R. E. Synovec, *Characterization and use of a Raman liquid-core waveguide sensor using preconcentration principles*, Talanta, 2003, **59(4)**, 809-816.

117 K. Carron, L. Peitersen, M. Lewis. *Octadecylthiol-modified surface-enhanced Raman spectroscopy substrates: a new method for the detection of aromatic compounds*, Environmental Science and Technology, 1992, **26(10)**, 1950-1954.

118 K. Mullen, K. Carron, *Adsorption of Chlorinated Ethylenes at 1-Octadecanethiol-Modified Silver Surfaces*, Analytical Chemistry, 1994, **66(4)**, 478-483.

119 B. J. Kennedy, R. Milofsky, K. T. Carron, *Development of a cascade flow cell for dynamic aqueous phase detection using modified SERS substrates*, Analytical Chemistry, 1997, **69(22)**,4708-4715.

120 T. Murphy, H. Schmidt, H.-D. Kronfeldt, *Use of sol-gel techniques in the development of surface-enhanced Raman scattering (SERS) substrates suitable for in-situ detection of chemicals in seawater*, Applied Physics B: Lasers and Optics, 1999, **69(2)**, 147-150.

121 T. Murphy, S. Lucht, H. Schmidt, H.-D. Kronfeldt, *Surface-enhanced Raman scattering (SERS) system for continuous measurements of chemicals in sea-water*, Journal of Raman Spectroscopy, 2000, **31(10)**, 943-948.

122 S. Lucht, T. Murphy, H. Schmidt, H.-D. Kronfeldt, *Optimized recipe for sol-gel-based SERS substrates*, Journal of Raman Spectroscopy, 2000, **31(11)**, 1017-1022.

123 J. H. Richardson, M. E. Ando, *Sub-part-per-trillion detection of polycyclic aromatic hydrocarbons by laser induced molecular fluorescence*, Analytical Chemistry 1977, 49(7), 955-959.

124 S. H. Lieberman, *Direct-push, fluorescene-based sensor systems for in-situ measurement of petroleum hydrocarbons in soils Field*, Analytical Chemistry and Technology, 1998, **2(2)**, 63-73.

125 J. J. S. Rodriguez, C. P. Sanz, *Fluorescence techniques for the determination of polycyclic aromatic hydrocarbons in marine environment: an overview*, Analusis, 2000, **28(8)**, 710-717.

126 D. Patra, *Applications and new developments in fluorescence spectroscopic techniques for the analysis of polycyclic aromatic hydrocarbons*, Applied Spectroscopy Reviews, 2003, **38(2)**, 155-185.

127 D. A. Cremers, L. J. Radziemski, *Laser Plasmas for Chemical Analysis, in Laser Spectroscopy and Its Applications*, L. J. Radziemski, R. W. Solarz, J. A. Paisner (Editors) Marcel Dekker, New York, NY, 1987.

128 J. B. Jeffries, G. A. Raiche, L. E. Jusinski, *Detection of chlorinated hydrocarbons via laser-atomization/laser-induced fluorescence*, Applied Physics B, 1992, **55(1)**, 76-83.

129 L. M. Berman, P. J. Wolf, *Laser-induced breakdown spectroscopy of liquids: aqueous solutions of nickel and chlorinated hydrocarbons*, Applied Spectroscopy 1998, **52(3)**, 438-443.

130 G. C. Guilbault, *Practical Fluorescence*, Marcel Dekker, New York, NY,1973.

131 J. R. Lakowicz (Editor), *Principles of Fluorescence Spectroscopy*, Plenum Pr (2nd edition), 1999.

132 P. Karlitschek, F. Lewitzka, U. Buenting, M. Niederkrueger, G. Marowsky, *Detection of aromatic pollutants in the environment by using UV-laser-induced fluorescence*, Applied Physics B: Lasers and Optics, 1998, **67(4)**, 497-504.

133 J. Bloch, B. Johnson, N. Newbury, J. Germaine, H. Hemond, J. Sinfield, *Field test of a novel microlaser-based probe for in-situ fluorescence sensing of soil contamination*, Applied Spectroscopy, 1998, **52(10)**, 1299-1304.

134 J. Wu Pepper, A. O. Wright, J. E. Kenny, *In-situ measurements of subsurface contaminants with a multi- channel laser-induced fluorescence system*, Spectrochimica Acta, Part A: Molecular and Biomolecular Spectroscopy, 2002, **58(2)**, 317-331.

135 N. J. Harrick, *Internal reflection spectroscopy*, Wiley, New York, 1967.

136 J. Fahrenfort, *Attenuated total reflection. A new principle for the production of useful infrared reflection spectra of organic compounds*, Spectrochim. Acta, 1961, **17**, 698-709.

137 A. W. Snyder, J.D. Love, *Optical Waveguide Theory*, Chapman and Hall, 1983.

138 M. Kraft, *Mid-infrared spectroscopy using optical waveguides in the marine environment*, Dissertation, Vienna University of Technology, Austria, 2000.

139 F. Regan, Meaney, M.; Vos, J. G.; MacCraith, B. D.; Walsh, J. E., *Determination of pesticides in water using ATR-FTIR spectroscopy on PVC/chloroparaffin coatings*, Anal. Chim. Acta, 1996, **334(1-2)**, 85-92.

140 M. Kraft, M. Karlowatz, B. Mizaikoff, R. Stück, M. Steden, M. Ulex, H. Amann, *Sensor head development for mid-infrared fiber-optic underwater sensors,* Measurement Science and Technology, 2002, **13(8)**, 1294-1303.

141 J. Yang, J.-W. Her, *Gas-Assisted IR-ATR Probe for Detection of Volatile Compounds in Aqueous Solutions*, Analytical Chemistry, 1999, **71(9)**, 1773–1779.

142 J. Yang, S.-S. Tsai, *Cooled internal reflection element for infrared chemical sensing of volatile to semi-volatile organic compounds in the headspace of aqueous solutions*, Analytica Chimica Acta, 2002, **462(2)**, 235–244.

143 F. O. Libnau, O. M. Kvalheim, A. A. Christy, J. Toft, *Spectra of water in the near- and mid-infrared region*, Vibrational Spectroscopy, 1994, **7(3)**, 243-254.

144 Z. Zhang M. J. Yang, J. Pawliszyn, *Solid-Phase Microextraction. A Solvent-Free Alternative for Sample Preparation*, Analytical Chemistry, 1994, **66(17)**, 844A-852A.

145 M. Jakusch, B. Mizaikoff, *Selective polymer materials: absolute determination of their sorption properties*, Proc. SPIE Int. Soc. Opt. Eng., 2001, **4205**(Advanced Environmental and Chemical Sensing Technology), 93-98.

146 X. Zhou, M. A. Arnold, *Response Characteristics and Mathematical Modeling for a Nitric Oxide Fiber-Optic Chemical Sensor*, Analytical Chemistry, 1996, **68(10)**, 1748-1754.

147 F. Meriaudeau, T. Downey , A. Wig , A. Passian, M. Buncick, T.L. Ferrell, *Fiber optic sensor based on gold island plasmon resonance*, Sensors and Actuators B, 1999 , **54**, 106 – 117.

148 Y. Chen, T.-C. Tan, *Modeling and experimental study of the transient behavior of plant tissue sensors in sensing dopamine*, Chemical Engineering Science, 1996, **51(7)**, 1027-1042.

149 S. Astié, A. M. Gué, E. Scheid, L. Lescouzères, A. Cassagnes, *Optimization of an integrated SnO_2 gas sensor using a FEM simulator*, Sensors and Actuators A,1998, **69(3)**, 205-211.

150 T. Erbey-Gruz, *Transport Phenomena in Aqueous Solutions*, Wiley: New York, 1974.

151 J. Brandup, E. H. Immergut, *Polymer Handbook*, 3rd ed.; John Wiley & Sons: New York, 1989.

152 V. G. Levich, *Physicochemical Hydrodynamics*, Prentice-Hall, Inc., Englewood Cliffs, NJ, 1962.

153 R. Krska, K. Taga, R. Kellner, A. Messica, A. Katzir, *A new fiber optic physico-chemical sensor for chlorinated hydrocarbons in water*, Fresenius Journal of Analytical Chemistry, 1992, **342(1-2)**, .

154 R. Krska, K. Taga, R. Kellner, *Simultaneous in-situ trace analysis of several chlorinated hydrocarbons in water with an IR fiber optical system*, Journal of Molecular Structure, 1993, **294**, 1–4.

155 H. H. Nijhuis, M.H.V. Mulder, C. A. Smolders, *Removal of trace organics from aqueous solutions. Effect of membrane thickness*, Journal of Membrane Science, 1991, **61**, 99–111.

156 R. Psaume, P. Aptel, Y. Aurelle, J. C. Mora, J. L. Bersillon, *Pervaporation: importance of concentration polarization in the extraction of trace organics from water*, Journal of Membrane Science, 1988, **36**, 373–384.

157 B. Raghunath, S. T. Hwang, *Effect of boundary layer mass transfer resistance in the pervaporation of dilute organics*, Journal of Membrane Science, 1992, **65**, 147–61.

158 G. Roy, J. A. Mielczarski, *Infrared detection of chlorinated hydrocarbons in water at ppb levels of concentration*, Water Research, 2002, **36**, 1902-1908.

159 D. Louch, S. Motlagh, J. Pawliszyn, *Dynamics of Organic Compound Extraction from Water Using Liquid-Coated Fused Silica Fibers*, Analytical Chemistry, 1992, **64(10)**, 1187-1199.

160 M. Jakusch, *Polymer coated infrared evanescent wave sensors - approaches for their systematic development*, Dissertation, Vienna University of Technology, Austria, 2000.

161 S. Patankar, *Numerical Heat Transfer and Fluid Flow*, Hemisphere, Washington,DC, 1980.

162 J. Ruzicka, G. D. Marshall, *Sequential injection: a new concept for chemical sensors, process analysis and laboratory assays,* Analytica Chimica Acta, 1990 **237(2)**, 329-343.

163 M. Valcárcel, M.D. Luque de Castro, *Flow Injection Analysis, principles and applications*, Ellis Horwood, Chicester, 1987.

164 J. Ruzicka, *The second coming of flow-injection analysis*, Analytica Chimica Acta, 1992, **261(1-2)**, 3-10.

165 R. Goebel, R. Krska, R. Kellner, R. Seitz, S. Tomellini, *Investigation of different polymers as coating materials for IR/ATR spectroscopic trace analysis for chlorinated hydrocarbons in water*, Applied Spectroscopy, 1994, **48(6)**, 678–683.

166 M. Jakusch, B. Mizaikoff, R. Kellner, *Optimized Sensitive Coatings for MIR Fiber Optic Sensors*, Proc. SPIE Vol. 1997, **3105**, 283-288.

167 A. Mohacsi, Z. Bozoki, R. Niessner, Direct diffusion sampling-based photoacoustic cell for in-situ and on-line monitoring of benzene and toluene concentrations in water, Sensors and Actuators B, 2001, **79(2-3)**, 127-131.

168 D. Bunimovich, A. Katzir, *Dielectric properties of silver halide and potassium halide crystals*, Applied Optics, 1993, **32(12)**, 2045-2048.

169 S. Shalem, A. German, N. Barkay, F. Moser, A. Katzir, *Fiber and Integrated Optics*, 1997, **16(1)**, 27-54.

170 M. Maimone, Coping with groundwater contamination, Chemical Engineering, 1997, **104(10)**, 195-202.

171 E. Müller-Erlwein, *Chemische Reaktionstechnik*, B.G. Teubner (Editor), Stuttgart, 1998.

172 L. Han, T. M. Niemczyk, Y. Lu, G. P. Lopez, Chemical sensors based on surface-modified sol-gel-coated infrared waveguides, Applied Spectroscopy, 1998, **52(1)**, 119-122.

173 L. Han, T. M. Niemczyk, D. M. Haaland, G. P. Lopez, Enhancing IR detection limits for trace polar organics in aqueous solutions with surface-modified sol-gel-coated ATR sensors, Applied Spectroscopy, 1999, **53(4)**, 381-389.

174 M. Janotta, M. Karlowatz, F. Vogt, B. Mizaikoff, Sol-gel based mid-infrared evanescent wave sensors for detection of organophosphate pesticides in aqueous solution, Analytica Chimica Acta, 2003, **496(1-2)**, 339-348.

175 M. Janotta, A. Katzir, B. Mizaikoff, Sol-gel-coated mid-infrared fiber-optic sensors**,** Applied Spectroscopy, 2003, **57(7)**, 823-828.

176 C. Vogt, A. Alfreider, H. Lorbeer, J. Ahlheim, B. Feist, O. Boehme, H. Weiss, W. Babel, L. Wuensche, *Two pilot plant reactors designed for the in situ bioremediation of chlorobenzene-contaminated ground water: hydrogeological and chemical characteristics and bacterial consortia*, Water, Air, & Soil Pollution: Focus, 2002, **2(3)**, 161-170.

177 P. Wycisk, H. Weiss, A. Kaschl, S. Heidrich, K. Sommerwerk, *Groundwater pollution and remediation options for multi-source contaminated aquifers (Bitterfeld/Wolfen, Germany),* Toxicology Letters, 2003, **140-141**, 343-351.

178 H. Peter, J. Grossmann, G. Schulz-Terfloth, *Rahmensanierungskonzept des Großprojektes Bitterfeld/Wolfen*, H.-P. Luehr (Editor), Grundwassersanierung 1995, IWS Schriftenreihe 23, Erich Schmidt-Verlag, Berlin, Germany, 1995, pp. 123–128.

179 P. Merkel, G. Teutsch, H. Weiss, H. H. M. Rijnaarts, *Innovative Reactive Barrier Technologies for Regional Contaminated Groundwater*, Proceedings of the Seventh International FZK/TNO Conference on Contaminated Soil (ConSoil 2000), Vol. 1, Thomas Telford publishing, London, 2000, pp. 532–540.

180 R. Goebel, R. W. Seitz, S. A. Tomellini, R. Krska, R. Kellner, *Infrared attenuated total reflection spectroscopic investigations of the diffusion behaviour of chlorinated hydrocarbons into polymer membranes*, Vibrational Spectroscopy, 1995, **8**, 141-149.

181 E. Rosenberg, R. Kellner, *IR-ATR spectroscopic determination of the diffusion coefficients of carbohydrates in polymer matrixes*, Proc.SPIE,1992, vol. 1575, 346-347.

182 J. Comyn, *Polymer Permeability*, Elsevier Applied Science, New York, 1985.

183 J. M. Vanguard, *Liquid Transport Processes in Polymeric Materials: Modeling and Industrial Applications*, Prentice-Hall, Engelwood Cliffs, NJ, 1991.

184 U. Mukai, K. K. Gleason, A. S. Argon, R. E. Cohen*, Poly(Dimethylsiloxane)/Nylon-6 Block-Copolymers - Molecular Mobility At the Interface*. Macromolecules 1995, **28(14)**, 4899-4903.

185 G. T. Fieldson, T. A. Barbari, *The use of attenuated total reflection FTIR spectroscopy to characterize penetrant diffusion in polymers*, Polymer, 1993, **34(6)** 1146-1153.

186 C. M. Balik, W. H. Siemendinger, *An attenuated total reflectance cell for analysis of small moclecule diffusion in polymer thin films with Fourier-transform infrareed spectroscopy*, 1998, **39(20)**, 4723-4728.

187 P. Peterkova, L'. Lapcik Jr*., Determination of the diffusion coefficient of water into atelocollagen type I thin films by attenuated total reflection Fourier transform infared spectroscopy*, Colloid Polymer Science, 2000, **278(10)**, 1014-1016.

188 R. Howley, B.D. MacCraith, K. O'Dwyer, P. Kirwan, P. McLoughlin, *A study of the factors affecting the diffusion of chlorinated hydrocarbons into polyisobutylene and*

polyethylene-co-propylene for evanescent wave sensing, Vibrational Spectroscopy 2003, **31(2)**, 271-278.

189 B. Murphy, P. Kirwan, P. McLoughlin, *Study of the impact of penetrant characteristics upon diffusion into Teflon membranes to further assess the performance of an ATR/FTIR sensor*, Analytical and Bioanalytical Chemistry, 2003, **377(1)**, 195-202.

190 Y. A. Elabd, M. G. Baschetti, T. A. Barbari, *Time-Resolved Fourier Transform Infrared/Attenuatetd Total Reflection Spectroscopy for the Measurement of Molecular Diffusion in Polymers*, Journal of Polymer Science Part B, 2003, **41(22)**, 2794-2807.

191 C. Phillips, *Model-based design optimization of heterogeneous micro-reactors and chemical*, MS Thesis Georgia Institute of Technology, 2003.

192 M. Janotta, F. Vogt, H.-S. Voraberger, W. Waldhauser, J.-M. Lackner, C. Stotter, M. Beutl, B. Mizaikoff, *Direct Analysis of Oxidizing Agents in Aqueous Solution with Attenuated Total Reflectance Mid-Infrared Spectroscopy and Diamond-like Carbon Protected Waveguides***,** Analytical Chemistry, 2004, **76(2)**, 384-391.

193 Permanent website: The United Nations Mine Action Services, http://www.un.org/Depts/dpko/mine.

194 U.S. Department of State, *Hidden killers 1998: The global landmine crisis*, Bureau, of Political–Military Affairs, Office of Humanitarian Demining Programs. (permanent website): http://www.state.gov/www/global/arms/rpt_9809_demine_toc.html, 1998.

195 J. Paik, C. P. Lee, M. A. Abidi, *Image processing-based mine detection techniques: A review*, Subsurface Sensing Technologies and Applications, 2002, **3(3)**, 153-202.

196 P. Machler, *Detection technologies for anti-personnel mines*, Proceedings Symposium on Autonomous Vehicles in Mine Countermeasures, 1995, **6**, 150–154.

197 J. Jr. Stepanic, H. Wustenberg, V. Krstelj, H. Mrasek, *Contribution to classification of buried objects based on acoustic impedance matching*, Ultrasonics, 2003, **41(2)**, 115-123.

198 L. Kempen, A. Katarzin, Y, Pizurion, C. Corneli, H. Sahli, *Digital signal image processing for mine detection, Part 2: Ground based approach*, Proceedings Euro Conference on Sensor Systems and Signal Processing Techniques applied to the Detection of Mines and Unexploded Ordnance, 1999, 54–59.

199 K. Russell, J. McFee, W. Sirovyak, *Remote performance prediction for infrared imaging of buried mines*, Proceedings SPIE Detection and Remediation Technologies for Mines and Minelike Targets II, 1997, **3079**, 762–769.

200 J. Stepanic, M. Malinovec, S. Svaic, V. Krstelj, *Parameterisation of non-homogeneities in buried object detection by means of thermography*, Infrared Physics & Technology, 2004, **45(3)**, 201-208.

201 M. Lundberg, I.Y.H. Gu, *A 3-D matched filter for detection of land mines using spatio-temporal thermal modelling*, Detection and Remediation Technologies for Mines and Minelike Targets V, SPIE Proceedings, 2000, **4038**, 179–188.

202 I. Boras, M. Malinovec, J. Stepanic, S. Svaic, *Modelling of buried object detection using thermography*, QIRT 2000, Reims, Proceedings, 2002, 176–181.

203 UN Mine Action Service, International Mine Action Standards, Chapter 9–Clearance requirements. Permament website: http://www.mineactionstandards.org/IMAS_archive/Final/09.10.pdf.

204 P. Pregowski, W. Swiderski, R. Walczak, *Surface and volume effects in thermal signatures of buried mines: experiment and modeling*, QIRT 1998, Lodz, Proceedings, 1998, 233–238.

205 A. F. H. Goetz, G. Vane, J. Solomon, B. N. Rock, *Imaging Spectrometry for Earth Remote Sensing*, Science, 1985*,* **228,** 1147–1153.

206 A. F. H. Goetz, "Imaging Spectrometry for Remote Sensing: Vision to Reality in 15 Years" Proceedings SPIE Aerosense Symposium, 1995, **2480**, 2–13.

207 A. F. H. Goetz, B. Curtiss, *Hyperspectral Imaging of the Earth: Remote Analytical Chemistry in an Uncontrolled Environment,* Field Analytical Chemistry and Technology, 1996, **1(2)**, 67-76.

208 J. W. Boardman, *Automated Spectral Unmixing of AVIRIS Data Using Convex Geometry Concepts*, Summaries of the Fourth Annual JPL Airborne Geoscience Workshop, JPL Pub. 1993, **93**, 53–56.

209 G. Vane, R. O. Green, T. G. Chrien, H. T. Enmark, E. G. Hansen, and W. M. Porter, *The Airborne Visible/Infrared Imaging Spectrometer (AVIRIS*), Remote Sensing of Environment, 1993, **44**, 127–144.

210 R. A. Schowengerdt, *Remote Sensing* Academic Press, 2nd edition, San Diego, USA, 1997.

211 W. L. Wolfe, *Introduction to Imaging Spectrometers,* D. C. O'Shea (Editors), SPIE, Bellingham, Washington USA, 1997.

212 T. M. Lillesand, R. W. Kiefer, J. W. Chipman, *Remote Sensing and Image Interpretation,* Wiley, New York, USA, 2003.

213 Permanent website: http://rst.gsfc.nasa.gov/Homepage/Homepage.html.

214 Permanent website:
http://www.ccrs.nrcan.gc.ca/ccrs/learn/tutorials/fundam/fundam_e.html.

215 M. M. Elcombe, *Some aspects of the lattice dynamics of quartz*, Proceedings of the Physics Society of London, 1967, **91**, 947-958.

216 L. S. Walter, J. W. Salisbury, *Spectral characterization of igneous rocks in the 8 to 12 micrometers region,* Journal of Geophysical Research, 1989, **94**, 9203-9213.

217 V. C. Farmer (Editor), *The Infrared Spectra of Minerals* Monograph No. 4, Mineralogical Society, London, UK, 1974.

218 Q. Williams, *Infrared, Raman and Optical Spectroscopy of Earth Materials,* T. J. Ahrens (Editor), *Mineral physics and crystallography : a handbook of physical constants*, AGU, Washington, DC, USA, 1995.

219 D. B. Nash, J. W. Salisbury, *Infrared reflectance spectra of plagioclase feldspars*: Geophysical Research Letters, 1991, **18**, 1151-1154.

220 J. W. Salisbury, D. M. D'Aria, E. J. Jarosewich, *Midinfrared (2.5-13.5 micrometers) reflectance spectra of powdered stony meteorites,* Icarus, 1991, **92**, 280-297.

221 J. W. Salisbury, L. S. Walter, N. Vergo, Dana M. D'Aria, *Infrared (2.1 – 25 micrometers) Spectra of Minerals*, Johns Hopkins University Press, Baltimore, MD , USA, 1991.

222 F. Seitz, D. Turnbull (Editors), *Solid State Physics*, Academic Press, New York, 1966, **18**, 274–420. (see also, 1966, **19**, 1-134).

223 R. J. Elliott, J. A. Krumhansl, P. L. Leath, *Theory and properties of randomly disordered crystals and related physical systems*, Reviews of Modern Physics, 1974, **46(3)**, 465-543.

224 F. L. Galeener, G. Lucovsky, *Longitudinal optical vibrations in glasses: germania and silica*, Physical Review Letters, 1976, **37(22)**, 1474-1478.

225 F. L. Galeener, *Band limits and the vibrational spectra of tetrahedral glasses*, Physical Review B, 1979, **19(8)**, 4292-4297.

226 P. H. Gaskell, D. W. Johnson, *The optical constants of quartz, vitreous silica and neutron-irradiated vitreous silica (I)*, Journal of Non-Crystalline Solids, 1976, **20(2)**, 153-169.

227 P. H. Gaskell, D. W. Johnson, *The optical constants of quartz, vitreous silica and neutron-irradiated vitreous silica. (II). Analysis of the infrared spectrum of vitreous silica*, Journal of Non-Crystalline Solids, 1976, **20(2)**, 171-191.

228 J. C. Phillips, *Spectroscopic and morphological structure of tetrahedral oxide glasses*, Solid State Physics, 1982, **37**, 93-171.

229 S. W. De Leeuw, M. F. Thorpe, *Coulomb splittings in glasses*, Physical Review Letters, 1985, **55(26)**, 2879-2882.

230 F. Ruiz, J. R. Martinez, J. Gonzalez-Hernandez, *A simple model to analyze vibrationally decoupled modes on SiO2 glasses,* Journal of Molecular Structure, 2002, **641(2-3)**, 243-250.

231 I. W. Boyd, *Deconvolution of the infrared absorption peak of the vibrational stretching mode of silicon dioxide: evidence for structural order?*, Applied Physics Letters, 1987, **51(6)**, 418-420.

232 D. W. Berreman, *Infrared Absorption at Longitudinal Optic Frequency in Cubic Crystal Films*, Physical Review, 1963, **130(6)**, 2193–2198.

233 J. E. Olsen, F. Shimura, *Infrared reflection spectroscopy of the silica-silicon interface*, Journal of Applied Physics, 1989, **66(3)**, 1353-1358.

234 I. W. Boyd, J. I. B. Wilson, *A study of thin silicon dioxide films using infrared absorption techniques,* Journal of Applied Physics, 1982, **53(6)**, 4166-4172.

235 C. T. Kirk, *Quantitative analysis of the effect of disorder-induced mode coupling on the infrared absorption in siclica*, Physical Review B, 1988, **28(2)**, 1255-1273.

236 O. E. Piro, E. E. Castellano, S. R. Gonzalez, *Attenuated total-reflectance spectra of strongly absorbing anisotropic single cystals: Trigonal α-quartz*, Physical Review B, 1988, **38(12)**, 8437–8443.

237 R. M. Almeida, C. G. Pantano, *Structural investigation of silica gel films by infrared spectroscopy*, Journal of Applied Physics, 1990, **68(8)**, 4225-4232.

238 H. R. Philips, *The infrared optical properties of SiO2 and SiO2 layers on silicon*, Journal of Applied Physics, 1979, **50(2)**, 1053-1057.

239 M. C. Payne, J. C. Inkson, *Longitudinal-optic-transverse-optic vibrational mode splittings in tetrahedral network glasses*, Journal of Non-Crystalline Solids, 1984, **68(2-3)**, 351-360.

240 A. Lehmann, L. Schumann, K. Huebner, *Optical phonons in amorphous silicon oxides. II. Calculation of phonon spectra and interpretation of the IR transmission of silicon oxide (SiOx)*, Physica Status Solidi B: Basic Research, 1984, **121(2)**, 505-511.

241 J. Wang, B. Zou, M. El-Sayed, *A Comparison between the polarized Fourier-transform infrared spectra of aged porous silicon and amorphous silicon dioxide films on Si (100) surface*, Journal of Molecular Structure, 1999, **508(1-3)**, 87-96.

242 J. L. Gole, F. P. Dudel, D. Grantier, D. A. Dixon, *Origin of porous silicon photoluminescence: Evidence for a surface bound oxyhydride-like emitter*, Physical Review B: Condensed Matter, 1997, **56(4)**, 2137-2153.

243 R. M. Almeida, *Detection of LO modes in glass by infrared reflection spectroscopy at oblique incidence*, Physical Review B, 1992, **45(1)**, 161-170.

244 B. Harbecke, B. Heinz, P.Grosse, *Optical Properties of Thin Films and the Berreman Effect*, Applied Physics A, 1985, **38**, 263-267.

245 K. Huebner, L. Schumann, A. Lehmann, H. H. Vajen, G. Zuther, *Detection of LO and TO phonons in amorphous silicon dioxide films by oblique incidence of IR light*, Physica Status Solidi B: Basic Research, 1981, **104(1)**, K1-K5.

246 R. M. Almeida, T. A. Guiton, C. G. Pantano, *Detection of longitudinal optical mode in vitreous silica by infrared diffuse reflectance spectroscopy*, Journal of Non-Crystalline Solids, 1990, **119(2)**, 238-241.

247 P. Innocenzi, P. Falcaro, D. Grosso, F. Babonneau, *Order-Disorder Transitions and Evolution of Silica Structure in Self-Assembled Mesostructured Silica Films Studied through FTIR Spectroscopy*, Journal of Physical Chemistry B, 2003, **107(20)**, 4711-4717.

248 J. A. Moreno, B. Garrido, J. Samitier, J. R. Morante, *Analysis of geometrical effects on the behavior of transverse and longitudinal modes of amorphous silicon compounds,* Journal of Applied Physics, 1997, **81(4)**, 1933-1942.

249 C. Z. Tan, J. Arndt, *Interaction of longitudinal and transverse optic modes in silica glass*, Journal of Chemical Physics, 2000, **112(13)**, 5970-5974.

250 E. Courtens, M. Foret, B. Hehlen, R. Vacher, *The vibrational modes of glasses*, Solid State Communications, 2001, **117**, 187-200.

251 N. Rochat, A. Chabli, F. Bertin, C. Vergnaud, P. Mur, S. Petitdidier, P. Besson; *Infrared analysis of thin layers by attenuated total reflection spectroscopy*, Material Science Eng., 2003, **B102**, 16–21.

252 I. I. Shaganov, T. S. Perova, R. A. Moore, K. Berwick, *Spectroscopic characteristics of SiO and SiO_2 solid films: Assignment and local field effect influence*, Journal of Materials Science: Materials in Electronics, 2001, **12**, 351-355.

253 J. Sarnthein, A. Pasquarello, R. Car, *Origin of the high-frequency doublet in the vibrational spectrum of vitreous SiO_2* , Science, 1997, **275 (5308),** 1925-1928.

254 B. C. Trasferetti, C. U. Davanzo, *s- and p-polarized infrared specular reflectance of vitreous silica at oblique incidences: detection of LO modes*. Applied Spectroscopy, 2000, **54(4)**, 502-507.

255 R. J. Bell, P. Dean, *Properties of vitreous silica. Analysis of random network models*, Nature, 1966, **212(5068)**, 1354-1356.

256 *The key problem for calculating individual* ed. M. Garbuny, Optical Physics, Academic Press, NY, 1965

257 A. M. Efimov, *Vibrational spectra, related properties, and structure of inorganic glasses*, Journal of Non-Crystalline Solids, 1999, **253**, 95-118.

258 A. M. Efimov, *Quantitative IR spectroscopy Applications to studying glass structure and properties,* Journal of Non-Crystalline Solids, 1996, **203**, 1-11.

259 T. G. Mayerhoefer, H. H. Dunken, R. Keding, C. Ruessel, *Interpretation and modeling of IR-reflectance spectra of glasses considering medium range order*, Journal of Non-Crystalline Solids, 2004, **333**, 172-181.

260 J. W. Salisbury, A. Wald, D. M. D'Aria, *Thermal infrared remote sensing and Kirchhoff's law 1. Laboratory measurements*, Journal Geophysical Research,1994, **99(11)**, 897–911.

261 S. M.Abo-Naf, F. H. El Batal, M. A. Azooz, *Characterization of some glasses in the system SiO_2-Na_2O-RO by infrared spectroscopy*, Materials Chemistry and Physics, 2003, **77(3)**, 846-852.

262 C. I. Merzbacher, W. B. White, *The structure of alkaline earth aluminosilicate glasses as determined by vibrational spectroscopy*, Journal of Non-Crystalline Solids, 1991, **130(1)**, 18-34.

263 A. M. Efimov, *IR fundamental spectra and structure of pyrophosphate glasses along the 2ZnO-P_2O_5-2Me_2O-P_2O_5 join (Me being Na and Li), Journal of Non-Crystalline Solids*, 1997, **209(3)**, 209-226.

264 T. Yoshidome, H. Kusumoto, O. Kuroki, S. Kamata, *Application of the attenuated-total-reflection technique to the measurement of silica-gel particle size*, Chemistry Letters, 1998, **(8)**, 747-748.

265 D. Sanders, W. B. Person, L. L. Hench, *Quantitatiive analysis of glass structure with the use of infrared reflection spectra* Applied Spectroscopy, 1974, **28(3)**, 247-255

266 W. J. Dell, P. J. Bray, S. Z. Xiao, *Boron-11 NMR studies and structural modeling of sodium borosilicate (Na2O-B2O3-SiO2) glasses of high soda content,* Journal of Non-Crystalline Solids, 1983, **58(1)**, 1-16.

267 J. Serra, P. Gonzalez, S. Liste, C. Serra, S. Chiussi, B. Leon, M. Perez-Amor, H. O. Ylanen, M. Hupa, *FTIR and XPS studies of bioactive silicate-based glasses,* Journal of Non-Crystalline Solids 2003, **332(1-3)**, 20-27.